NASA/CR—2006-214091

NASA Hydrogen Research for Spaceport and Space Based Applications

Tim Anderson
University of Florida, Gainesville, Florida

July 2006

NASA STI Program . . . in Profile

Since its founding, NASA has been dedicated to the advancement of aeronautics and space science. The NASA Scientific and Technical Information (STI) program plays a key part in helping NASA maintain this important role.

The NASA STI Program operates under the auspices of the Agency Chief Information Officer. It collects, organizes, provides for archiving, and disseminates NASA's STI. The NASA STI program provides access to the NASA Aeronautics and Space Database and its public interface, the NASA Technical Reports Server, thus providing one of the largest collections of aeronautical and space science STI in the world. Results are published in both non-NASA channels and by NASA in the NASA STI Report Series, which includes the following report types:

- TECHNICAL PUBLICATION. Reports of completed research or a major significant phase of research that present the results of NASA programs and include extensive data or theoretical analysis. Includes compilations of significant scientific and technical data and information deemed to be of continuing reference value. NASA counterpart of peer-reviewed formal professional papers but has less stringent limitations on manuscript length and extent of graphic presentations.

- TECHNICAL MEMORANDUM. Scientific and technical findings that are preliminary or of specialized interest, e.g., quick release reports, working papers, and bibliographies that contain minimal annotation. Does not contain extensive analysis.

- CONTRACTOR REPORT. Scientific and technical findings by NASA-sponsored contractors and grantees.

- CONFERENCE PUBLICATION. Collected papers from scientific and technical conferences, symposia, seminars, or other meetings sponsored or cosponsored by NASA.

- SPECIAL PUBLICATION. Scientific, technical, or historical information from NASA programs, projects, and missions, often concerned with subjects having substantial public interest.

- TECHNICAL TRANSLATION. English-language translations of foreign scientific and technical material pertinent to NASA's mission.

Specialized services also include creating custom thesauri, building customized databases, organizing and publishing research results.

For more information about the NASA STI program, see the following:

- Access the NASA STI program home page at *http://www.sti.nasa.gov*

- E-mail your question via the Internet to *help@sti.nasa.gov*

- Fax your question to the NASA STI Help Desk at 301–621–0134

- Telephone the NASA STI Help Desk at 301–621–0390

- Write to:
  NASA STI Help Desk
  NASA Center for AeroSpace Information
  7121 Standard Drive
  Hanover, MD 21076–1320

NASA/CR—2006-214091

NASA Hydrogen Research for Spaceport and Space Based Applications

Tim Anderson
University of Florida, Gainesville, Florida

Prepared under Grant NAG3–2930

National Aeronautics and
Space Administration

Glenn Research Center
Cleveland, Ohio 44135

July 2006

This report contains preliminary findings, subject to revision as analysis proceeds.

Level of Review: This material has been technically reviewed by NASA technical management.

Available from

NASA Center for Aerospace Information
7121 Standard Drive
Hanover, MD 21076–1320

National Technical Information Service
5285 Port Royal Road
Springfield, VA 22161

Available electronically at http://gltrs.grc.nasa.gov

Contents

NASA Hydrogen Research for Spaceport and Space Based Applications

Tim Anderson
University of Florida
Gainesville, Florida 32611

Introduction

The NASA FY03 grant is the second funding opportunity for hydrogen research at selected Florida universities. The University of Florida has developed a very strong hydrogen-technology base with two consecutive NASA grants.

The goal of this effort for is to continue the leading edge research and technology development into hydrogen production processes, sensors and instrumentation, cryogenic transport and storage solutions.

Figure 1 provides the grant budget distribution and its comparison to the previous grant.

The budget for this research grant includes 15 research projects, education and outreach activities, system and trade studies, and project management.

Twenty-two Co-Principal Investigators and a number of post-docs and graduate students have actively worked on 15 research tasks. The objectives and the accomplishments of their research projects are given in this report.

The four research thrusts, their faculty leaders, as well as outreach activities are detailed below.

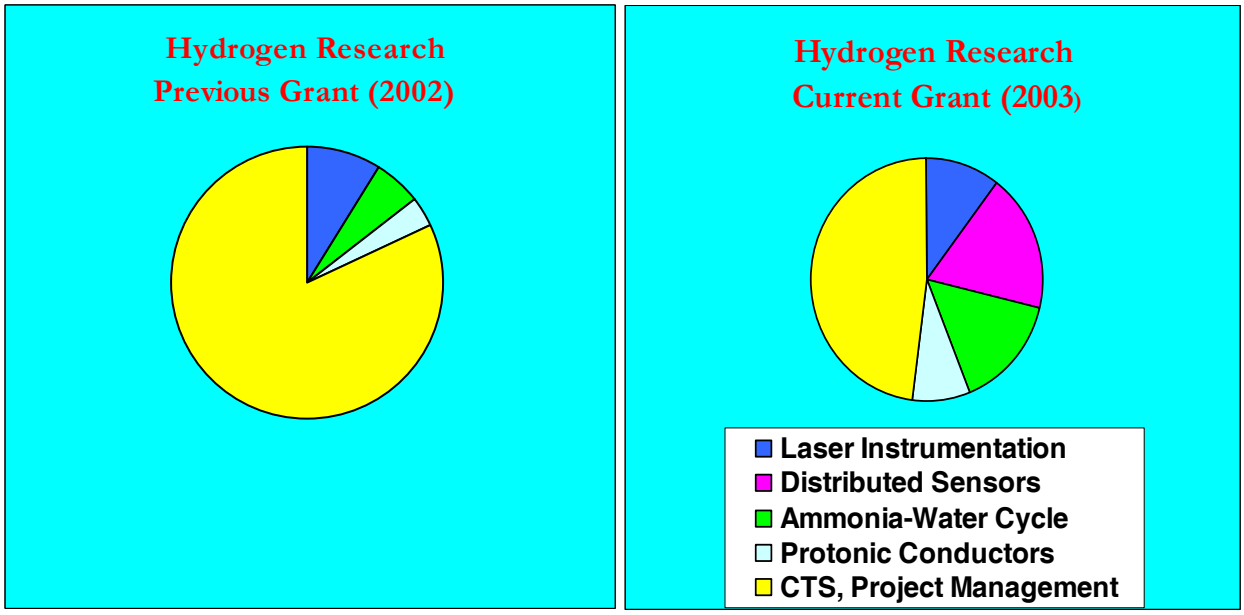

CTS: Cryogenic Transport and Storage

Figure 1.—NASA Hydrogen Research Grant Budget at University of Florida.

Hydrogen Production
Skip Ingley

A local hydrogen production may eliminate some of the traditional hazards of NASA's use of hydrogen. For example, for each space-shuttle launch, hydrogen is shipped to the Kennedy Space Center (KSC) by Air Products, Inc. from their New Orleans facility. This means some 50 tractor-trailers must drive approximately 700 miles to deliver hydrogen for every launch. By creating a local hydrogen-production facility, the safety hazards of long-distance transportation can be avoided and the cost of hydrogen will be reduced.

There are two hydrogen production processes under this grant. The goal of the Ammonia-Water Combined Power and Refrigeration Cycle project is to design and construct a combined cycle that creates 5 kW of electricity, a refrigeration effect and 18 L/min hydrogen gas from a low temperature heat source and to house the system within a mobile test facility. The mobile facility will serve as an educational tool to demonstrate various uses for hydrogen and methods for its production around the state.

The system and trade studies were performed for the Ammonia-Water Combined Power and Refrigeration Cycle by using ASPEN chemical process modeling software. The details are given in this report.

The overall objective of the Advanced Protonic Conductors project is to demonstrate the feasibility of producing hydrogen from hydrocarbon based fuels using advanced proton conducting membrane. The objectives of this phase are to develop thin film proton conducting membranes on porous supports and to advance the fundamental understanding of these materials. The anticipated result is demonstration of high hydrogen fluxes through these thin supported membranes.

Distributed Sensors for Hydrogen-Leak Detection
Mark Law and Jenshan Lin

Hydrogen storage and transport requires careful leak monitoring to prevent dangerous explosions and fires. Ideally, this can be accomplished with a set of small sensors mounted along hydrogen transport piping and storage vessels. These sensors should be able to communicate with one another so that a leak-detection message can be passed along to a control node that alerts human operators to the location and magnitude of the leak. These sensors would be small, inexpensive, and consume little power to enable long operation on a single battery.

The goal of the distributed sensors for hydrogen-leak detection project is to demonstrate novel hydrogen sensors including wide energy band-gap based sensors and biological assays sensors. By using low power solid state sensors, the integrated wireless hydrogen sensor can be made compact and lightweight to facilitate a fast deployment of a hydrogen leak detection network. This program will focus on the development of the pieces required for a hydrogen leak detection sensor network.

In the beginning of the project period, the first prototype sensor needed to operate at elevated temperature. Through the improvement in device structure, room-temperature (25 °C) sensing using AlGaN/GaN MOS-HEMT sensor was achieved. Toward the end of this project period, the novel ZnO nanorod sensor, which has much lower power consumption yet better sensitivity, was developed. This paves the way for the development of self-powered wireless hydrogen nano-sensor to be developed in the next phase.

Laser Instrumentation for Hydrogen-Leak Detection
David Hahn

Research in laser instrumentation for hydrogen-leak detection includes Raman spectroscopy, Raleigh and Mei light scattering techniques as well as work on laser-induced breakdown spectroscopy (LIBS). The goal is to develop a unit that can be used for field testing. The proposed research stems from NASA's

long standing efforts to develop and implement real-time hydrogen leak detection schemes in support of Space Shuttle operations.

Cryogenic Transport and Storage
James Klausner

Cryogenic fluids have found many practical applications in today's world, from cooling superconducting magnets to fueling launch vehicles. In many of these applications the cryogenic fluid is initially introduced into piping systems that are in excess of 150 K higher than the fluid. This leads to voracious evaporation of the fluid and significant pressure fluctuations, which is accompanied by thermal contraction of system components. This process is known as chilldown, and although it was first investigated more than 4 decades ago, very little data are available on the momentum and energy transport during this transient process. Consequently, the development of predictive models for the pressure drop and heat transfer coefficient has been hampered. In order to address this deficiency, an experimental facility has been constructed that enables the flow structure to be observed while temperatures and pressures at various locations are measured.

Research in terrestrial and in-space cryogenic transport and storage focuses on optimal solutions for the transportation and storage of cryogenic fluids at NASA's KSC. The research also addresses technical issues regarding in-space transport and storage of cryogenic hydrogen.

Outreach
Howard Beck and Canan Balaban

The education/outreach effort consists of a website. The website documents and describes hydrogen research activities carried out at the University of Florida and other universities that may be collaborating with UF. All researchers involved, their research activities, and publications reside in the website. The hydrogen technology web course is also posted at the web site. The website connects all the researchers and improves communications within the program and with external hydrogen and energy research communities. The target audience for this web site is research professionals, students, the public, and government agencies.

The web site is functional and in use. In addition to the NASA Supported Hydrogen Research, a web site on "UF Faculty Expertise in Energy" was developed. The links for both sites are given below:

http://www.mae.ufl.edu/NASAHydrogenResearch
http://www.mae.ufl.edu/Energy

1. System and Trade Studies

Consultant: Dale W. Kirmse

Background

The system and trade studies were performed for the Ammonia-Water Combined Power and Refrigeration Cycle which is one of the Hydrogen Production Processes.

Dale Kirmse, recently retired Professor from UF's Chemical Engineering Department, worked as a consultant to perform simulation, system/technology trades studies. ASPEN (Aspen Technology, Inc.) chemical process modeling software was used to perform the studies.

Accomplishments

Since the Florida Solar Energy Center (FSEC) has a number of hydrogen production processes under way, the system and trade study efforts were coordinated. UF team visited FSEC group, to establish comparison criteria for the hydrogen production processes under this grant.

Dale Kirmse submitted 4 reports. A summary of each report is given below.

Report 1: Ammonia-Water Combined Cycle - Model 1

Summary

Initial steady state ASPEN models of the Ammonia-Water Combined Power and Refrigeration Cycle process have been developed. Simple process modules and simplifying operation assumptions were used in this initial model. Heater modules were used to simulate heat exchangers and a stream splitter block was used to simulate the rectifier. Simplifying assumptions included no pressure losses through operating equipment. The recommended computational sequence is to break the cycle between the boiler and separation operations to form an equivalent open cycle, steady state model. The process flow sheet is given below.

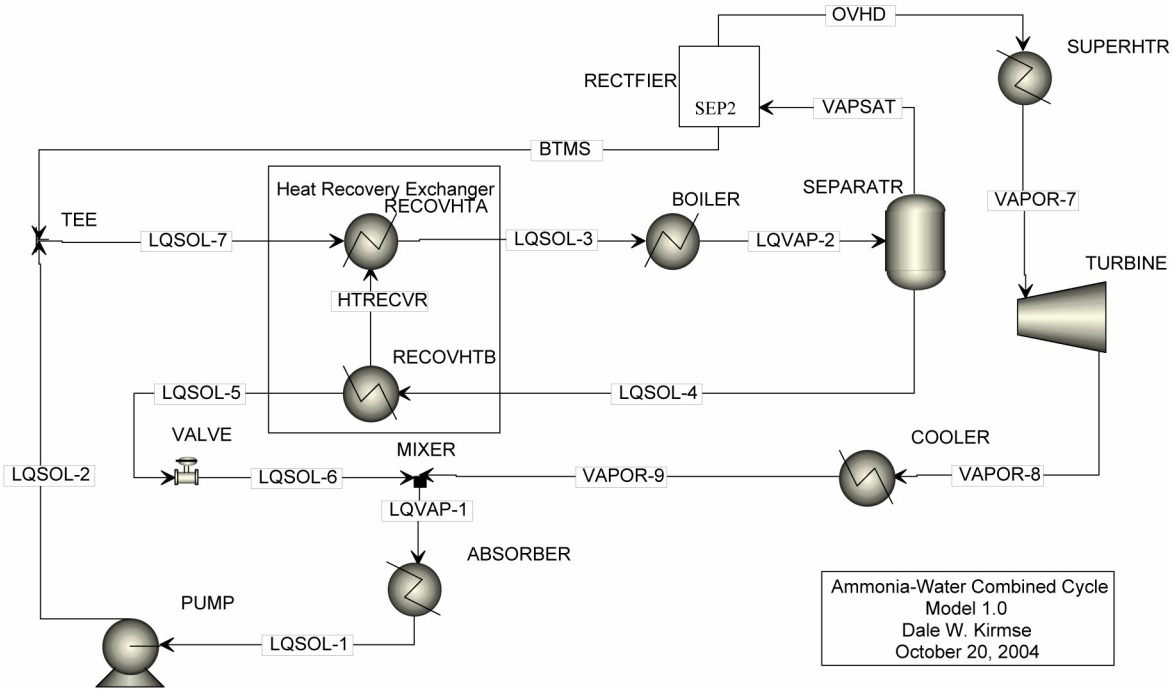

Figure 1.—Ammonia-water combined cycle model 1.0 flow sheet.

Report 2: Ammonia-Water Combined Cycle - Model 2

Summary

An open cycle, steady state ASPEN model of the Ammonia-Water Combined Power and Refrigeration Cycle has been developed. The simplistic modules used in the initial model have been replaced with rigorous modules. This model represents the demonstration facility current design. The process flow sheet is given below.

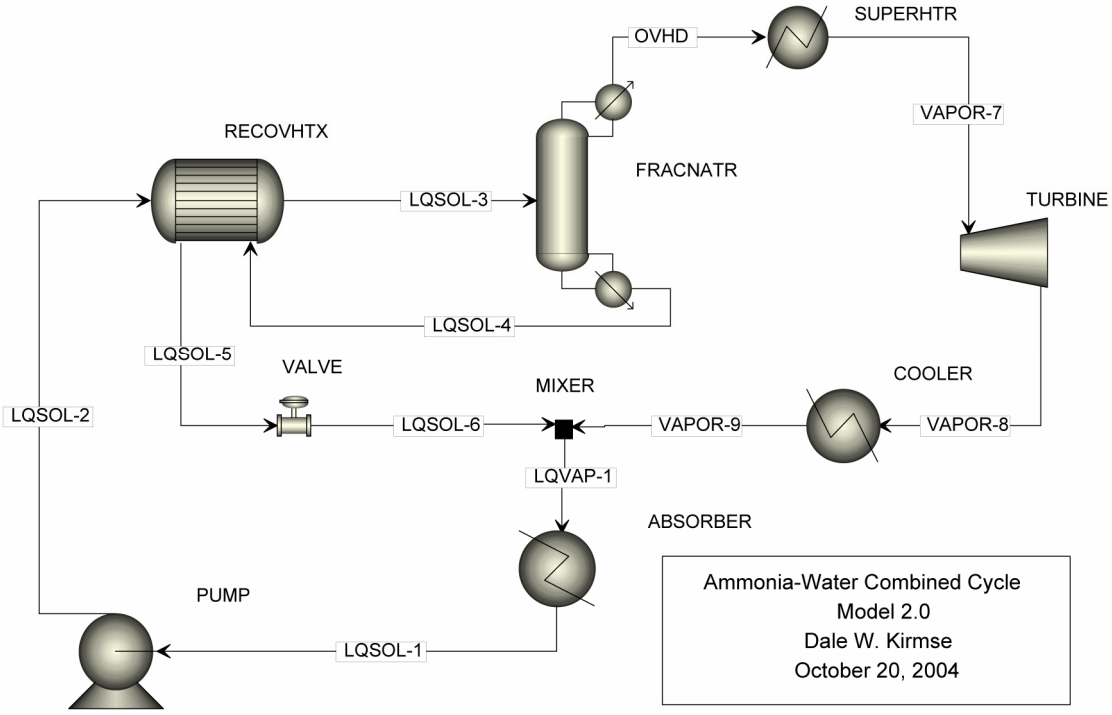

Figure 2.—Ammonia-water combined cycle model 2.0 flow sheet.

Report 3: Ammonia-Water Combined Cycle - Response Exploration

Summary

The responses to changes in parameter values in the open cycle, steady state ASPEN Model 2 of the Ammonia-Water Combined Power and Refrigeration Cycle have been studied. The sensitivity study found that four of the independent variables (the ammonia fraction of the strong aqueous solution, absorber pressure, fractionator pressure, and reboiler temperature) evoked strong responses to cycle performance. The process flow sheet and turbine exhaust temperature sensitivity to pressure are given in figures 3 and 4.

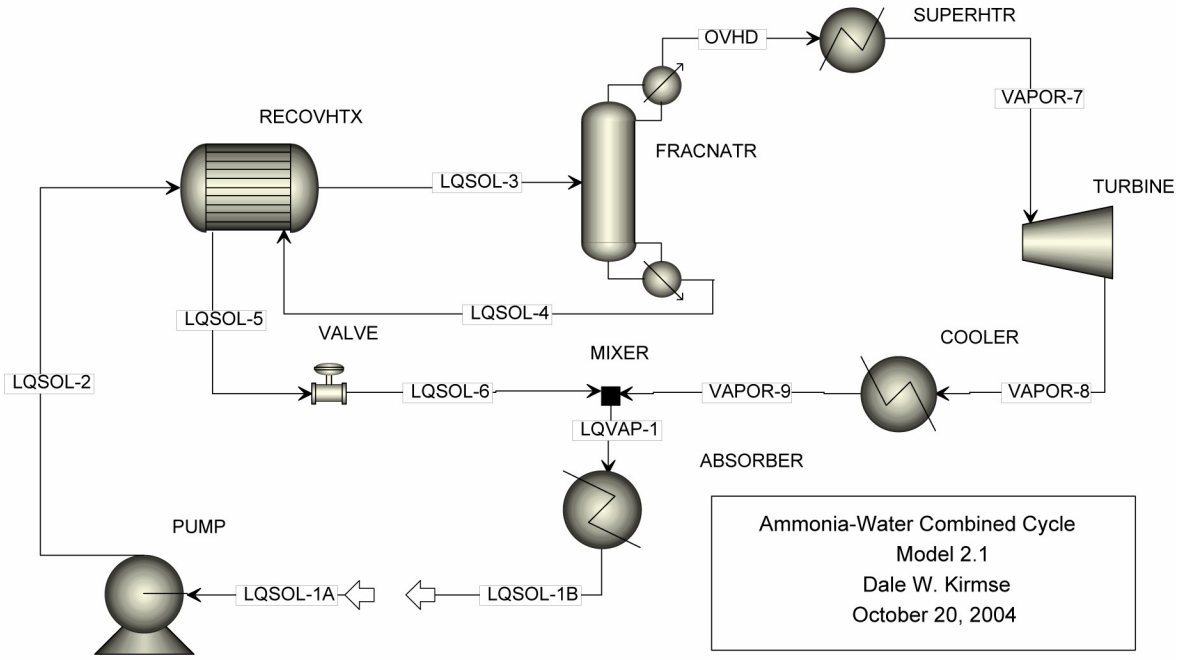

Figure 3.—Ammonia-water combined cycle model 2.1 flow sheet.

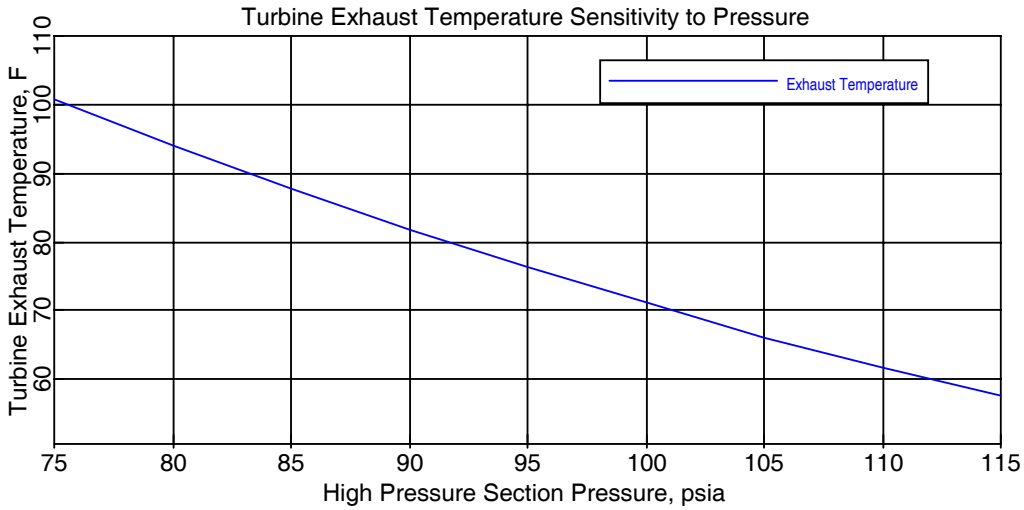

Figure 4.—Turbine exhaust temperature sensitivity to high pressure section pressure.

Report 4: Ammonia-Water Combined Cycle - Module/Process Analysis

Summary

Steady state ASPEN models of individual unit operations and processes of the Ammonia-Water Combined Power and Refrigeration Cycle were developed and analyzed. Each of the modules was inserted on a flow sheet and tested to make sure that the individual blocks and streams behaved as expected.

The reports submitted by Dale W. Kirmse are very detailed. Please contact Canan Balaban (cbalaban@ufl.edu) to request the detailed reports.

2. Hydrogen Production Processes

Faculty Lead: Skip Ingley, Mechanical and Aerospace Engineering

Project Title: The Ammonia-Water Combined Power and Refrigeration Cycle

Task PI: H.A. (Skip) Ingley, P.E., Mechanical and Aerospace Engineering
Graduate Students: Robert Reed, Gerard O'Sullivan, Mark Taurence, Numpol Sathonpattanakij, Allen Mathis, and Sirisha Govindaraju

Project Goals

The project goal is to design and construct a combined cycle that creates 5kW of electricity, a refrigeration effect and 18 L/min hydrogen gas from a low temperature heat source and to house the system within a mobile test facility. The mobile facility will serve as an educational tool to demonstrate various uses for hydrogen and methods for its production around the state.

Accomplishments

The project includes several sub-tasks: a 1st law analysis of the system, the design and construction of the combined cycle shown in figure 1, including the heating and cooling water systems, and the design of the mobile test facility with a viewing area and a demonstration of how the device can produce hydrogen and cooling, with subsequent conversion to electricity with a fuel cell.

Constraints have been placed on pressures and temperatures of the system to both simulate a low-temperature heat source such as that available from flat-plate solar collectors or waste heat and produce 5 kW of electricity in the generator. The high and low cycle pressures are defined as 110 and 40 psig. The temperatures exiting the boiler/generator and absorber are fixed at 170 and 100 °F, respectively. Results from the 1st law analysis for the thermodynamic analysis show a required heat input 387.6 MBTUH and heat rejection of 372.9 MBTUH to produce 4600 BTU/h of cooling and 5.6 kW of shaft power at the turbine (0.6 kW of which is required to overcome the inefficiency of the generator). Assumptions for the 1st law analysis are zero pressure drops through the pipes and components, negligible pump work, 80 percent isentropic turbine efficiency, 90 percent electric generator efficiency, and pure ammonia vapor exiting the rectifier.

The 1st law analysis was used to design each component of the combined cycle. Design is given below for each of the following: absorber, vapor generator/separator, rectifier, super-heater, cooler, turbine/generator set, electrolyzer, power conditioner, fuel cell, and process water systems (heating hot water and cooling water).

Absorber: A falling film absorber is being used due to the large liquid to vapor interface and large cooling area. It is constructed from flat plate heat exchanger plates, such as those commonly used in the dairy industry and thus readily available. The pressure vessel is constructed from mild steel. An alternative absorber was also designed using a packed column/heat exchanger arrangement. The basic cycle can accommodate either of these absorber packages. The study and design of the falling film absorber was the subject of a Master's thesis for Sirisha Govindaraju who graduated in 2004.

Vapor Generator/Separator: The vapor generator is a shell and tube type heat exchanger. A commercially available heat exchanger has been purchased and modified to serve as the vapor generator.

Rectifier: The rectifier consists of a vertical length of pipe packed with a material such as burl saddles, followed by a cooling coil. The purity of the ammonia vapor is critical to the cooling capacity, so

the rectifier stack has a modular construction for simple modification. It is mounted directly above the vapor generator to allow the reflux to be re-boiled.

Super-heater: As superheating is detrimental to cooling capacity, the superheater is used to reheat the rectified vapor up to the original boiler temperature. It is part of the rectifier stack, and identical in construction to the cooling coil.

Cooler: The cooler is used to cool air using the cold vapor at the turbine exit. An intercooler from a small diesel truck is used as an air-to-air heat exchanger.

Turbine: The turbine is of a scroll type because of its compact size and steady power output. A scroll compressor was purchased and modified to operate as an expander. Testing of this device has been conducted to determine its efficiency and operating characteristics. Any efficiency below 80 percent will cause the complete loss of cooling capability for the specified operating conditions. The scroll compressor has proven to be inadequate for the efficiencies required. A new scroll expander was designed to provide the efficiencies required. The subject of this investigation led to a Master's thesis by Robert Reed (2005). This work was recently presented to the 2005 World Solar Congress held in Orlando Florida and is published in the Congress proceedings.

Electric generator: The generator provides 400 Hz power, requiring the researchers to provide power conditioning.

Electrolyzer: The electrolyzer is required to produce hydrogen with a standard purity of 99.9 percent at 40 psig operating pressure. The IMET Electrolysis from Hydrogen System Inc. has been used as a model for calculations. However its cost was prohibitive. An alternate electrolyzer has been purchased and tested. The operating pressure and temperature ranges are 50 to 150 psig and 36 to 104 °F, respectively. The unit is capable of delivering hydrogen at 99.9 percent purity as predicted from calculations. A functionl test has been successfully completed by one our graduate students, Mark Taurence. Mark has connected the electrolyzer to the Ballard fuel cell demonstration and demonstrated its ability to operate the various components of the demonstration unit.

Fuel cell: The fuel cell selected to utilize the gaseous hydrogen produced by the electrolyzer is the Ballard Nexa. This PEM fuel cell provides 1.2 kW of DC power with a voltage range of 22 to 50 V. The fuel cell is on site and has already been used in a study on the effects of air contaminants on PEM fuel cell performance. The subject of this study provided a Master's thesis for Gerard O'Sullivan (2005). A paper on this subject was presented and published in the proceedings of the 2005 World Solar Congress.

Process water systems: The boiler for the heating hot water system was selected to satisfy the calculated heat input requirement, leaving extra capacity to allow for reheating of the cooling water by a maximum of 5 °F and for an estimated 10 percent of losses through the piping. The cooling tower was also selected for the cooling water system to satisfy and exceed the heat rejection requirement, as well as the load and size constraints. A remote sump option for the cooling tower was selected to reduce the operating weight by locating the majority of the water outside of the facility. The assumption used to calculate the required flow rates of the process water systems is a 10° □ T for the water through the absorber, rectifier, vapor generator, and super-heater.

Both items have been installed in the mobile test facility. The piping for the cooling water system is schedule-40 PVC for the cooling water and schedule-40 steel with fiberglass pipe insulation and an ASJ jacket for the heating hot water system. The layout, sizing and installation of the pipe and pumps is completed. The system is currently being tested. The process water flow diagram is given in figure 2.

Mobile Test Facility: Overview: The mobile test facility is a modified mobile building unit to house the 5 kW combined cycle with the capability of being moved/towed from place to place. The trailer is able to support the total load of all the components of the combined cycle.

Design and Layout: A 1-hr fire-rated mechanical room has been built at the end of the trailer to house the boiler as required.

Fire Protection: The University of Florida building codes do not require fire sprinklers. Carbon monoxide, ammonia, and smoke detectors as well as ammonia respirators and fire extinguishers are being provided at different locations. At least two means of egress have been provided

Selection: The trailer size is 14 by 60 ft and 8 ft tall. All interior wall sections with view panels will be provided by the researchers. A schematic of the trailer is given in figure 3. The trailer includes a 100 panel and a through-the-wall air conditioning unit.

Hydrogen/fuel cell demonstration: The portion of the system that illustrates the application of hydrogen technology is the fuel cell demonstration. A Ballard Nexa Fuel Cell uses the hydrogen provided by the electrolyzer. The fuel cell provides a net output of 1.2 kW with a DC voltage range from 22 to 50 V. This output will power several components on a graphical representation of a vehicle.

A large decal of an outline of a car has been prepared. This is visible from the viewing area of the trailer. Within this decal the fuel cell and all necessary connections are visible. The fuel cell is connected to three motors and two lamps. The two motors rotate the wheels of the car, a fan motor blows cool air into the viewing area, and two halogen lamps represent the rear and head lights. The overall purpose of this display is to show the usefulness of the fuel cells' power.

The display components have been purchased and assembled.

Two thesis topics have resulted from this work leading to the graduation of two Masters level students in Mechanical and Aerospace Engineering. Another graduate student working on this project acquired a non-thesis Masters degree. The two thesis topics included research of the effects of air contaminants on the performance of a PEM fuel cell ("The Effect of Ambient Air Contaminants on the Performance of a Proton Exchange Membrane Fuel Cell," Gerard Michael O'Sullivan, 2005) and the study of a scroll expander as applied to the combined ammonia/water combined cycle ("Study of the Feasibility and Energy Savings of Producing and Pre-Cooling Hydrogen with a 5kW Ammonia Based Combined Power/Cooling Cycle," Robert Reed, 2005). Currently three other graduate students are preparing to continue these studies with focus on the control and optimization of the 5 kW ammonia/water combined cycle and the destructive effects of urban air contaminants on PEM fuel cells.

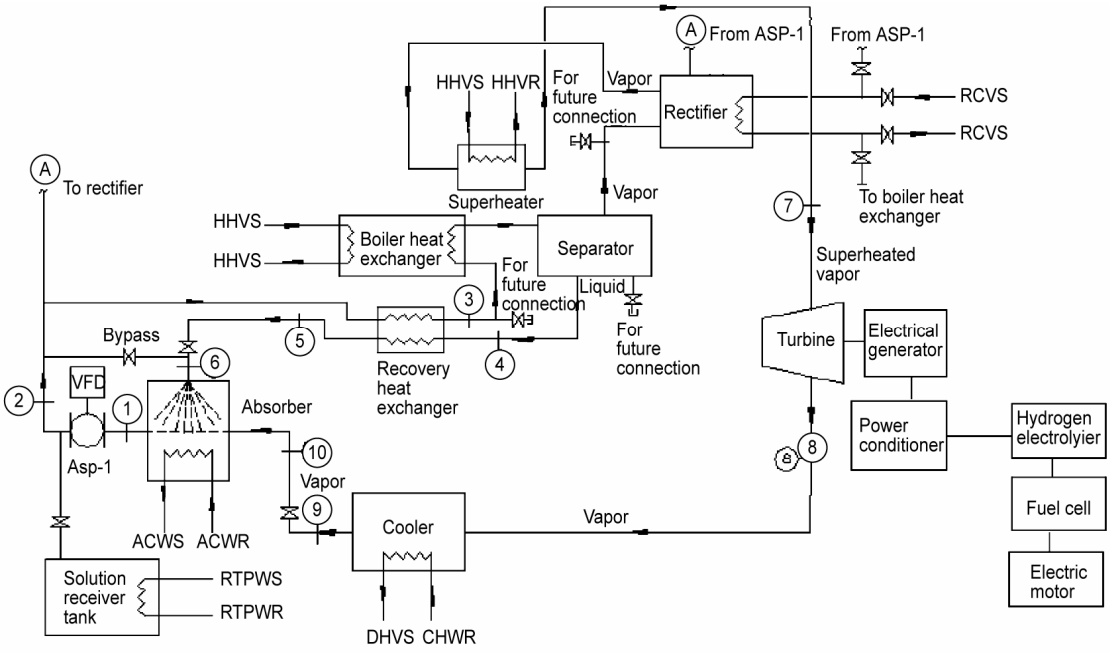

Figure 1.—Schematic of the combined cycle showing the state point numbers, system components, and flow directions.

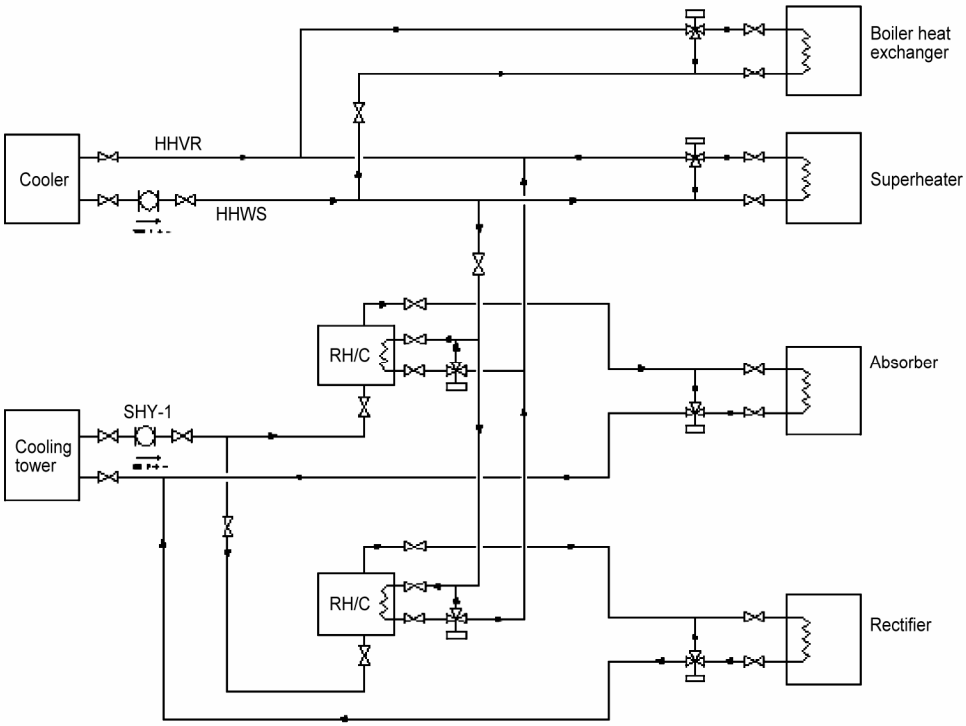

Figure 2.—Process water flow diagram.

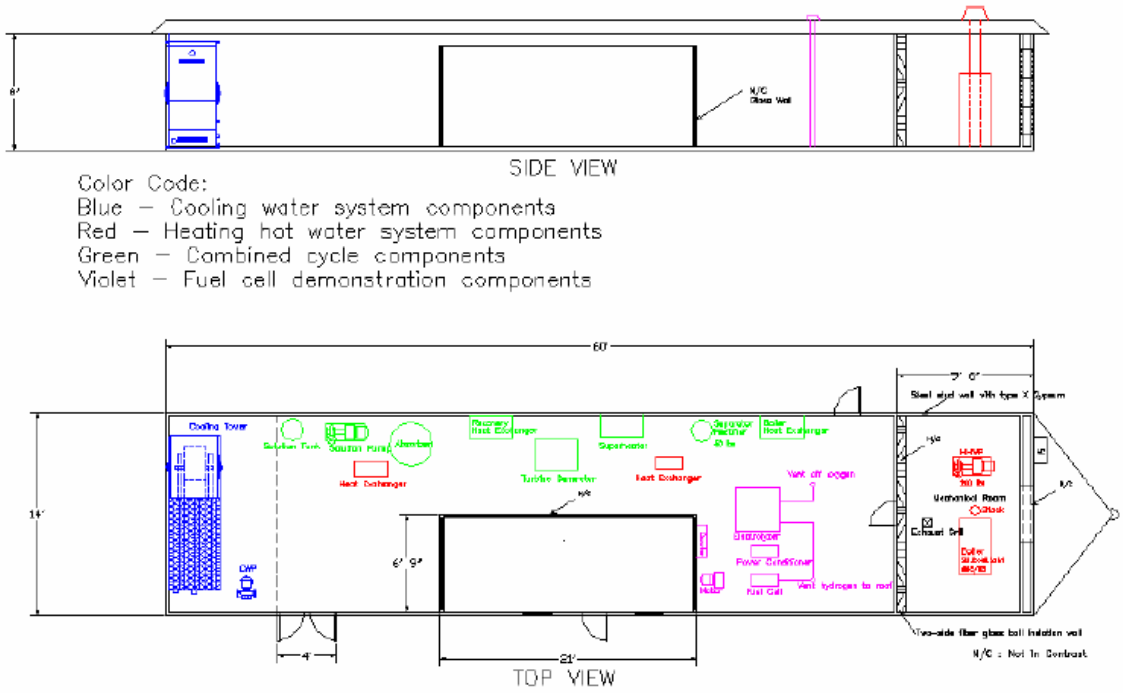

Figure 3.—Mobile test facility floor plan.

Figure 4.—Mobile Test Facility.

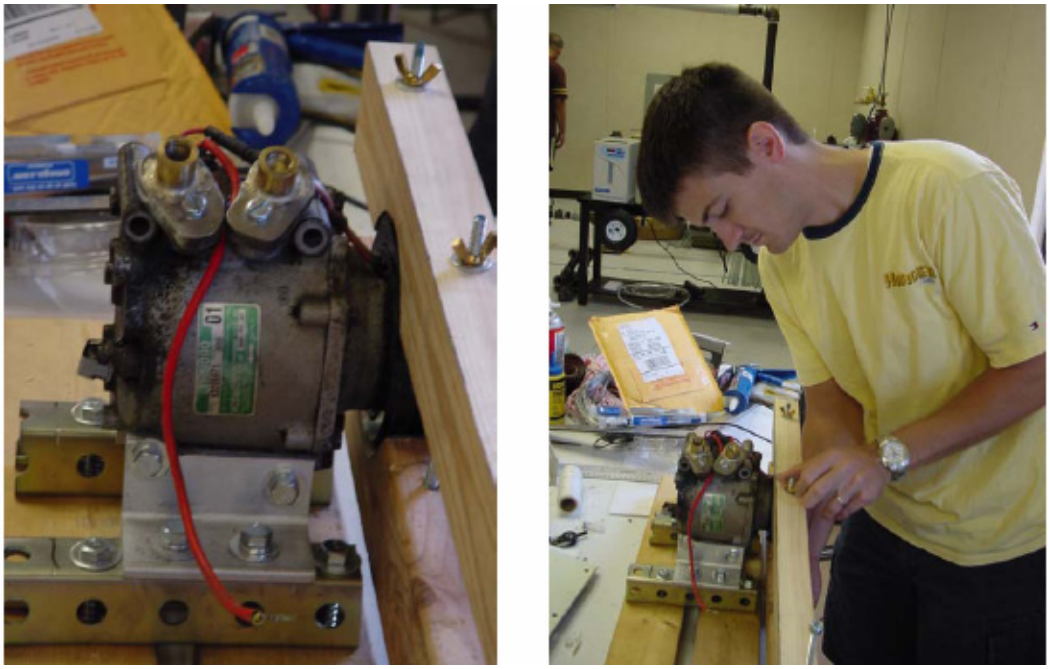

Figure 5.—(a) Scroll expander and (b) Scroll expander test set-up.

Figure 6.—Cooling Tower.

Figure 7.—Heating Hot Water Boiler.

Figure 8.—Fuel Cell Test.

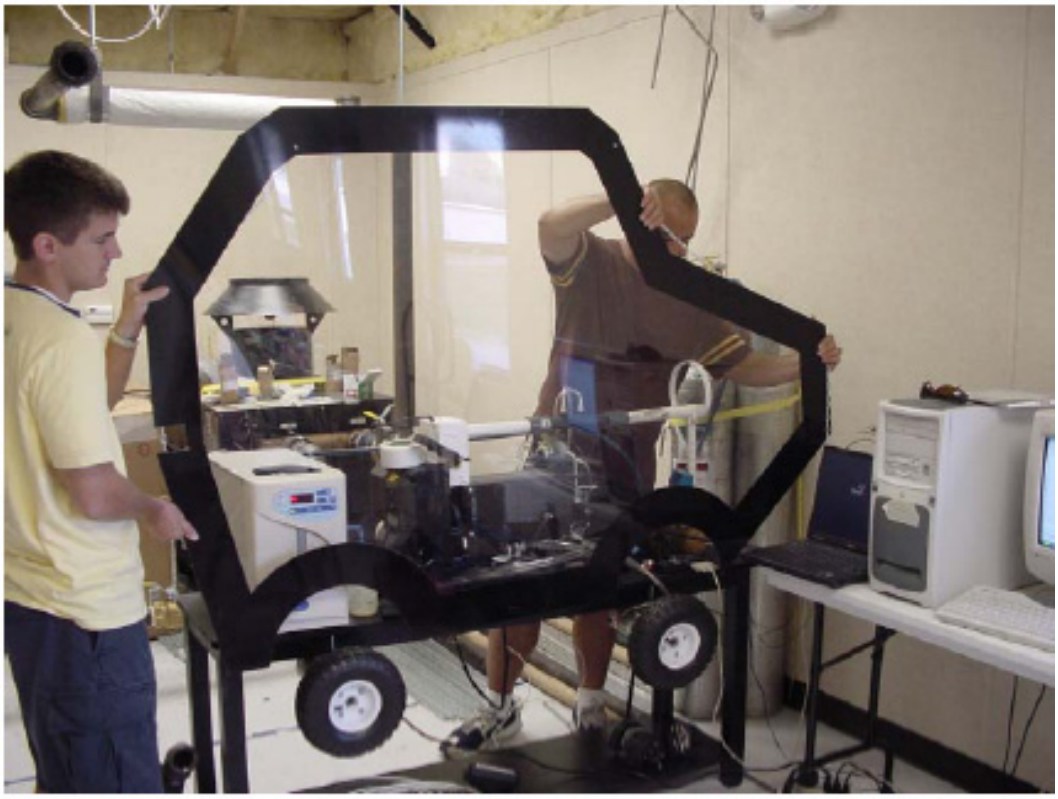

Figure 9.—Demonstration of outline of a car.

Publications

1. Herbert Ingley and Robert Reed, Optimization of a Scroll Expander Applied to an Ammonia/Water Combined Cycle System for Hydrogen Production, Paper no. 1645, 2005 Congress Proceedings of World Solar Congress, Orlando Florida.
2. Herbert Ingley and Gerard O'Sullivan, The Effects of Air Contaminants on PEM Fuel Cell Performance, 2005 Congress proceedings of World Solar Congress, Orlando Florida.

Project Title: Advanced Protonic Conductors

Task PI: Eric. D. Wachsman, Department of Materials Science and Engineering

Project Goals

Membrane reactors can be used to produce hydrogen from hydrocarbon feedstocks, from natural gas to coal to a variety of hydrocarbon containing waste streams such as landfill gas and swamp gas. The overall objective of this project is to demonstrate the feasibility of producing hydrogen from hydrocarbon based fuels using advanced proton conducting membrane. The objectives of this phase are to develop thin film proton conducting membranes on porous supports and to advance our fundamental understanding of these materials. The anticipated result is demonstration of high hydrogen fluxes through these thin supported membranes.

Background

Hydrogen is the most abundant chemical-energy resource in the world. Historically, hydrogen has been produced from fossil fuels and for the foreseeable future will continue to be so. The major source of H_2 is steam reformation of natural gas. Therefore, improvements in the efficiency and cost of H_2 production from natural gas are necessary in the near term. Gas separation membranes and membrane reactors based on ion conducting ceramics may provide the technological advance necessary to increase the efficiency and reduce the cost of H_2 production from natural gas. However, other sources of H_2 must be developed for the envisioned hydrogen economy, and coal provides the greatest U.S. domestic resource-based option. The U.S. DOE is developing a FutureGen plant based on coal gasification, solid oxide fuel cells (SOFCs), and ion conducting membranes that will produce H_2 and electricity with zero emissions and carbon sequestration; thereby, not contributing to global warming.

Membrane reactor technology holds the promise to circumvent thermodynamic equilibrium limitations by *in situ* removal of product species, resulting in improved chemical yields. Mixed-conducting oxide-membrane technology presents the possibility for a dramatic reduction in the cost of converting petroleum and coal derived feed stocks to hydrogen and other value-added hydrocarbons. The membranes are based on metal oxides (e.g., $SrCe_{1-x}M_xO_3$, where M is a metal dopant, e.g., Eu) that exhibit both ionic and electronic (mixed) conductivity. Because of their significant electronic conductivity, these mixed ionic-electronic conductors (MIECs) have an internal electrical short and the ionic species selectively permeates through a dense film of the material under a differential partial pressure, as shown conceptually for H_2 permeation in figure 1. The potential permeation flux rates of these materials are extremely high.

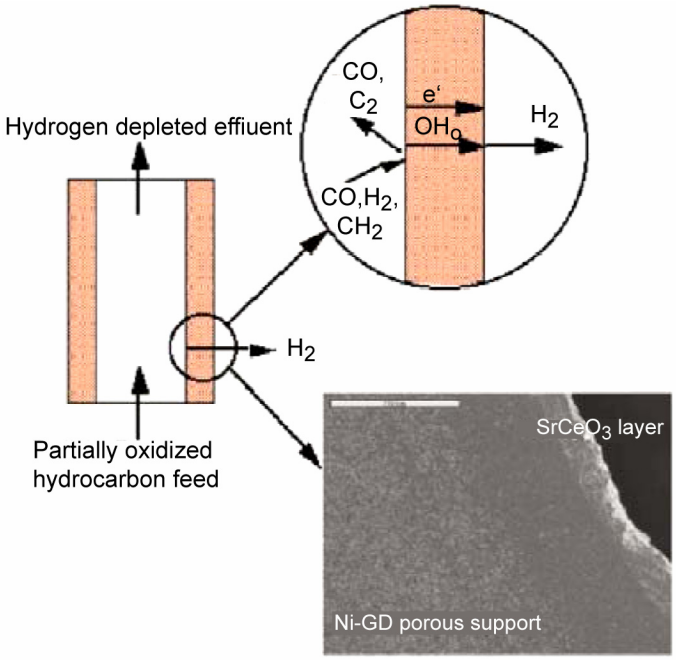

Figure 1.—Integration of proton transport membranes (including SEM of membrane) in conversion of hydrocarbon fuels to H_2.

Membrane reactors can be used to produce hydrogen from hydrocarbon feedstocks, from natural gas to coal to a variety of hydrocarbon containing waste streams such as landfill gas and swamp gas. The overall objective of this project is to demonstrate the feasibility of producing hydrogen from hydrocarbon based fuels using advanced proton conducting membranes. The objectives of this phase are to optimize electron and proton conductivity in $SrCeO_3$ membrane materials, develop thin film proton conducting membranes on porous supports and to advance our fundamental understanding of these materials. The anticipated result is demonstration of high hydrogen fluxes through these thin supported membranes.

Accomplishments

Fundamental Investigation of Proton Conductors

Electrical Properties of Eu-doped $SrCeO_3$

Defect structure.—Based on internal and external equilibria of the system, the ionic and electronic defect diagram of Eu-doped $SrCeO_3$ was successfully developed as shown in figure 2. The possibility of interstitial defects was neglected because they are energetically unfavorable in the perovskite structure.

Effect of Eu-doping level.—The conductivities of $SrCe_{1-x}Eu_xO_3$ (x = 0.05, 0.1, 0.15, 0.2) were measured in hydrogen using impedance spectroscopy. The highest conductivity was achieved with the 10 mol% Eu-doped $SrCeO_3$ as shown in figure 3.

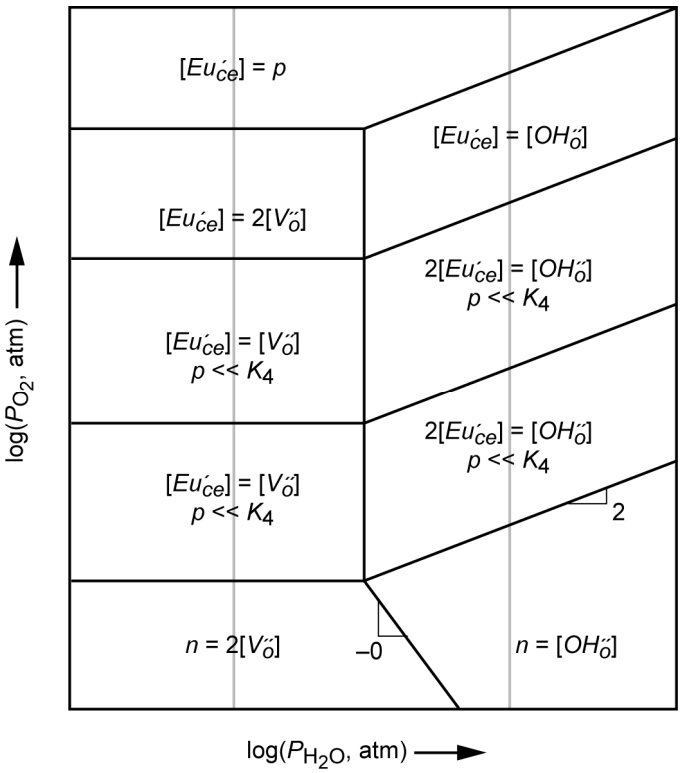

Figure 2.—Ionic and electronic defect diagram in the P_{O2}–P_{H2O} plane.

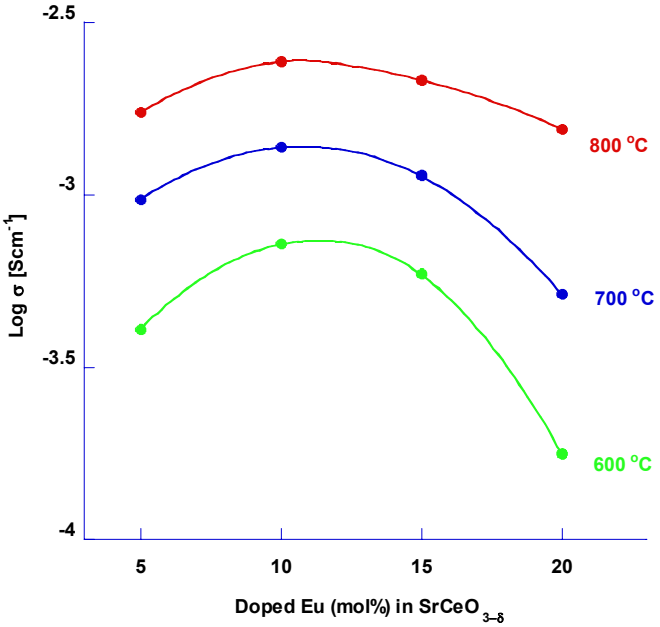

Figure 3.—Conductivity as a function of Eu-dopant level for $SrCe_{1-x}Eu_xO_3$ (x = 0.05, 0.1, 0.15, 0.2) in H_2.

Effect of oxygen partial pressure.—The conductivity of $SrCe_{0.9}Eu_{0.1}O_3$ was measured in a hydrogen-nitrogen mixture and in a nitrogen-oxygen mixture using impedance spectroscopy. The results are given in figure 4. $SrCe_{0.9}Eu_{0.1}O_3$ exhibits n-type electronic conductivity in the hydrogen-nitrogen mixture (fig. 4(a)), while the conductivity of the same material is of p-type when measured in the nitrogen and oxygen

mixture (fig. 4(b)). The n-type conductivity of $SrCe_{0.9}Eu_{0.1}O_3$ in the hydrogen-nitrogen mixture is relatively high at temperatures above 700 °C, indicating that this material should have good hydrogen permeability at temperatures above 700 °C.

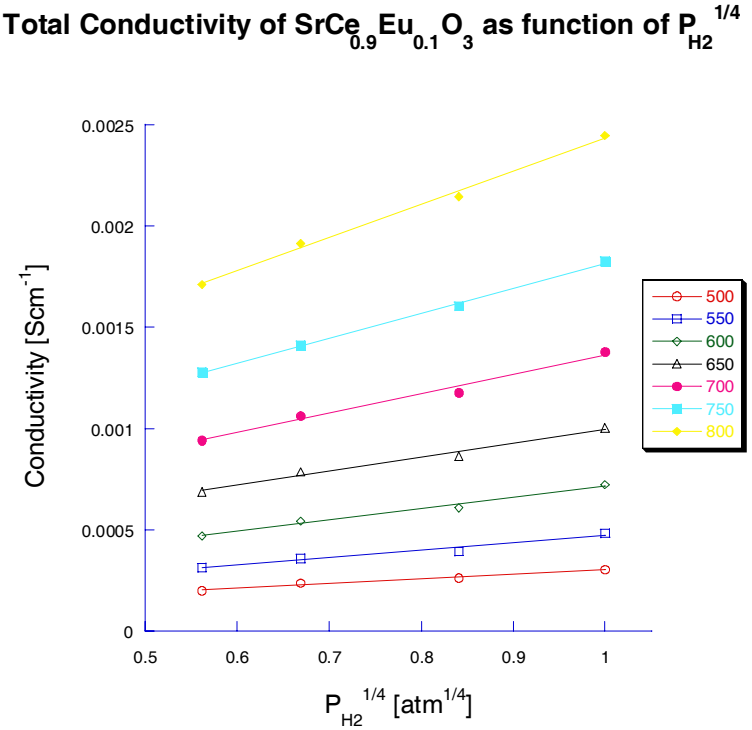

Figure 4(a).—Total conductivity of $SrCe_{0.9}Eu_{0.1}O_3$ as a function of $P_{H2}^{1/4}$ at different temperatures.

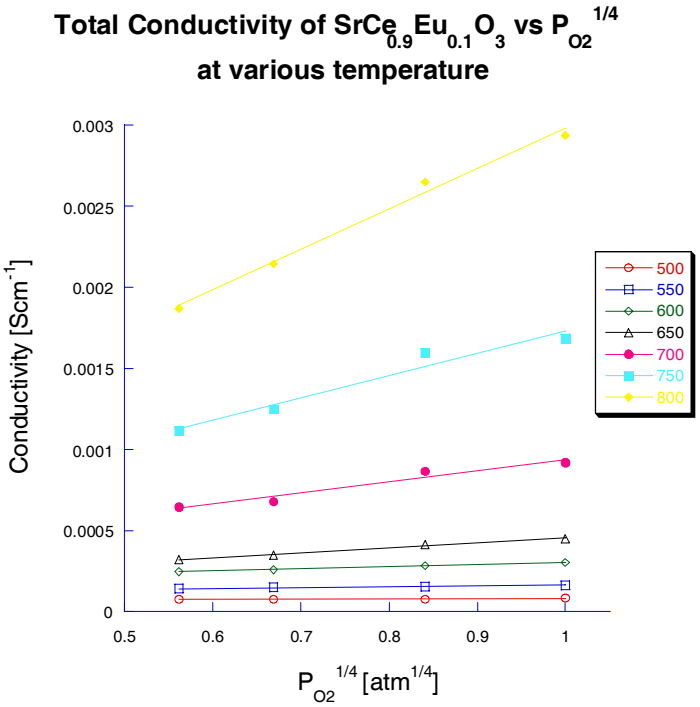

Figure 4(b).—Total Conductivity of $SrCe_{0.9}Eu_{0.1}O_3$ as a function of $P_{O2}^{1/4}$ at different temperatures.

UF Proprietary Proton Conductor

The transference number of the UF proprietary proton conductor was investigated to determine the extent of mixed conduction (protonic and electronic). The UF proprietary proton conductor was used as electrolyte in the following hydrogen concentration cell:

$$\text{dry } H_2(P_{H_2}, I)\text{+Ar, Pt/sample / Pt, dry } H_2(P_{H_2}, II\text{, higher)+Ar}$$

The EMF was measured at 500, 550 and 600 °C. The measured voltage is determined by the following equation:

$$E_{measured} = t_H \frac{RT}{2F} Ln \frac{P_{H2}(I)}{P_{H2}(II)}.$$

The results are shown in figure 5. The transference number is about 0.772, 0.785 and 0.788 at 600, 550 and 500 °C, respectively. This shows that it is a proton conductor in this temperature range. It is thus a proton conductor that can be used as the solid electrolyte in fuel cells. But the electronic conduction is not high enough to make the UF proprietary proton conductor a mixed conductor.

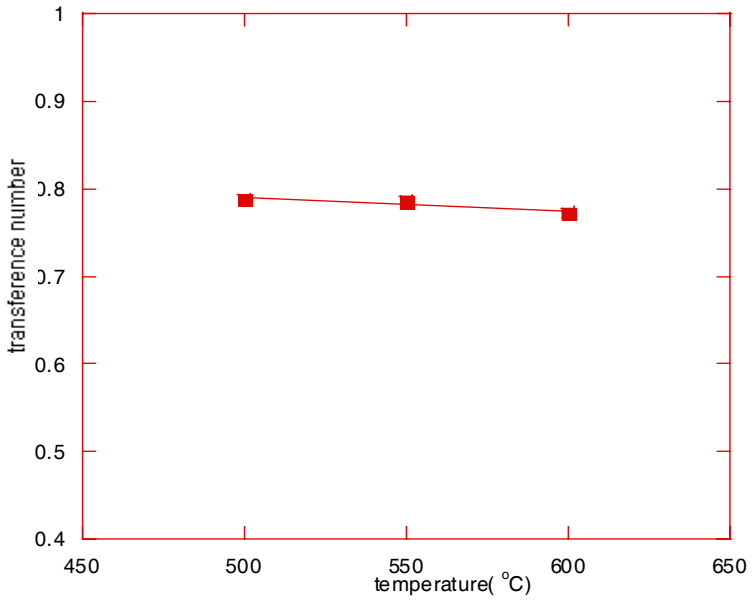

Figure 5.—Proton transference number as function of temperature.

Hydrogen Permeation Membrane Development

Membrane Supporting Tube: Materials and Fabrication

NiO-GDC.—The initial concept for a supported membrane focused on co-sintering a nickel oxide and gadolinium-doped ceria (NiO-GDC) support and a europium-doped strontium cerate (ESC) film. The porous support would result from in-situ reduction of NiO to Ni in hydrogen. For this concept to succeed, the ESC must be thermodynamically stable with both the NiO and GDC in air, and the ESC and NiO-GDC must have comparable thermal expansion properties in air and hydrogen.

The thermodynamic stability of ESC with both GDC and NiO was investigated in parallel with the thermal expansion properties of these materials. Figure 6(a) demonstrates the lack of reactivity between ESC and GDC at 1500 °C. Unfortunately, as shown in figure 6(b), ESC does react with NiO above 1400 °C. At 1400 °C, only ESC and NiO are present. While at 1500 °C, the powder had completely reacted and the resultant peaks were identified as CeO_2 and NiO. Thus, based on reactivity, a NiO-GDC support would work if the membrane is sintered ≤1400 °C.

Figure 7 demonstrates the thermal expansion behavior of both ESC and NiO-GDC in (a) air and (b) hydrogen. The thermal expansion behavior of the ESC was similar in both air and hydrogen (thermal expansion coefficient of 9.4 in air and 9.0 in hydrogen). However, thermal expansion behavior of both 40 wt% NiO-GDC and 60 wt% NiO-GDC changed dramatically in hydrogen above 550 °C.

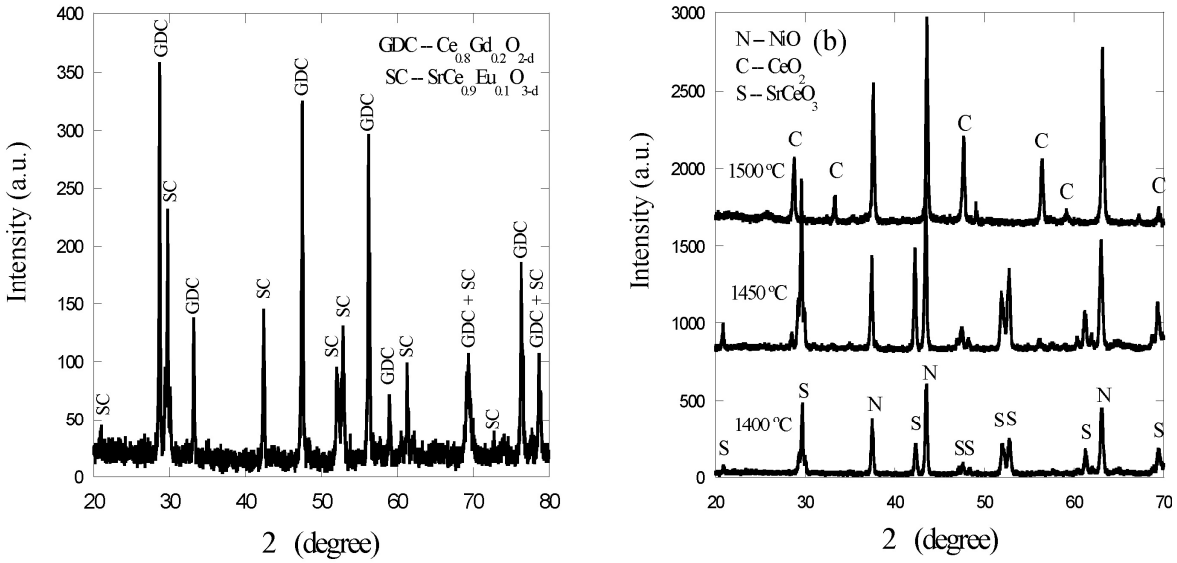

Figure 6.—X-ray diffraction pattern showing (a) no reaction between ESC and GDC at 1500 °C and (b) complete reaction between ESC and NiO at 1500 °C, but no reaction at 1400 °C.

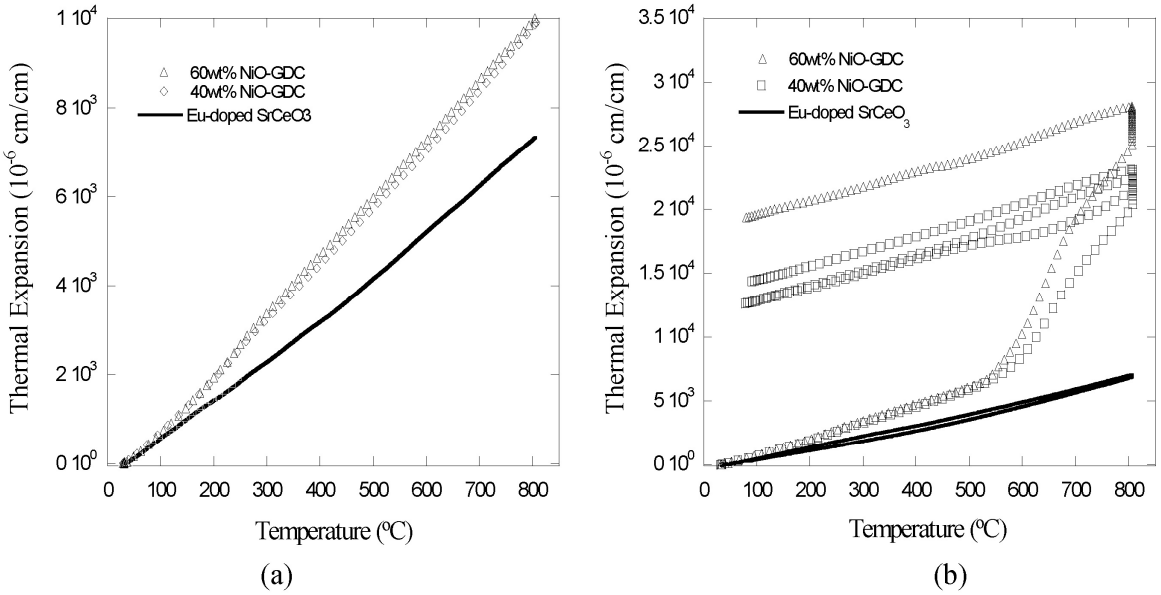

Figure 7.—Thermal expansion behavior of ESC and NiO-GDC in (a) air and (b) hydrogen

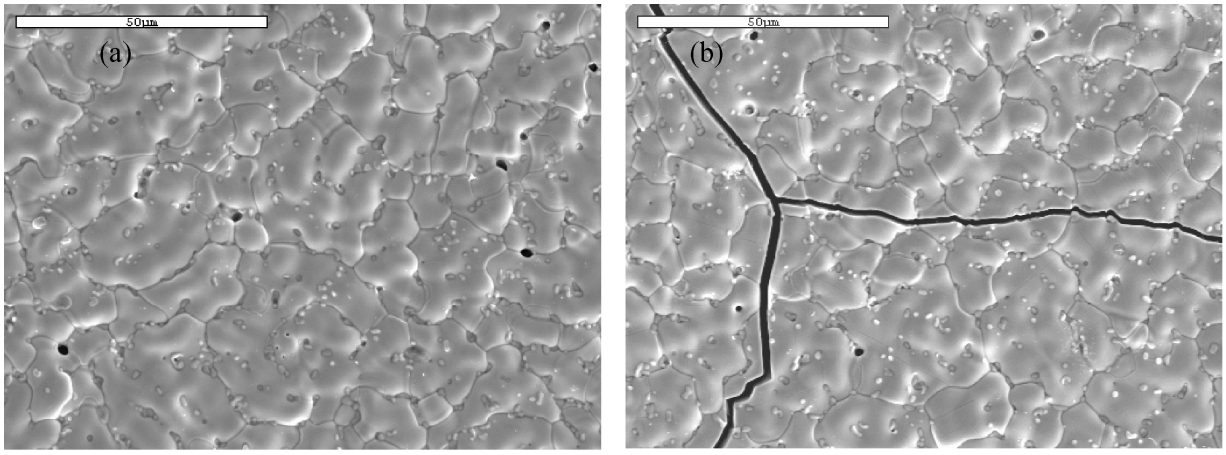

Figure 8.—Scanning electron micrographs of ESC film (a) before hydrogen treatment and (b) after hydrogen treatment

Although the difference in thermal expansion between ESC and NiO-GDC in air can be tolerated, the difference in hydrogen results in failure of the membrane-support as shown in figure 8. Figure 8(a) illustrates the surface of a film before hydrogen treatment while figure 8(b) shows cracks which have propagated from the support through the film after hydrogen treatment.

The results indicate that the NiO-GDC system is not appropriate for an ESC supported membrane that is sintered above 1400 °C.

YSZ.—Another possible system investigated was yttria-stabilized zirconia (YSZ). Unfortunately, the YSZ and ESC react at 1500 °C as shown in figure 9.

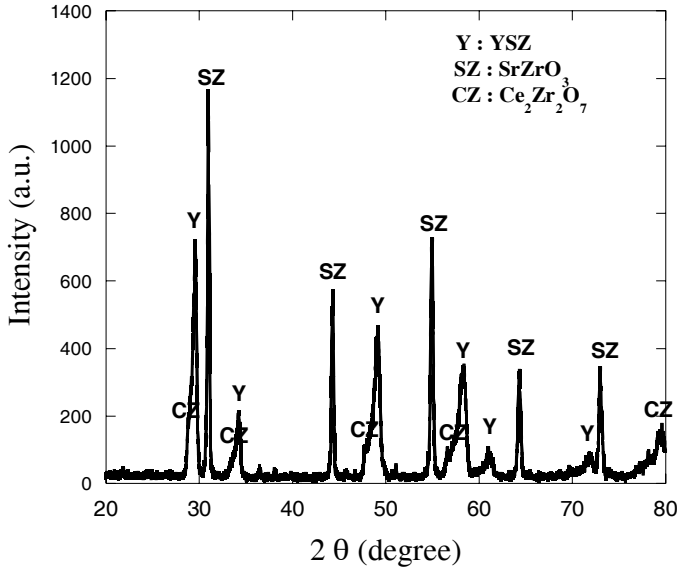

Figure 9.—X-ray diffraction pattern demonstrating the reaction between YSZ and ESC at 1500°C.

Membrane supporting tube based on NiO-SC.—Undoped strontium cerate (SC) was investigated as a support material. The main complication using SC as the support material is the reaction between SC and NiO at 1450 °C which is below the sintering temperature used with the GDC and YSZ supports. Two approaches were taken to overcome this problem. First, SC tape was prepared using carbon rather than NiO as the pore former. The green strength of the SC-carbon tape was too low to prepare porous support tubes via the rolling method. Second, SC tape was prepared with NiO, and temperatures below 1450 °C were investigated. The slurry composition for the SC-NiO tape is shown in table 1.

TABLE 1.—SLURRY COMPOSITION OF SC CONTAINING NICKEL CATALYST FOR TAPE CASTING PROCESS

Process step	Material	Function	Weight (g)
Mill for 24 hr (1st stage)	$SrCeO_3$	Powder	52.55
	NiO		22.52
	Solsperse	Dispersant	0.75
	Toluene	Solvent	13.11
	E.A		8.18
Add to above and mill for 24 hr (2nd stage)	DBP	Plasticizer	3.30
	PEG		0.66
	PVB	Binder	4.50

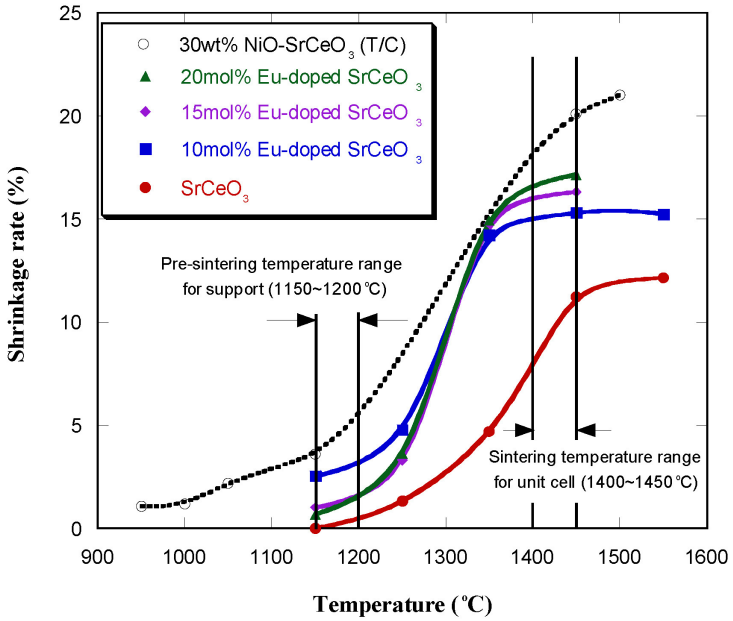

Figure 10.—Shrinkage rates for the un-doped and europium-doped strontium cerate, prepared by uniaxial pressing, and un-doped strontium cerate with nickel oxide, prepared by tape casting, according to the sintering temperatures.

The shrinkage behavior of uniaxially pressed ESC and SC and tape casted SC-NiO was studied. The shrinkage rates for the SC, ESC, and SC-NiO, shown in figure 10, demonstrate that the ESC sinters more easily than SC below 1450 °C and that the ESC and SC-NiO have comparable shrinkage rates which are necessary for dense thin film preparation. The limited sinterability of SC should improve the porosity of the support tube. Also, the samples with higher europium dopant levels demonstrate similar shrinkage rates.

The change in apparent porosity before and after hydrogen treatment for both 10 and 30 wt% NiO-SC samples is shown in figure 11. At 1425 °C, the apparent porosity for the 10 wt% NiO sample only increased from 5 to 12.5 percent while for the 30 wt% NiO sample the apparent porosity increased from 5 to 25 percent. Following in situ reduction of NiO to Ni, the SC support containing 30 wt% NiO is satisfactorily porous.

The thermal expansion behaviors of ESC and 30 wt% NiO-SC must be similar in both air and in hydrogen to avoid failure of the ESC film since the samples are sintered in air and tested in hydrogen. The expansion behavior of ESC is very similar to that of 30 wt% NiO-SC in air as shown by figure 12(a) and the ESC films do not crack after sintering which is confirmed by the SEM micrograph shown in figure 13(a). In hydrogen, the thermal expansion coefficient (TCE) of the 30 wt% NiO-SC is approximately 13 percent higher than the TCE of ESC. As shown by figure 13(b), this expansion difference is not significant enough to result in cracking of the ESC film.

The film shown in figure 13 was formed using a slurry coating process combined with a filtration apparatus. Earlier films that were formed by a conventional slurry coating process developed pin-hole defects. The new coating method eliminated the pin-hole defects.

The new coating method allowed for preparation of 6 in. NiO-SC support tubes with a dense ESC film. The film remains crack free after treating in hydrogen.

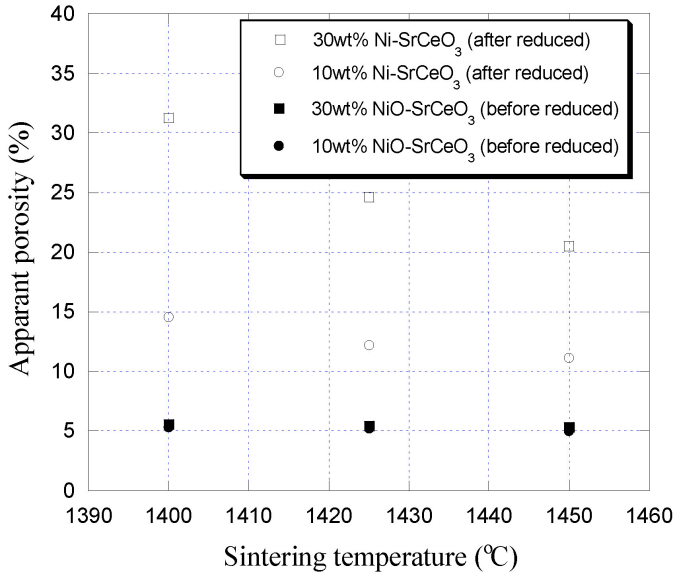

Figure 11.—Apparent porosity for the sintered NiO-SC support before and after reduction

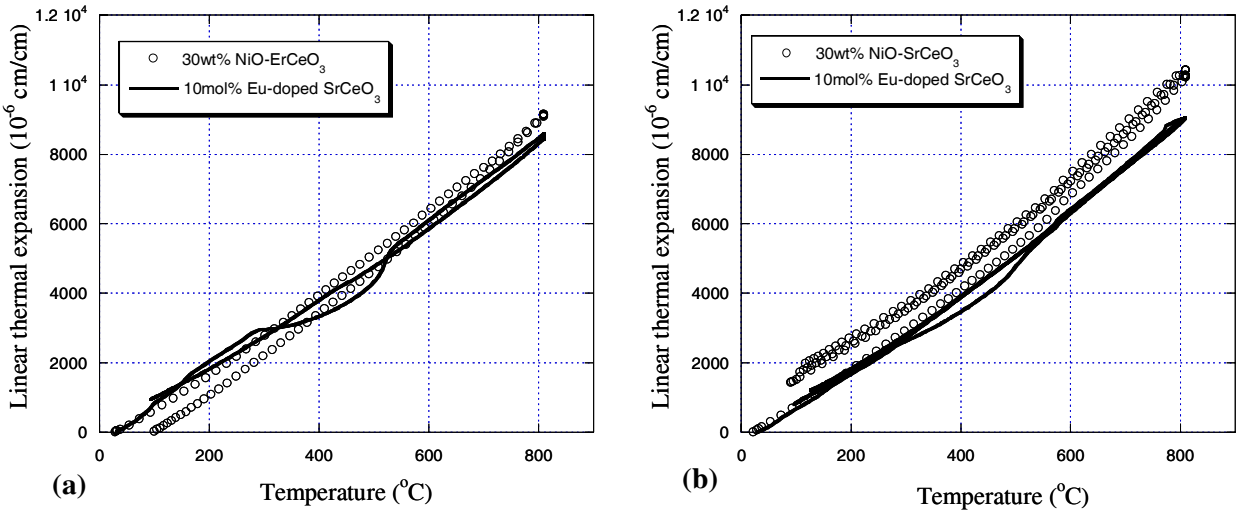

Figure 12.—Thermal expansion behavior of ESC and NiO-SC in (a) air and (b) hydrogen.

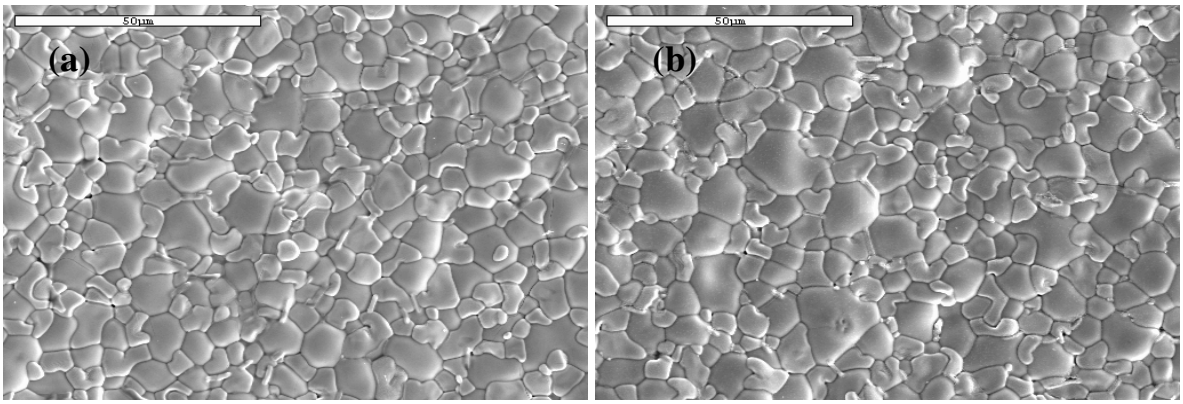

Figure 13.—Scanning electron micrographs of ESC film on NiO-SC support (a) before and (b) after hydrogen treatment.

Preparation of ESC Film on NiO-SC Support

According to our investigations, the final sintering temperature should be below 1450 °C to prevent a reaction between NiO and strontium cerate (SC), and above 1400 °C to obtain dense films of Eu-doped strontium cerate (ESC). In addition, the pre-sintering temperature for the NiO-SC support should be in the range of 1150 to 1200 °C, in order to obtain compatible shrinkage rates between NiO-SC and ESC film at the sintering range. The cracking of the NiO-SC support was observed when the support was pre-sintered at temperatures below 1150 °C. The optimal pre-sintering and sintering temperature ranges are given in figure 10.

As summarized in table 2, the preparation of the ESC hydrogen membrane on NiO (or Ni)-SC tubular support consists of four steps; and the pictures of a 6-in. unit cell thus prepared at each preparation step are shown in figure 14.

TABLE 2.—PREPARATION STEPS OF THE TUBULAR HYDROGEN MEMBRANE CELL AND RELATED PROCESSES

Preparation step	Related process
Green state tube	Slurry preparation, tape casting and rolling (Tubular type 30 wt% NiO in $SrCeO_3$ support)
Partially sintered support and membrane coating	Pre-sintering NiO-SC support at 1150 to 1200 °C
	Citrate process/solid state reaction (Preparation 10 mol% Eu-doped $SrCeO_3$)
	Slurry coating ESC on NiO-SC support (combined with a filtration apparatus)
Sintered cell	Sintering ESC/NiO-SC at 1400 to 1450 °C
Reduced cell	Reducing NiO to Ni in support by annealing in H_2

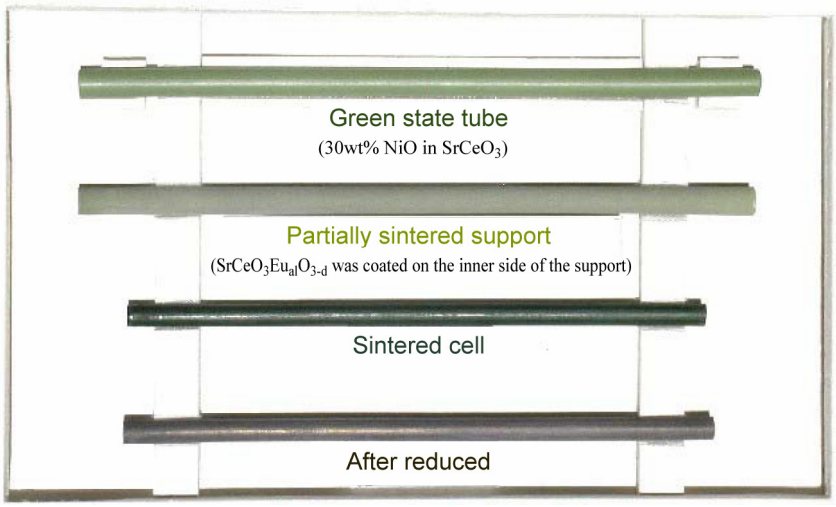

Figure 14.—Pictures of a 6-in. unit cell of 10 mol% Eu-doped $SrCeO_3$ membrane coated on the inner side of NiO(or Ni)-$SrCeO_3$ tubular support at each processing step.

Hydrogen Permeation

By assembling the unit cell with gas inlet and outlet systems, we obtained a hydrogen permeation reactor, the picture of which is shown in figure 15. Installing the hydrogen permeation reactor in a furnace and connecting the reactant and sweep gases, we are now ready for testing the hydrogen permeability of the 6-in. unit cell. Mass flow controllers are used to control the gas flow rate, and hydrogen permeation rate is measured by a mass spectrometer. The actual experimental set-up is shown in figure 16.

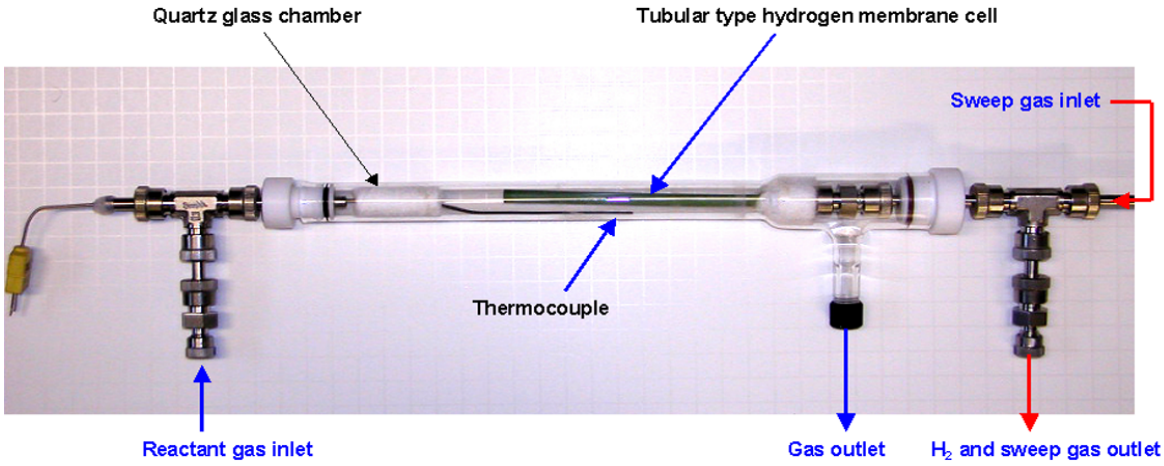

Figure 15.—The hydrogen permeation reactor with the 6-in. unit cell.

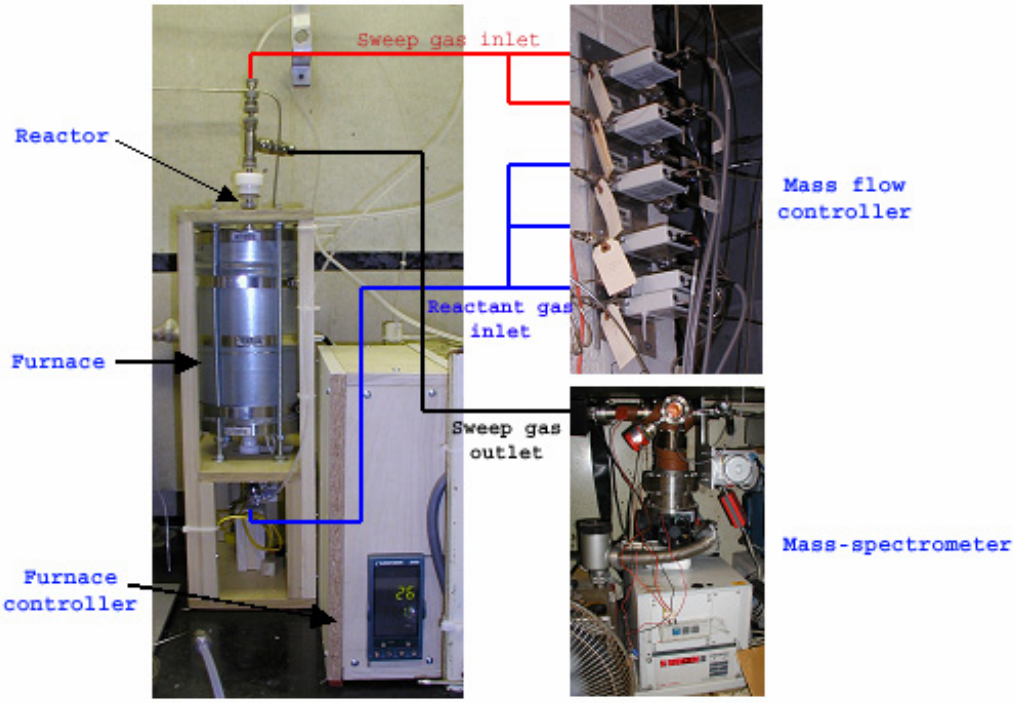

Figure 16.—Experimental set-up for hydrogen permeation test.

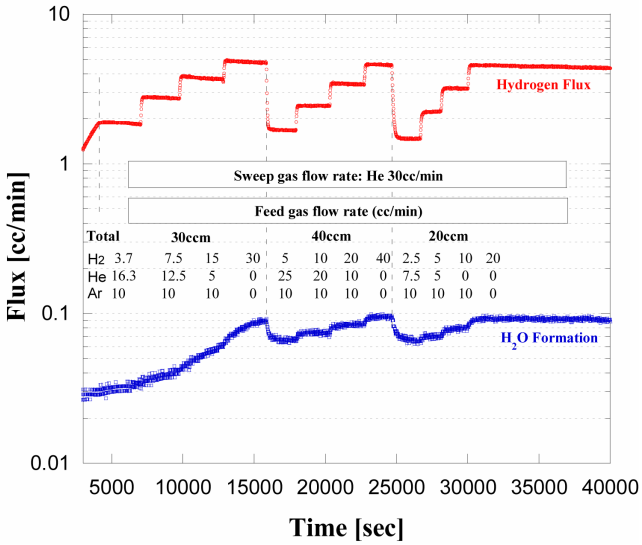

Figure 17.—Hydrogen flux and water vapor formation at 900 °C. Corresponding experimental conditions are given in the figures.

Gas flow rates were controlled by mass flow controllers. One side of the membrane cell was exposed to H_2 (99.999 percent) diluted to the desired concentration using He (99.999 percent) and/or Ar (99.999 percent) at 20 cm^3/min total flow rate (feed gas). The other side was swept with He at 20 cm^3/min (sweep gas). Hydrogen permeation was measured using a mass spectrometer. Figure 17 shows hydrogen fluxes obtained from the hydrogen permeation reactor at 900 °C under different experimental conditions. It is obvious that the hydrogen flux is sensitive to the partial pressure of hydrogen in the feed gas. The water vapor fluxes are also shown in the figures.

The result shows that at 900 °C a single tube of our current generation of membrane is capable of producing about 5 cc/min of pure H_2. The hydrogen flux can be significantly increased by optimizing the membrane, and proportionally increased by increasing the number of tubes.

Publications and Presentations

Publications

1. "Hydrogen Permeability and Microstructure Effect on Mixed Protonic-Electronic Conducting Eu-doped Strontium Cerate," S.-J. Song, E.D. Wachsman, J.M. Rhodes, H.-S. Yoon, G. Zhang, K.-H. Lee, S.E. Dorris and U. Balachandran, Journal of Materials Science, accepted.
2. "Hydrogen Production from Fossil Fuels with High Temperature Ion Conducting Ceramics," E. D. Wachsman and M.C. Williams, *Interface*, 13–3, 32–37 (2004).
3. "Hydrogen Permeability of $SrCe_{0.95}Eu_{0.05}O_{3-\delta}$ (x = 0.05, M = Eu, Sm)," S.J. Song, E.D. Wachsman, J. Rhodes, S. E. Dorris and U. Balachandran, *Solid State Ionics*, **167**, 99–105 (2004).
4. "Numerical Modeling of Hydrogen Permeation in Chemical Potential Gradients," S. J. Song, E. D. Wachsman, J. Rhodes, S.E. Dorris and U. Balachandran, *Solid State Ionics*, **164**, 107–116 (2003).
5. "Defect Structure and n-Type Electrical Properties of $SrCe_{0.95}Eu_{0.05}O_{3-\delta}$," S.J. Song, E.D. Wachsman, S.E. Dorris and U. Balachandran, *Journal of the Electrochemical Society*, **150**, A1484 (2003).
6. "Electrical Properties of p-Type Electronic Defects in the Protonic Conductor $SrCe_{0.95}Eu_{0.05}O_{3-d}$," S.J. Song, E.D. Wachsman, S.E. Dorris and U. Balachandran, *Journal of the Electrochemical Society*, **150**, A790 (2003).

7. "Defect Structure and n-Type Electrical Properties of $SrCe_{0.95}Eu_{0.05}O_{3-\delta}$," S. Song, E.D. Wachsman, S.E. Dorris and U. Balachandran, *Solid State Ionic Devices III*, Electrochem. Soc., E.D. Wachsman, K.S. Lyons, M. Carolyn, F. Garzon, M. Liu and J. Stetter, Ed., **2002–26**, 456–470 (2003).

Presentations

1. "Fabrication of Dense Eu-doped $SrCeO_{3-d}$ Membrane on Ni-$SrCeO_3$ Tubular Type Support," H.-S. Yoon, E.D. Wachsman and J.M. Rhodes, 29th International Cocoa Beach Conference and Exposition on Advanced Ceramics and Composites, Cocoa Beach, January 2005.
2. "Preparation of Thin Film Inorganic Hydrogen Separation Membranes on Ni-GDC Tubular Type Supporters Using Tape Casting Process," H.-S. Yoon, S.-J. Song, E.D. Wachsman and J.-H. Lee, 28th International Cocoa Beach Conference and Exposition on Advanced Ceramics and Composites, Cocoa Beach, January 2004.
3. "Hydrogen Permeability of Mixed Protonic-Electronic Conducting Multivalent Cation Doped Strontium Cerate," S.-J. Song, E.D. Wachsman, J. Rhodes, H.-S. Yoon and G. Zhang, 204th Meeting of The Electrochemical Society, Orlando, October 2003.
4. "Preparation of Dense Barium Cerate Film on Planar Porous Substrate for Hydrogen Seperation Membranes," R. Bagul, H.-S. Yoon, S.-J. Song and E.D. Wachsman, 204th Meeting of The Electrochemical Society, Orlando, October 2003.
5. "Hydrogen Permeation Through Mixed Protonic-Electronic Conducting Perovskites," E.D. Wachsman, Gordon Research Conference on Solid State Studies in Ceramics, August 10–15, 2003, New London, NH.
6. "Hydrogen Separation with Protonic Conductors," E.D. Wachsman, Gordon Research Conference on Chemistry of Hydrocarbon Resources, January 12–17, 2003, Ventura, CA.

3. Sensors for Hydrogen Leak Detection

Faculty Lead: Mark Law and Jenshan Lin, Electrical and Computer Engineering

Overview

In this FY03 program, we have successfully demonstrated novel hydrogen sensors including wide energy band-gap based sensors and biological assays sensors. We also demonstrated the feasibility of remote detection using wireless transceiver and microcontroller. By using low power solid state sensors, the integrated wireless hydrogen sensor can be made compact and lightweight to facilitate a fast deployment of a hydrogen leak detection network.

In the beginning of the project period, our first prototype sensor needs to operate at elevated temperature. Through the improvement in device structure, we achieved room-temperature (25 °C) sensing using AlGaN/GaN MOS-HEMT sensor. Toward the end of this project period, we developed the novel ZnO nanorod sensor, which has much lower power consumption yet better sensitivity. This paves the way for the development of self-powered wireless hydrogen nano-sensor to be developed in the next phase.

Project Title: Wide Energy Band-Gap Based Gas Sensors

Task PI: Fan Ren, Department of Chemical Engineering
Co-I: Steve J. Pearton, Department of Materials Science and Engineering
Collaborator: Jenshan Lin, Department of Electrical and Computer Engineering

Project Goals

Demonstrate room temperature hydrogen sensor with wide energy bandgap semiconductor devices.

Summary

This report describes the development of solid-state hydrogen sensors using GaN-based devices and ZnO-based devices. Device structures and measured performances of hydrogen detection using GaN Schottky diode, AlGaN/GaN Schottky diode, AlGaN/GaN HEMT, Pt-ZnO Schottky diode, and ZnO nanorod are compared. These devices, operating with low power consumption, are suitable for integration with electronic circuits to form a low power wireless hydrogen sensor module. A prototype of wireless sensor system is also described.

Accomplishments

Background

Sensors for hydrogen leak detection are crucial to ensure safety in many applications that use hydrogen as fuel, e.g., space exploration missions in NASA, hydrogen-powered vehicles in automobile industry. Semiconductor gas sensors that have advantages of small size and reusability are promising technologies for hydrogen leak detection. The solid-state sensors, which respond to chemical detection with an electrical signal, can also be easily integrated with solid-state electronic circuits that process and transmit the sensor data. If the sensor data is transmitted using radio waves, a wireless sensor network can be designed to link multiple sensors together to a central monitoring station. Research efforts are currently carried out in different disciplines to achieve this goal. Nevertheless, the fundamental chemical sensing mechanism occurred in the sensor device plays the most important role, and the search for the optimum

hydrogen sensor has been an interesting research subject recently. Pioneering research in the past few years have produced promising results. The silicon-based approach developed in NASA used Schottky diodes as the sensors in a hydrogen detection system for various space exploration missions. The approach can also integrate novel technologies such as MEMS, nanomaterials, and SiC (ref. 1). Through this program, we demonstrated several different types of hydrogen sensors using GaN-based diodes and transistors (ref. 2). In this report, the development of GaN-based hydrogen sensors using diodes and MOS-HEMT is reviewed and their performances are compared. As nanotechnology getting matured, nano-scale devices were proposed for gas sensing. In the end of this project period, our research effort shifted to using ZnO nanorods/nanowires as hydrogen sensor. Regardless of the type of the sensor, as long as the sense of hydrogen results in a change in its electrical characteristics, the sensor device can be integrated with electronics to form a complete sensor system and network. The integration with electronic circuits and a prototype wireless sensor system are also described in this report.

GaN-Based Hydrogen Sensor

GaN Schottky Diode Sensor

Figure 1 shows the microphotographs of the GaN Schottky diode hydrogen sensor and the test fixture where the substrate was mounted on for testing in chamber. Figure 2 shows the cross-sectional view of the Schottky diode structure. Front-side ohmic contacts of Ti/Al/Pt/Au were formed by lift-off and subsequent annealing at 600 °C. The Schottky contacts were formed by lift-off of e-beam deposited Pd or Pt, 24 and 15 nm thick respectively. The contact diameter is 80 μm in both cases. The devices were wire-bonded to a test fixture using Ti/Au bond-pads and Au wires for contact (ref. 3).

Figure 3 shows the forward current-voltage characteristics of the Pd/GaN diode at 170 °C in pure N_2 and 10 percent H_2 in N_2 ambients. The addition of 10 percent H_2 to the ambient produces a shift of 74 mV at a forward current of 2 mA. Note that at higher voltage and current bias, the signal change is even more discernable, e.g., 1 mA at a forward bias of 1 V or 100 mV at a bias current of 6 mA. The sensing mechanism in semiconductor gas sensors is thought to be creation of a polarized layer in the semiconductor surface by hydrogen atoms diffusing through the metal contact (refs. 4 and 5). The adsorbed hydrogen is then assumed to change the work function of the metal (ref. 5). Recent elastic recoil detection measurements on Pt-GaN Schottky diodes confirm the presence of hydrogen at the metal semiconductor interface after exposure to molecular hydrogen at 400 °C (ref. 6).

The time response of the GaN Schottky diode hydrogen sensor is demonstrated in figure 4. In this case, Pd/GaN diodes were biased at a constant forward bias of 0.5 V at 150 °C and the resulting forward current measured as a function of time as the ambient was cycled from N_2 to 10 percent H_2 in N_2 and then back to N_2. The forward bias current increase about 0.3 mA as H_2 is introduced and the subsequent decay back towards the initial current as N_2 is introduced into the chamber. The increase in forward current is very rapid after switching in the 10 percent H_2 in N_2 gas. From the observation of this rapid rise in current, we believe that diffusion of hydrogen through the metal contact is not the limiting factor in the time response of the diodes but rather the mass transport of gas into the enclosure. Similarly, the longer recovery times are at least partially caused by the time needed to completely flush the H_2 out of the measurement enclosure.

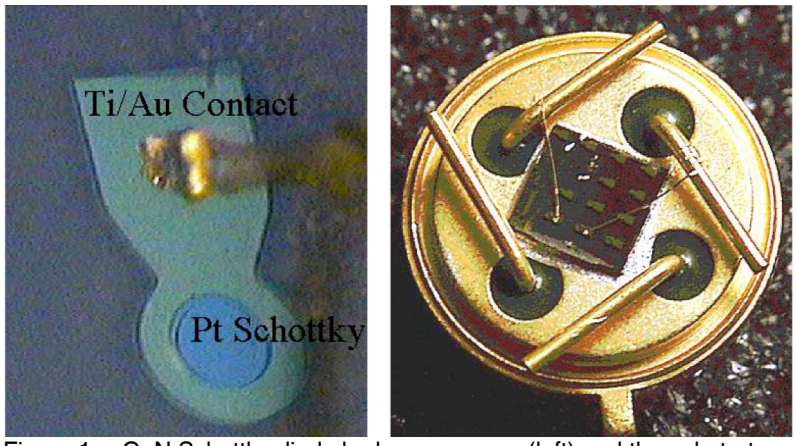

Figure 1.—GaN Schottky diode hydrogen sensor (left) and the substrate mounted on a test fixture used for testing in chamber (right).

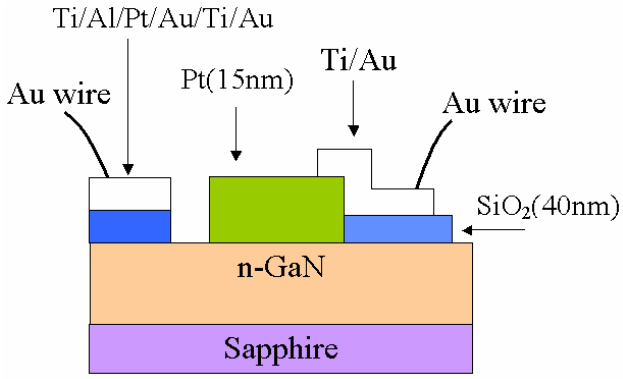

Figure 2.—Cross-sectional view of the GaN Schottky diode structure.

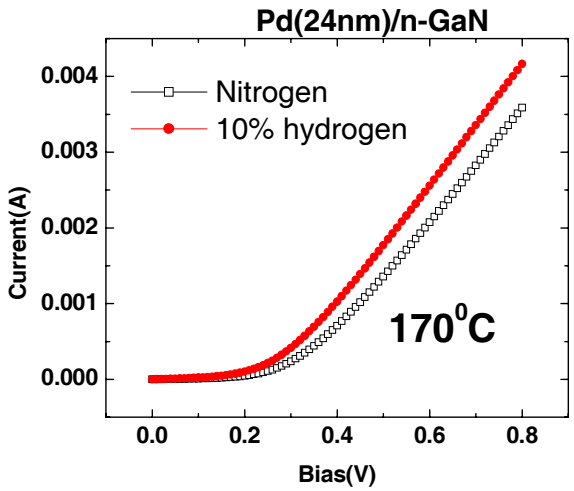

Figure 3.—Current-voltage characteristics of the GaN Schottky diode hydrogen sensor at 170 °C in pure N_2 and 10 percent H_2 in N_2 ambients.

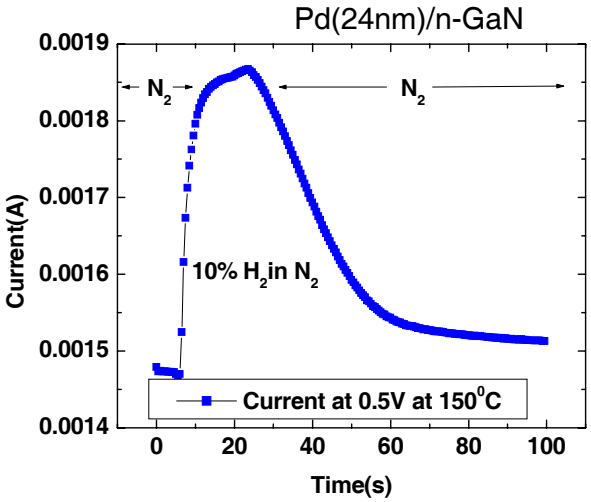

Figure 4.—Time response of the GaN Schottky diode hydrogen sensor at 150 °C.

Figure 5.—AlGaN/GaN Schottky diode hydrogen sensor (left) and the substrate mounted on a test fixture used for testing in chamber (right).

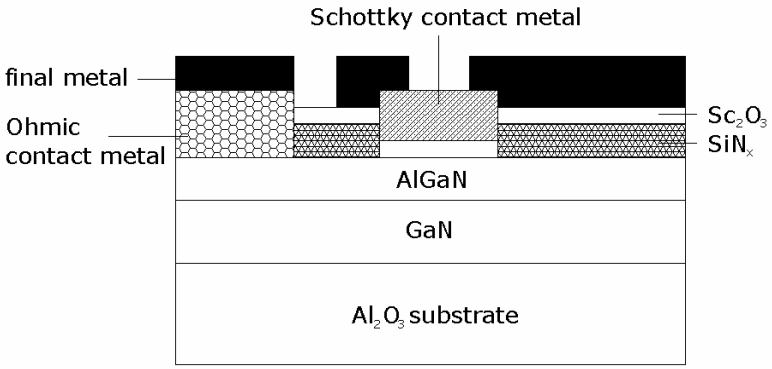

Figure 6.—Cross-sectional view of the AlGaN/GaN Schottky diode structure.

Schottky Diode Sensor on AlGaN/GaN HEMT Structure

A variation of Schottky diode sensor was fabricated on AlGaN/GaN High Electron Mobility Transistor (HEMT) layer structure. Figure 5 shows the microphotographs of the AlGaN/GaN MOS diode hydrogen sensor and the test fixture where the substrate was mounted on for testing in chamber. Figure 6 shows the cross-sectional view of the AlGaN/GaN Schottky diode structure.

This diode structure also has the capability of detecting hydrogen. Figure 7 shows the time response of the AlGaN/GaN Schottky diode sensor when ambient conditions of pure N_2 and 10 percent H_2 in N_2 were cycled through the test chamber. The diode was biased at 2 V with a bias current of about 10 mA. The introduction of hydrogen into the chamber caused a current increase of more than 0.4 mA. The measured measurement result also demonstrated the reversibility of this diode sensor.

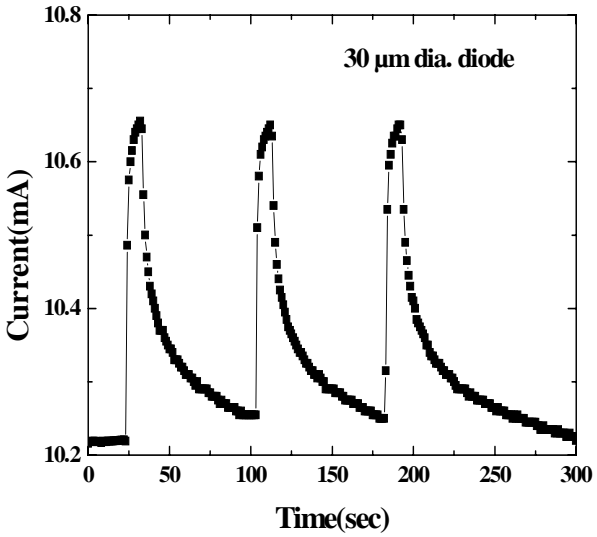

Figure 7.—Time response of the AlGaN/GaN Schottky diode sensor.

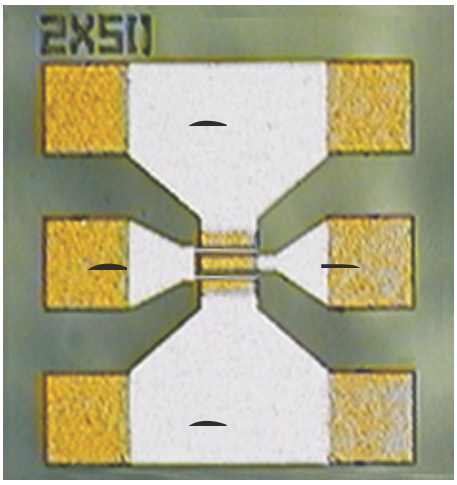

Figure 8.—AlGaN/GaN MOS. HEMT sensor

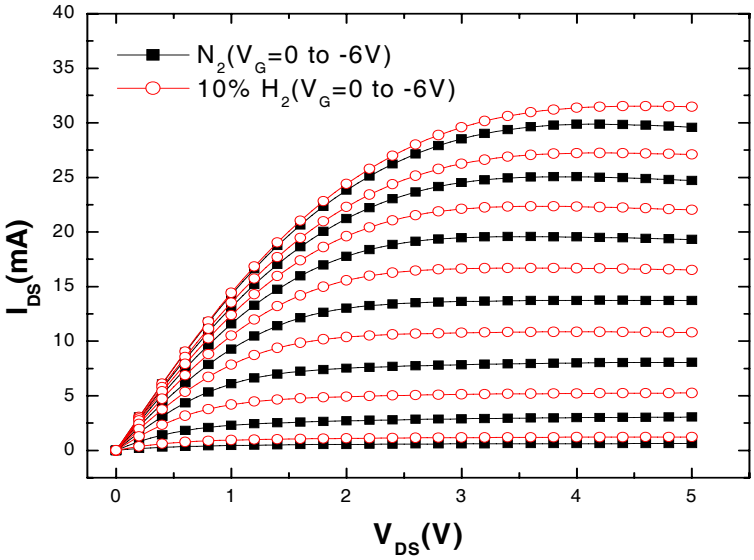

Figure 9.—I-V curves of the AlGaN/GaN MOS-HEMT sensor.

AlGaN/GaN MOS HEMT Sensor

In addition to Schottky diodes, the AlGaN/GaN HEMT structure can also be used to make a sensor based on three-terminal transistor topology. In this case, drain to source current is measured, which is modulated by the gate that is affected by the hydrogen concentration in the ambient. A MOS-HEMT sensor was designed and fabricated (ref. 2). Figure 8 shows the micrograph of the sensor. The structure is the same as other FET-type transistors. Sc_2O_3 was used as the gate oxide. The DC I-V measurement shown in figure 9 confirms its transistor characteristics and the response to hydrogen. As can be seen in the figure, this sensor has largest current change in response to hydrogen when biased in the range of 10 to 20 mA.

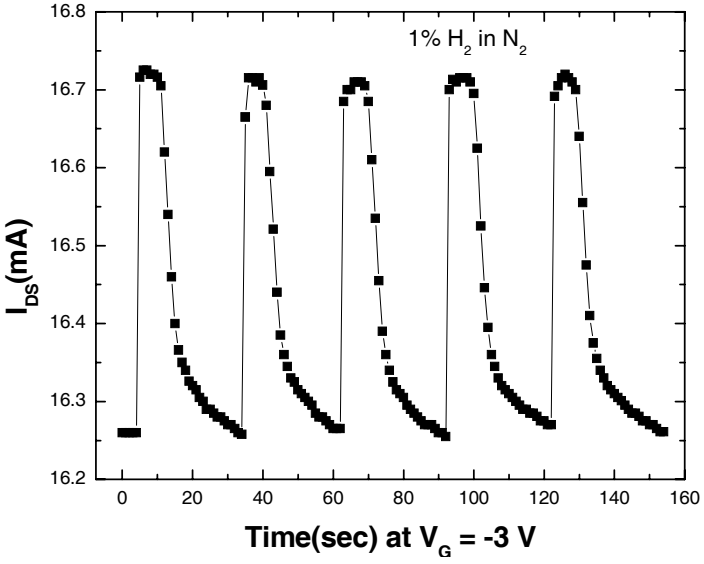

Figure 10.—Time response of the AlGaN/GaN MOS-HEMT sensor.

Figure 10 shows the time response of the AlGaN/GaN MOS-HEMT sensor when ambient conditions of pure N_2 and 1 percent H_2 in N_2 were cycled through the test chamber. The gate was biased at –3 V with a bias current of about 16.25 mA in pure N_2. As 1 percent H_2 was introduced into the chamber, the current increased to 16.7 mA. This 0.45 mA increase is about the same as observed in the case of AlGaN/GaN diode sensor fabricated on the same layer structure, but with only 1 percent H_2. The factor of 10 improvement is due to the gain of the HEMT transistor. The result clearly shows the advantage of using AlGaN/GaN MOS-HEMT as hydrogen sensor as compared to Schottky diodes. The sharp response also shows the fast response time of less than one second and the reusability. In addition, since the sensor device uses the same HEMT layer structure that can be used to build radio frequency transceiver circuits, potential monolithic integration of sensor device and wireless transceiver is feasible. Noted that GaN-based HEMT is expected to be the first GaN-based electronic device to be commercialized for next generation radar and wireless communication systems. Since GaN-based devices can operate at elevated temperatures, the GaN-integrated wireless sensor can be used in harsh environment where sensor devices fabricated on other semiconductor technologies cannot survive.

ZnO-Based Sensor

Pt-ZnO Schottky Diode Sensor

We have been investigating ZnO for sensor application since it is a stable and bio-safe material (bandgap = 3.3 eV). A Pt-ZnO Schottky diode was fabricated, as shown in figure 11.

The I-V characteristic of the Pt-ZnO diode is shown in figure 12. The I-V curve changes in response to different levels of hydrogen concentration. In pure N_2, the characteristic is similar to other diodes with exponential increase in current at forward bias. As hydrogen concentration increases, the current at reverse bias increases and the forward bias turn on characteristics gradually disappears. This interesting behavior shows that as hydrogen concentration increases, the device behaves more like a resistor than a diode. At 1 percent H_2 level, the device is essentially a resistor of 83 Ω. Compared to GaN Schottky diode, this Pt-ZnO is more sensitive and can detect ppm level hydrogen concentration change.

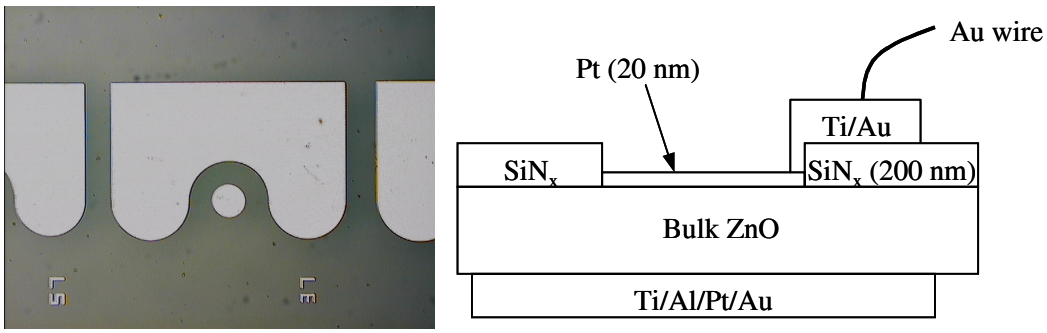

Figure 11.—Pt-ZnO Schottky diode photo (left) and structure (right).

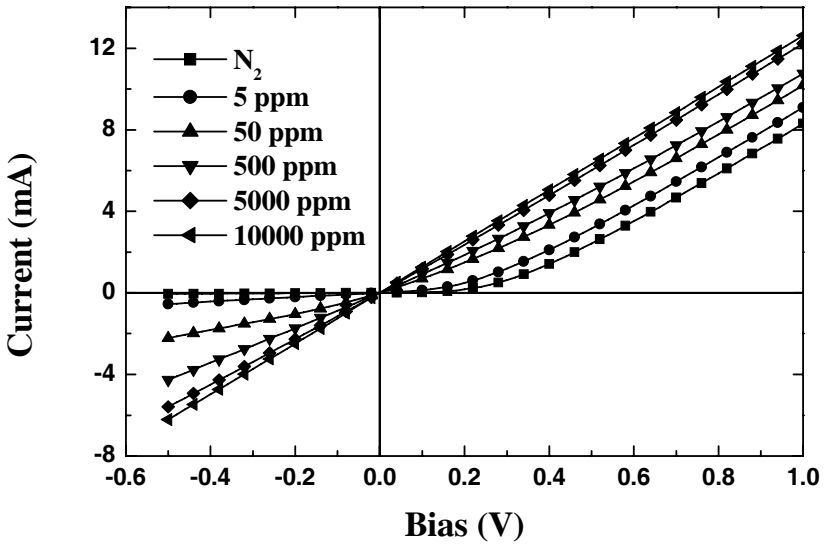

Figure 12.—Current-voltage characteristics of Pt-ZnO Schottky diode sensor in response to different levels of hydrogen concentration.

ZnO Nanorod Sensor

ZnO can also be used to fabricate nanoscale devices like nanowires and nanorods (ref. 7). A depletion-mode Field-Effect Transistor (FET) was demonstrated using a ZnO nanorod (ref. 8), as shown in figure 13. The device was found to be sensitive to UV with significant changes in DC I-V characteristics (current increased by larger than 4 times). A comparison of I-V characteristics measured at room temperature is shown in figure 14.

The result indicates that ZnO has a very good potential for low power operation since the current is very low. By integrating with low power electronic circuits, a long lifetime battery-powered wireless sensor can be achieved. With energy harvesting devices, a self-powered wireless sensor is also possible.

The same ZnO nanorod can be used for hydrogen detection as well. Figure 15 shows the photo of a ZnO nanorod hydrogen sensor. Compared to figure 13, the gate metal is removed. The nanorod channel resistance is modulated by the hydrogen concentration. Figure 16 shows the measured I-V characteristics of ZnO nanorod sensor under pure N_2 and 10 percent H_2 in N_2, at different temperatures. The existence of H_2 changed the resistance of ZnO nanorod, and the change is larger at higher temperature. Compared to ZnO Schottky diode sensor, the current change is smaller, which suggests that an array of multiple ZnO nanorods is needed to increase the sensitivity.

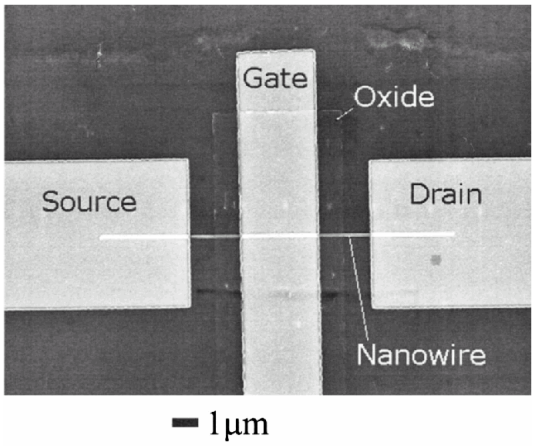

Figure 13.—ZnO nanorod FET.

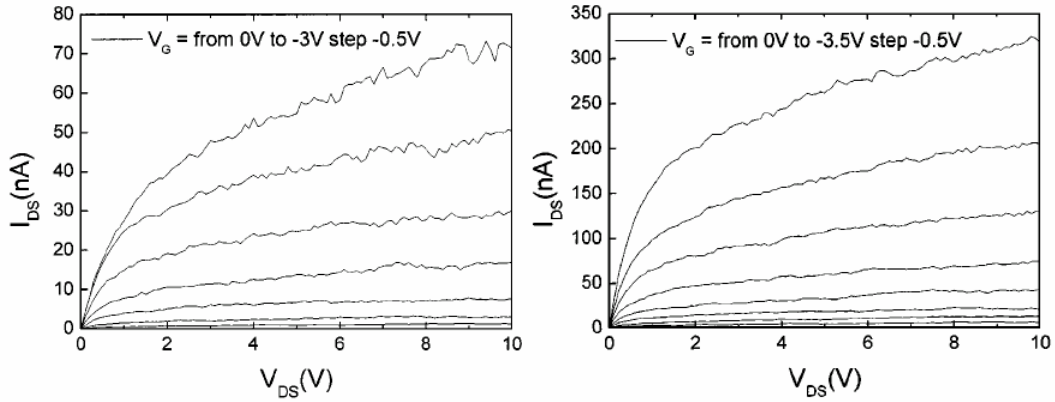

Figure 14.—I-V characteristics of ZnO nanorod FET measured at room temperature in the dark (left) and under UV illumination (right).

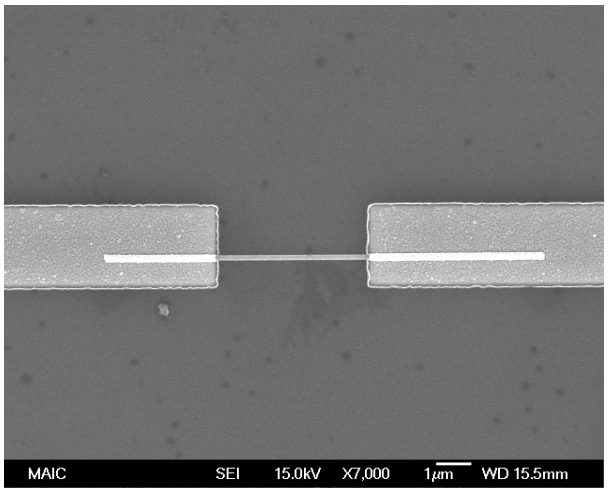

Figure 15.—ZnO nanorod sensor with length = 3.5 μm and diameter = 130 nm.

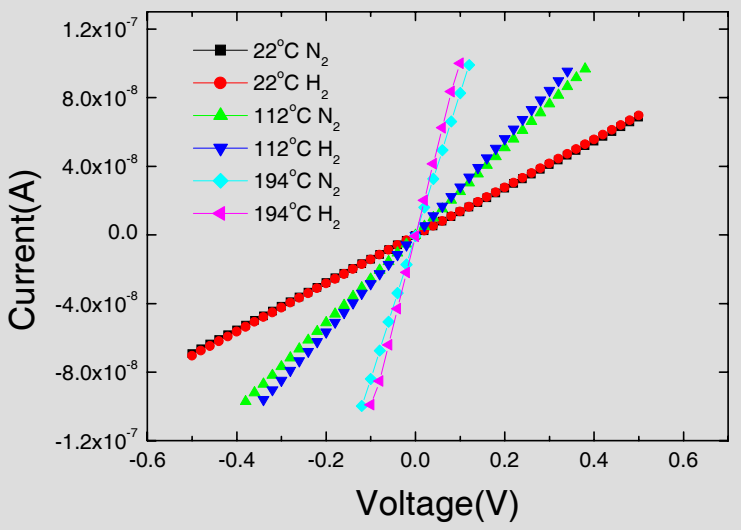

Figure 16.—Measured I-V characteristics of ZnO nanorod sensor.

Wireless Sensor System Prototype

Integration with Wireless Transceiver

There are strong reasons for developing distributed arrays of integrated semiconductor gas sensors for detecting hydrogen leaks and being able to transmit data on the location of the leaks back to a central monitoring station or control facility. In addition, these detectors would have dual-use in automobiles and aircraft, fire detectors, and exhaust diagnosis from industrial processes.

By using low noise amplifier, microprocessor, and wireless transceiver, we have successfully demonstrated a low-cost wireless sensor system prototype (ref. 3). Figure 17 shows the remote wireless transmitter module and the monitoring receiver module. The size of the prototype module is smaller than palm-size and can be easily integrated in a wireless sensor network.

Operation of Wireless Hydrogen Sensor System Prototype

The detailed block diagram of the modules is shown in figure 18. The remote wireless transmitter module has an input terminal that can detect voltage-current change from any sensor with electrical signal output. In the case of hydrogen sensor, voltage sensing is used. If the sensor is small enough, it can be integrated with the module. A low noise amplifier amplifies the sensor signal for digital signal processing in the micro-controller. The micro-controller has built-in analog-digital converter and encoder for secured wireless transmission. After the signal processing, the sensor data is sent by a transceiver and an antenna operating at 916 MHz. The antenna was designed as a low-cost low-profile printed loop antenna fabricated on the circuit board inside the module.

On the receiver side, same antenna and transceiver are used as radio frequency interface. After the signal is received and down-converted to low frequency, the same micro-controller is used to process and decode the sensor data. The sensor data is then displayed on the LCD screen. The voltage reading on the screen is the same voltage detected at the remote sensor, and the change would indicate the detection of hydrogen leakage. A more complicated system can be built upon this platform. For example, a programmed threshold level to trigger the alarm and shut off the gas valve. With various multiple access techniques, e.g., code-division multiple access (CDMA), a wireless hydrogen sensor network can be realized.

Figure 17. Photos of the remote wireless transmitter module (left) and the monitoring receiver module (right).

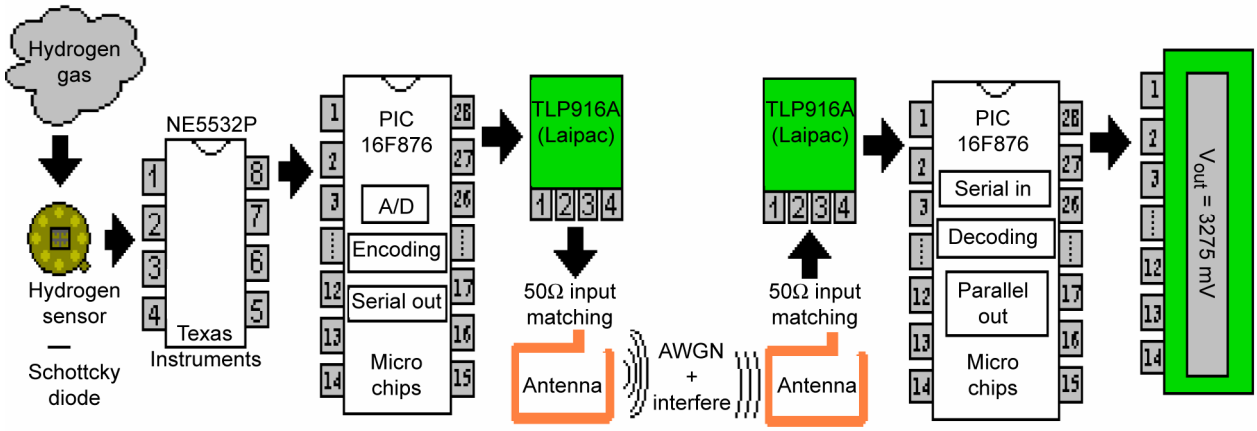

Figure 18.—Prototype wireless hydrogen sensor system. Left hand side of the figure shows the wireless transmitter module and its block diagram. Right hand side of the figure shows the monitoring receiver module and its block diagram. Small loop antennas are integrated inside the module

Publications

The research findings in this project period have resulted in several published papers in referred journals and conference proceedings. The following three selective publications describe the most details:

1. A.EL. Kouche, J. Lin, M.E. Law, S. Kim, B.S. Kim, F. Ren, S.J. Pearton, "Remote Sensing System for Hydrogen Using GaN Schottky Diodes," *Journal of Sensors and Actuators B: Chemical*, vol. 105/2, pp. 329–333, 2005.
2. S.J. Pearton, B.S. Kang, Suku Kim, F. Ren, B.P. Gila, C.R. Abernathy, J. Lin, and S.N.G. Chu, "GaN-based diodes and transistors for chemical, gas, biological and pressure sensing," *J. Phys.: Condensed Matter*, vol. 16, issue 29, pp. R961–R994, July 2004.
3. J. Lin, A. EL. Kouche, M.E. Law, F. Ren, B.S. Kang, S.J. Pearton, D.P. Norton, and C.R. Abernathy, "GaN-Based and Zno Nanorod Sensors for Wireless Hydrogen Leak Detection," Proceedings of the 207th Meeting of the Electrochemical Society, Quebec City, Canada, May 15–20, 2005. (Invited Paper)

References

1. G.W. Hunter, P.G. Neudeck, C.C. Liu, B. Ward, Q.H. Wu, P. Dutta, M. Frank, J. Trimbol, M. Fulkerson, B. Patton, D. Makel, V. Thomas, "Development of chemical sensor arrays for harsh environments and aerospace applications," Sensors, 2002. Proceedings of IEEE , vol. 2, pp. 1126–1133, 12–14 June 2002.
2. S.J. Pearton, B.S. Kang, Suku Kim, F. Ren, B.P. Gila, C.R. Abernathy, J. Lin, and S.N.G. Chu, "GaN-based diodes and transistors for chemical, gas, biological and pressure sensing," J. Phys.: Condensed Matter, vol. 16, issue 29, pp. R961–R994, 2004.
3. A.EL. Kouche, J. Lin, M.E. Law, S. Kim, B.S. Kim, F. Ren, S.J. Pearton, "Remote Sensing System for Hydrogen Using GaN Schottky Diodes," Journal of Sensors and Actuators B: Chemical, 2004
4. J.B. Casady, A.K. Agarwal, S. Seshadri, R.R. Siergiej, L.B. Rowland, M.F. MacMillan, D.C. Sheridan, P. A. Sanger and C. D. Brandt, Solid-State Electron. 42 2165(1998).
5. O. Ambacher, M. Eickhoff, G. Steinhoff, M. Hermann, L. Gorgens, V. Werss, et al., Proc ECS, 214 27 (2002).
6. L.Y. Chen, G.W. Hunter, P.G. Neudeck, D.L. Knight, C.C. Liu, and Q.H. Wu, Proceeding of the Third International Symposium on Ceramic Sensors, H.U. Anderson, M. Liu, and N. Yamazoe, Editors, Electrochemical Society Inc. Pennington, NJ, pp.92–98, (1996).
7. Y.W. Heo, V. Varadarajan, M. Kaufman, K. Kim, D.P. Norton, F. Ren, and P.H. Fleming, "Site-specific growth of Zno nanorods using catalysis-driven molecular-beam Epitaxy," Applied Physics Letters, vol. 81, no. 16, 14 October 2002.
8. Y.W. Heo, L C. Tien, Y. Kwon, D.P. Norton, S.J. Pearton, B.S. Kang, and F. Ren, "Depletion-mode ZnO nanowire field-effect transistor," Applied Physics Letters, vol. 85, no. 12, 20 September 2004.

Project Title: Sensing Hydrogen by Using Biological Assays

Task PI: Z. Hugh Fan, Mechanical and Aerospace Engineering
Collaborator: Jenshan Lin, Electrical and Computer Engineering

Project Goals

The goal of this project is to develop a novel hydrogen sensor using an enzyme-catalyzed reaction and microfluidic technology. The anticipated benefits over the state-of-the-art palladium- or its alloy-based hydrogen sensors include the ability to operate at ambient temperatures, the ability to operate in background gases due to the specificity of the enzyme, fast response time, and no recovery time.

Accomplishments

Concept

The principle of using a biological assay for detecting hydrogen is shown as follows:

$$H_2 + 2BV^{2+} \xrightarrow{hydrogenase} 2H^+ + 2BV^+$$

The enzyme, hydrogenase, catalyzes the oxidation of H_2; BV^{2+} (benzyl viologen) acts as the electron acceptor, producing BV^+ that can be detected electrochemically. The enzyme was the cytoplasmic hydrogenase from *Ralstonia eutropha*, supplied by a collaborating research group in Germany.

Experimental Setup

The H_2 testing station was assembled as shown in figure 1. It consists of a H_2 tank, a flow cell, an electrochemical detector, and a data acquisition system. Varying concentrations of H_2 gas (mixed with N_2) flows through the electrochemical flow cell. The cell contains 1 mL of an aqueous solution with the pressure at ~1 atm and at ambient temperature. The electrochemical detection is achieved using a potentiostat that controls the cell voltage and measures the electrical current.

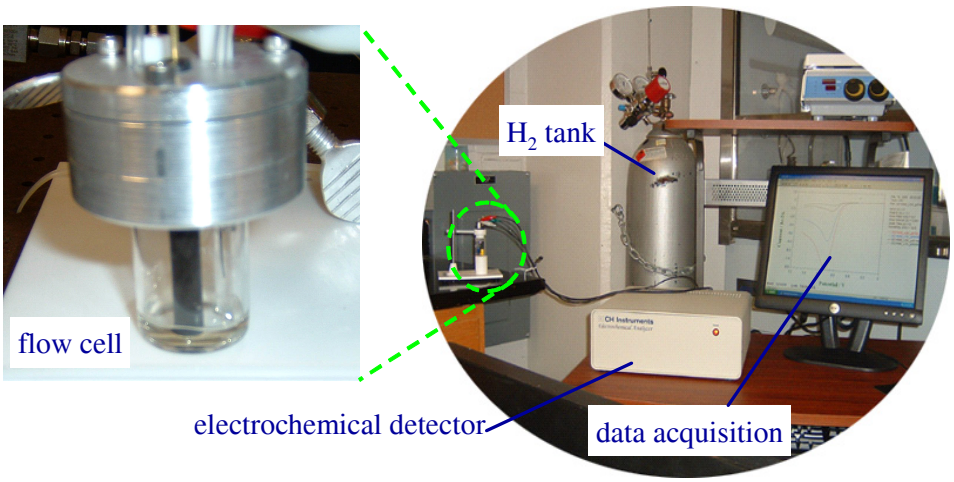

Figure 1.—The H_2 testing station consists of a H_2 tank, a flow cell, an electrochemical detector, and a data acquisition system. An exploded view of the electrochemical flow cell is shown on the left.

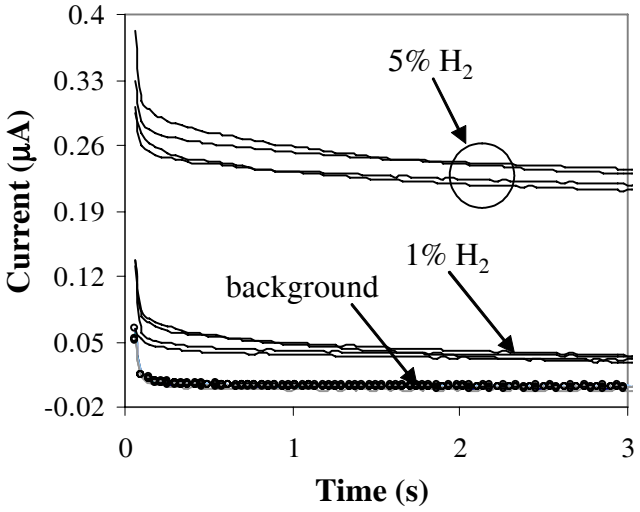

Figure 2.—Hydrogen detection using chronoamperometry. Four repeats were performed at each H_2 concentration (diluted in N_2). Background is 100 percent N_2.

Electrochemical Detection

When a H_2 gas sample flowed through the detection system, H_2 was collected by reacting with a reagent mixture containing hydrogenase. The resultant product, BV^+, was measured using chronoamperometry technique and the electrochemical current was used as the detection signal. An example showing the detection of H_2 is in figure 2.

Calibration Curve

After optimizing the experimental protocol to achieve repeatable detection at low H_2 concentration, we obtained the calibration curve shown in figure 3. A linear response was observed from 1 to 100 percent H_2, and electrochemical signal is normalized against enzyme reaction time. A calibration curve was also developed from gas mixtures containing 20 percent O_2, which is similar to atmospheric air.

Work in Progress

We are implementing our detection protocol on a microfluidic platform. Expected improvements by miniaturization include (a) more efficient use of expensive reagents (i.e., enzymes), (b) increased sensitivity, and (c) faster response time. We have fabricated several microfluidic designs on a plastic chip, in which we have been able to accomplish simultaneous gas-liquid flow. We have also been able to demonstrate and calibrate electrochemical detection of BV^{2+} in the microfluidic platform.

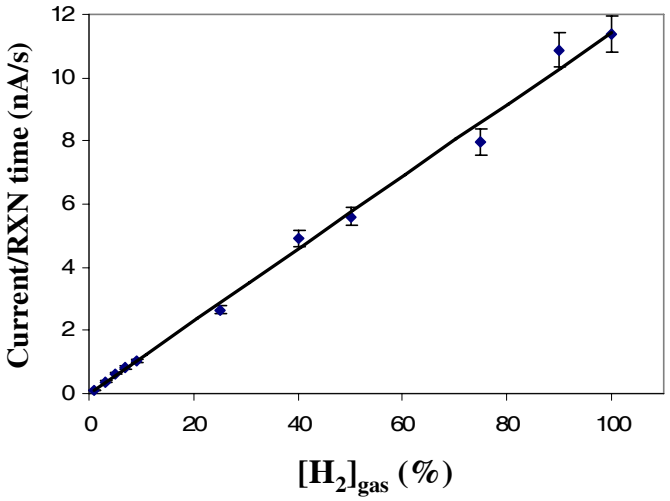

Figure 3.—Calibration curve for current (normalized by enzyme reaction time) and percentage of H_2 in gas streams mixed with N_2. The current is obtained by chronoamperometric detection of BV^+, which is the reaction product of BV^{2+} and H_2 catalyzed by hydrogenase.

4. Instrumentation for Hydrogen Leak Detection

Faculty Lead: David Hahn, Mechanical and Aerospace Engineering

Project Title: Raman Spectroscopy For Remote Detection of Hydrogen Leaks

Task PI: David W. Hahn, Department of Mechanical and Aerospace Engineering

Project Goals

Leak detection of rocket propellants, notably hydrogen, is an ongoing area of concern for the space shuttle program. To aid in safety and efficiency, it is desirable to have remote leak detection capabilities that will enable standoff interrogation of various hydrogen handling facilities, such as transfer lines and piping, as well as shuttle launch pad detection. This research involves the development of diagnostic tools for portable, remote hydrogen leak detection using laser-based techniques. Laser-based approaches will include Rayleigh/Mie light scattering and Raman spectroscopy. The proposed research will focus on Rayleigh/Mie/Raman integration using temporal and spectral data analysis in combination with pulsed laser excitation to discriminate from background contaminants and to optimize leak detection at the leak source. The overall project goal is the development of a field-portable sensor package for field evaluation.

Accomplishments

Project Summary

Leak detection of rocket propellants, notably hydrogen, is an ongoing area of concern for the space shuttle program. To aid in safety and efficiency, it is desirable to have remote leak detection capabilities that will enable standoff interrogation of various hydrogen handling facilities, such as transfer lines and piping, as well as shuttle launch pad detection. This research involves the development of diagnostic tools for portable, remote hydrogen leak detection using laser-based techniques. A laser-based approach will utilize Raman spectroscopy to detect diatomic hydrogen in the gaseous state. The research has focused on Raman spectroscopy using temporal and spectral data analysis in combination with pulsed laser excitation to discriminate from background contaminants and to optimize leak detection at the leak source. The overall project goal is the development, testing, field evaluation, and optimization of a field-portable sensor package.

Project Overview

Research to date has focused on the development of diagnostic tools for portable and remote hydrogen leak detection using laser-based approaches, namely Raman spectroscopy. The research has focused on Raman spectroscopy integration using temporal, statistical, and spectral data analysis in combination with pulsed laser excitation to discriminate from background contaminants and to optimize leak detection at the leak source.

The technique of Raman spectroscopy is based on the inelastic scattering of electromagnetic radiation due to interactions of the incident radiation with the vibrational energy states of the scattering species. The nature of Raman spectroscopy makes selection of the excitation laser important. Notably, the process of Raman scattering is a relatively weak one as compared to elastic scattering. For example, the Raman scattering cross-section of hydrogen (H_2) is $9x10^{-30}$ cm^2/sr, which is nearly two orders of magnitude less than the Rayleigh scattering cross-section of hydrogen. However, the Raman scattering cross-section scales nominally as the inverse of the fourth power of excitation wavelength. It is therefore desirable to use as short a wavelength as possible for excitation, although consideration must also be given to

fluorescence, which can interfere with the Raman-shifted hydrogen signal. Research led to the selection of a frequency-tripled (355 nm) Nd:YAG laser as the appropriate laser source.

Summary of Progress

Optical Configuration

Using the laboratory hydrogen test cell developed last program year, tests were performed to determine the optimal excitation wavelength. Using the 6-in. path length cell, the hydrogen Raman signal was quantified over a range of hydrogen concentrations. All hydrogen concentrations were prepared in nitrogen to avoid the possibility of any explosions initiated by the laser pulse. As noted earlier, the response for 355-nm excitation revealed a 16-fold increase in response slope, hence all recent work was focused on the use of 355-nm excitation. Detailed measurements of the hydrogen Raman signal were recorded as a function of hydrogen concentration for two separate laser pulse energies (125 and 250 mJ). In addition, Raman data was recorded for two different size collection lens, namely a 2 in. lens and a 4 in. lens. These data enable additional investigation of the scaling of the Raman signal with laser pulse energy and solid collection angle.

The Raman signal is expected to be directly proportional to the laser pulse energy and the solid angle of collection. This latter quantity should scale as the square of the collection lens diameter. To quantify this scaling, the Raman signal is presented in figure 1 as a function of the laser pulse energy times the square of the collection lens for a fixed hydrogen concentration of 12.5 percent. As observed in figure 1, the linear response validates the theoretical scaling, enabling use of the data collected to extrapolate to different laser pulse energies and collection optics. This data was useful for the design and testing of the prototype field instrument.

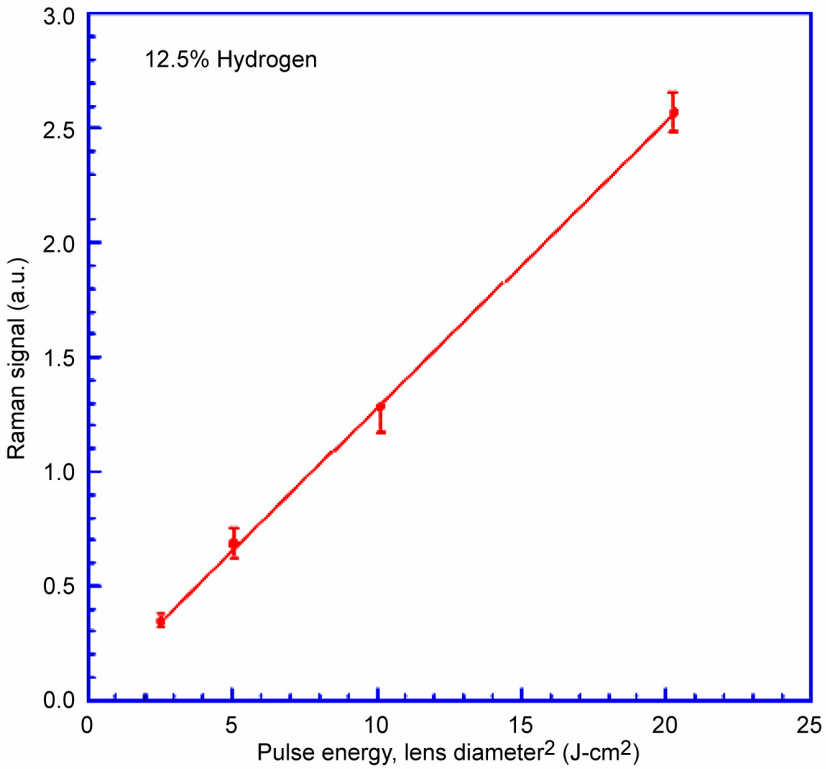

Figure 1.—Raman response vs. the laser pulse energy times the collection solid angle.

Photon Arrival Rates

The quantification of photon arrival rates for Raman detection of hydrogen gas can be predicted based on the optical configuration and the Raman cross-sections for hydrogen. The geometry for Raman detection of hydrogen is shown below in figure 2. Theoretically, the photon arrival rate may be expressed as

$$S_{Raman} = F_o \, \sigma' \, N \, (h\nu)^{-1} \, dV \, d\Omega,$$

where N is the hydrogen molecular density, σ' is the Raman scattering cross-section for hydrogen at the desired wavelength, $h\nu$ is the photon energy, dV is the excitation or scattering volume, and $d\Omega$ is the solid collection angle. The Raman scattering cross-section for hydrogen is 1.0×10^{-29} cm^2/sr at 355 nm. Using a laser pulse energy of 125 mJ/pulse, a 4 in. diameter collection lens, and a separation distance of 8 ft, and 1 percent hydrogen in the 6 in. cell, the calculated photon arrival rate is 2×10^4 photons per pulse. Assuming typical fiber optic and spectrometer losses (20 μm slit size), the estimated photon rate at the photomultiplier tube was about 500 photons/pulse.

Raman detection limits were calculated experimentally using the slopes of the Raman signal response function, based on laboratory measurements. Specifically, using a 125 mJ/pulse laser, which is consistent with the new field-instrument laser, and a 4 in. collection lens, the Raman signal as a function of hydrogen concentration was evaluated. The data were collected at a separation distance (gas cell to collection optics) of 8 ft. Using the slope to extrapolate the detection limit at three times the noise limits (3σ), the detection limit was calculated at 1 percent hydrogen.

Hardware for Field Instrument

A key component of the recent work was design and construction of the remote Raman instrument that is suitable for field evolution. Field measurements provide the range of conditions, such as ambient aerosol loadings, varying wind, temperature and humidity, which are not readily created in a laboratory setting. The prototype instrument was assembled using the following design and components, as illustrated in figure 3. The laser was a BigSky CFR 200 with frequency-tripling package that provides 95 mJ/pulse of 355-nm laser light. The maximum repetition rate is 10 Hz, and the approximate full-width half-maximum pulse width is 10 ns. A rack mountable power supply was purchased. The light is collected with a bi-furcated fiber optic and input to two matching custom-designed (Ocean Optics) monochrometers, with the output directed to two matched photomultiplier tubes. The system was constructed during December 2004. Photographs of the system, including the overall optical layout, monochrometers, and system configuration are shown in the following figures.

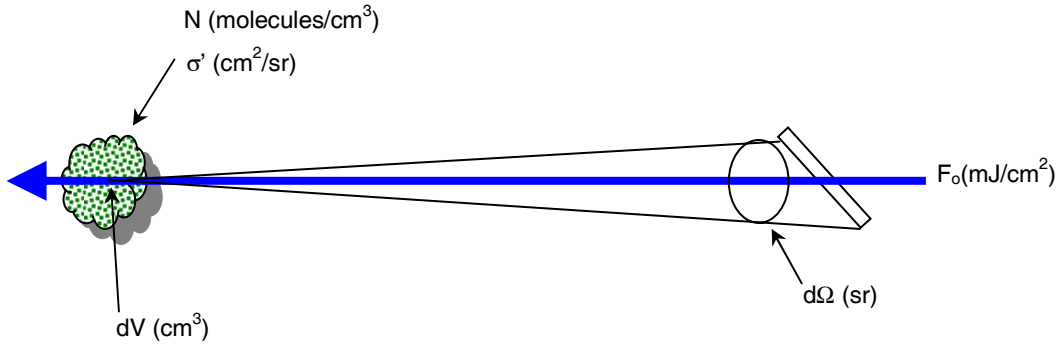

Figure 2.—Collection geometry for Raman photon flux calculations.

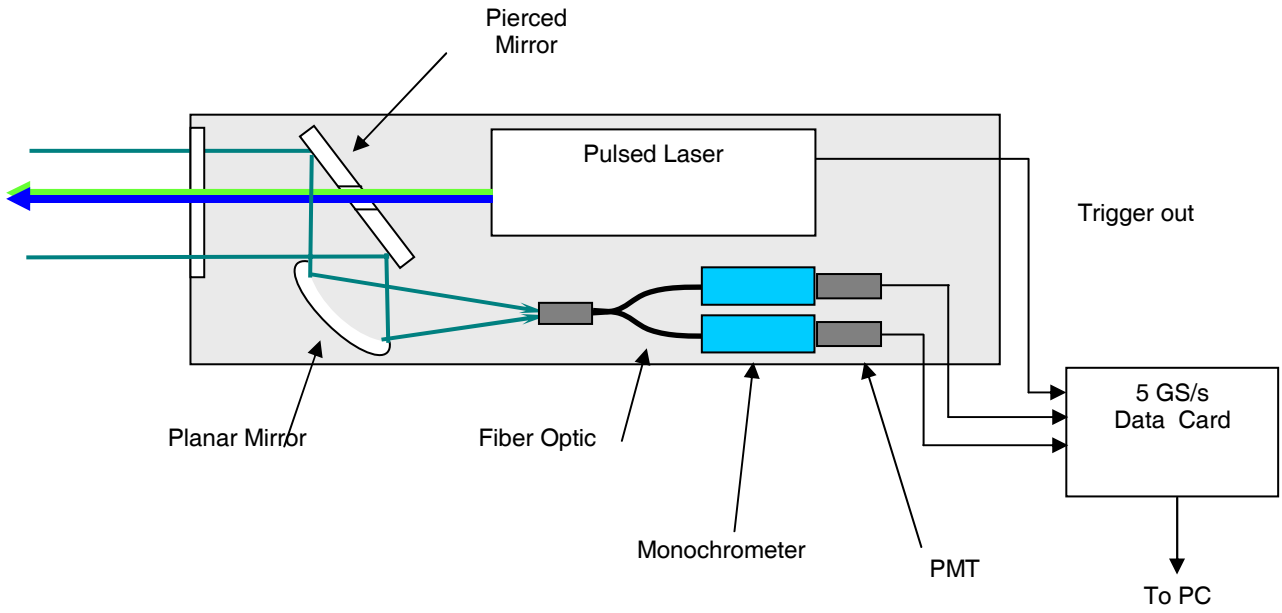

Figure 3.—Schematic of the field instrument for Raman detection of hydrogen.

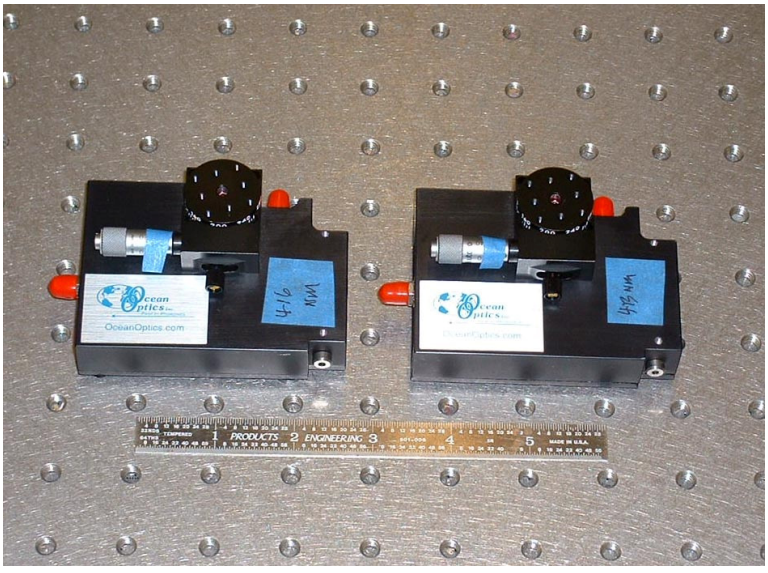

Figure 4.—Custom monochrometers for the Raman instrument.

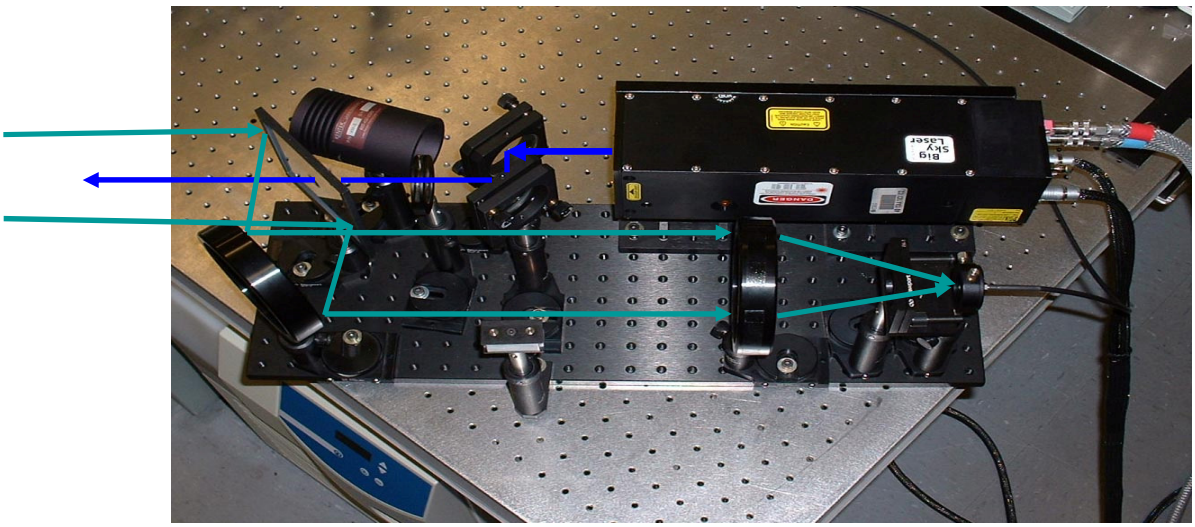

Figure 5.—Photograph of the Raman instrument, showing the optical paths of the output beam (blue) and the collected signal (green).

Figure 6.—Photographs of the prototype detector and instrument rack (which includes laser power supply).

Instrument Assessment

Preliminary measurements were conducted in the laboratory using the field instrument. No significant hydrogen signal was detected with the configuration under the laboratory conditions. This was attributed to the lack of sufficient signal throughput through the custom-made monochrometer modules. Because the modules were custom designed, it was fully anticipated that adjustments would have to be made to optimize the tradeoff between throughput and resolution. The original 10-μm slits were determined to be too narrow. Ocean Optics has provided additional entrance and exit slits at no cost to enable optimization of the Raman signal. The redirection of the program funding did not enable complete testing of the optimized field instrument. It is expected that the current instrument is capable of operating in a field environment, although it is difficult to extrapolate laboratory results to the field conditions. For example, the laboratory work utilized sealed optical chambers for all work, as the direct venting of hydrogen was deemed a safe practice. The test cell windows are known to be a significant source of spectral noise; hence moving to an open-air outdoor situation might increase instrument performance. Alternatively, the ambient environment offers the potential for other sources of spectral noise, such as fluorescence from organic compounds, which may degrade overall instrument detection limits. Only a detailed field analysis will answer such questions.

In summary, the current program demonstrated that Raman spectroscopy utilizing time-resolved, pulsed-laser excitation is a viable technology for hydrogen lead detection. Furthermore, current off-the-shelf components (lasers, detectors, and signal processors) are available to implement this technology, as demonstrated during this project.

5. Cryogenic Transport and Storage (CTS)

Faculty Lead: James Klausner, Mechanical and Aerospace Engineering

Project Title: Terrestrial Cryogenic Two-Phase Flow and Heat Transfer

Task PI: James F. Klausner, Department of Mechanical and Aerospace Engineering
Co-I: Renwei Mei, Department of Mechanical and Aerospace Engineering

Project Goals

Cryogenic fluids flowing through pipelines often operate in a two-phase flow regime. In order to design transport systems for two-phase flows it is critical to be able to predict the pressure gradients and heat transfer coefficients associated with the fluid and thermal conditions. The most reliable two-phase flow models for predicting pressure gradient and heat transfer coefficients in pipe flow are specific to a particular flow configuration or flow regime, i.e., bubbly, stratified, annular, slug etc… Extensive flow regime pattern recognition experiments have been carried through with air/water, oil/gas, and refrigerant two-phase flows. From these experiments flow regime maps have been constructed. However, the general validity of such maps has not yet been demonstrated. Very sparse information on two-phase flow regimes with cryogenic fluids is available. Thus, designers of cyrogenic systems rely on generic flow regime maps. There exists a significant need to collect flow regime data for the flow of cryogenic fluids for a variety of operating conditions and gravitational environments. It is anticipated that the data collected from this investigation will be used to explore the applicability of existing flow regime maps to cryogenic fluids. The results will provide designers of cryogenic systems the means to identify the operating flow regimes.

In addition, hundreds of two-phase flow pressure gradient and heat transfer models have been proposed in the literature. The reason so many different models have been proposed is that each is only efficacious over a narrow parameter space. When new data are available that are not well predicted from existing models, there is a tendency to develop a new model. There exists very little experimental data concerning two-phase pressure gradients and heat transfer for the flow of cryogenic fluids, especially in the low turbulent Reynolds number range with low heat fluxes. There exists a significant need to compile a data based on cryogenic two-phase pressure gradient and heat transfer. There also exists a need to develop mechanistically based pressure gradient and heat transfer models that have general validity over a wide parameter space, which will be carried out as part of the experimental investigation. It is anticipated that these data will allow the development of pressure gradient and heat transfer models that may be used by designers of cryogenic thermal transport equipment.

Accomplishments

Abstract

Cryogenic fluids have found many practical applications in today's world, from cooling superconducting magnets to fueling launch vehicles. In many of these applications the cryogenic fluid is initially introduced into piping systems that are in excess of 150 K higher than the fluid. This leads to voracious evaporation of the fluid and significant pressure fluctuations, which is accompanied by thermal contraction of system components. This process is known as chilldown, and although it was first investigated more than 4 decades ago, very little data are available on the momentum and energy transport during this transient process. Consequently, the development of predictive models for the

pressure drop and heat transfer coefficient has been hampered. In order to address this deficiency, an experimental facility has been constructed that enables the flow structure to be observed while temperatures and pressures at various locations are measured. This study focuses on the inverse numerical procedure used to extract the transient heat transfer coefficient information from the data collected; this information is then used to evaluate the performance of various correlations for heat transfer coefficient in the flow boiling regime. The method developed utilizes flow structure information and temperature measurements, in conjunction with numerical computations for the temperature field within the tube wall, to calculate the heat transfer coefficient. This approach allows the transition point between the film boiling regime and the nucleate boiling regime to be determined, and it also elucidates the variation of the heat transfer coefficient along the circumference of a horizontal tube, with the heat transfer on upper portion being significantly smaller than that at the bottom.

Introduction

Cryogenic fluids have been used in various applications throughout the years. One application that has historically been of great interest is the use of cryogenic fluids for rocket propulsion. This interest has been sparked by the fact that "cryogenic propellants are more energetic and environmentally friendly than current storable propellant" (ref. 1) and the storage systems for these cryogenic propellants "have an advantage in reduced weight compared to super-critical tanks" (ref. 1). As the propellant tanks are filled, the cryogenic fluid is introduced into a transfer line that is in thermal equilibrium with environment, which results in voracious boiling within the line; this phenomenon is referred to as line "chilldown" or line "cool-down". Chilldown is characterized by large temperature differences, rapid transients and pressure fluctuations.

The phenomenon of chilldown is of interest since it directly impacts the design of delivery systems for the propellant. For example the magnitude of the pressure oscillation determines the thickness of the material used for the transfer lines and the heat transfer rate determines the type and thickness of insulation that is used. Hence a proper understanding of the process allows for a more economical design of cryogenic propellant delivery systems.

The vast majority of the studies carried out on chilldown have focused on developing models to predict the time taken to complete chilldown, as well as, predict the temperature and pressure during the process (refs. 2 to 6). These studies utilize correlations for the heat transfer coefficient that were developed for either steady flows or non-cryogenic flows; neither of which applies to the chilldown process and as a result only fair agreement is obtained when compared to experimental results.

The lack of correlations for heat transfer coefficient during chilldown stems from the fact that directly measuring the heat transfer coefficient during cooldown is difficult. This study focuses on an inverse heat conduction technique that enables the transient heat transfer coefficient during chilldown to be determined. An important feature of this technique is that it accounts for the flow structure in calculating the heat transfer coefficient.

Experimental Facility

The experimental facility constructed to investigate the chilldown process is schematically illustrated in figure 1. The liquid nitrogen supply is stored in a 1580 kPa (230-psi) dewar. The driving potential for the nitrogen flow through the facility is supplied by the dewar pressure. Upon exiting the dewar, the nitrogen is subcooled by a shell and tube heat exchanger, which works on the Joule-Thomson effect on the shell side, before entering a 12.5 mm i.d. vacuum jacketed Pyrex visual test section, where the flow structure is captured using a high resolution CCD camera system. The nitrogen then travels through a fixed length of 304 stainless steel pipe (with i.d. 12.5 mm, thickness 1.27 mm, conductivity 14.7 W/m-K, and specific heat capacity J/kg-K at 30 °C) and through the venturi flow meter before being dumped into an expansion tank, and then is evacuated from the facility via a ventilation system. This pipe is selected to ensure that any circumferential temperature variations are not "smeared out" due to conduction.

Validyne (Validyne Engineering) pressure transducers and type E thermocouples are used to measure the temperature and pressure at various locations. A highly sensitive differential pressure transducer measures the pressure drop across the visual test section, while inline thermocouples measure the temperature of the fluid entering and leaving. The flow then enters into the heat transfer measurement section of the facility, located 70 cm downstream of the visual test section. In this section two inline thermocouples measure the temperature of the fluid at the inlet and outlet, while a series of thermocouples are placed circumferentially on the surface of the pipe and on the outer surface of the melamine insulation, so that the temperature profile on the top, bottom and either side of the pipe is obtained (see fig. 2). These thermocouples are kept in place using Teflon (DuPont) tape to ensure that adequate thermal contact is maintained. After the heat transfer section, the two-phase flow is passed through two heaters, which vaporize any remaining liquid, to ensure single–phase vapor enters the venturi. A thermocouple and pressure transducer located prior to the venturi allow for the correction of compressibility effects to be taken into account in the mass flow rate computations. A Validyne differential pressure transducer measures the pressure drop across the venturi. The analog signals from the instruments are transferred and recorded by a 16-bit Measurement Computing data acquisition board and multiplexer system.

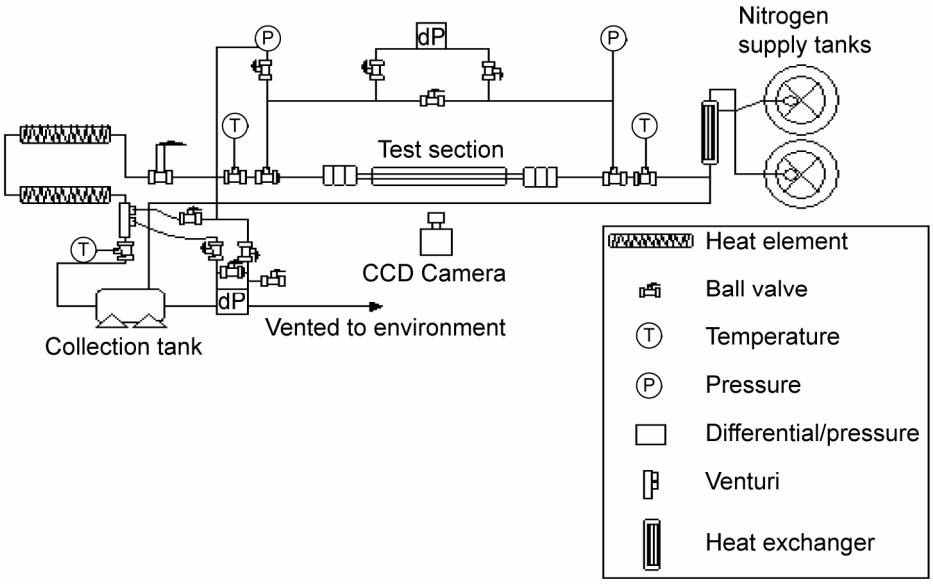

Figure 1.—Cryogenic two-phase flow experimental facility.

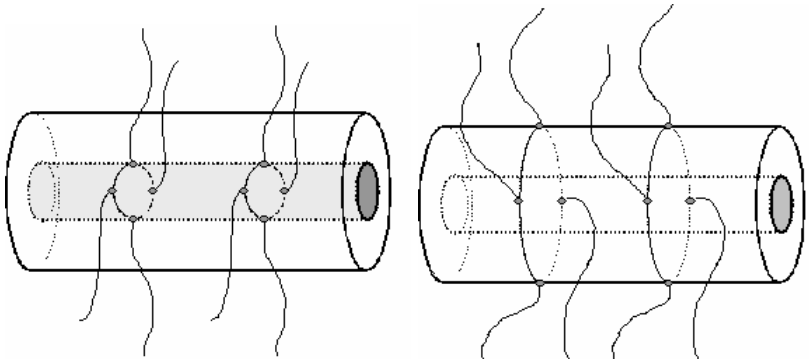

Figure 2.—Thermocouple arrangements along the pipe wall and along the insulation of the heat transfer section.

The instruments have been independently calibrated and tested to ensure they function properly. The reported accuracy of the Validyne pressure transducers is ±0.25 percent of full scale (0 to 200 psi for the static pressure transducers, 0 to 1.25 psi for the differential pressure transducer across the test section, and 0 to 12.5 psi for the differential pressure transducer across the venturi) and this was confirmed in the laboratory. The static pressure transducers are accurate to ±3.5 kPa while the differential pressure transducer across the visual test section is accurate to within ±0.06 kPa and that measuring the pressure drop across the venturi is accurate to within ±0.35 kPa. Over the large temperature range experienced in these experiments the thermocouples used are accurate to within ±1.7 °C.

Extracting the Heat Transfer Coefficient

The inverse heat conduction method employed in this study varies from previous methods in that it does not involve solving a system of least-squares equations. A comprehensive review of traditional inverse heat conduction methods is given in (ref. 7).

The process used here for extracting the transient heat transfer coefficient on the inside of the pipe involves a number of iterative steps, which are reported as three major steps. These major steps are illustrated in figure 3 and are carried out for each instance of time.

This approach is based on the fact that it is possible to use numerical computations to solve the heat conduction equation in the wall of a pipe, and once the initial and boundary conditions are known the temperature profile may be calculated. Thus it is possible to guess the heat transfer coefficient inside the pipe and knowing the heat transfer coefficient on the outside of the pipe, the temperature profile is

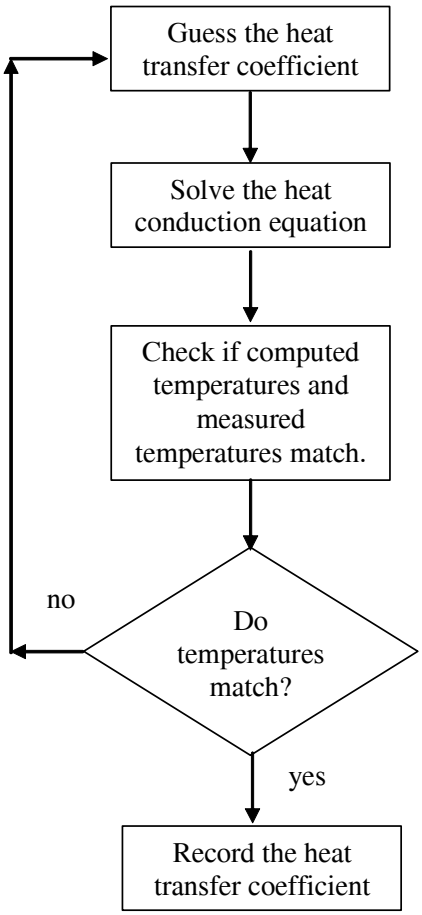

Figure 3.—Flow chart for transient heat transfer coefficient extraction process.

calculated. The temperature calculated at the outer wall is then compared with the measured outer wall temperature; if they match then the guessed heat transfer coefficient is taken as the actual heat transfer coefficient otherwise a new guess is made and the process is repeated until the computed and measured temperatures match.

Computing the Temperature Field in the Pipe Wall

This procedure encompasses solving the heat conduction equation for the pipe wall. An integral part of this process is the implementation of the boundary conditions. The initial condition is simple as it is the state in which the pipe is in thermal equilibrium with the environment, a constant temperature throughout.

The unsteady 3–D form of the heat conduction equation in cylindrical coordinates is written as follows:

$$c\rho\frac{\partial T}{\partial t}=\frac{\partial}{\partial z}\left(k\frac{\partial T}{\partial z}\right)+\frac{1}{r}\frac{\partial}{\partial r}\left(rk\frac{\partial T}{\partial r}\right)+\frac{1}{r}\frac{\partial}{\partial \phi}\left(\frac{k}{r}\frac{\partial T}{\partial \phi}\right), \tag{1}$$

where ρ is the density of the material, c is the heat capacity, t is the time variable, T is the temperature, r is the radial coordinate, z is the axial coordinate and ϕ is the azimuthal coordinate. This equation is non-dimensionalized using the following parameters:

$$\varphi=\frac{T-T_{sat}}{T_w-T_{sat}};\ z'=\frac{z}{d};\ r'=\frac{r}{d};\ c'=\frac{c}{c_0};\ k'=\frac{k}{k_0};\ \rho'=\frac{\rho}{\rho_0}$$

where T_{sat} is the saturation temperature of the fluid within the pipe, T_w is the temperature on the outer wall of the pipe, d is the pipe wall thickness, and the subscript 0 denotes the property is to be evaluated at the initial temperature, T_0. Thus the original equation is thus reduced to (3)

$$\frac{\rho_0 c_0 d^2}{k_0}\rho' c'\frac{\partial \varphi}{\partial t}=\frac{\partial}{\partial z'}\left(k'\frac{\partial \varphi}{\partial z'}\right)+\frac{1}{r'}\frac{\partial}{\partial r'}\left(r'k'\frac{\partial \varphi}{\partial r'}\right)+\frac{1}{r'}\frac{\partial}{\partial \phi}\left(\frac{k'}{r'}\frac{\partial \varphi}{\partial \phi}\right). \tag{2}$$

It must be noted here that the thermal properties (k and c) of the pipe material vary significantly over the range of temperatures measured in the experiments. These variations are taken into account by curve-fitting the property values as functions of temperature and assigning the values based on the temperature at the given point.

Equation (2) is discretized using a finite volume formulation. A backward Euler scheme is applied to the temporal term while a central difference scheme is used for the spatial terms. The resulting system of equations is solved using the Alternating Direction Implicit (ADI) method described in (ref. 8).

Before the system of equations may be solved, the energy flowing into the system from the ambient must be known; hence the heat transfer coefficient for the outside of the pipe insulation must be determined. This is accomplished through a steady-state calibration process in which cool nitrogen vapor is passed through the heat transfer section at various mass flow rates. A relationship between heat flux into the pipe insulation versus temperature difference (ambient temperature less the insulation surface temperature) is determined. A constant heat transfer coefficient yields a linear relationship as shown in figure 4, and the slope is the heat transfer coefficient for the outer surface of the pipe. The measurement of q''_w is quite difficult due to the small temperature rise in the cryogenic vapor, thus there is some scatter in figure 4. However, the measured heat transfer coefficient, 4.38 W/m^2-K, is quite small, compared with convective heat transfer on the inner pipe wall. The errors in the calibration have a negligible impact on the computed thermal field in the pipe wall.

Thus the outer pipe boundary condition may be written as,

$$-k\frac{\partial T}{\partial r}=h_{out}\left(T_{out}-T_{\infty}\right), \tag{3}$$

which is then non-dimensionalized to give,

$$-k'\frac{\partial \varphi}{\partial r'}=\frac{h_{out}d}{k_0}\varphi+\frac{d}{k_0}\left(\frac{h_{out}T_{sat}-h_{out}T_{\infty}}{T_{wall}-T_{sat}}\right). \tag{4}$$

Here h is the heat transfer coefficient, and subscripts *out* and ∞ represent the outer surface of the pipe, and the outer insulation surface, respectively. The insulation temperature is taken to be uniform at the measured temperature.

The heat transfer coefficient on the inside of the pipe is the quantity that is guessed during the calculation. However, because two-phase flow is present for much of the experiment, the flow structure is wavy-stratified and there is a significant difference between the temperature at the top of the pipe and the

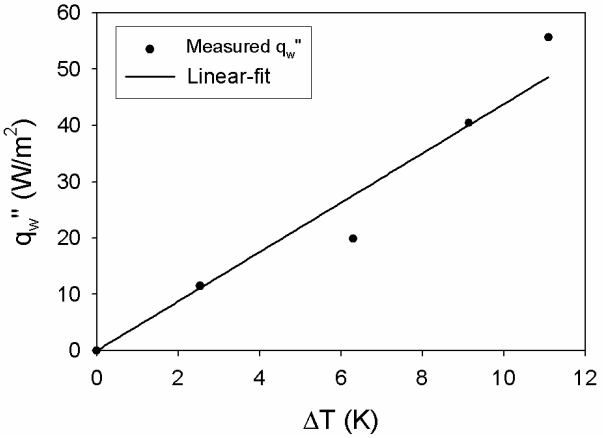

Figure 4.—Calibration curve for determining heat transfer coefficient on the outer surface of the pipe.

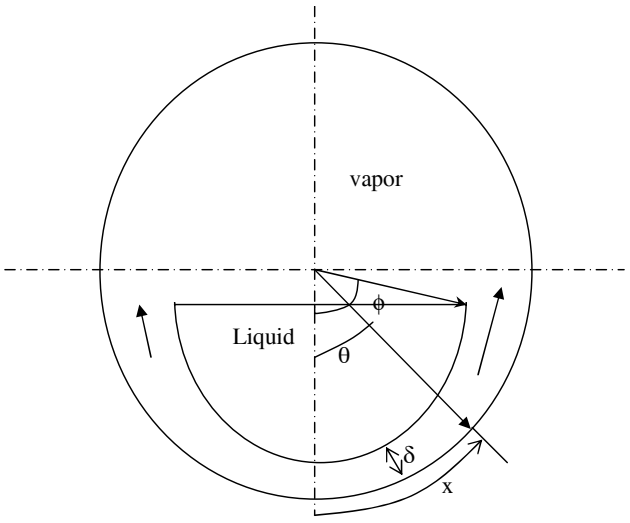

Figure 5.—Film boiling structure in stratified flow (Liao et al. (ref. 9)).

temperature at the bottom the pipe. This must be due to circumferential variations in the heat transfer coefficient. This problem is dealt with adequately by assuming that the heat transfer coefficient is constant in the region where only vapor is in contact with the pipe wall. In the region where the liquid film resides, a "geometry influencing factor" developed by Liao et al. (ref. 9) is used to circumferentially vary the heat transfer coefficient. The "geometry influencing factor" is function of the angle θ shown in figure 5 and is determined to be inversely proportional to the heat transfer coefficient.

The value of the geometry influencing factor, $F(\theta)$is given by,

$$F(\theta) = \left(\frac{\frac{4}{3}\int_0^{\theta} \sin^{\frac{1}{3}} \theta' d\theta'}{\sin^{\frac{4}{3}} \theta} \right)^{\frac{1}{4}}. \tag{5}$$

Thus the inner pipe boundary condition may be written as,

$$-k\frac{\partial T}{\partial r} = h_{in}\left(T_{in} - T_{fl}\right), \tag{6}$$

which is then non-dimensionalized to give,

$$-k'\frac{\partial \varphi}{\partial r'} = \frac{h_{in}d}{k_0}\varphi + \frac{d}{k_0}\left(\frac{h_{in}T_{sat} - h_{in}T_{fl}}{T_{wall} - T_{sat}}\right). \tag{7}$$

Here the subscript *in* and *fl* represent the inner surface of the pipe, and the fluid flowing through the pipe, respectively. The fluid temperature is determined using an internal thermocouple that measures the temperature at the inlet of the heat transfer section.

The heat transfer coefficient along the inside of the pipe varies with the thickness of the vapor film as shown in figure 6, and is also dependent on the height of the liquid film, which is determined using the images captured using the CCD camera.

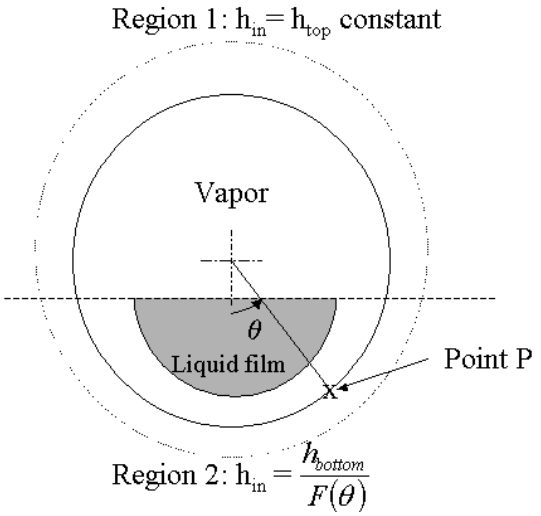

Figure 6.—Distribution of heat transfer coefficient on the inside surface of the pipe.

Iteration Process for Guessing the Inner Heat Transfer Coefficient

Any number of methods may be used to obtain a new guess for the inner heat transfer coefficient; a systematic method for iterating is recommended. In this work after the initial guess is made subsequent guesses are determined using linear interpolation or linear extrapolation. Hence the new guess for inner heat transfer coefficient is given by,

$$h_{new} = \varepsilon\left(\frac{h_{pres} - h_{prev}}{T_{pres} - T_{prev}}\right)\left(T_{known} - T_{prev}\right) + h_{prev}, \tag{8}$$

ε is scaling factor that reduce oscillations and takes the value 0.1 in this work., and the subscripts *pres*, *prev*, *new*, and *known* denote the present quantity, the previous quantity, the new quantity, and the known quantity respectively.

Test for Convergence

The final step in the process is checking the computed temperature against the measured temperature. This is done using the temperature at the top and bottom of the pipe. Once the computed temperature is within $\pm 1\times10^{-5}$ K, the temperatures are considered a match. Care must be taken when determining the limit within which to consider the temperatures to be matched; if the value selected is too small the computation time increases significantly and the marginal improvement in accuracy does not justify the increased computational cost.

Results and Discussion

In order to access the performance and validity of this inverse method, it was first used to calculate the heat transfer coefficients for a single-phase flow simulation in which the heat transfer coefficient is known and varies in time and secondly it was used to calculate the actual heat transfer coefficient for single-phase nitrogen flowing through the experimental facility, with the results being compared with the predictions of the Dittus-Boelter correlation for cooling. In the first test case, the heat transfer coefficient followsw a parabolic path with time. The results of these numerical tests are shown in figures 7 and 8. The second case compares with actual experimental data.

By examining figure 7 it is seen that a parabolic varying heat transfer coefficient is be captured quite accurately with this approach, and from figure 8 it is observed that the technique agrees very well with the predictions of the Dittus-Boelter correlation.

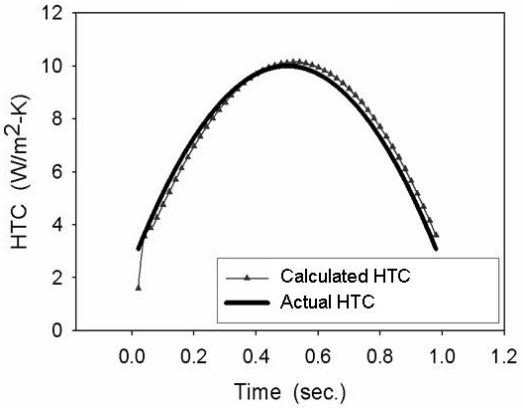

Figure 7.—Computation of a parabolic varying heat transfer coefficient using the inverse method.

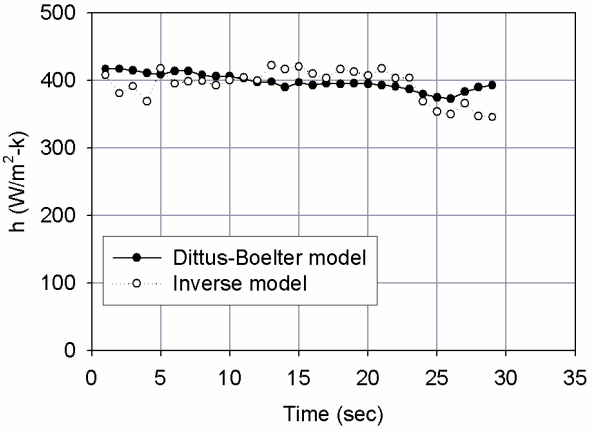

Figure 8.—Comparison of heat transfer coefficient computed using inverse procedure and the Dittus-Boelter model for single-phase nitrogen flow.

Since the technique performed satisfactorily for the single-phase case it was then applied to the chilldown experimental data. The results shown here are for two experimental cases, with different average mass fluxes; one at 229 kg/m^2-s and the other at 77 kg/m^2-s (the actual mass flux values are given in figures 11 and 12 respectively). The results are shown in figures 9 and 10. A comparison of figures 9 and 10 leads to the following observations:

- The chilldown time is much shorter for the higher mass flux case as seen by comparing figures 9(a) and 10(a). This is to be expected since the higher mass flux case yields higher heat transfer coefficients.
- The heat transfer coefficient at the bottom of the pipe is at least one order of magnitude greater than the heat transfer coefficient at the top, which is seen by comparing figure 9(b) and (d) and figure 10(b) and (d). This is expected, as the lower region of the pipe is where the liquid phase resides.
- The transition between film boiling and nucleate boiling (Leidenfrost point) is clearly seen as reflected in the dramatic increase in heat transfer coefficient at the bottom of the pipe, as seen in figures 9(c) and 10(c).

An interesting point to note is that the maximum heat transfer coefficient reached in the lower mass flux case is actually greater than that reached in the higher mass flux case, see figures 9(c) and 10(c). One possible reason for this is that in the lower mass flux case there may be a greater amount of thermal energy remaining in the pipe wall, which drives ebullition from the surface. In the higher mass flux regime, ebullition may be suppressed.

It is also observed that the unsteady nature of the flow is reflected in the heat transfer coefficients, which is best seen by comparing the heat transfer (fig. 9(b) and (c)) to the instantaneous mass flux values (fig. 11) for the experiment with average mass flux of 229 kg/m^2-s.

The initial phases of the two experiments exhibit different behavior, which is seen in figures 11 and 12. In the lower mass flux case, a surge of vapor was observed when the nitrogen was introduced into the system, which was not observed in the higher mass flux case. These behaviors were captured in the heat transfer computations.

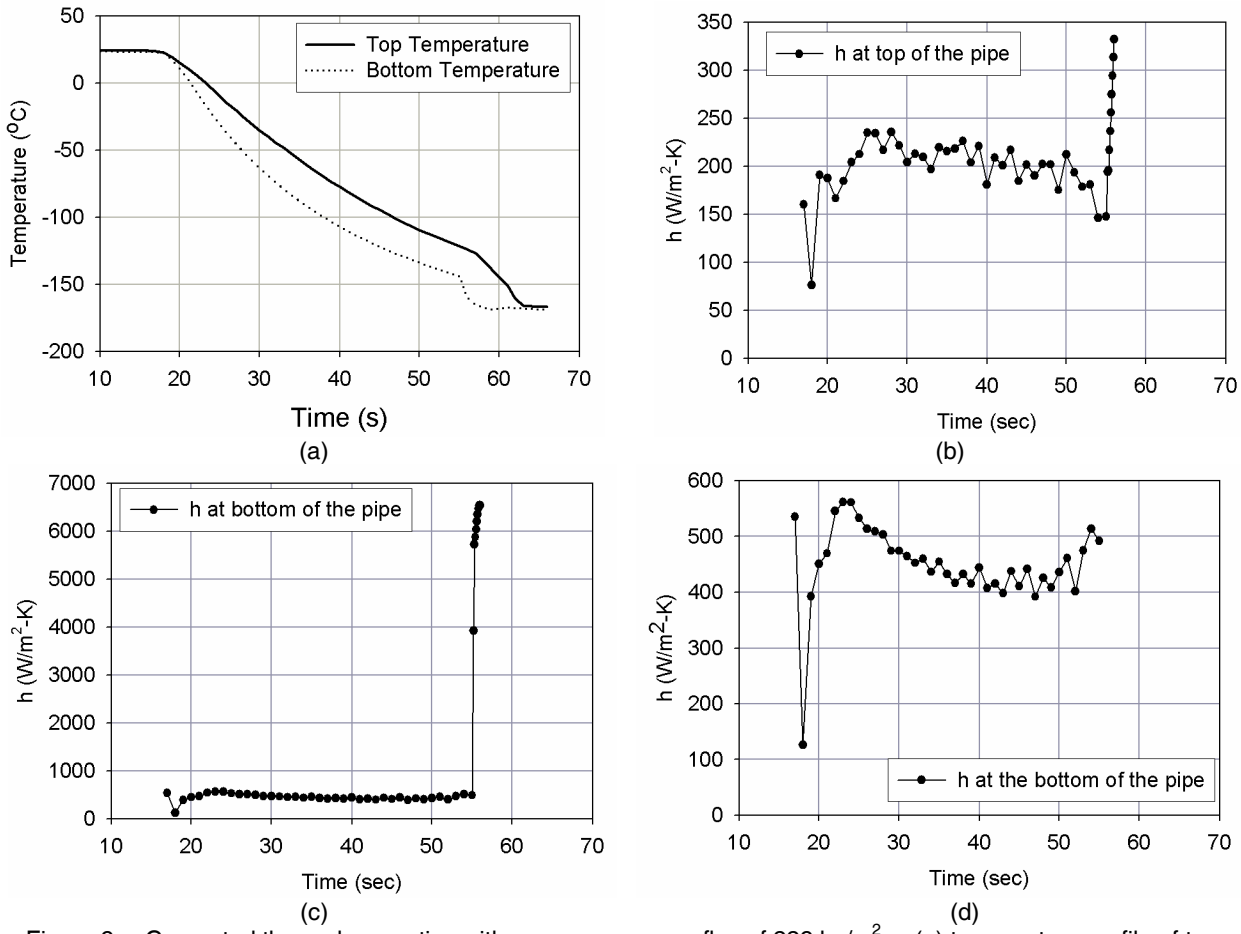

Figure 9.—Computed thermal properties with an average mass flux of 229 kg/m^2-s; (a) temperature profile of top and bottom pipe wall temperature, (b) heat transfer coefficient at the top, (c) heat transfer coefficient at the bottom and (d) heat transfer coefficient at the bottom with the vertical axis rescaled.

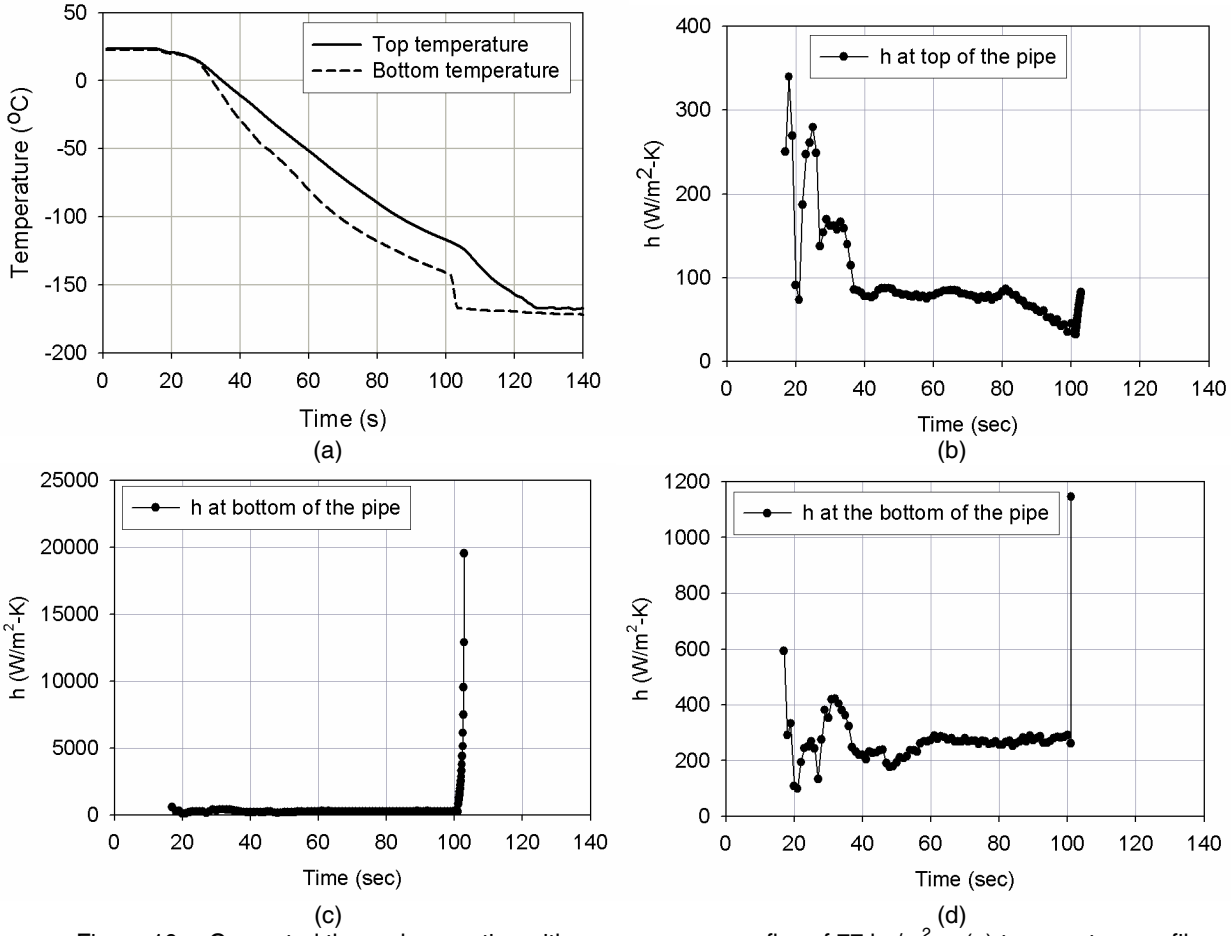

Figure 10.—Computed thermal properties with an average mass flux of 77 kg/m^2-s; (a) temperature profile of top and bottom pipe wall temperature, (b) heat transfer coefficient at the top, (c) heat transfer coefficient at the bottom and (d) heat transfer coefficient at the bottom with the vertical axis rescaled.

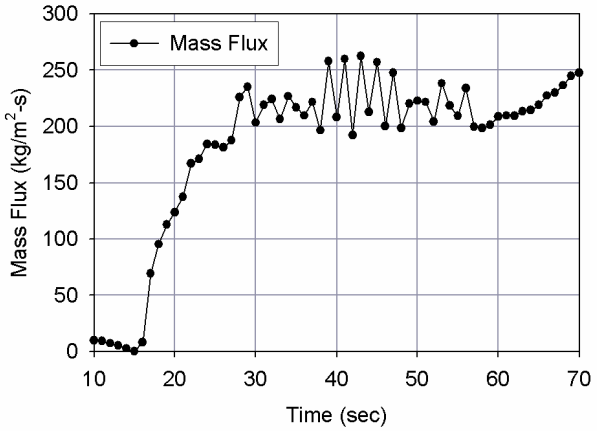

Figure 11.—Mass flux variation for experiment with average mass flux of 229 kg/m^2-s.

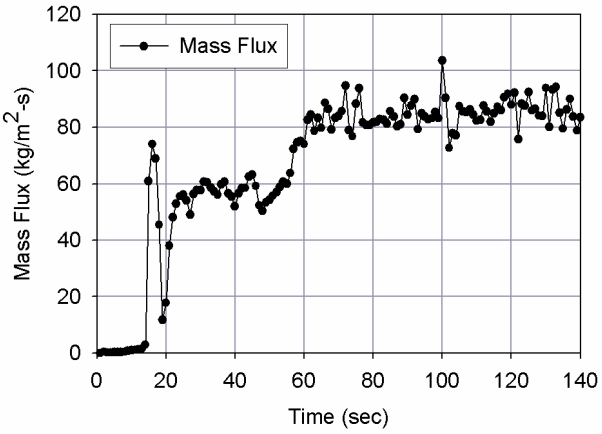

Figure 12.—Mass flux variation for experiment with average mass flux of 77 kg/m^2-s.

Conclusion

In this study an inverse numerical procedure for predicting the transient heat transfer coefficient for two-phase flows has been developed. It is seen to perform well for the single-phase test cases. The large circumferential variation of the heat transfer coefficient that occurs during the cryogenic chilldown process is clearly highlighted and the Leidenfrost point is clearly identified. This technique will facilitate the development of heat transfer coefficient correlations for cryogenic chilldown.

Nomenclature

c	heat capacity $\left[J/kgK \right]$
d	internal diameter of pipe [m]
$F(\theta)$	geometry influencing factor
h	heat transfer coefficient $\left[W/m^2 K \right]$
k	thermal conductivity $\left[W/mK \right]$
q''	heat flux $\left[W/m^2 \right]$
T	temperature [K]
t	time [s]
ΔT	temperature difference [K]
z, r, and ϕ	cylindrical coordinates
φ	non-dimensional temperature
ε	scaling factor
ρ	density $\left[kg/m^3 \right]$

Subscripts

0	reference value
bottom	bottom of the pipe
fl	fluid flowing inside pipe

in	inner surface of the pipe
known	measured quantity
new	next computational step
out	outer surface of pipe
pres	current computational step
prev	previous computational step
sat	saturated condition
top	top of the pipe
w	pipe wall
∞	outer insulation surface

Superscript

‘	dimensionless variable

References

1. VanOverbeke, J.T., 2004, “Thermodynamic Vent System Test in a Low Earth Orbit Simulation,” 40th Joint Propulsion Conference and Exhibit, Fort Lauderdale, Florida, U.S.A., July 11–14.
2. Burke, J.C., Byrnes, R.W., Post, A.H., and Ruccia, F.E., 1960, “Pressurized Cooldown of Cryogenic Transfer Lines,” Advances in Cryogenic Engineering, **4**, pp. 378–394.
3. Bronson, J.C., Edeskuty, J.F., Fretwell, J.H., Hammel, E.F., Keller, W.E., Meier, K.L., Schuch, A.F., and Willis, W.L., 1962, “Problems in Cool-down of Cryogenic Systems,” Advances in Cryogenic Engineering, **7**, pp. 198–205.
4. Steward, W.G., Smith, R.V., and Brennan J.A., 1970, “Cooldown Transients in Cryogenic Transfer Lines,” Advances in Cryogenic Engineering, **15**, pp. 354–363.
5. Papadimitriou, P., and Skorek, T., 1992, “One-dimensional Thermohydraulic Code THESEUS and its Application to Chilldown Process Simulation in Two-phase Hydrogen Flows,” Cryogenics, **32**, pp. 362–370.
6. Cross, M.F., Majumdar, A.K., Bennett, J.C., and Malla, R.B., 2002, “Modeling of Chill Down in Cryogenic Transfer Lines,” Journal of Spacecraft and Rockets, **39**, pp. 284–289.
7. Özi□ik, M.N., 1993, Heat Conduction (2nd ed.), Wiley-Interscience, New York.
8. Hirsch, C., 1990, Numerical Computation of Internal and External Flow, Volume 1, Fundamental of Numerical Discretization, Wiley, Indianapolis, Indiana.
9. Liao, J., Yuan, K., Mei, R., Klausner, J.F., Chung, J., 2005, “Cryogenic Chill-Down Model Inside Transportation Pipelines,” Proceedings of the ASME Summer Heat Transfer Conference, San Francisco, CA.

Project Title: Cryogenic Two-Phase Flow and Heat Transfer in Reduced Gravity

Task PI: Wei Shyy, Department of Mechanical and Aerospace Engineering
Co-I: Jacob N. Chung, Department of Mechanical and Aerospace Engineering

Project Goals

The efficient and safe utilization of cryogenic fluids in thermal management, power and propulsion, and life support systems during space missions involves the transport, handling, and storage of these fluids in reduced gravity. Due to their low boiling points, two-phase flows are encountered in most of the cryogenic operations. The complexity of the problem results from the intricate interaction of the fluid dynamics and heat transfer, especially when phase-change (boiling and condensation) is involved. Because of the large stratification in densities between the liquid and vapor phases, the reduced gravity condition in space would strongly change the terrestrial flow patterns and accordingly affect the momentum and energy transport characteristics. This research focuses on addressing specific fundamental and engineering issues related to the microgravity two-phase flow and heat transfer of cryogenic fluids that require advanced numerical simulations in concert with validating experimentation. The outcome of the research will provide cryogenic practitioners the practical analysis tools required to address specific issues impacting the safe and efficient operation of liquid hydrogen cryogenic transport systems in reduced gravity.

Accomplishments

Abstract

For the cryogenic two-phase flow and heat transfer study, we have focused on the liquid nitrogen convective film boiling process in both terrestrial gravity and microgravity. Two types of experiment were performed. One is aimed at the chilldown phenomena of an unheated tube. The other investigates the constant wall heat flux heating condition. An experimental apparatus was designed and built. Flow pattern and wall temperature history during the chilldown and constant heating condition were obtained. We have measured the wall temperature history at three downstream locations. The terrestrial chilldown process is divided into three stages based on the temperature of the tube wall. At the beginning of the chilldown process, the wall temperature of the test section is near the room temperature, which is much high than that of the liquid nitrogen. The initial stage is therefore associated with the film boiling that causes the two-phase flow to take the form of a vapor core with scattered small liquid fragments. When the wall temperature decreases further, the two-phase flow is experiencing a transition from the film boiling to the stratified flow. Finally when the wall is chilled down enough, a stable stratified two phase flow was observed. Flow visualization under the microgravity condition was performed and it was found that suspended liquid chunks were floating in a vapor stream.

For the constant heating case, two different flow rates were investigated. Both wall temperatures and flow visualizations were attempted. The wall temperature and flow pattern would achieve relatively steady state condition under a constant heating condition. For the lower flow rate case, the two-phase flow pattern for the terrestrial case is influenced by the wall temperature level and the gravity in very similar ways as the chilldown case. For the higher flow rate case, the gravity effect is negligible. Therefore, the results are similar between the terrestrial and the microgravity cases.

As a first step towards the film boiling numerical study, a direct numerical simulation of bubble dynamics with large liquid-to-vapor density ratio and phase change has been developed using a sharp-interface moving boundary numerical method. The numerical techniques are based on a fixed-grid, finite volume method capable of treating the interface as a sharp discontinuity. The unsteady, axisymmetric

Navier-Stokes equations and energy equation in both liquid and vapor phases were computed. The mass, momentum and energy conditions are explicitly matched at the phase boundary to determine the interface shape and movement. The cubic B-spline is used in conjunction with a fairing algorithm to yield smooth and accurate information of curvatures. For a stationary and growing bubble, the predicted growth rate was found to agree with the theoretical limit of $t^{1/2}$. However, for a rising and growing bubble, the predicted growth rate was approaching the theoretical limit of $t^{2/3}$ for a spherical bubble but did not reach it exactly owing to bubble deformation. For a rising and growing bubble, the location of the highest heat flux was found and the deviation largely depends on the Reynolds number.

Introduction

Role of Cryogenics in Space Exploration

The extension of human space exploration from a low earth orbit to a high earth orbit, then to Moon, Mars, and possibly asteroids and moons of other planets is one of NASA's biggest challenges for this new millennium. Integral to this is the effective, affordable, and reliable supply of cryogenic fluids. The efficient and safe utilization of cryogenic fluids in thermal management, power and propulsion, and life support systems of a spacecraft during space missions involves the transport, handling, and storage of these fluids in reduced gravity. The uncertainties about the flow pattern and heat transfer characteristics pose a severe design concern. Moreover, the thermo-fluid dynamics of two-phase systems in reduced gravity encompasses a wide range of complex phenomena that are not understood sufficiently for engineering design to proceed. For the two-phase flow and heat transfer study, we have focused on the forced-convection film boiling process owning to the low boiling points for the cryogenic fluids. The objective is therefore to provide heat transfer coefficients and two-phase flow patterns that are useful for the initial phase (film boiling) of the chilldown process of cryogenic fluid flow and transport.

Chilldown process, which is important during initial cryogenic fluid transport, is however not fully understood. In this paper, liquid nitrogen chilldown process was investigated and divided into three stages based on the flow image and temperature data.

Due to their low boiling points, boiling and two-phase flows are encountered in most of the cryogenic operations. The complexity of the problem results from the intricate interaction of the fluid dynamics and heat transfer, especially when phase-change (boiling and condensation) is involved. Because of the large stratification in densities between the liquid and vapor phases, the reduced gravity condition in space would strongly change the terrestrial flow patterns and accordingly affect the momentum and energy transport characteristics. Boiling and two-phase flow behave quite differently when the gravity levels are varied. The proposed research will focus on addressing specific fundamental and engineering issues related to the microgravity two-phase flow and boiling heat transfer of cryogenic fluids that require well-designed and meaningful experimentation. The outcome of the research will provide fundamental understanding on the transport physics of cryogenic boiling and two-phase flows in reduced gravity.

Boiling Curve

A boiling curve shows the relationship between the heat flux that the heater supplies to the boiling fluid and the heater surface temperature. According to the typical boiling curve as shown in figure 1, a chilldown (quenching) process usually starts from point E and then goes towards point D in the film boiling regime as the wall temperature decreases. Point D is called the Leidenfrost point which signifies the minimum heater temperature required for the film boiling. For the film boiling process, the wall is so hot that liquid will vaporize before reaching the heater surface which causes the heater to be always in contact with vapor. When cooling beyond the Leidenfrost point, if a constant heat flux heater were used, then the boiling would shift from film to nucleate boiling (some where between points A and B) directly with a substantial decrease in the wall temperature because the transition boiling is an unstable process.

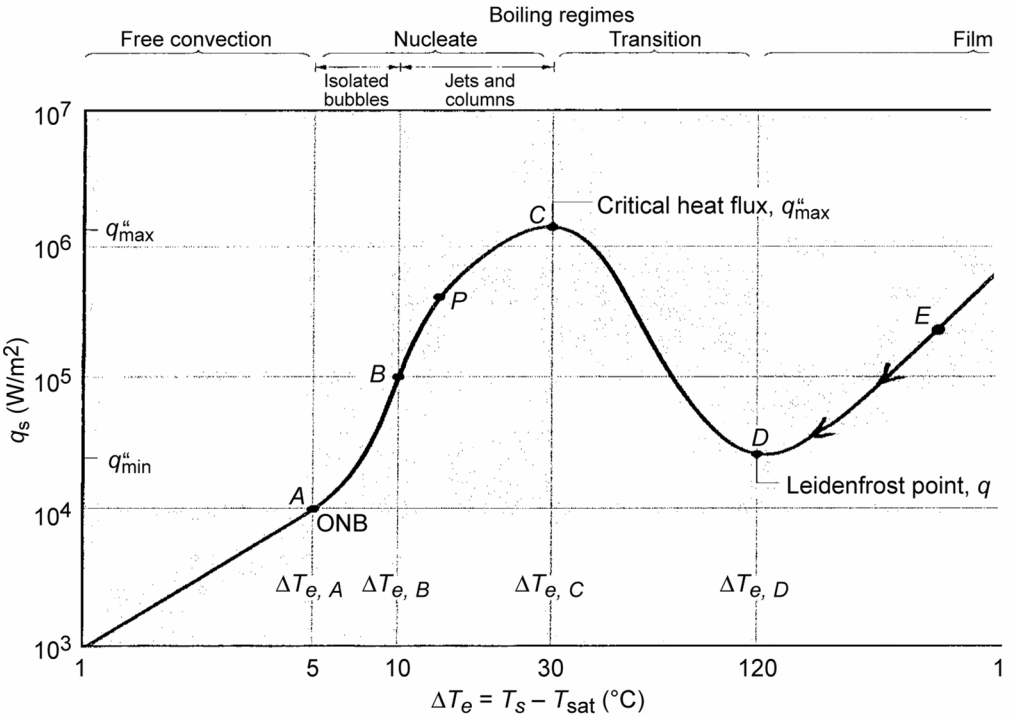

Figure 1.—Typical boiling curve.

The Effects of Gravity

Because of many difficulties and limitations involved in the drop tower microgravity experiments, meaingful terrestrial experiments would therefore serve as a valuable tool to provide quidance and check for microgravity experimentation. The following is a scaling analysis that examines the gravity effects. For annular-flow film boiling, the effect of gravity is assessed based on the ratio of Gr/Re^3, where Gr is the Grashof number and Re is the Reynolds number. The gravity effect is measured by the natural convection contribution which is characterized by the Gr while the forced convective film boiling is scaled by the Reynolds number. According to Gebhart et al. (Buoyancy-Induced Flow and Heat Transport, Hemisphere Publishing Company, 1988), Re^3 is used in the denominator when the flow is perpendicular to gravity for a horizontal tube. Re^2 is used when the flow is in the same direction of gravity. All the thermal properties are those of vapor because of film boiling. Figure 9 shows a plot for this ratio with the flow velocity range of 0 to 1 m/s.

Based on figure 2, we would also perform terrestrial gravity experiment with the vapor velocity greater than 10 cm/s which corresponding to Gr/Re^3 less than 0.2. The natural convection is negligible for Gr/Re^3 less than 0.225 according to Gebhart et al. (1988). For a vapor velocity of 10 cm/s, the corresponding liquid velocity is approximately 0.02 cm/s which is the velocity of liquid when it first exits the tank.

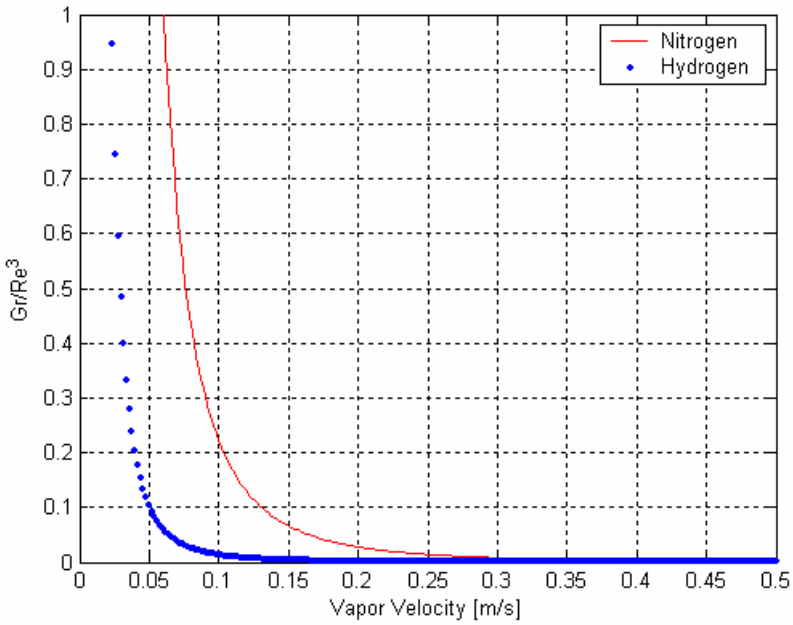

Figure 2.—Gr/Re^3 vs. vapor velocity.

Literature Review

Momentum and energy transport in two-phase flow and boiling under microgravity is a relatively new field. This is a complex problem for the scientific community to solve. The rewards are rich, however, as new ways to propel future space missions and more intensive space activities have been planned. Currently, there exists a limited quantity of literature, data, and test facilities to even begin to answer these questions. Microgravity cryogenic boiling research was initiated more than fifty years ago, but the progress has been limited. The following summarizes the accomplishments.

Terrestrial Cryogenic Boiling and Two-Phase Flow

Numerous studies of cryogenic boiling in the one-g environment were conducted in the 1950's and 60's. Reference 1 is a comprehensive review of the experimental studies and heat transfer correlations. For the fluids oxygen, nitrogen, hydrogen and helium, it was found that for pool boiling, the Kutateladze (ref. 3) correlation had the greatest reliability for nucleate boiling while the Breen and Westwater (ref. 4) correlation was best for film boiling. Maximum nucleate flux data were reasonably well predicted by the Kutateladze correlation. Although these correlations were selected as the best available, neither has particularly good agreement with experimental data. For the case of forced convection boiling, Reference 1 reported that no correlation was found to be distinctly better. Some simple predictive methods were found to work as well as more complex schemes. In all boiling cases, it was questioned as to whether or not the predictive correlations include all of the significant variables that influence the boiling process. In particular, it was suggested that more detailed and better controlled experiments are needed and that more attention to surface and geometry effects is required.

Reference 2 is another comprehensive review of cryogenic boiling heat transfer addressing hydrogen, nitrogen and oxygen. It was reported that nucleate pool boiling results cannot be correlated by a single line but cover a range of temperature difference for a given heat flux. The spread is attributed to surface condition and geometry, and orientation. Maximum heat flux can be reduced by about 50 percent when going from normal-g to near zero-g. Reference 2 reported a fair amount of data for film pool boiling. Film boiling heat flux is reduced considerably at near zero-g conditions. Only a very limited amount of data is available for subcooled or saturated forced convection boiling and few conclusions were drawn. The lack of data for cryogenic forced convection boiling is also reported by Brentari and Smith (ref. 5).

Relatively recent correlations have been published for normal-g saturated flow boiling of cryogens (ref. 6 to 9) using the Convection, Boiling and Froude numbers as correlating parameters.

Reduced Gravity Cryogenic Boiling and Two-Phase Flow

In general, there is little heat transfer data for cryogenic flow boiling in reduced gravity. We were able to find just two reports. Adham-Khodaparast et al. (ref. 10) have investigated the flow film boiling during quenching of R-113 on a hot flat surface. They used microsensors to record instantaneous heat flux and heater surface temperature during the film boiling on board a KC-135 aircraft. They reported lower heat transfer rates during microgravity as compared to normal gravity and contributed that to thickening of the vapor layer. The wall superheat and the surface heat flux at the onset of rewetting and maximum heat flux were found to increasde with the inlet liquid subcooling, mass flux and gravity level. The effect of gravity was determined to be more important for low flow rates and less relevant for high flow rates. Antar and Collins (ref. 11) reported flow visualization and measurements for flow film boiling of liquid nitrogen in tubes on board KC-135 aircraft. They were particularly interested in the vapor/liquid flow pattern and the thermal charateristics. They identified a new vapor/liquid flow pattern that is unique in low gravity. Antar and Collins (ref. 11) observed that a sputtering leading core followed by a liquid filament annular flow pattern. This new flow pattern is composed of a long and connected liquid column that is flowing in the centerof the tube and is surround by a thick vapor layer. The vapor annulus that separates the liquid filament from the wall is much thicker than that observed in the terrestrial experiment. They attributed the filamentary flow to the lack of difference in the speed of vapor and liquid phases. On the heat transfer side, they reported that the quench process is delayed in low gravity and the tube wall cooling rate was diminished under microgravoty conditions.

Experimental System

Flow loop.—Figure 3 shows the schematic of the boiling and two-phase flow apparatus and figure 4 is a photographic view of the this apparatus located in two side-by-side cubicles for drop tower microgravity experiment. The experimental loop mainly consists of a bellows-controlled reservoir, a cryogenic valve, test section inlet portion, test section, test section outlet portion, liquid separator, lighting and video system. A vacuum jacket is provided to insulate the glass tube test section.

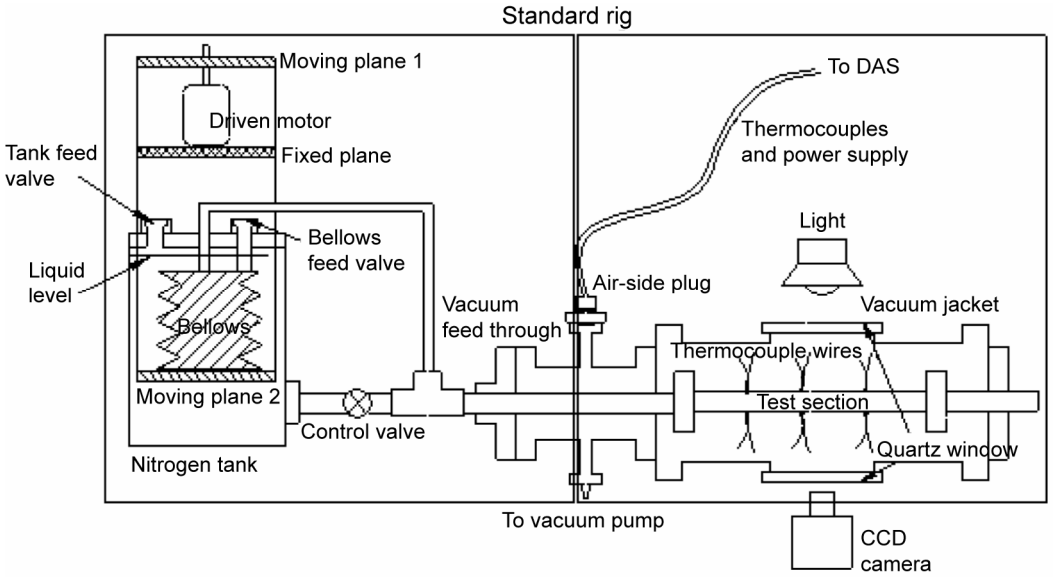

Figure 3.—Schematic of cryogenic boiling and two-phase flow test apparatus.

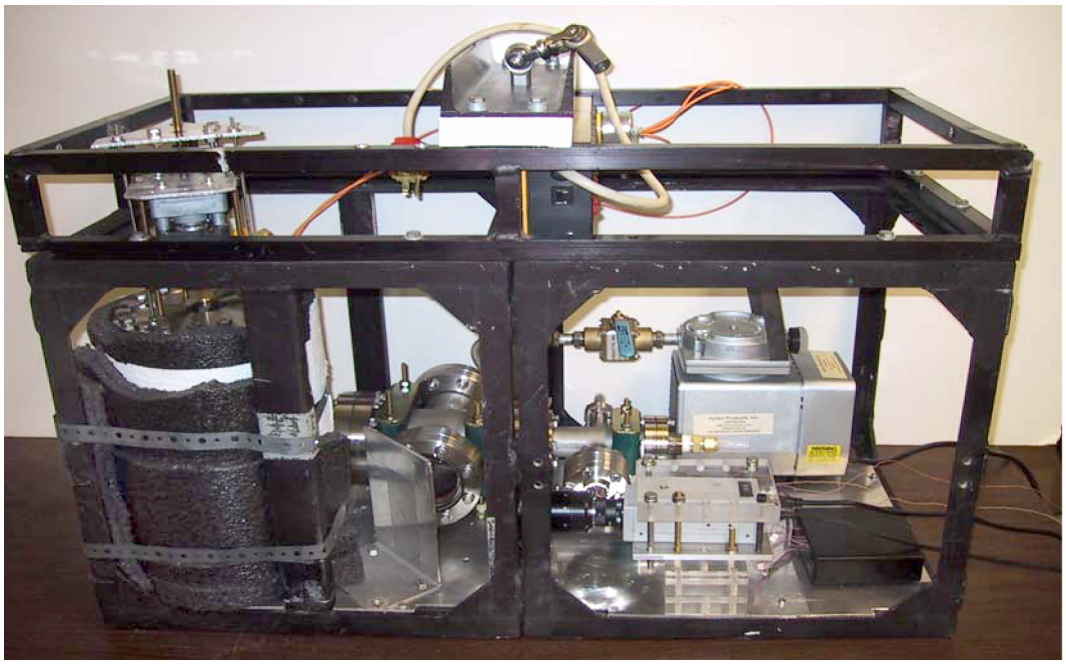

Figure 4.—Experimental apparatus located in cubicles

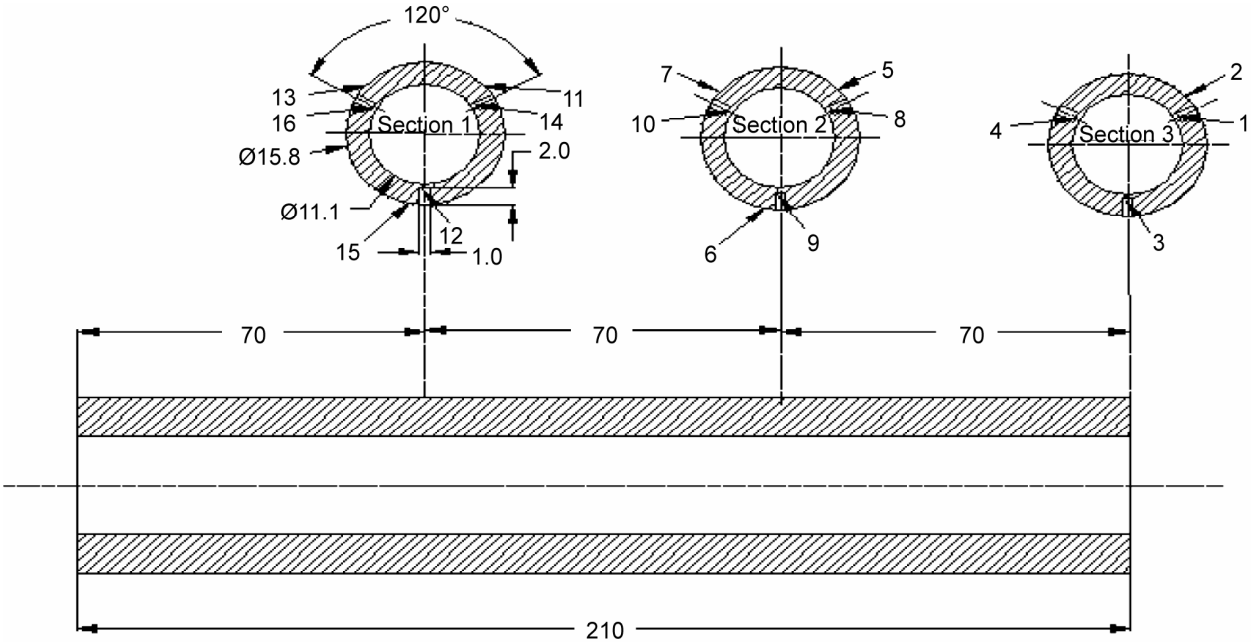

Figure 5.—Locations of the 16 thermocouples on test section.

Reservoir.—Liquid nitrogen is supplied by a cylindrical stainless steel reservoir that is fitted with a bellows driven by a constant speed motor to provide a constant flow rate. Form insulation is applied to the reservoir and the whole loop besides the test section.

Test section.—Two different test sections were used in the experiments. The first is an unheated Pyrex (Corning, Inc.) glass tube which was used for the chilldown study while the second test section is a heated quartz tube coated with a thin film of Tin Oxide to provide a constant heat flux. The non-heated test section is a Pyrex glass tube of 25-cm long. The inner and outer diameters of the test section are 11.1 and 15.8 mm, respectively. At both ends of the test section, stainless steel flanges and adaptors are used to connect the test section to the test section inlet and outlet portions. Also some traditional methods were

adopted to seal the glass to the steel. A total of 16 type-T thermocouples are placed on the glass tube, 9 are embedded very close to the inner surface of the tube wall through drilled holes. These 9 thermocouples are placed at three downstream locations. At each downstream location, there are three thermocouples located circumferentially at equal separation distance. The other 7 thermocouples are used to measure the outside wall temperatures of the glass tube. Figure 5 illustrates the locations of the thermocouples. Figure 6 is a photograph of the test tube with attached thermocouples.

The heated quartz tube has an o.d. of 9.5 mm (3/8 in.) and i.d. of 7.0 mm. The length of the quartz tube is 16.3 cm (6.4 in.. A transparent thin film of Tin Oxide covers 8. 6cm of the tube. The thin film provides a constant heat flux when heated by a dc power supply. At each ends of the thin film an electrode with a length of 1.3 cm (0.5 in.) connects the quartz tube to the power supply.

Because its wall is so thin as compared to the previous Pyrex tube, drilling holes on the quartz tube for inserting thermocouples is not feasible. To obtain the circumferential temperature measurements in this situation, we put three teflon ferrules on three locations of the quartz tube. On each of the ferrules, tiny holes are drilled to let the thermocouples go through such that they can be fastened. Figure 7 shows the schematic of the heated quartz tube and provides the locations of the thermocouples.

Flow section.—Standard 3/8 in. stainless steel tubes are used for the flow loop besides the test section. Swagelok fittings with teflon ferrules were used at the glass to metal connections.

Cryogenic valve.—A cryogenic valve with ½ in. NPT threads on both sides is used to connect the reservoir to the test section inlet. The cryogenic valve is electronically controlled. During the experiment, after the reservoir is cooled the valve is opened and liquid nitrogen is released to chill down the test section.

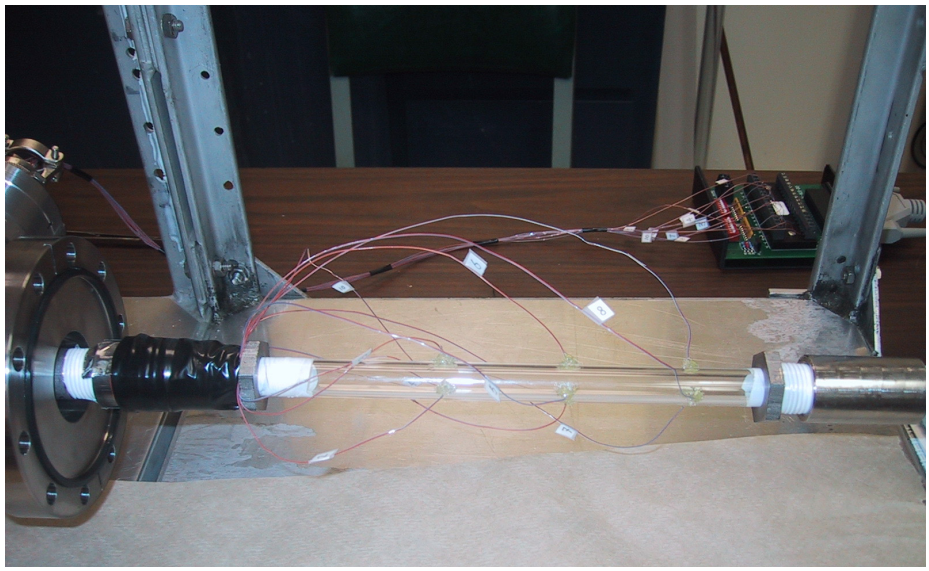

Figure 6.—Photograph of cryogenic two-phase flow test apparatus.

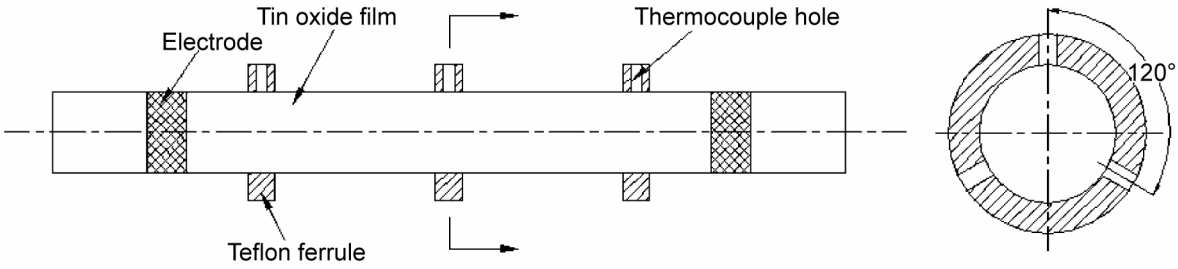

Figure 7.—Sketch of the heated quartz tube.

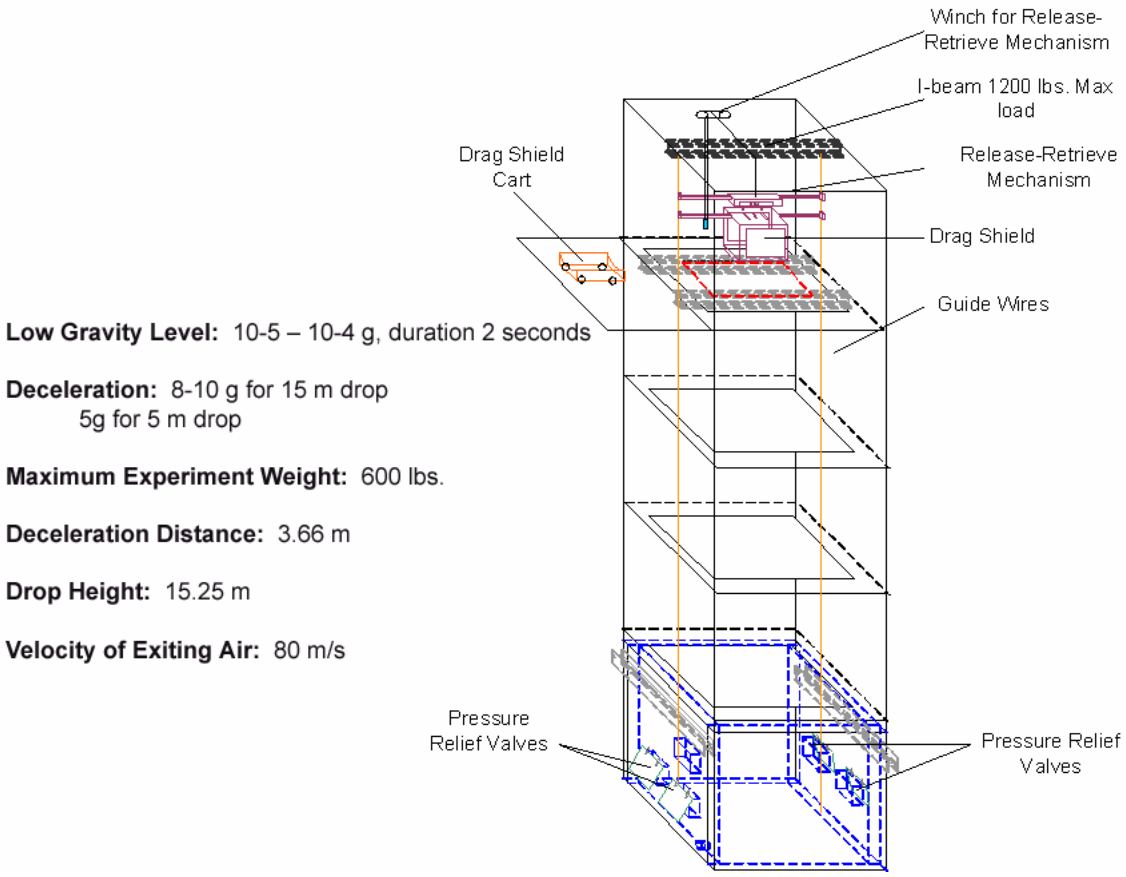

Figure 8.—A schematic of the drop tower system.

Video system.—The video system consists of a high speed CCD camera (CV-730) with a ½ in. HAD Interline Transfer CCD sensor and fluorescent light. The camera's electronic shutter speed was from 1/1,000 to 1/10,000 sec. A Ceptre PD-1212ARD5 (12 VDC 1.2 A) power supply was used to provide power to the camera. Fluorescent light can provide comparably enough light and generate less heat.

Data acquisition component.—Signals from the thermocouples are sent to the computer through a temperature acquisition board plugged into the PCI slot. Video images are also monitored and recorded by connected the CCD camera to the computer with a frame grabber board. During microgravity tests, long thermocouple extension wires are used to connect the thermocouple to the temperature acquisition board, so that temperature data can be collected during the drop with comparable accuracy. When the heated quartz tube is used, the constant heat flux was maintained by a HP E3631A DC power supply.

For the microgravity test, all the experimental components are put into and fastened to two standard rigs. A portable vacuum pump is also attached onboard to maintain the vacuum condition for the test section during the microgravity test. Figure 5 shows the whole system inside the standard rigs.

Drop tower apparatus.—The microgravity environment was provided by the University of Florida drop tower. The drop tower is 5-story high and is equipped with an airbag for deceleration. Figure 8 shows the overall drop tower schematic. At the current drop height of 15.25 m, UF's drop tower produces 1.7 sec of free fall. The experiment is actually located in a drag shield which prevents the experiment from the aerodynamic drag. As a result, the microgravity level is measured between 10^{-5} to 10^{-4} g.

Experimental Results

Two types of experiments were conducted, the first type is the so called “pipe chilldown” experiment, where there is no heater associated with the test tube. During the chilldown, pipes experience a fast cooling on the walls. The purpose of the chilldown experiment is to provide an overall calibration of the system that includes both flow visualization and heat transfer measurements, and also to offer flow patters and heat transfer characteristics during pipe chilldown process that takes place in many cryogenic applications. The second type experiment is aimed at a fundamental understanding for a steady state condition, where the tube wall outer surface is coated with a thin Tin oxide-film to maintain the wall at a constant heat flux. This type of experiment is intended for the understanding of the two-phase flow and heat transfer under a steady heating boundary condition.

Chilldown Experiment

During the chilldown experiment, liquid nitrogen enters the Pyrex glass tube that is at the room temperature (25 °C). The bulk velocity of the two-phase flow is estimated at 5 cm/s. From figure 2, it is clear that the two-phase flow investigated here is totally dominated by gravity. Because the glass tube is unheated, the tube wall is going through a transient cooling process. In the following, the measured wall temperature history is presented first and then flow visualization pictures are given to provide the correlations between the wall temperature and flow pattern.

Tube Wall Temperature History

Terrestrial gravity case.—For the chilldown process, the temperature histories of the tube walls were measured by the thermocouples at three downstream locations as shown in figure 4. The results are given in figure 9. Based on the characteristics of the temperature curves, the chilldown process is generally divided into three stages. At the beginning of the process, the wall temperature of the test section is near room temperature, which is much higher than the temperature of the liquid nitrogen.

Based on the flow visualization presented later, the initial stage is associated with a hot wall which causes the two-phase flow to take the form of a vapor core with scattered small liquid chunks. In general, the temperatures measured by thermocouples that are located in the bottom of the tube (Ch 12, 15, 9, 6 and 3) are lower than those from thermocouples embedded in the upper portion. This is mainly due to the gravity effects that bring direct liquid impingement cooling to the bottom walls.

A distinctive character of the bottom wall temperature history is the sharp increase in the slope at the wall temperature of about 190 K. This phenomenon is seen at all three downstream locations. The physical explanation is based on the transition of boiling regimes from film boiling to nucleate boiling as mentioned earlier and shown in figure 1.

Finally when the wall is chilled down enough such that the wall temperature (<140 K, point A in fig. 1) is too low to support nucleate boiling, the heat transfer switches to single-phase forced convective boiling.

Based on the temperature data, the heat transfer coefficient history for the bottom wall at Section 1 is estimated and plotted in figure 10. The magnitudes of the heat transfer coefficient really reflect the boiling regimes, which conforms with the fact that nucleate boiling is the most efficient and the film boiling is much less effective. The horizontal line indicates the heat transfer coefficient value calculated using the steady state nucleate boiling correlation developed by Van Dresar et al. (ref. 9). The correlation value sits in the middle of our experimental data points which confirms that nucleate boiling is indeed responsible for the highest sloped portion of the temperature curve.

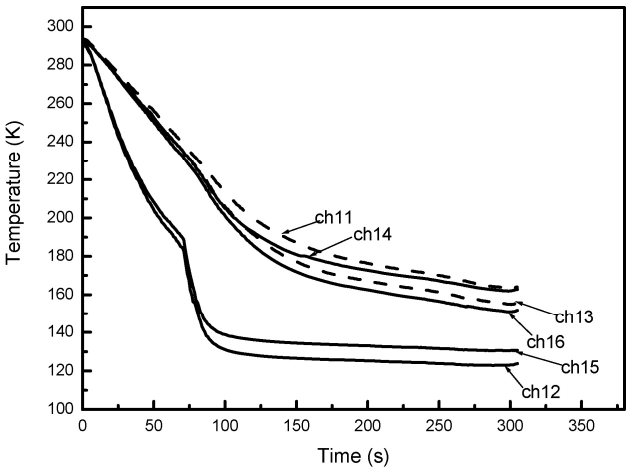

(a) Temperature profile of section 1.

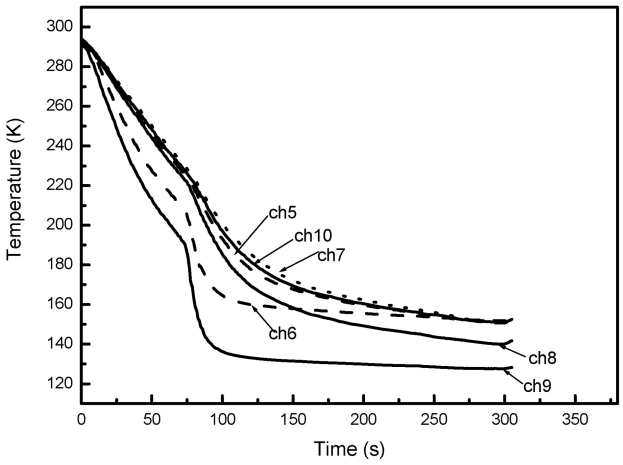

(b) Temperature profile of section 2.

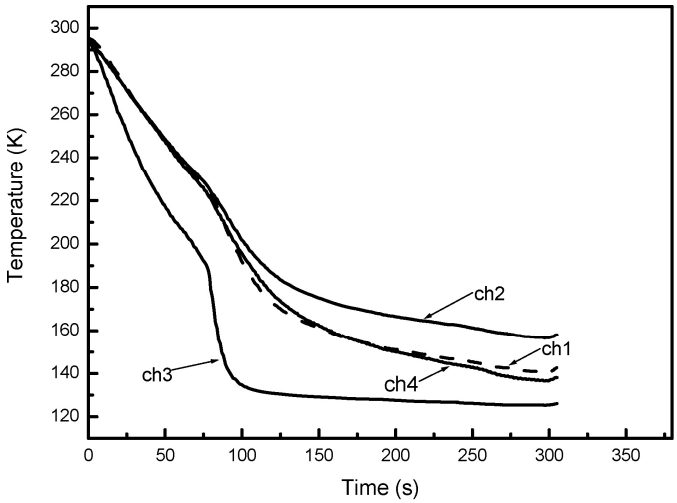

(c) Temperature profile of section

Figure 9.—Temperature profiles at three downstream locations during the chilldown process.

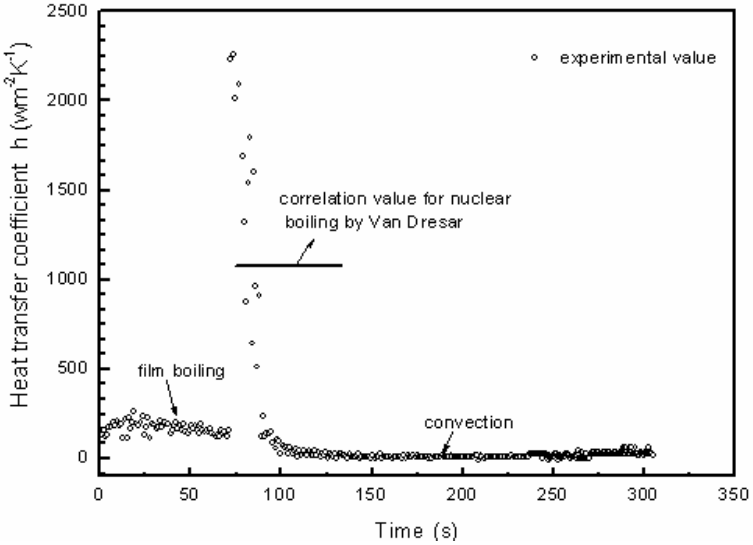

Figure 10.—Estimated heat transfer coefficients.

Microgravity case.—Because that our drop tower can only provide 1.7 sec of microgravity period, it is not feasible for the chilldown experiment. However, we can speculate that the wall temperature history curve in microgravity would be very similar to those of the two upper portion locations (Ch. 11 and 14 or 13 and 16). In microgravity, there would be no stratification and perfect inverted annular flow would prevail, which causes the vapor to cover all the tube wall and leave liquid in the central core area.

Flow Visualization

Terrestrial condition.—The experimental apparatus was first used to provide flow visualization results for the chilldown process of a Pyrex glass tube. This initial phase of experimentation would provide not only some physical understanding of the two-phase flow characteristics during the chilldown process, but also the performance evaluation for the apparatus which includes both image and data acquisition. The chilldown process is divided into three stages based on the temperature of the tube wall as discussed above. At the beginning of the chill down procession, the wall temperature of the test section is near the room temperature, which is much higher than the temperature of the liquid nitrogen.

The initial stage as shown in figure 11 is therefore associated with a hot wall which causes the two-phase flow to take the form of a vapor core with scattered small liquid chunks.

When the wall becomes slightly cooler, the inverted annular flow is seen as given in figure 12 where the liquid is occupying most of the tube with a vapor layer adjacent to the tube wall. For both cases as shown in figures 11 and 12, it is believed that film boiling is the main mechanism

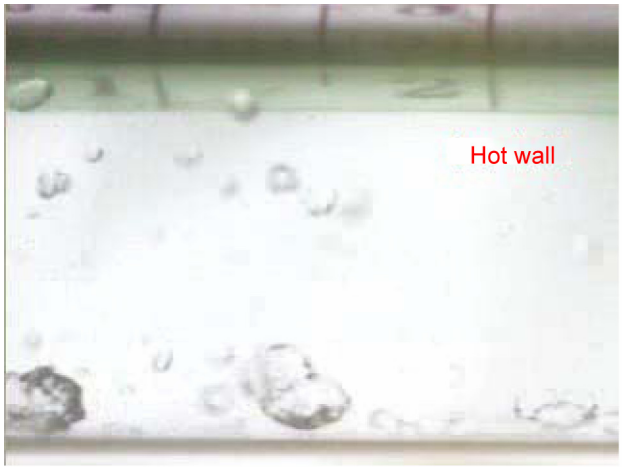

Figure 11.—Initial stage of chilldown—vapor core liquid chunks.

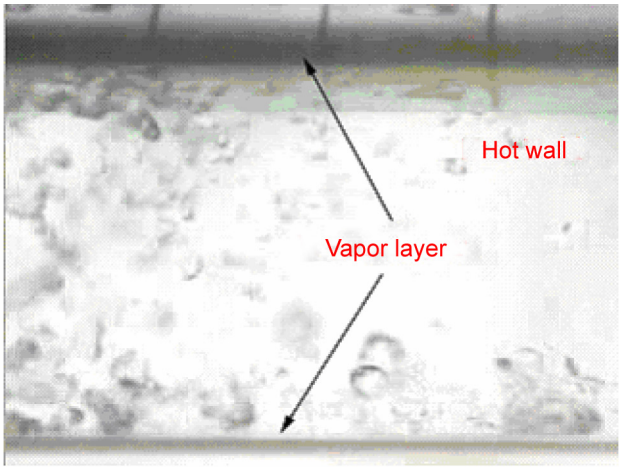

Figure 12.—Initial stage—inverted with scattered annular flow.

Figure 13.—Transition stage.

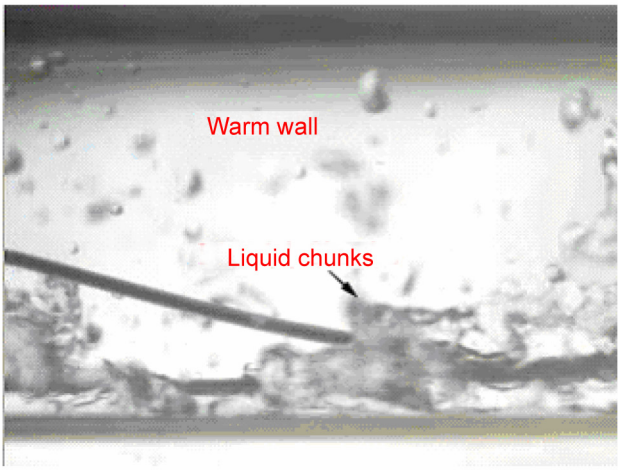

Figure 14.—Transition stage.

(portion between D and E in fig. 1). When the wall decreases in temperature further, the two-phase flows are experiencing a transition from the film boiling (inverted annular flow) to the stratified flow. Figures 13, 14 and 15 show the transition flows for warm tube walls where liquid chunks are starting to accumulate near the bottom side of the tube wall due to the gravity effects. Finally when the wall is chilled down enough, a stable stratified two phase flow was observed. As shown in figures 16, 17, and 18, a stable and continuous liquid layer is located on the bottom of the tube and a pure vapor core is flowing on top of the liquid layer. It is believed that for the stratified flow, nucleate boiling (portion between A and B in fig. 1) is taking place between the liquid layer and the cold bottom wall while the film boiling is the mode between the vapor core and the tube wall. Therefore under the stratified flow, there is a circumferential temperature variation on the tube wall.

Based on our estimation from the video images, the velocity of the vapor is around 5 cm/s. Therefore the gravity effect overpowers the flow inertia according to figure 2. This is the reason why we observed the stratified flow in this terrestrial experiment.

Figure 15.—Transition stage.

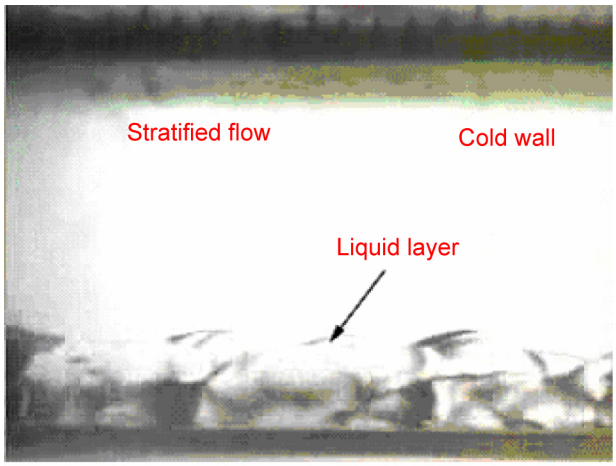

Figure 16.—Cold wall—stratified flow.

Figure 17.—Cold wall—stratified flow.

Figure 18.—Cold wall—stratified flow.

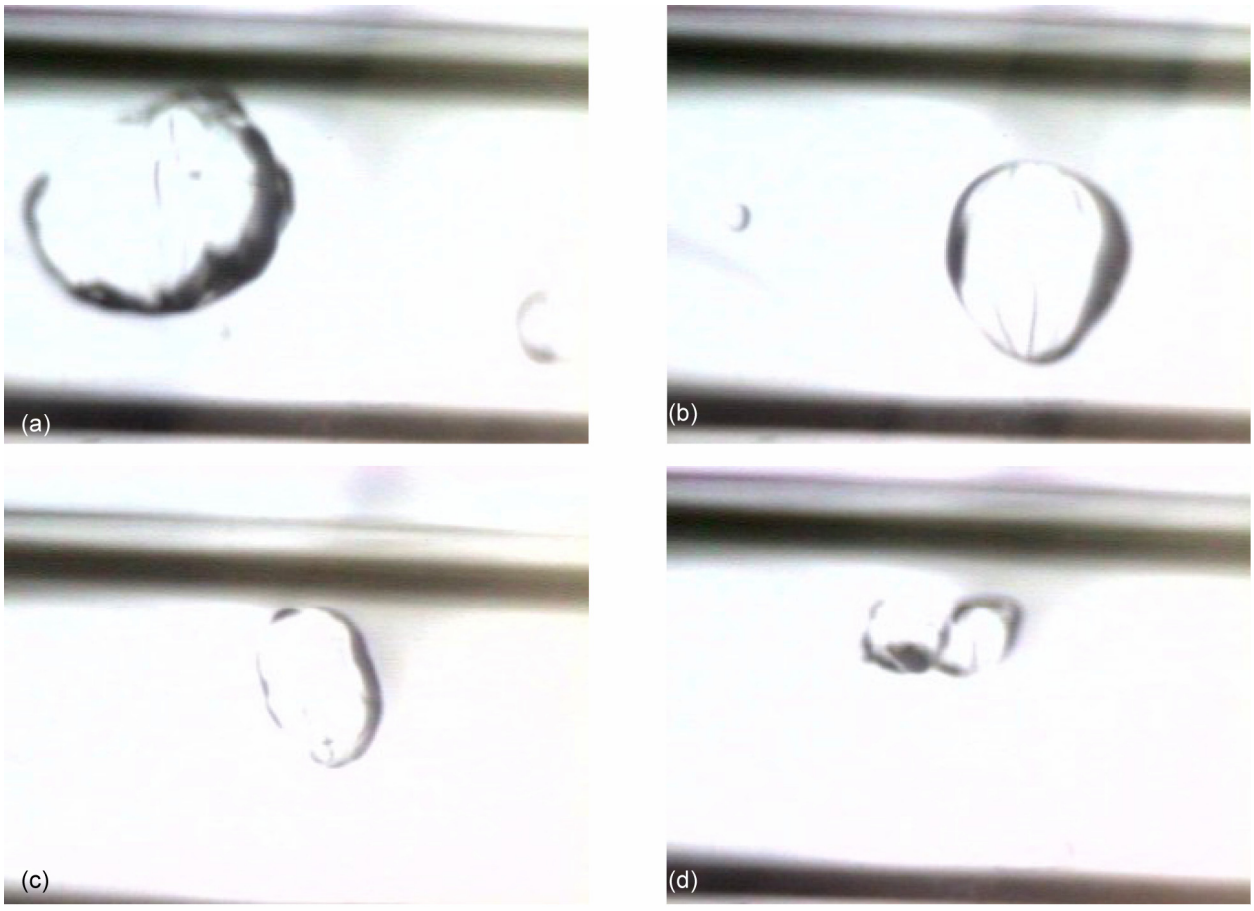

Figure 19.—Photographs of flow pattern in microgravity.

***Microgravity condition.*—**Figure 19 provides a series of four pictures for the chilldown experiment in a microgravity condition. We followed a large chunk of liquid as it traveled downstream. It is seen that basically it is an inverted annular flow where the vapor is filling the tube with liquid chunks in the center. The size of the liquid chunk is decreasing due to vaporization as it flows downstream.

Constant Wall Heat Flux Experiment

Since the wall is heated at a constant heat flux, the flow and heat transfer inside the tube is expected to develop into a steady condition. The applied heat flux is 13002 w/m^2**.** Two different motor speeds of 5 and 15 rpm were used in the constant heat flux experiment. The bulk velocities are estimated at 7.3 and 23.5 cm/s for 5 and 15 rpm, respectively. As a result, the 5 rpm case is somewhat affected by the gravity and the 15 rpm case is almost independent of gravity as indicated by figure 2. For the 5-rpm case, we only have terrestrial results while for the 15-rpm case, both terrestrial and microgravity data were obtained in a single run.

5-rpm Terrestrial Experiment

As shown in figure 7 for the 5 rpm case, wall temperatures were measured at three circumferential points for each of the three downstream locations. Because of similarities, only the temperatures at first downstream location are plotted and given in figure 20. Curve 1 shows the temperature recorded at the 12 o'clock point and curves 2 and 3 are for the 4 and 8 o'clock points, respectively. After 275 sec, the system has reached relatively steady state. As mentioned above, the 5-rpm case is affected by gravity to some extent and the flow visualization discussed next supports this prediction. The gravity effects would lead to circumferential temperature differences. The temperatures at the two lower points are about 20 K colder, that is due to more liquid fragments in the lower half due to gravity. Figure 21 gives the corresponding heat transfer coefficients for the same three points.

Figure 22 provides the flow visualization photographs for the 5-rpm terrestrial experiment. As compared to the chilldown experiment where the wall is unheated, the general size of the liquid phase is smaller and liquid fragments are more widely dispersed for the heated wall case. The effects of gravity are obvious that more liquid pieces in the lower half of the tube.

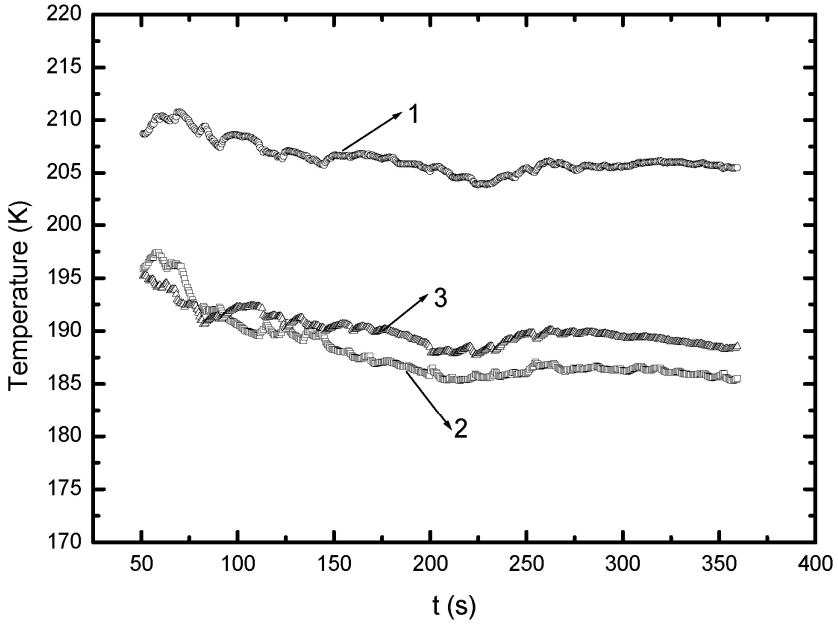

Figure 20.—Wall temperatures at three circumferential locations.

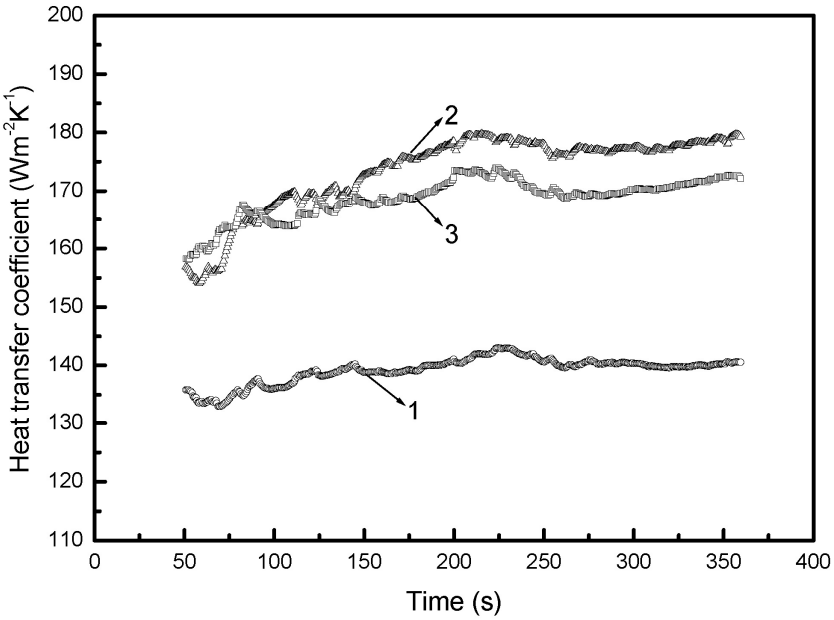

Figure 21.—Heat transfer coefficient at three circumferential locations.

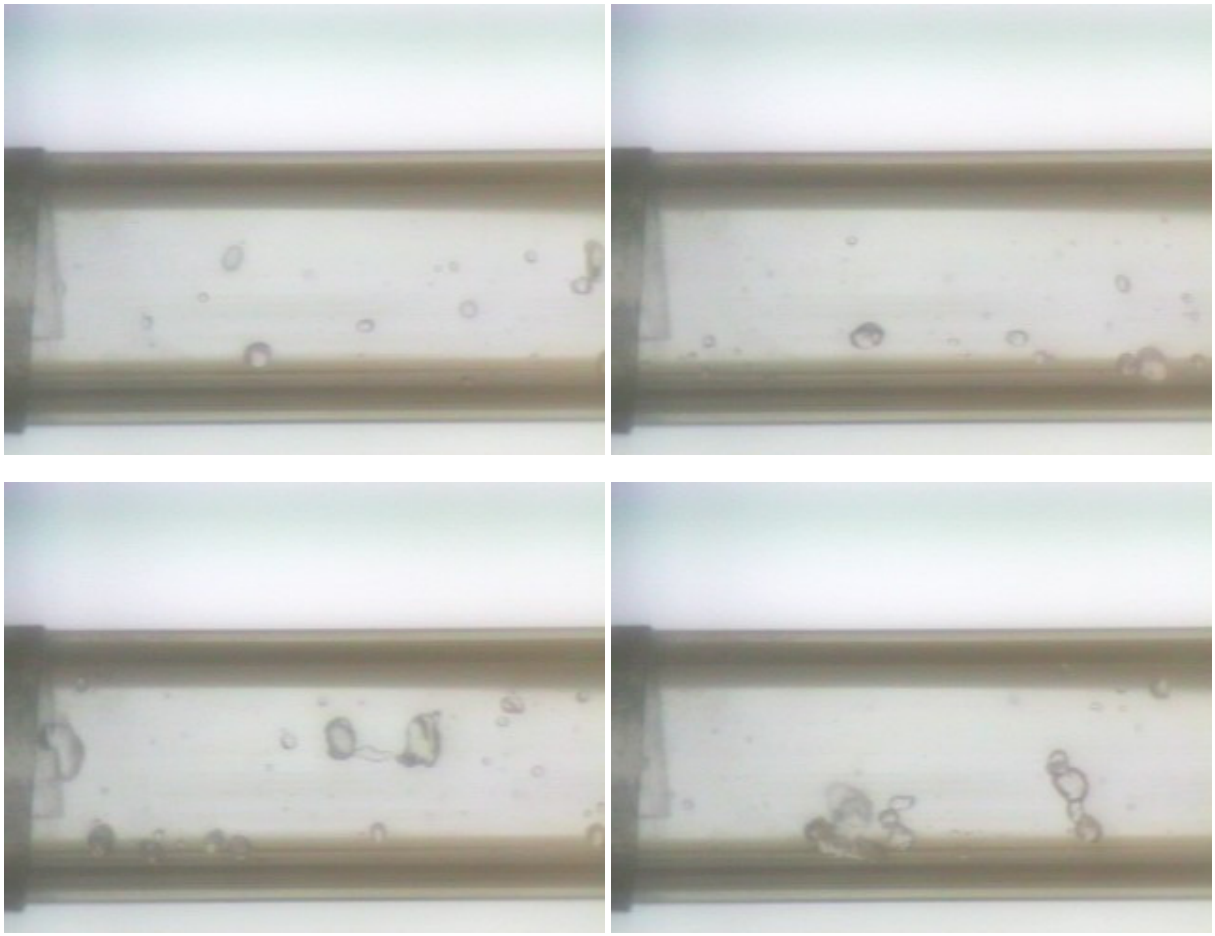
Figure 22.—Flow visualization of heated tube under terrestrial condition.

15-rpm Terrestrial and Microgravity Experiment

For the 15-rpm experiment with a heated tube, identical heating was used as the 5-rpm terrestrial case. But the flow rate is about three times higher. It is noted that for the combined experiment, terrestrial results precede the microgravity counterparts. First, the wall temperature measurement results are given in figure 23. Because of the limitations in a drop tower experiment, temperatures were measured only in two locations, one near the inlet and the other close to the outlet. Also we only measured one point (the 12 o'clock position) at each downstream location due to the expected circumferential similarity in microgravity. According to the discussion above, the gravity effect is supposed to be minimum and indeed the wall temperature measurement and the flow visualization both reflect this theoretical prediction.

In figure 23, the temperature levels registered by the thermocouple near the inlet exhibit only a very slight decrease during the microgravity period while near the outlet, a slight increase is measured. The temperature difference between the two downstream locations is a general feature of constant wall heating. To explain the microgravity results, we need to take a look at the flow visualization pictures as shown in figure 24. Because of the higher speed in the 15-rpm case, the liquid is broken down more in the form of mist. For the terrestrial condition, the mist seen as gray-shaded portion blankets the bottom wall as a thin layer. While in microgravity, the flow is a perfect inverted annular pattern where the liquid mist is occupying the central core. There are two main effects due the absence of gravity. The first is a slight acceleration of the flow as a result of the decrease in wall friction due to the replacement of the mist layer by the vapor adjacent to the wall. The second is the loss of the circumferential conduction in the wall. In terrestrial gravity, there is a circumferential temperature gradient in the wall that results in the conduction flow of heat from the top half to the bottom half. The slight decrease in the wall temperature near the inlet is thought to be due to the first effect as a faster flow gives rise to a higher heat transfer coefficient, while the slight increase near the outlet is due to the second effect that stops the flow of heat from the top of the wall.

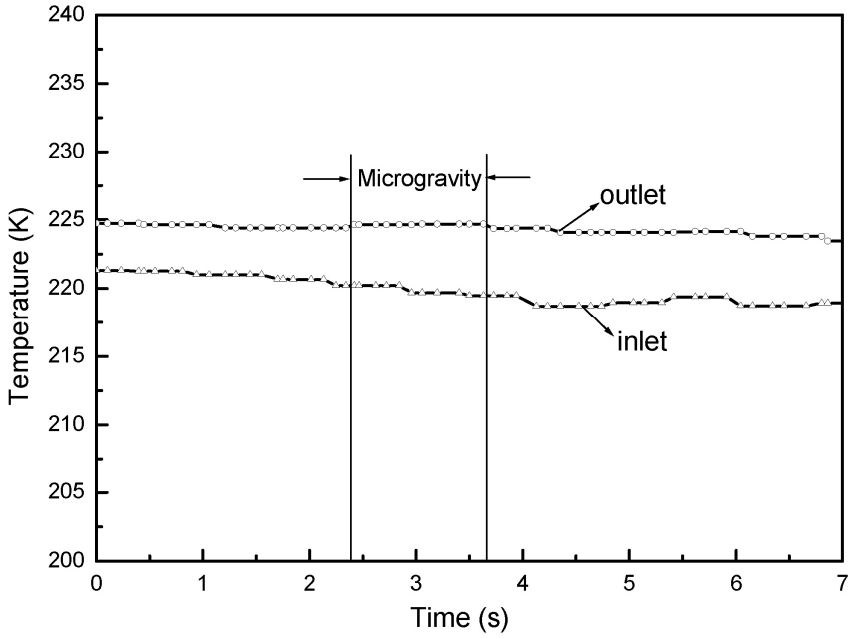

Figure 23.—Wall temperature measurement results.

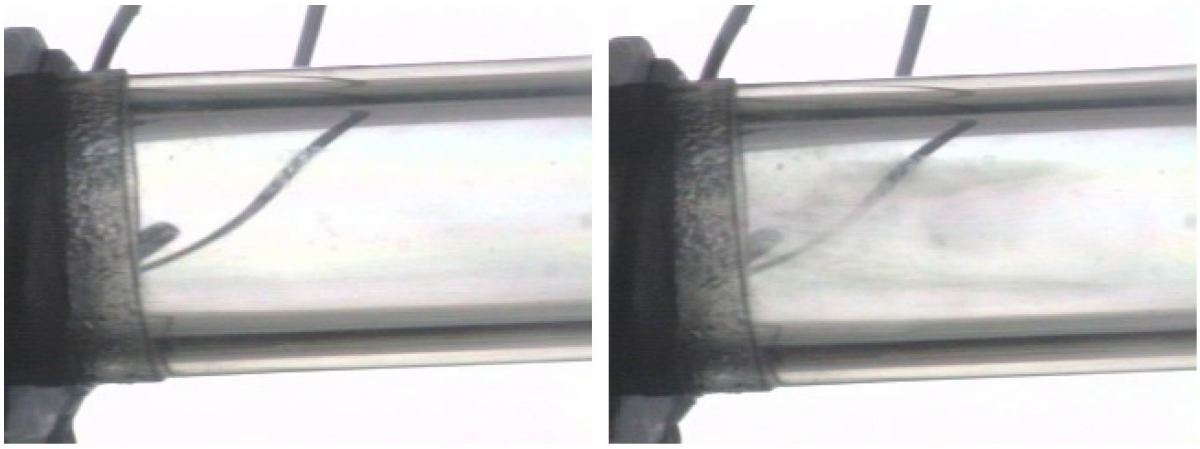

Before Drop: 1-g During Drop: micro-g

Figure 24.—Flow visualization of constant wall heat flux tube.

Numerical Simulation

As a first step towards the numerical simulation of film boiling, a detailed treatment of the liquid-vapor interface with phase change should be performed. We have chosen a single bubble during a dynamic translational motion as the model case. In the numerical simulation, a single bubble is rising through a superheated liquid, so the bubble is growing due to boiling and experiencing a shape change due to hydrodynamic force. A fixed-grid direct numerical simulation method has been developed and verified for single bubble boiling and condensation phenomena. The original contribution of this research is the first introduction of a sharp interface between the vapor and liquid phases, which allows the simulation of density ratios up to the order of 1000. The interface location is obtained as part of the solution which accounts for all coupled dynamic and thermal effects.

For a stationary and growing bubble, the predicted growth rate was found to agree with the theoretical limit of $t^{1/2}$ where t is the time. However, for a rising and growing bubble, the predicted growth rate was approaching the theoretical limit of $t^{2/3}$ for a spherical bubble but did not reach it exactly owing to bubble deformation.

Numerical Method

In the present approach, we employ a combined Eulerian-Lagrangian strategy. The fixed Cartesian grid is used as the Eulerian framework of the algorithm to facilitate the field equation computation. Within this framework, separate marker points, connected by piece-wise polynomials, are adopted to represent the interface to form the Lagrangian portion of the method. With moving boundaries, the motion of the interface is tracked through the translation of the marker points over the stationary, Cartesian grid. In each phase, a finite volume, fractional step method is employed to solve the coupled governing equations of momentum, energy and mass transfer. A cut-cell approach is developed to handle arbitrary intersections between an interface and the grid line. In the interface region, the grid will be recombined to form non-Cartesian cells. Consistent interpolation formulas are chosen for estimation of the fluxes along any of the cell surfaces. Both inviscid and viscous terms can be handled to maintain a globally second-order accurate algorithm. Here, this approach is further extended to treat liquid-vapor interaction. The schematic of the computational domain is given in figure 25.

Results

Figure 26 shows the bubble shape changes for varying density ratios without phase change. The system condition of the bubble are Re (Reynolds number) = 100, We (Weber number) = 4, Fr (Froud

number) = 1.0. Figure 27 represents the effects of Reynolds number and the Weber number. The density ratio is 1605 and the dynamic viscosity ratio is 22. Figure 28 is a summary of the bubble shape change for various Reynolds and Weber numbers. Figure 29 shows the bubble shapes for a rising bubble with phase change with density effects. The system condition is Re = 100, We = 4, Fr = 1.0. Figure 30 shows the streamline structures for the same cases in figure 29.

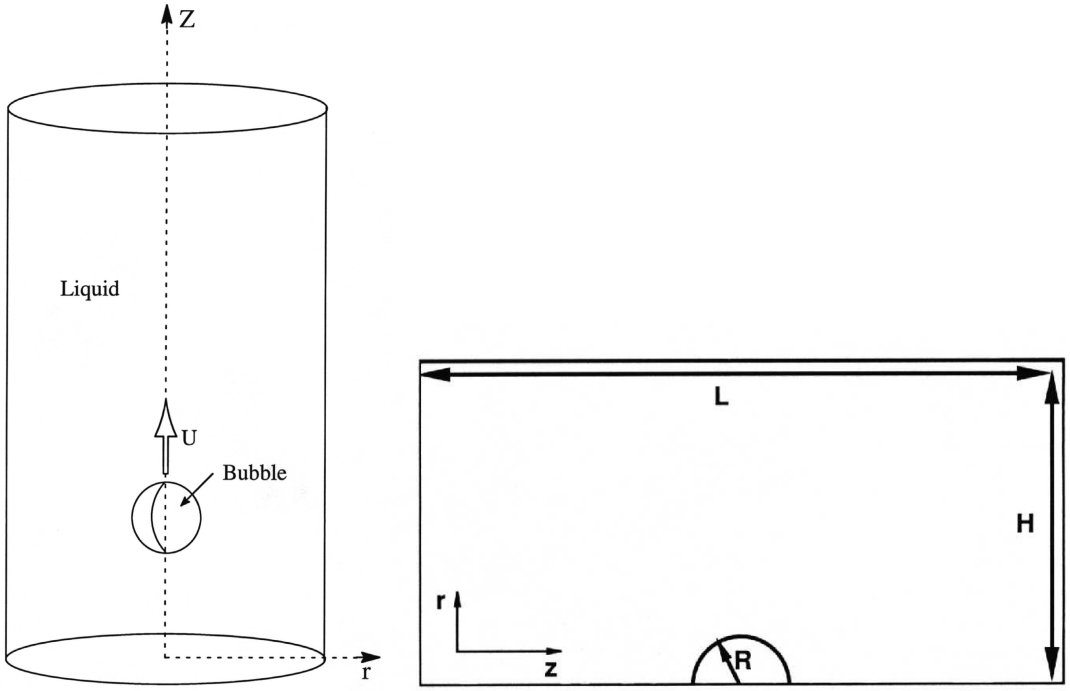

Figure 25.—Schematic of computational system.

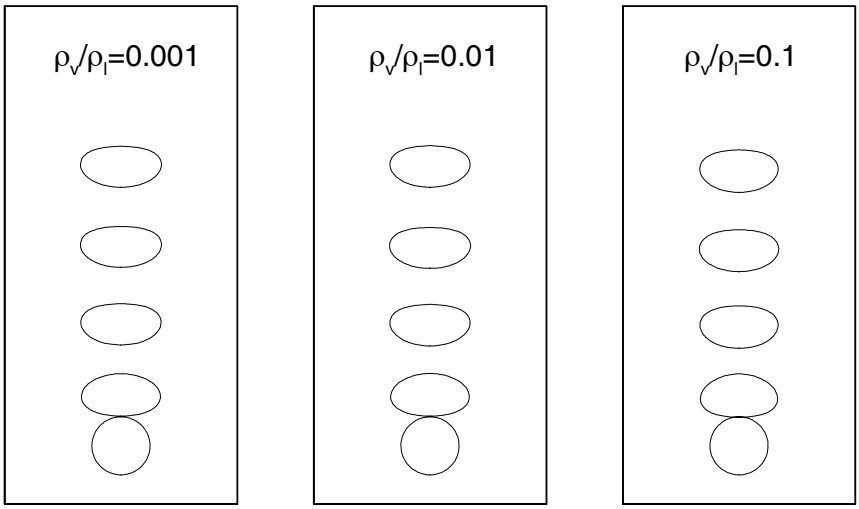

Figure 26.—Buoyancy driven bubble without phase change: density effect.

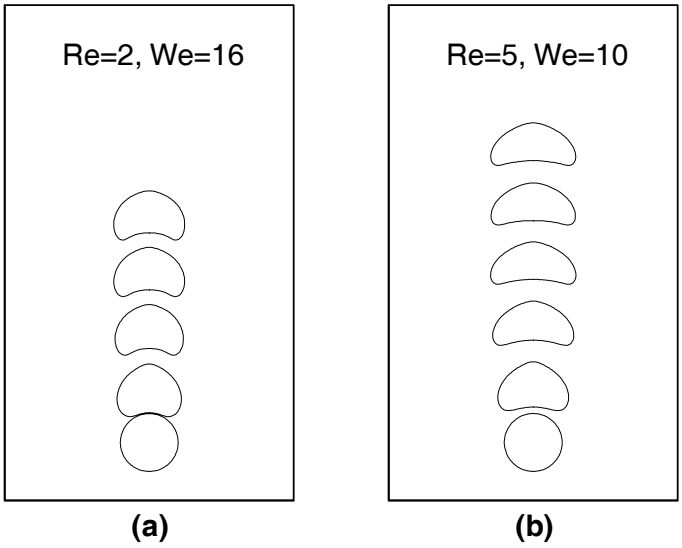

Figure 27.—Buoyancy driven bubble without phase change: Reynolds and Weber number effect.

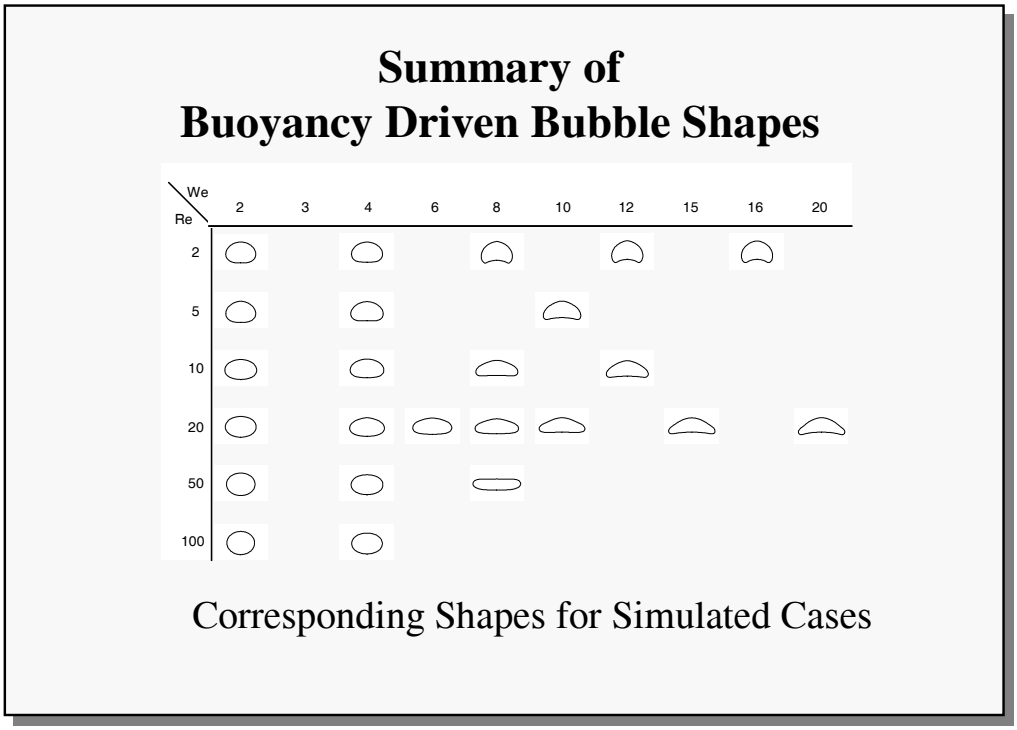

Figure 28.—Summary of bubble shapes for different Re and We.

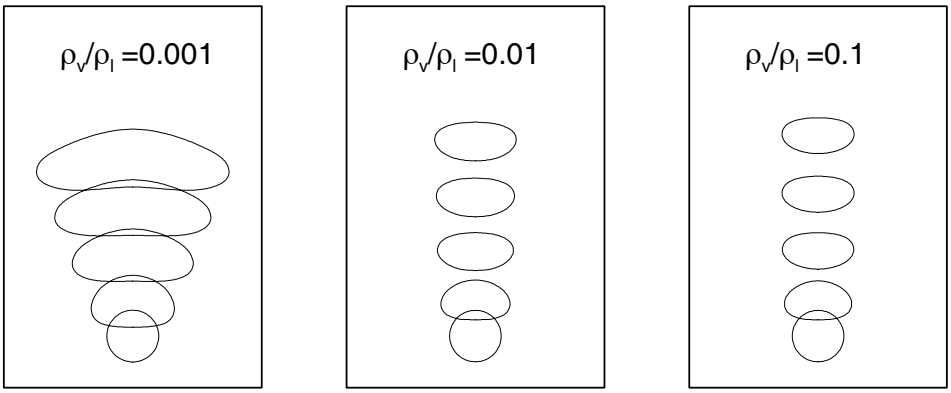

Figure 29.—Rising bubble with phase change: density effect.

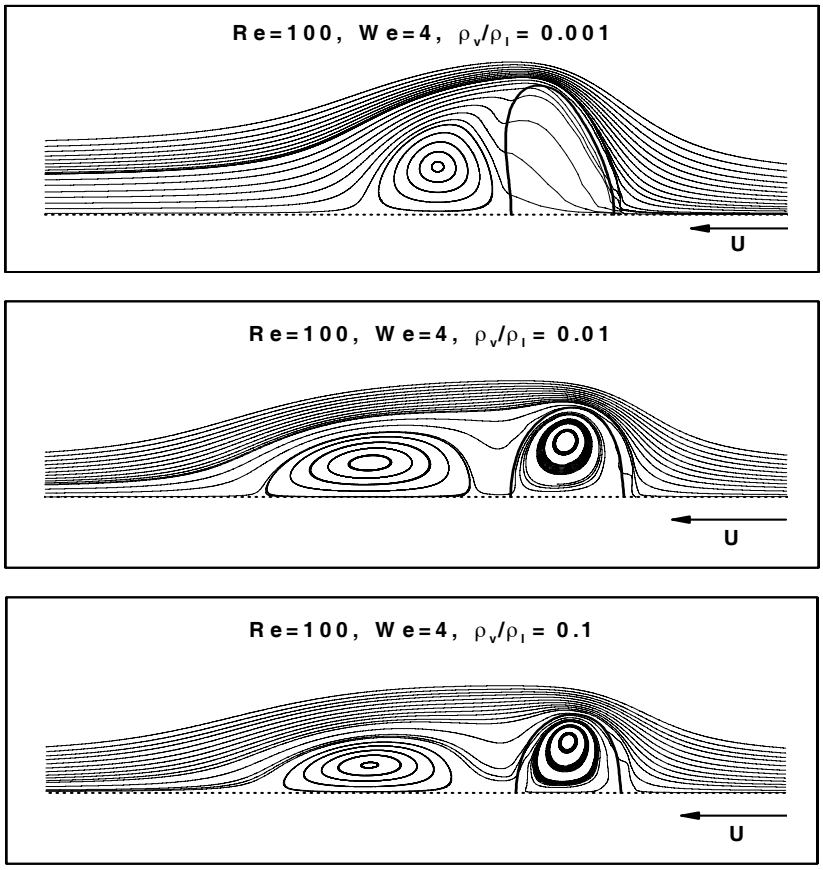

Figure 30.—Streamline structures of the bubbles.

Conclusion of Numerical Study

- A direct numerical simulation capability has been developed for bubble dynamics with phase change. The flow, thermal fields and interface motion are all obtained as part of the solution process.
- The methodology is unique in terms of the combined capabilities of resolving sharp interfaces, honoring mass conservation, handling large property ratios and phase change.

- Major dimensionless parameters, with and without phase change, are varied to probe the physical and numerical issues involved. For a stationary and growing bubble, the predicted growth rate was found to agree with the theoretical limit of $t^{1/2}$ where t is the time. However, for a rising and growing bubble, the predicted growth rate was approaching the theoretical limit of $t^{2/3}$ for a spherical bubble but did not reach it exactly owing to bubble deformation.

References

1. Brentari, E.G., Giarratano, P.J., and Smith, R.V., "Boiling Heat Transfer for Oxygen, Nitrogen, Hydrogen, and Helium, NBS Technical Note No. 317, National Bureau of Standards, 1965.
2. Beader, J.D., Miller, W.S., and Kalvinskas, L.A., "Boiling Heat Transfer for Cryogenics," NASA Contractor Report CR–243, National Aeronautics and Space Administration, 1965.
3. Kutateladze, S.S., "Heat Transfer in Condensation and Boiling," State Sci. and Tech. Pub. Of Lit. on Machinery, Moscow (Atomic Energy Commision Translation 3770, Tech. Info Service, Oak Ridge, Tennessee, 1949, 1952.
4. Breen, B.P. and Westwater, J.W., "Effect of Diameter of Horizontal Tubes on Film Boiling Heat Transfer," Chem. Engr. Progr. vol. 58, no. 7, pp. 67–72, 1962.
5. Brentari, E.G. and Smith, R.V., "Nucleate and Film Pool Boiling Design Correlatios for O_2, N_2, H_2 and He," International Advances in Cryogenic Engineering, vol. 10, pp. 325–341, 1965.
6. Shah, M.M., "Prediction of Heat Transfer During Boiling of Cryogenic Fluids Flowing in Tubes," Cryogenics, vol. 24, pp. 231–236, 1984.
7. Kandlikar, S.G., "A General Correlation For Saturated Two-Phase Flow Boiling Heat Transfer Inside Horizontal and Vertical Tubes," ASME J Heat Transfer, vol. 112, pp. 219–28, 1990.
8. Gungor, K.E. and Winterton, R.H.S., "Simplified General Correlation for Saturated Flow Boiling and Comparisons of Correlatios With Data," Chem Eg Res Des, vol. 65, pp. 148–56, 1987.
9. Van Dresar, N.T., Siegwarth, J.D., and Hasan, M.M., "Convective Heat Transfer Coefficients For Near-Horizontal Two-Phase Flow of Nitrogen and Hydrogen at Low Mass and Heat Flux," Cryogenics, vol. 41, pp.805–811, 2002.
10. N. Antar and Collins, Flow boiling during quenching in low gravity environment, Int. Journal of Microgravity Science and Technology, vol. 3, pp. 118–128, 1997
11. Gebhart, B., Jaluria, Y., Mahajan, R.L. and Sammakia, B., *Buoyancy-Induced Flow andHeat Transport*, Hemisphere Publishing Company, 1988.

Project Title: Chill Down Process of Hydrogen Transport Pipelines

Task PI: Renwei Mei, Department of Mechanical and Aerospace Engineering
Co-I: James Klausner, Department of Mechanical and Aerospace Engineering

Project Goals

The objective of this research task is to experimentally and computationally study the unsteady dynamics of a liquid hydrogen wave front translating down a pipeline during the chill down mode and develop a comprehensive computational model to predict the associated flow fields, thermal fields, and residence time. In order to accomplish the objective, the following tasks are planned: a) experimentally study the dynamics of a propagating liquid hydrogen wave front, b) experimentally measure the heat transfer rate associated with film boiling beneath the wave front, c) experimentally investigate transient nucleate boiling heat transfer associated with liquid film flow, d) develop a comprehensive computational model to predict the flow and temperature fields associated with propagating liquid hydrogen waves, and e) develop engineering models for cryogenic practitioners to predict the required chill down residence time under a variety of different operating conditions.

Accomplishments

Abstract

A pseudo-steady model has been developed to predict the chilldown history of pipe wall temperature in the horizontal transport pipeline for cryogenic fluids. A new film boiling heat transfer model is developed by incorporating the stratified flow structure for cryogenic chilldown. A modified nucleate boiling heat transfer correlation for cryogenic chilldown process inside a horizontal pipe is proposed. The efficacy of the correlations is assessed by comparing the model predictions with measured values of wall temperature in several azimuthal positions in a well controlled experiment by Chung et al. (2004). The computed pipe wall temperature histories match well with the measured results. The present model captures important features of thermal interaction between the pipe wall and the cryogenic fluid, provides a simple and robust platform for predicting pipe wall chilldown history in long horizontal pipe at relatively low computational cost, and builds a foundation to incorporate the two-phase hydrodynamic interaction in the chilldown process.

Introduction

The cryogenic chilldown is encountered in many applications but is of particular importance in cryogenic transportation pipelines. For example, in rockets or space shuttle launch facility, cryogenic liquids as fuel are filled from the storage tank to the internal fuel tanks of a space vehicle through a complex pipeline system. To avoid evaporated fuel entering the space vehicle, a cryogenic chilldown prior to the filling is required to reduce the pipe wall temperature to the saturation temperature of the cryogenic liquid.

Cryogenic chilldown involves complicated hydrodynamic and thermal interactions among liquid, vapor, and solid pipe wall. There exist few basic experimental studies and modeling efforts for chilldown of cryogenic fluids. Studies on cryogenic chilldown started in 1960's accompanying the development of rocket launching system. Early experimental studies were conducted by Burke et al. (ref. 1), Graham (ref. 2), Bronson et al. (ref. 3), Chi and Vetere (ref. 4), Steward (ref. 5) among other researches. Bronson et al. (ref. 3) studied the flow regime in a horizontal pipe during the chilldown by liquid hydrogen. The results revealed that the stratified flow is prevalent in the cryogenic chilldown.

Flow regimes and heat transfer regimes in the horizontal pipe chilldown were also studied by Chi and Vetere (ref. 4). Information of flow regimes was deduced by studying the fluid temperature and volume fraction during the chilldown. Several flow regimes were identified: single phase vapor, mist flow, slug flow, annular flow, bubbly flow, and single-phase liquid flow. Heat transfer regimes were identified as: single-phase vapor convection, film boiling, nucleate boiling, and single-phase liquid convection.

Recently, Velat et al. (ref. 6) systematically studied cryogenic chilldown in a horizontal pipe. Their study included: visually recording the chilldown in a transparent Pyrex pipe, which is used to identify the flow regime and heat transfer regime; collecting temperature histories at different positions of wall in the chilldown; recording pressure drop along the pipe. Chung et al. (ref. 7) conducted a similar study on the nitrogen chilldown at relatively low mass flux and provided the data needed to assess various heat transfer coefficients in the present study.

Burke et al. (ref. 1) developed a crude chilldown model based on the 1–D heat transfer through the pipe wall and the assumption of infinite heat transfer rate from the cryogenic fluid to the pipe wall. The effects of flow regimes on the heat transfer rate were neglected. Graham et al. (ref. 2) correlated heat transfer coefficient and pressure drop with the Martinelli number (ref. 8) based on their experimental data. Chi (ref. 9) developed a 1–D model for energy equations of the liquid and the wall, based on film boiling heat transfer between the wall and fluid. An empirical equation for predicting chilldown time and temperature was proposed.

Steward (ref. 5) developed a homogeneous flow model for the chilldown. The model treated the cryogenic fluid as a homogeneous mixture. The continuity, momentum and energy equations of mixture were solved to obtain density, pressure and temperature of mixture. Various heat transfer regimes were considered: film boiling, nucleate boiling and single-phase convection heat transfer. Separate treatment of different heat transfer regimes resulted in a significant improvement in the prediction of the chilldown process. Homogeneous mixture model was also employed by Cross et al. (ref. 10) who obtained a correlation for the wall temperature in the chilldown with an oversimplified heat transfer model of the heat transfer between the wall and the fluid.

Stratified flow regime, which is the prevalent flow regime in horizontal chilldown, was first studied by Chen and Banerjee (refs. 11 to 13). They developed a separated flow model for the simulating cool-down by a stratified flow in a hot horizontal pipe. Both phases were modeled using 1–D mass and momentum conservation equations. The wall temperature was computed using a 2–D transient heat conduction equation. Their prediction for wall temperature agreed well with their experimental results. Although a significant progress was made on handling the momentum equations, the heat transfer correlations employed were not as advanced.

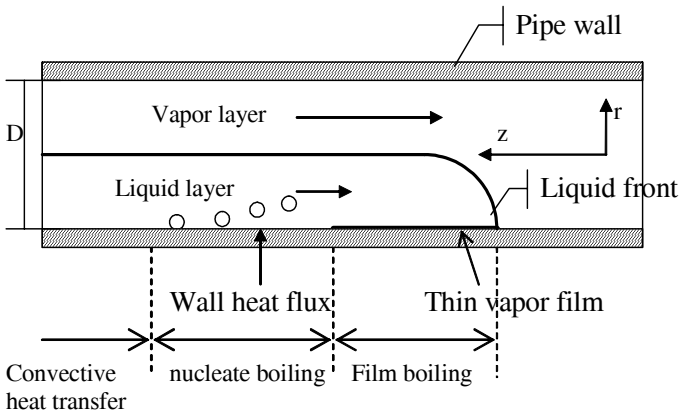

Figure 1.—Schematic of chilldown heat transfer regimes in a horizontal pipe.

Typical chilldown involves several heat transfer regimes as shown in figure 1. Near the liquid front is the film boiling. The knowledge of the heat transfer in the film boiling regime is relatively limited, because i) film boiling has not been the central interest in industrial applications; and ii) high temperature difference causes the difficulties in experimental investigations. For the film boiling on vertical surfaces, early work was reported by Bromley (ref. 14), Dougall and Rohsenow (ref. 15) and Laverty and Rohsenow (ref. 16). Film boiling in a horizontal cylinder was first studied by Bromley (ref. 17); and the Bromley correlation was widely used. Breen and Westwater (ref. 18) modified Bromley's equation to account for very small tubes and large tubes. If the tube is larger than wavelength associated with the Taylor instability, the heat transfer correlation is reduced to Berenson's correlation (ref. 19) for a horizontal surface.

Empirical correlations for film boiling were proposed by Hendrick et al. (refs. 20 and 21), Ellerbrock et al. (ref. 22), von Glahn (ref. 23), Giarratano and Smith (ref. 24). These correlations relate a simple or modified Nusselt number ratio to the Martinelli parameter. Giarratano and Smith (ref. 24) gave detailed assessment on these correlations. All these correlations are for steady state cryogenic film boiling. They may not be suited for transient chilldown application.

When the pipe chills down further, film boiling ceases and transient boiling occurs, followed by nucleate boiling. The heat transfer in the transient boiling is even more complicated and it is usually assumed that the boiling switches from film boiling to nucleate boiling right away. The position of film boiling transitioning to the nucleate boiling is often called rewetting front, because from that position the cold liquid starts touching the pipe wall. Usually the Leidenfrost temperature indicates the transition from the film boiling to the nucleate boiling.

The study on the convection nucleate boiling is extensive. A general correlation for saturated boiling was introduced by Chen (ref. 25). Gungor and Winterton (ref. 26) modified Chen's correlation and extend it to subcooled boiling. Enhancement and suppression factors for macro-convective heat transfer were introduced. Gunger and Winterton's correlation can fit experimental data better than the modified Chen's correlation (ref. 27) and Stephan and Auracher correlation (ref. 28). Kutateladze (ref. 29) and Steiner (ref. 30) also provided correlations for cryogenic fluids in pool boiling and forced convection boiling. Although they are not widely used, they should be more applicable for cryogenic fluids as the correlation was directly based on cryogenic conditions.

As the wall temperature drops further, the nucleate boiling is replaced by pure convection. The convection heat transfer can be modeled using Dittus-Boelter equation (ref. 31) for the fully developed turbulent pipe flow or corresponding laminar heat transfer equation for laminar pipe flow (ref. 31). The condition in which nucleate boiling switches to single-phase convection heat transfer is that all nucleate sites are suppressed.

Although two-fluid model can describe the fluid dynamics aspect of the chilldown process, it suffers from computational instability for moderately values of slip velocity between two phases which limits its application. To gain fundamental insight into the thermal interaction between the wall and the cryogenic fluid and to be able to rapidly predict chilldown in a long pipe, an alternative pseudo-steady model is developed. In this model, liquid wave front speed is assumed to be constant and is the same as the bulk liquid speed (ref. 32). It is also assumed that steady state thermal fields for both the liquid and the solid exist in a reference frame that is moving with the wave front. The heat transfer between the fluid and the wall is modeled using different heat transfer correlations depending on the operating heat transfer regime at a given location. Various improvements on the correlations are introduced, including the development of a new film boiling heat transfer coefficient. The governing equation for the solid thermal field becomes a parabolic equation that can be efficiently solved. It must be emphasized that a great advantage of the pseudo-steady model is that one can assess the efficacy of the film boiling model independently from that of the nucleate boiling model since the down stream information in the nucleate boiling regime cannot affect the temperature in the film boiling regime. In another word, even if the nucleate boiling heat transfer coefficient is inadequate, the film boiling heat transfer coefficient can still be assessed in the film boiling regime by comparing with the measure temperature for the right period of time. After the satisfactory performance is achieved for the film boiling regime, the nucleate boiling heat transfer model

can be subsequently assessed. In the Results section, those detailed assessments of the heat transfer coefficients are provided by comparing the computed temperature variations with the experimental measurements of Chung et al. (ref. 7). Satisfactory results are obtained.

Nomenclature

Bo	Boiling number
c	solid heat capacity
c_p	heat capacity
D	pipe diameter
d	thickness of pipe wall
g	gravity
h	heat transfer coefficient
h_{pool}	pool boiling heat transfer coefficient
h_{conv}	convection boiling heat transfer coefficient
h_{fg}	latent heat
Ja	Jacob number
k	thermal conductivity
k_{eff}	effective thermal conductivity
Nu	Nusselt number
p	pressure
R	radius of pipe
R_1 and R_2	inner and outer radius of pipe
Ra	Rayleigh number
Re	Reynolds number
Pc	Peclet number
Pr	Prandtl number
S	suppression factor
T	temperature
T_1	Leidenfrost temperature
T_2	transition temperature between nucleate boiling to convection heat transfer
T_o	room temperature
t	time
U	velocity
u and v	vapor film velocity
x and y	vapor film coordinates
Z	transformed coordinate
z, r, and φ	cylindrical coordinates
α	liquid volume fraction
χ_{tt}	Martinelli number
δ	vapor film thickness
ε	emissivity
ϕ	azimuthal coordinate
μ	viscosity
θ	dimensionless temperature; azimuthal coordinate
σ	liquid surface tension; Stefan Boltzmann constant

Subscripts

0	characteristic value
i and o	inner and outer pipe

l	liquid
v	vapor
w	wall
sat	saturated

Superscripts

’	dimensionless variable

Formulation

In pseudo-steady chilldown model, it is assumed that both the liquid and its wave front moves at a constant speed *U* which is taken from estimated experimental condition in the present model. Thus the main emphasis of the present study is on the modeling of the heat transfer coefficients in different heat transfer regimes and the computation of the thermal field within the solid pipe.

Solid Heat Transfer

The thermal field inside the solid wall is governed by the 3–D unsteady energy equation:

$$\rho c \frac{\partial T}{\partial t} = \frac{\partial}{\partial z}\left(k \frac{\partial T}{\partial z} \right) + \frac{1}{r}\frac{\partial}{\partial r}\left(rk \frac{\partial T}{\partial r} \right) + \frac{1}{r}\frac{\partial}{\partial \varphi}\left(\frac{k}{r} \frac{\partial T}{\partial \varphi} \right) \tag{1}$$

Since the wave front speed *U* is assumed to be a constant, it can be expected that when the front is reasonably far from the entrance region of the pipe, the thermal field in the solid is in a steady state when it is viewed in the reference frame that moves with the wave front. Thus, the following coordinate transformation is introduced,

$$Z = z + Ut \, . \tag{2}$$

Equation (1) is then transformed to:

$$\rho c U \frac{\partial T}{\partial Z} = \frac{\partial}{\partial Z}\left(k \frac{\partial T}{\partial Z} \right) + \frac{1}{r}\frac{\partial}{\partial r}\left(rk \frac{\partial T}{\partial r} \right) + \frac{1}{r}\frac{\partial}{\partial \varphi}\left(\frac{k}{r} \frac{\partial T}{\partial \varphi} \right). \tag{3}$$

For further simplification, the following dimensionless parameters are introduced,

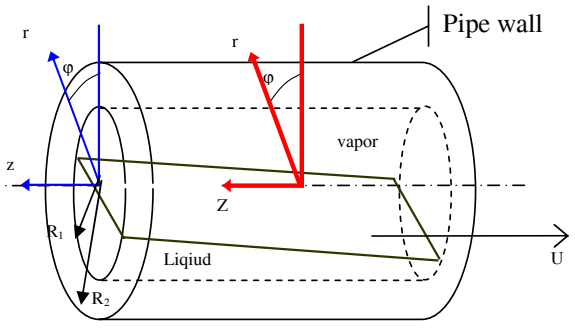

Figure 2.—Coordinate systems: laboratory frame is denoted by *z*, moving frame is denoted by *Z*.

$$\theta = \frac{T - T_w}{T_w - T_{sat}},\ Z' = \frac{Z}{d}, r' = \frac{r}{d}\quad c' = \frac{c}{c_0} \text{ and } k' = \frac{k}{k_0} \tag{4}$$

where k_0 is the characteristic thermal conductivity, and c_0 is the characteristic heat capacity. Equation (3) can be normalized as

$$\mathrm{Pc} * c' \frac{\partial \theta}{\partial Z'} = \frac{\partial}{\partial Z'}\left(k' \frac{\partial \theta}{\partial Z'}\right) + \frac{1}{r'}\frac{\partial}{\partial r'}\left(r'k' \frac{\partial \theta}{\partial r'}\right) + \frac{1}{r'}\frac{\partial}{\partial \varphi}\left(\frac{k'}{r'}\frac{\partial \theta}{\varphi}\right), \tag{5}$$

where $\mathrm{Pc} = \dfrac{\rho c_0 U d}{k_0}$ is the Peclet number.

Under typical operating condition for the cryogenic chilldown process, Pc ~ $O(10^2)$ – $O(10^3)$. The first term on the RHS of eq. (5) is small compared with the rest of terms and thus can be neglected. eq. (5) becomes

$$\mathrm{Pc} * c' \frac{\partial \theta}{\partial Z'} = \frac{1}{r'}\frac{\partial}{\partial r'}\left(r'k' \frac{\partial \theta}{\partial r'}\right) + \frac{1}{r'}\frac{\partial}{\partial \varphi}\left(\frac{k'}{r'}\frac{\partial \theta}{\varphi}\right), \tag{6}$$

which is parabolic. Hence in the Z'-direction, only one condition is needed. In the φ-direction, periodic boundary conditions are used. On inner and outer surfaces of the pipe wall, where $r = R_1$ and R_2, proper boundary conditions for the temperature are required.

For convenience, $Z' = 0$ is set at the liquid wave front. In the region of $Z' < 0$, the inner wall is exposed to the pure vapor. Although there may be some liquid droplets in the vapor that can cause evaporative cooling when the droplets deposit on the wall and the cold flowing vapor can absorb some heat from the wall, the heat flux due to these two mechanisms is small compared with the heat transfer between liquid and solid wall in the region of $Z' > 0$. Hence, heat transfer for $Z' < 0$ is neglected and it is assumed that $\theta = 1$ at $Z' = 0$. The computation starts from the $Z' = 0$ to $Z' \to \infty$, until a steady state solution in the Z'-direction is reached. An implicit scheme in the Z'-direction is employed to solve eq. (6).

Liquid and Vapor Flow

The two-phase flow is assumed to be stratified as was observed in (ref. 7). Both liquid and vapor phases are assumed to be at the saturated state. Liquid volume fraction determining which part of wall is in contact with the liquid or the vapor, is specified at every cross-section along the Z'-direction based on experimental information. The visual studies (refs. 6 and 7) show that the liquid volume fraction increases gradually, rather than abruptly, near the liquid wave front and becomes almost constant during most of the chilldown. Hence, the following liquid volume fraction α as a function of time is used in the computation of the solid-fluid heat transfer coefficient,

$$\begin{aligned} \alpha &= \alpha_0 \sin\left(\frac{t}{t_0} \cdot \frac{\pi}{2}\right) \qquad t < t_0 \\ \alpha &= \alpha_0 \qquad\qquad\qquad t \geq t_0 \end{aligned}, \tag{7}$$

where t_0 is characteristic chilldown time, and α_0 is characteristic liquid volume fraction. Here the time when the nucleate boiling is almost suppressed and slope of the wall temperature profile becomes flat is set as characteristic chilldown time.

The vapor phase velocity is assumed to be a constant. However, it was not directly measured. It is computationally determined by trial-and-error by fitting the computed and measured wall temperature variations for numerous positions.

Heat Transfer Between Cryogenic Fluid and Solid Pipe Wall

During the chilldown, the fluid in contact with the pipe wall is either liquid or vapor. The mechanisms of heat transfer between the liquid and the wall and between the vapor and the wall are different. Based on experimental measurements and theoretical analysis, liquid-solid heat transfer accounts for a majority of the total heat transfer. However, the prediction for heat transfer is much more complicated than the heat transfer between the vapor and the wall. The heat transfer between the liquid and the wall is discussed first.

Heat Transfer Between Liquid and Solid wall

Heat transfer between liquid and solid wall includes film boiling, nucleate boiling, and single-phase convection heat transfer. The transition from one type of boiling to another depends on many parameters, such as wall temperature, wall heat flux, and various properties of fluid. For simplicity, a fixed temperature approach is adopted to determine the transition points. That is, if the wall temperature is higher than the Leidenfrost temperature, film boiling dominates. If the wall temperature is between Leidenfrost temperature and a transition temperature, T_2, nucleate boiling takes place. Here, the transient boiling regime between film boiling and nucleate boiling is neglected. The reason is mainly the difficulty associated with the determination of the conditions for the transient boiling to occur and the lack of a reliable transient heat transfer correlation. If the wall temperature is below the transition temperature T_2, pure convection heat transfer dominates. The values of Leidenfrost temperature and transition temperature are determined by matching model prediction with the experimental results.

Film boiling heat transfer.—Because of the nature of high wall superheat in chilldown, the film boiling plays a major role in chilldown in terms of the time span and in terms of the total amount of heat removed from the wall. Currently there exists no specific film boiling correlation for chilldown applications with such high superheat. If one uses conventional film boiling correlations, necessary modifications for cryogenic application must be made for chilldown.

One of cryogenic film boiling heat transfer correlations was provided by Giarratano and Smith (ref. 24)

$$\left(\frac{\mathrm{Nu}}{\mathrm{Nu}_{calc}}\right) * \mathrm{Bo}^{-0.4} = f(\chi_{tt}) \tag{8}$$

where Nu_{calc} is the Nusselt number for the forced convection heat transfer. In this correlation, the heat transfer coefficient is the averaged value for the whole cross section. Similar correlations for cryogenic film boiling also exist in literature. The correlations were obtained from measurements conducted under steady states. The problem with the use of this steady state film boiling correlation is that it does not take into account the change of flow regime as encountered in the chilldown. For example, for the same quality, the heat transfer rate in annular flow is much different from that in stratified flow, while those empirical correlations cannot take such difference into account.

Furthermore, in this study, local heat transfer coefficient is needed in order to incorporate the thermal interaction with the pipe wall. Since the two-phase flow regime information is available through visualization in the present study, the modeling effort needs to take into account the knowledge of the flow regimes.

There are several correlations for the film boiling based on the analysis of vapor film boundary layer and stability of the thin vapor film, such as Bromley's correlation (ref. 17) and Breen and Westerwater's correlation (ref. 18) for film boiling on the outer surface of a hot tube, Frederking and Clark's (ref. 33) and Carey's (ref. 34) correlations for film boiling on the surface of a sphere. However, none of these was obtained for cryogenic fluids or for film boiling on the inner surface of a pipe.

A new correlation for the film boiling in cryogenic chilldown inside a tube is presented here. The schematic of film boiling inside a pipe is shown in figure 3 with a cross-sectional view. Bulk liquid is

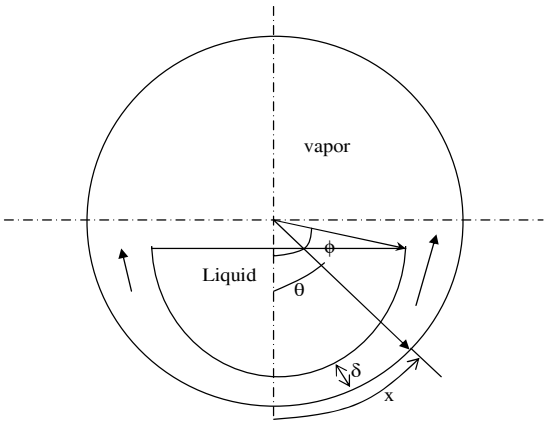

Figure 3.—Schematic diagram of film boiling in stratified flow.

near the bottom of the pipe. Beneath the liquid is a thin vapor film. Due to buoyancy force, the vapor in the film flows upward along the azimuthal direction. Heat is transferred through the thin vapor film from the solid to the liquid. Reliable heat transfer correlation for film boiling in pipes or tubes requires the knowledge of the thin vapor film thickness which can be obtained by solving the film layer continuity, momentum, and energy equations.

To simplify the analysis for the vapor film heat transfer, it is assumed the liquid velocity in the azimuthal direction is zero and the vapor flow in the direction perpendicular to the cross-section is negligible. It is further assumed that the vapor film thickness is small compared with the pipe radius and vapor flow is in steady state, incompressible and laminar. The laminar flow assumption can be confirmed *post priori* as the Reynolds number, Re, based on the film velocity and film thickness is typically of $O(10^0 \sim 10^0)$. In terms of the x- and y-coordinates and (u, v) velocity components shown in figure 3, the governing equations for the vapor flow are similar to boundary-layer equations:

$$\frac{\partial u}{\partial x} + \frac{\partial v}{\partial y} = 0, \tag{9}$$

$$u\frac{\partial u}{\partial x} + v\frac{\partial u}{\partial y} = -\frac{1}{\rho_v}\frac{\partial p}{\partial x} + \nu_v \frac{\partial^2 u}{\partial y^2} - g\sin\theta, \tag{10}$$

$$u\frac{\partial T}{\partial x} + v\frac{\partial T}{\partial y} = \alpha_v \frac{\partial^2 T}{\partial y^2}, \tag{11}$$

where subscribe v refers to properties of vapor.

Because the length scale in the azimuthal (x) direction is much larger than the length scale at the normal (y) direction, the v-component may be neglected. Furthermore, the convection term is assumed small and is neglected. The resulting momentum equation is simplified to

$$\frac{1}{\rho_v}\frac{\partial p}{\partial x} = \nu_v \frac{\partial^2 u}{\partial y^2} - g\sin\theta. \tag{12}$$

The vapor pressure can be evaluated by considering the hydrostatic pressure from liquid core as:

$$p = p_0 + \rho_l g R\left(\cos\left(\frac{x}{R}\right) - \cos\phi\right) \tag{13}$$

where ϕ is angular position where the film merges with the vapor core. The momentum equation becomes

$$\frac{(\rho_l - \rho_v)}{\rho_v} g \sin\left(\frac{x}{R}\right) + \nu_v \frac{\partial^2 u}{\partial y^2} = 0. \tag{14}$$

The vapor velocity boundary condition is $u = 0$ at $y = 0$ and $u = u_l = 0$ at $y = \delta$. The vapor velocity profile is:

$$u = \frac{(\rho_l - \rho_v)}{2\nu_v \rho_v} g \sin\left(\frac{x}{R}\right) * \left(\delta y - y^2\right). \tag{15}$$

The mean velocity $\bar{u}$ is

$$\bar{u} = \frac{1}{\delta}\int_0^\delta u dy = \frac{(\rho_l - \rho_v)\delta^2 g}{12\nu_v \rho_v} \sin\left(\frac{x}{R}\right). \tag{16}$$

The energy and mass balances on the vapor film requires that

$$\frac{k_v}{h_{fg}} dx * \left[-\left(\frac{\partial T}{\partial y}\right)_{y=\delta}\right] = d\dot{m} = \rho_v d(\bar{u}\delta). \tag{17}$$

Neglecting the convection, the vapor energy equation is:

$$\frac{\partial^2 T}{\partial y^2} = 0. \tag{18}$$

The following linear temperature profile is thus obtained,

$$\frac{T - T_{sat}}{T_w - T_{sat}} = 1 - \frac{y}{\delta}. \tag{19}$$

Substituting the temperature and velocity profiles into eq. (17) yields

$$\frac{\delta}{R}\frac{d}{d\theta}\left(\left(\frac{\delta}{R}\right)\sin\theta\right) = \frac{12 k_v \nu_v}{h_{fg}(\rho_l - \rho_v) g R^3}\left(T_w - T_{sat}\right). \tag{20}$$

Equation (20) has analytical solution:

$$\frac{\delta}{R} = 2\left(\frac{6\mathrm{Ja}}{\mathrm{Ra}}\right)^{\frac{1}{4}} F(\theta), \tag{21}$$

where Ja is Jacob number and Ra is Raleigh number:

$$\mathrm{Ja} = \frac{c_{p,v}\left(T_w - T_{sat}\right)}{h_{fg}}, \tag{22}$$

$$\mathrm{Ra} = \frac{gD^3\left(\rho_l - \rho_v\right)}{\nu_v \alpha_v \rho_v}, \tag{23}$$

and $F(\theta)$

$$F(\theta) = \left(\frac{\frac{4}{3}\int_0^{\theta} \sin^{1/3}\theta' d\theta'}{\sin^{4/3}\theta} \right)^{\frac{1}{4}} \tag{24}$$

describes the geometric dependence of vapor film thickness.

The mean velocity $\bar{u}$ as a function of θ is thus

$$\bar{u} = \left(\frac{\left(T_w - T_{sat}\right)\left(\rho_l - \rho_v\right) gR}{12\nu_v \rho_v^2 h_{fg}} \right)^{\frac{1}{2}} F^2(\theta)\sin(\theta). \tag{25}$$

Curves for $F(\theta)$ and $F^2(\theta)\sin\theta$ based on numerical integration are shown in figure 4. The vapor film thickness has a minimum at $\theta = 0$ and is nearly constant for $\theta < \pi/2$. It rapidly grows after $\theta > \pi/2$. The singularity at the top of tube when $\theta \rightarrow \pi$ is of no practical significance since the film will merge with the vapor core at the vapor-liquid interface. The vapor velocity is controlled by $F(\theta)^2\sin\theta$ which is zero at the bottom of the pipe and increases almost linearly in the lower part of the tube where the vapor film

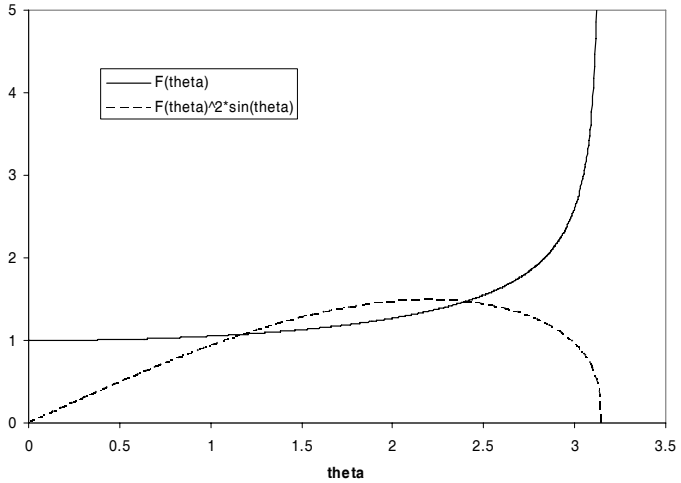

Figure 4.—Numerical solutions of the vapor thickness and velocity influence functions.

thickness does not change substantially. In the upper part of the tube, due to the increase in the vapor film thickness, the vapor velocity gradually drops back to zero at the top of the tube. Thus a maximum velocity may exist in the upper part of the tube.

The local film boiling heat transfer coefficient is easily obtained from the linear temperature profile. It is

$$h = \frac{k_v}{\delta} = 0.6389 \frac{k_v}{DF(\theta)} \left(\frac{\mathrm{Ra}}{\mathrm{Ja}} \right)^{\frac{1}{4}}. \tag{25}$$

Nucleate Boiling and Convection Heat Transfer

For the nucleate flow boiling heat transfer, Gungor and Winterton's correlation (ref. 26) is widely used due to its relatively better accuracy in predicting heat transfer coefficients. However, a closer examination on this correlation shows that it is based mainly on the following parameters: Pr, Re, and quality *x*. Similar to the development of conventional film boiling correlations, these parameters all reflect overall properties of the flow in the pipe and are not directly related to flow regimes. Thus it cannot be used to predict the local heat transfer coefficients in chilldown.

Chen's (ref. 25) flow boiling correlation is based on separating the heat transfer to micro- and macro-convection heat transfer. Micro-convection heat transfer represents the contribution from boiling heat transfer, and macro-convection represents the contribution from the forced convection heat transfer. However his correlation fits best for annular flow because of the derivation of suppression factor. In stratified flow regime, which is common in cryogenic chilldown, Chen's correlation may not be applicable.

Several correlations have been tried in this study, including Gungor and Winterton's correlations (ref. 26), Chen's correlation (ref. 25), and Kutateladze's correlations (ref. 29). None gives a satisfactory heat transfer rate that is need to match the experimentally measured temperature histories in (ref. 7) in the nucleate boiling regime. Among them, Kutateladze's correlation gives more reasonable result. In this correlation, the total heat transfer coefficient *h* is

$$h = h_{conv} + h_{pool}, \tag{26}$$

where h_{conv} is given by Dittus-Boelter equation for fully developed pipe flow,

$$h_{conv} = 0.023 * \mathrm{Re}_l^{0.8}\ \mathrm{Pr}_l^{0.4} * k_l / D \tag{27}$$

and pool nucleated boiling heat transfer coefficient h_{pool} is

$$h_{pool} = 0.487 * 10^{-10} * \left[\frac{k_l \rho_l^{1.282} p^{1.750} \left(c_{p,l} \right)^{1.5}}{\left(h_{fg} \rho_v \right)^{1.5} \sigma^{0.906} \mu_l^{0.626}} \right] \Delta T^{1.5}, \tag{28}$$

in which ΔT is wall superheat.

Kutateladze's correlation (ref. 29) was proposed without considering the effect of nucleate site suppression. This obviously leads to an overestimation of the nucleate boiling heat transfer rate. Hence a modified version of Kutateladze's correlations (28) is used,

$$h = h_{conv} + S * h_{pool}, \tag{29}$$

with *S* being the suppression factor and h_{pool} is given by (28).

When ΔT drops to a certain range all the nucleate sites are suppressed. The heat transfer is dominated by single phase forced convection. The heat transfer coefficient can then be predicated using Dittus-Boelter equation, eq. (27), if flow is turbulent, or eq. (30), if flow is laminar.

$$h_{conv} = 4.36 * k_l / D . \tag{30}$$

Heat Transfer between Vapor and Solid Wall

The heat transfer between the vapor and the wall can be estimated by treating the flow as a fully developed convection flow, neglecting the liquid droplets that are entrapped in the vapor. The heat transfer coefficient of vapor forced convection flow is

$$h_v = 0.023 * \mathrm{Re}_v^{0.8} \, \mathrm{Pr}_v^{0.4} * k_v / D \ \text{(turbulent flow)} \tag{31}$$

or

$$h_v = 4.36 * k_v / D \ \text{(laminar flow)} \tag{32}$$

Heat Transfer between Solid Wall and Environment

For a cryogenic flow facility, although serious insulation is applied, the heat leakage to environment is still considerable due to the large temperature difference between the cryogenic fluid and the environment. It is necessary to evaluate the heat leakage from the inner pipe to environment in order to make realistic assessment of the model prediction with the experimental results (ref. 7).

Vacuum insulation chamber between the inner and outer pipes is used in cryogenic transport pipe (ref. 7), as shown in figure 5. Radiation heat transfer exists between the inner and outer pipe. Furthermore, the space between the inner and outer pipe is not an absolute vacuum. There is residual air that causes free convection between the inner and outer pipes driven by the temperature difference of the inner and outer pipe.

The radiation between the inner pipe and outer pipe becomes significant when the inner pipe is chilled down. The heat transfer coefficient is proportional to the difference of the fourth power of wall temperatures. Exact evaluation of the radiation heat transfer between the inner and outer pipe is a difficult task. Hence a simplified model based on the overall radiation heat transfer between long concentric cylinders with constant temperature at inner pipe and outer pipe (ref. 31) is used to evaluate the heat transfer rate at every axial location of the pipe. It is not quantitatively correct, but can provide reasonable estimate for the magnitude of the radiation heat transfer between pipes through the vacuum. The local radiation heat transfer rate per unit area on the surface of inner pipe q''_{rad} is

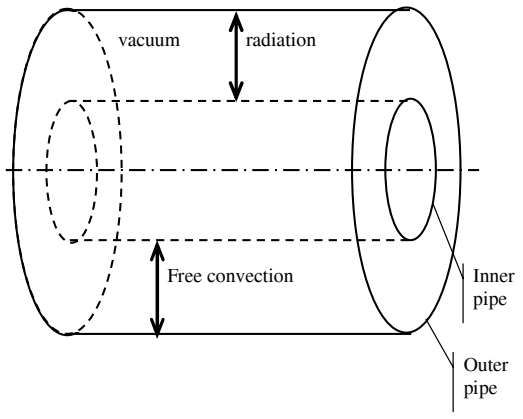

Figure 5.—Schematic of vacuum insulation chamber.

$$q'_{rad} = \frac{\sigma(T_{wall}^4 - T_o^4)}{\frac{1}{\varepsilon_i} + \frac{1-\varepsilon_o}{\varepsilon_o}\left(\frac{r_i}{r_o}\right)}, \tag{33}$$

where the σ is Stefan Boltzmann constant, (r_i, ε_i) and (r_o, ε_o) are the radius and emissivity of inner pipe and outer pipe, respectively, and T_{wall} is the local inner wall temperature, T_o is the room temperature that is assumed constant in the entire outer pipe. Here the emissivity is also assumed to be constant during the entire chilldown process.

For the free convection heat transfer due to the residual air in the vacuum chamber between the inner pipe and outer pipe, Raithby and Hollands' correlation (ref. 35) is used for the heat transfer rate. The average heat transfer rate per unit length of the cylinder is

$$q'_{frc} = \frac{2\pi k_{eff}}{\ln\left(r_o \diagup r_i\right)}\left(T_i - T_o\right), \tag{34}$$

where T is assumed constant on the inner and outer wall along the azimuthal directions, and k_{eff} is the effective thermal conductivity.

Results and Discussions

In experiment by Chung et al. (ref. 7), liquid nitrogen was used. The flow regime is revealed to be stratified flow by visual observation, as shown in figure 7, and wall temperature history in several azimuthal positions is measured by thermal couples and recorded on a computer.

Experiment of Chung et al.

In experiment of Chung et al. (ref. 7), a concentric pipe test section (fig. 6) was used. The chamber between the inner and outer pipe is vacuumed, but about 20 percent air remained. The inner diameter (i.d.) and outer diameter (o.d.) of inner pipe are 11.1 and 15.9 mm, and i.d. and o.d. of outer pipe are 95.3 and 101.6 mm, respectively. Numerous thermal couples were placed at different locations of the inner pipe. Some were embedded very closely to the inner surface of the inner pipe while others measure the outside wall temperature of inner pipe. Experiments were carried out at room temperature and atmosphere pressure. Liquid nitrogen flows from a reservoir to the test section driven by gravity. As liquid nitrogen flows through the pipe, it evaporates and chills the pipe. Some of the typical visual results are shown in figure 7. The measured average liquid nitrogen velocity is $U \sim 5$ cm/s. Vapor velocity is not measured in this experiment. In this study, it is determined through trial-and-error by fitting the computed and measured temperature histories. The characteristic liquid volume fraction is 0.3 from the recorded video images. The characteristic time used in this computation is $t_0 = 100$ s. The Leidenfrost temperature for the nitrogen is around 180 K; hence the temperature when the film boiling ends and nucleates boiling starts is set at 180 K. The transition temperature at which the nucleate flow boiling switches to purely convection heat transfer is 140 K based on experimental results. The material of the inner pipe and outer pipe used in the experiment of (ref. 7) are Pyrex glass with emissivity of 0.82 at room temperature.

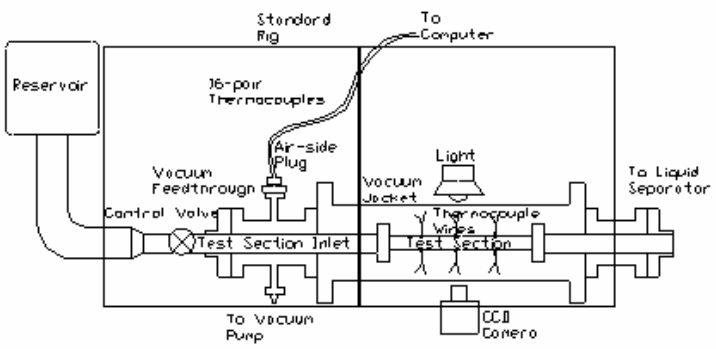

Figure 6.—Schematic of Chung et al.'s cryogenic two-phase flow test apparatus (ref. 7).

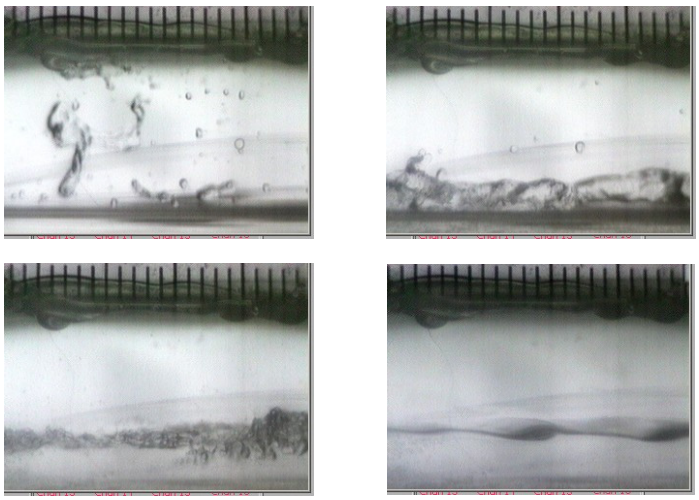

Figure 7.—Experimental visual observation of Chung et al.'s cryogenic two-phase flow test (ref. 7).

Comparison of Pipe Wall Temperature

In the computation, there are 40 grids along the radial direction and 40 grids along azimuthal direction for the inner pipe (fig. 8). The results of temperature profile at 40×40 grids and higher grids resolution show that 40×40 grids are sufficient. Figures 9 and10 compare the measured and computed wall temperature as a function of time at positions 11, 12, 14 and 15 shown in figure 8. For the modified Kutateladze's correlation a suppression factor 0.01 is used. Vapor velocity is 0.5m/s based on the best fit. The overall temperature histories agree well in the film boiling stage. Thus, the film boiling heat transfer coefficient based on the first principle and incorporated the flow structure gives very reliable prediction. It must also be noted that the value of the Leidenfrost temperature does not affect the computed temperature history prior to that transition point since the governing equation is parabolic. The good agreement before the Leidenfrost temperature is reached is entirely due to the superior performance of the new film boiling heat transfer coefficient.

During the stage of the rapidly decreasing wall temperature after the Leidenfrost temperature, the computed wall temperature drops slightly faster than the measured value. The rapid decrease in the wall temperature is due to initiation of nucleate boiling which is more efficient for heat transfer than the film boiling. Reasonable agreement between the computed and measured histories in this nucleate boiling regime is due to: i) the good agreement already achieved in the film boiling stage; ii) valid choice for the Leidenfrost temperature that switches the heat transfer regime correctly; and iii) appropriate modification of Kutateladze's correlations.

In the final stage of chilldown, the wall temperature decreases slowly, and the computed wall temperature shows the same trend as the measured one but tends to be a little lower. Figure 11 shows the temperature distribution of a given cross-section at different times of chilldown. Because the upper part of pipe wall is exposed to nitrogen vapor, cooling effect is much reduced.

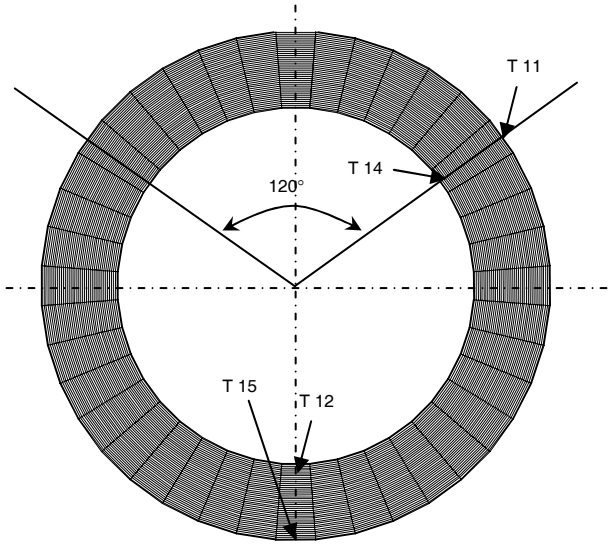

Figure 8.—The computational grids arrangement and positions of thermal couples.

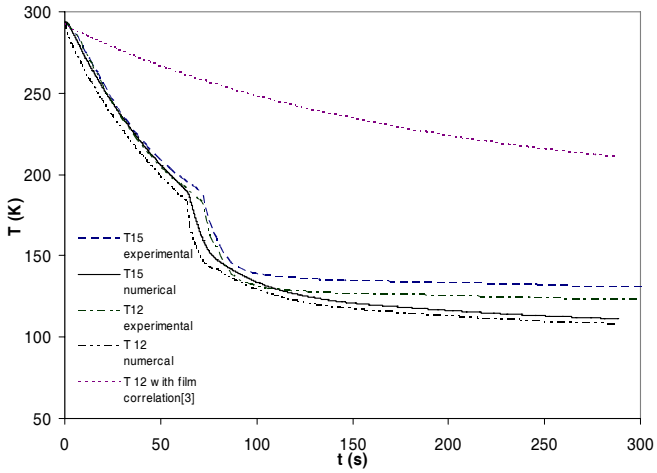

Figure 9.—Comparison of wall temperature of transducer 12 and 15, which is at the bottom of pipe, between the experiment and computation. For comparison purpose, the solution in the *Z*-direction is converted to time *t*.

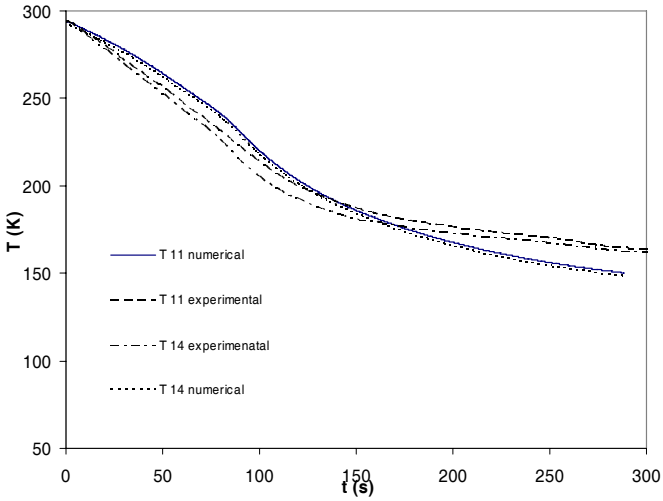

Figure 10.—Comparison of wall temperature of transducer 11 and 14, which are at the upper part of the pipe, between the experiment and computation. For comparison purpose, the solution in the *Z*-direction is converted to time *t*.

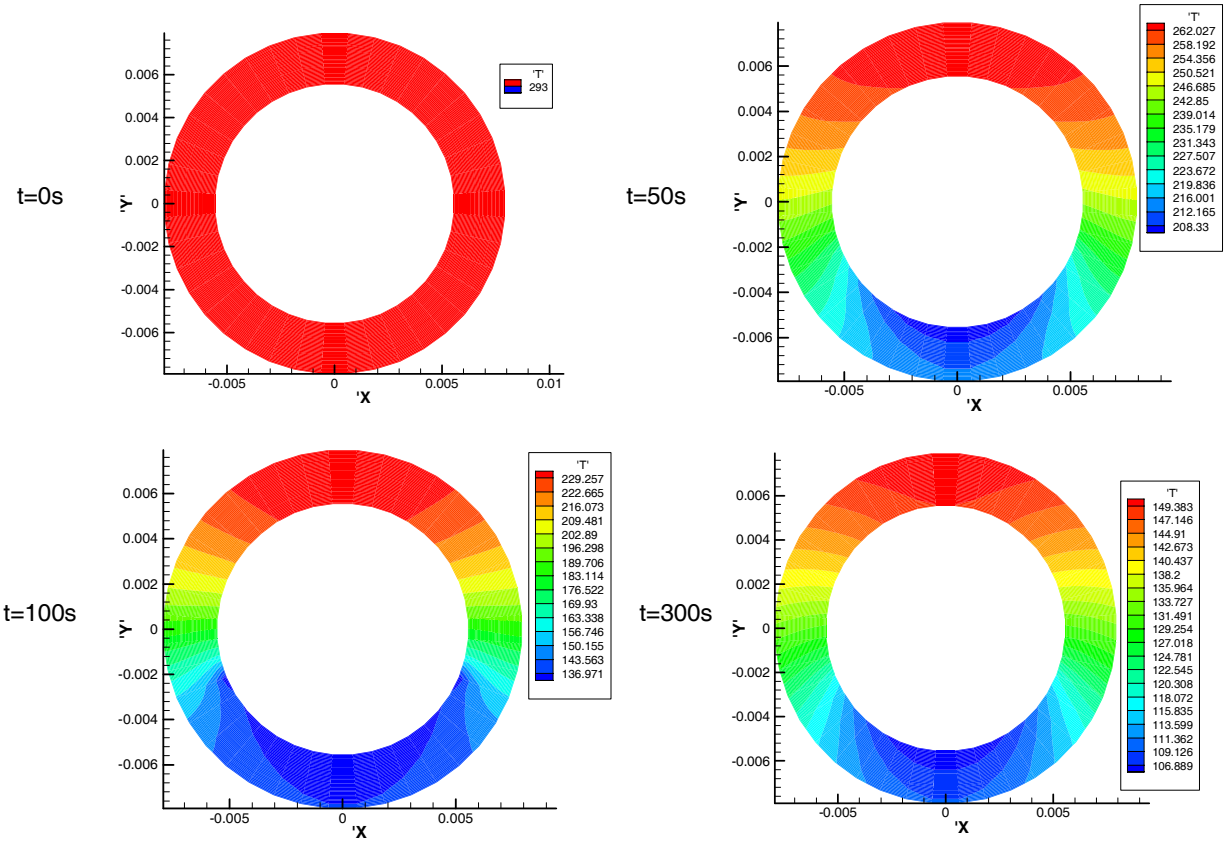

Figure 11.—Wall temperature distribution across the section at t = 0, 50, 100 and 300 sec.

Discussions and Remarks

In figure 9, the wall temperature based on the film boiling correlation of Giarratano and Smith (ref. 24) is also shown. Apparently, the correlation of Giarratano and Smith (ref. 24) gives a very low heat transfer rate so that the wall temperature remains high. This comparison confirms our earlier argument that correlations based on the overall flow parameter, such as quality and averaged Reynolds number, are not applicable for the simulation of unsteady chilldown.

The nucleate flow boiling correlations of Gungor and Winterton (ref. 26), Chen (ref. 25), Kutateladze's correlations (ref. 29) are also compared in this study. Gungor and Winterton's correlation fails to give a converged heat transfer rate during the transition from the film boiling to the nucleate boiling. Chen's correlation overestimates the heat transfer rate, and cause unrealistically large temperature drop on the wall, which results in the halt of the computation. Only Kutateladze's correlation gives a reasonable heat transfer rate. However, the temperature drop near the bottom of the pipe is still faster than the measured one as shown in figure 9. This may be due to the fact that most of nucleate boiling correlations were obtained from experiments of low wall superheat. However, in this cryogenic chilldown, wall superheat is much higher than that in the normal nucleate boiling experiments. Another reason is that the original Kutateladze's correlation does not include suppression factor. This leads to overestimating heat transfer coefficient. The modified Kutateladze's correlation with suppression factor gives reasonable chilldown result in figure9.

Further examination of figures 9 and 10 indicates that although we have considered the heat leak from the outer wall to the inner wall through radiation and free convection, the computed temperature is still lower than the measured temperature during the final stage of chilldown, where the heat transfer rate between fluid and wall is low due to lower wall superheat and possibly heat leak. The temperature difference between the computed and measured values at position 12 and position 15 suggests that there may be additional heat leak, which affects the measurements but is not taken in account in the present modeling.

In this study, the pseudo-steady chilldown model is developed to predict the chilldown process in a horizontal pipe in stratified flow regime. This model can also be extended to describe annular flow chilldown in the horizontal or the vertical pipe with minor changes on the boundary condition for solid temperature. It can also be extended to study the chilldown in the slug flow as long as we specify the contact period between the solid and the liquid or the vapor. The disadvantage of the current pseudo-steady chilldown model is that the fluid interaction inside the pipe is largely neglected and both vapor and liquid velocities are assumed to be constant. Compared with a more complete model that incorporates the two-fluid model, the present pseudo-steady chilldown model requires more experimental measurements as inputs. However, the pseudo-steady chilldown model is computationally more robust and efficient for predicting chilldown process. It provides overall reasonable results for the solid wall temperature. While a more complete model for chilldown process that incorporates the mass, momentum, and energy equations of vapor and liquid is being developed to reduce the dependence of the experimental inputs for the liquid velocity and trial-and-error for the vapor velocity, the present study has revealed useful insights into the key elements of two-phase heat transfer encountered in the chilldown process which have been largely ignored. It also laid the necessary modeling foundation for the incorporation of the two-fluid model.

Conclusions

A pseudo-steady chilldown computational model has been developed to understand the heat transfer mechanisms of cryogenic chilldown and predict the chilldown wall temperature history in a horizontal pipeline. The model assumes the constant speed of the moving liquid wave front, and steady state of the thermal field in the solid in a reference frame that moves with the liquid wave front, and saturated temperature of both liquid and vapor so that the 3–D unsteady problem can be transformed to a 2–D, parabolic problem. A new film boiling heat transfer coefficient in the cryogenic chilldown condition is developed using the first principle and incorporating the stratified flow structure. The existing nucleate

boiling heat transfer correlations may not work well under cryogenic condition. A modified Kutateladze's correlations with suppression factor adequately describes heat transfer coefficient. With the new and modified heat transfer correlations, the pipe wall temperature history based on the pseudo-steady chilldown model matches well with the experimental results by Chung et al. (ref. 7) for almost the entire chilldown process. The pseudo-steady chilldown model has captured the important features of thermal interaction between the pipe wall and the cryogenic fluid.

References

1. Burke, J.C., Byrnes, W.R., Post, A.H., and Ruccia, F.E., 1960, "Pressure Cooldown of Cryogenic Transfer Lines," Advances in Cryogenic Engineering, **4**, pp. 378–394.
2. Graham, R.W., Hendricks, R.C., Hsu, Y.Y., and Friedman, R., 1961, "Experimental Heat Transfer and Pressure Drop of Film Boiling Liquid Hydrogen Flowing through A Heated Tube," Advances in Cryogenic Engineering, **6**, pp. 517–524.
3. Bronson, J.C., Edeskuty, F.J., Fretwell, J.H., Hammel, E.F., Keller, W.E., Meier, K.L., Schuch, and A.F, Willis, W.L., 1962, "Problems in Cool-Down of Cryogenic Systems," Advances in Cryogenic Engineering, **7**, pp. 198–205.
4. Chi, J.W.H., and Vetere, A.M., 1963, "Two-Phase Flow During Transient Boiling of Hydrogen and Determination of Nonequilibrium Vapor Fractions," Advances in Cryogenic Engineering, **9**, pp. 243–253.
5. Steward, W.G., Smith and R.V., Brennan, J.A., 1970, "Cooldown Transients in Cryogenic Transfer Lines," Advances in Cryogenic Engineering, **15**, pp. 354–363.
6. Velat, C., Jackson, J., Klausner, J.F., and Mei, R., 2004, "Cryogenic Two-Phase Flow during Chilldown," in Proceedings of the ASME HT-FED Conference, Charlotte, NC.
7. Chung, J.N., Yuan, K., and Xiong, R., 2004, "Two-Phase Flow and Heat Transfer of a Cryogenic Fluid during Pipe Chilldown," Proceedings of 5th International Conference on Multiphase Flow, Yokohama, Japan, pp. 468.
8. Martinelli, R.C., and Nelson, D.B., 1948, "Prediction of Pressure Drop During Forced –Circulation Boiling of Water," Transaction of ASME, **70**, pp. 695–701.
9. Chi, J.W.H., 1965, "Cooldown Temperatures and Cooldown Time During Mist Flow," Advances in Cryogenic Engineering, **10**, pp. 330–340.
10. Cross, M.F., Majumdar, A.K., Bennett Jr., and J.C., Malla, R. B., 2002, "Model of chilldown in Cryogenic Transfer Linear," Journal of Spacecraft and Rockets, **39**, pp. 284–289.
11. Chan, A.M.C., and Banerjee, S., 1981, "Refilling and Rewetting of a Hot Horizontal Tube part I: Experiment," Journal of Heat Transfer, **103**, pp. 281–286.
12. Chan, A.M.C., and Banerjee, S., 1981, "Refilling and Rewetting of a Hot Horizontal Tube part II: Structure of a Two-Fluid Model," Journal of Heat Transfer, **103**, pp. 287–292.
13. Chan, A.M.C., and Banerjee, S., 1981, "Refilling and Rewetting of a Hot Horizontal Tube part III: Application of a Two-Fluid Model to Analyze Rewetting," Journal of Heat Transfer, **103**, pp. 653–659.
14. Bromley, J.A., 1950, "Heat Transfer in Stable Film Boiling," Chemical Engineering Progress, **46**, no. 5, pp. 221–227.
15. Dougall, R.S., Rohsenow, W.M., 1963, "Film boiling on the inside of vertical tubes with upward flow of the fluid at low qualities," MIT report no 9079–26, MIT.
16. Laverty, W.F., and Rohsenow, W.M., 1967, "Film Boiling of saturated Nitrogen Flowing in a Vertical Tube," Journal of Heat transfer, **89**, pp. 90–98.
17. Bromley, J.A., 1950, "Heat Transfer in Stable Film Boiling," Chemical Engineering Progress, **46**, no. 5, pp. 221–227.
18. Breen, B.P., and Westwater, J.W., 1962, "Effect if Diameter of Horizontal Tubes on Film Heat Transfer," Chemical Engineering Progress, **58**, no.7, pp. 67.

19. Berenson, P.J., 1961, "Film-Boiling Heat Transfer from a Horizontal Surface," Journal of Heat Transfer, **83**, pp. 351–358.
20. Hendricks, R.C., Graham, R.W., Hsu, Y.Y., and Friedman, R., 1961, "Experimental Heat Transfer and Pressure Drop of Liquid Hydrogen Flowing Through a Heated Tube," NAS TN D–765.
21. Hendricks, R.C., Graham, R.W., Hsu, Y.Y., and Friedman, R., 1966, "Experimental Heat Transfer Results for Cryogenic Hydrogen Flowing in Tubes at Subcritical and Supercritical Pressure to 800 pounds per Square Inch Absolute," NASA TN D–3095.
22. Ellerbrock, H.H., Livingood, J.N.B., and Straight, D.M., 1962, "Fluid-Flow and Heat-Transfer Problems in Nuclear Rockets," NASA SP–20.
23. von Glahn, U.H., 1964, "A Correlation of Film-Boiling Heat Transfer Coefficients Obtained with Hydrogen," Nitrogen and Freon 113 in Forced Flow, NASA TN D–2294.
24. Giarratano, P.J., Smith, R. V., 1965, "Comparative study of Forced Convection Boiling Heat Transfer Correlations for Cryogenic Fluids," Advances in Cryogenic Engineering, **11**, pp. 492–505.
25. Chen, J.C., 1966, "Correlation for Boiling Heat Transfer to Saturated Fluids in Convective Flow," Industry Engineering Chemistry Process Design and Development, **5**, pp. 322–329.
26. Gungor, K.E., Winterton, R.H.S., 1996, "A General Correlation for Flow Boiling in Tubes and Annuli," International Journal of Heat Mass Transfer, **29**, No.3, pp. 351–358.
27. Bennett, D.L., and Chen, J.C., 1980, "Forced Convection for the in Vertical Tubes for Saturated Pure Components and Binary Mixture," A.I.Ch.E. Journal, **26**, pp. 454–461.
28. Stephan, K., and Auracher, H., 1981, "Correlation for Nucleate Boling Heat Transfer in Forced convection," International Journal of Heat Mass Transfer, **24**, pp.99–107.
29. Kutateladze, S.S., 1952, "Heat Transfer in Condensation and Boiling," Atomic Energy Commission Translation 3770, Tech. Info. Service, Oak Ridge, Tennessee.
30. Steiner, D., May 1986, "Heat Transfer During Flow Boiling of Cryogenic Fluids in Vertical and Horizontal Tubes," Cryogenics, **26**, pp. 309–318.
31. Incropera, F.P., Dewitt, D.P., 2002, Fundamentals of Heat and Mass Transfer, 5th edition, John Willey& Sons.
32. Thompson, T.S., 1972, "An Analysis of the Wet-Side Heat-Transfer Coefficient during Rewetting of a Hot Dry Patch," Nuclear Engineering and Design, **22**, pp. 212–224.
33. Ferderking, T.H.K., and Clark, J.A., 1963, "Nature Convection Film Boling on A Sphere," Advanced Cryogenic Engineering, **8**, pp. 501–506.
34. Carey, V.P., 1992, Liquid-Vapor Phase-Change Phenomena, Taylor & Francis Press.
35. Raithby, G.D., and Hollands, K.G.T., 1975, "A General Method of Obtaining Approximate Solutions to Laminar and Turbulent Free Convection Problems," Advances in Heat Transfer, 11, pp.265–315 Academic Press, New York.

Project Title: Composite Pressure Vessels
Micromechanics, Fracture Mechanics and Gas Permeability of Composite Laminates for Cryogenic Storage Systems

Task PI: Bhavani Sankar, Department of Mechanical and Aerospace Engineering
Co-I: Peter Ifju, Department of Mechanical and Aerospace Engineering
Graduate Student: Sukjoo Choi

Project Goals

Honeycomb sandwich panels find a wide range of structural applications due to their high strength and stiffness-to-weight ratio compared to other material systems. Structural honeycombs are composed of two thin, stiff, strong sheets serving as the primary load carrying elements and a thick layer of low-density cellular material, providing shear resistance and stiffness. Current use of honeycomb material ranges from secondary structure in commercial aircraft to primary structure in military aircraft, helicopters, and even space shuttles. New challenges to damage tolerance emerge as more frequent use of this material tales place in advanced aerospace applications.

As the cost of space operations increase, new designs for reusable launch vehicles have come to be light as a necessary solution for future space missions. In this research, interfacial mixed-mode fracture of the face-sheet and the core is evaluated both experimentally and analytically in environments similar to those encountered in cryo-tanks used in reusable launch vehicles. Interfacial fracture toughness tests are performed at near liquid nitrogen temperature as well as room temperature to determine temperature effects on the critical strain energy release rate of the sandwich system. The tests will be modeled analytically using ABAQUS (ABAQUS, Inc.) finite element software to check agreement between analytical and experimental results, and develop a predictive capability for future RLV designs. In addition to studying the interfacial fracture behavior of sandwich composites, it is necessary to understand the micro cracking of face sheets that may cause hydrogen leakage.

The micro cracking behavior of the liquid hydrogen composite tank at cryogenic temperature has been investigated using the micromechanics methods. The micro cracks on composite laminates cause the leakage of liquid hydrogen because thermal stress in the composite laminates increases due to the difference of the coefficients of thermal expansion (CTE) between fiber and matrix at cryogenic temperatures. The micro cracks normal to the interface between composite laminates are propagated repeatedly without rupturing the fiber. The interfacial failure between orthotropic materials due to micro cracking is investigated. The stress singularity near the micro crack perpendicular to an interface between two dissimilar orthotropic materials can be obtained using the Stroh's method. The finite element analysis was performed to verify the analytical result under identical boundary condition. In the experimental approach, the four-point bending test is conducted with carbon composite laminate.

The singularity result from the analytical approach can be integrated into the experimental approach to predict the interfacial fracture behavior near crack-tip. Furthermore, the relationship between crack density and strain energy release rate can be obtained using the finite element method. The results will be used to suggest efficient and safe designs for composite hydrogen storage systems. Analysis of a hydrogen storage system under more realistic loading conditions, modeling progressive damage, and permeability modeling will be conducted in the future.

Accomplishments

Abstract

An experimental program was conducted to investigate the effect of cryogenic cycling on the permeability for various composite material systems. A permeability test apparatus was fabricated based

on volume of gaseous Helium displaced. Laminated composites with various configurations and textile composite specimens were used. The permeability test was conducted at room temperature. However the specimens were cryo-cycled by cooling them to liquid nitrogen temperature and then bringing them back to room temperature. It is found that the permeability increases rapidly with the number of cryo-cycles but attains a constant vale after about 5 cycles. Grouping of similar plies was found to be detrimental compared to dispersing the plies. Textile composites have lower permeability than laminated tape composites even with increasing number of cryogenic cycle. Nano-particles dispersed in laminated composites did not show improvement in permeability. Optical microscopic inspection revealed the types of micro cracks and delamination formed in different specimens and provided some insight on the variation of permeability in different systems.

Introduction

Composite materials offer many advantages, such as lightweight, high specific stiffness and specific strength, and low coefficient of thermal expansion. The next generation of space vehicles is supposed to provide a 10-fold reduction in the cost of launching payloads into space, from $10,000 to $1,000 per pound. Reducing the structure weight of the vehicle is of paramount importance in reducing the launch cost. Composite materials such as graphite/epoxy offer many advantages such as low density, high specific stiffness and specific strength, and low coefficient of thermal expansion. Therefore, fiber reinforced composite materials are candidate materials for cryogenic storage systems e.g., the liquid hydrogen (LH2) tank. However, laminated fiber composites are susceptible to micro cracking at extremely low temperatures. Then, the microcracks, which usually develop in the transverse plies, could become delaminations. The delaminations connect the microcracks in adjacent layers and provide a leakage path for the cryogen. This probably led to the catastrophic failure of the sandwich structure (ref. 1). This failure motivates the present study on micromechanics analysis methods to predict microcracks in laminated composites.

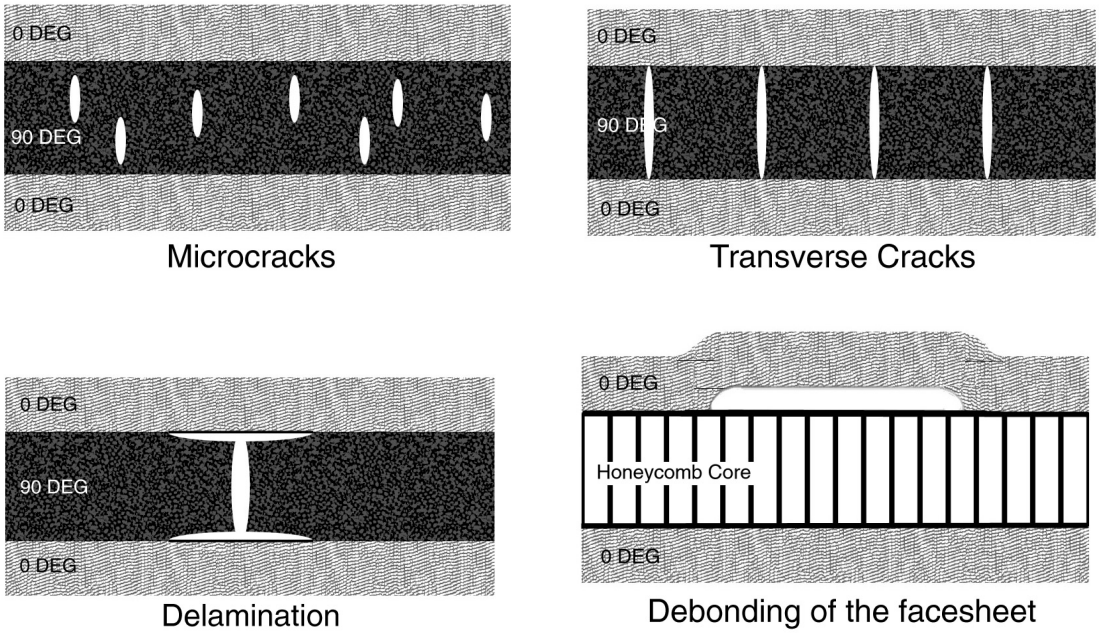

Figure 1.—Damage progression at cryogenic conditions.

The damage progression of laminated composites at cryogenic temperatures is illustrated in figure 1. At cryogenic temperatures, the microcracks initiate and propagate in laminated composites due to difference in thermal contraction between the fiber and matrix phases. When microcracks in the polymer matrix develop and reach the adjacent layers, the transverse cracks initiate. When the transverse crack develops further, the crack deflects through the interface between layers and delamination initiates. In the case of composite sandwich construction, debonding of the facesheet develops.

In a previous study we investigated possible causes of failure in laminated composites at cryogenic conditions (ref. 2). First, a micromechanics method was developed to predict the thermal stresses at microscale in fiber-reinforced composites at cryogenic conditions. Second, fracture toughness of a transverse crack in composite laminates was evaluated to investigate the effect of cryogenic conditions on transverse crack propagation. Third, the permeability of various composite materials was evaluated to investigate the effect of cryogenic cycling on permeability. This report details the permeability tests and the results obtained thereof. Results from micromechanics and fracture mechanics studies are not included in this report and they can be found in (ref. 2). Summaries of those studies are given below for the sake of completion.

Micromechanics Analysis of Laminated Composites at Cryogenic Conditions

From a macroscopic perspective, the composite material is considered to be homogeneous and transversely isotropic, or orthotropic in general. For example, the laminated plate theory has been formulated based on this assumption. Even when 3–D analyses are used for composite structures, each ply or layer of the composite is modeled as a homogeneous orthotropic material. This macroscopic approximation has been found to be satisfactory in most analyses including thermal stress analyses. Thus most of the thermal stress problems in composites focus on the differences in thermal expansion coefficients between the plies. However, in extreme situations a micromechanics approach wherein the fiber and matrix phases are differentiated is necessary for accurate prediction of stresses, and hence failure. The present problem falls in this category. In order to predict the failure of a composite structure at the macroscopic scale, investigation of micromechanical behavior and understanding the failure mechanisms in the fibers and matrix at a micro-scale are necessary (ref. 3).

To make effective use of fiber-reinforced composites, we need a methodology to predict the thermo-mechanical properties at various temperatures as a function of fiber, matrix and interphase properties. These properties will be a strong function of temperature. Micromechanics is the study of such macroscopic properties from that of the constituent materials. In this study, micro-cracking behavior of the liquid hydrogen composite tank at cryogenic temperature is investigated using the micromechanics method. Failure of the composite tank under thermal and mechanical loads is evaluated by utilizing the commercial finite element software ABAQUS®. Also, the analysis is useful in developing new composite material systems for the liquid hydrogen composite tank by changing the combination of constituent properties.

In the present study the micromechanics method is combined with a global laminate analysis to predict the stresses in the fiber and matrix phases accurately. The method is useful to predict development of micro-cracks in a composite laminate at cryogenic temperatures. In order to predict the development of microcracks in fiber composites, one needs accurate description of the stresses in the matrix phase and also along the fiber-matrix interface. The problem of thermal stresses is complicated by the temperature dependent properties of the constituent materials. In the present study a global/local approach is used wherein traditional structural analysis is used to obtain information on macro-strains in a ply in the composite laminate. Then the macro-strains along with the local temperature are used in a micromechanical analysis to obtain detailed information on the stresses in the constituent phases. Two types of representative volume elements (RVE) are used in the micromechanical analyses. In the first one the RVE is a square with a circular fiber at the center of the square. In the second a hexagonal RVE is used. The differences in thermal stresses in the two RVE's are discussed. The temperature dependent properties of the matrix material are taken into account in the micromechanics. However, the fiber

properties are assumed to be independent of temperature. The microstresses in different types of laminates used in a typical liquid hydrogen tank are studied and the possibility of micro-cracking is discussed. The results indicate that the maximum tensile stresses in the brittle matrix reach values very close to the tensile strength of the matrix material, raising the possibility of micro-crack development in composite liquid hydrogen storage systems. Details of the micromechanics analysis and the results can be found in reference 2.

Fracture Toughness of a Transverse Crack at Cryogenic Conditions

Microcracks develop in the face sheets of the sandwich structure due to the thermal cycling. The microcracks, which usually develop in the transverse plies, can propagate to an adjacent layer and become transverse cracks as shown in figure 2. When the transverse crack deflects to the ply-interface, it becomes a delamination. The delaminations connect the microcracks in adjacent layers and provide a leakage path for the cryogen. For the liquid hydrogen composite tank, this hydrogen leakage through the interface sheet causes the catastrophic failure of the sandwich structure (ref. 1).

When a microcrack propagates in a given material, the stress distribution normal to the crack plane can be described by the equation in figure 3. Normal stresses at a crack-tip are governed by the stress singularity λ and stress intensity factor K_I. Zak and Williams (ref. 4) found the normal stresses ahead of a crack-tip are proportional to $r^{-\lambda}$ $(0 < \mathrm{Re}\,[\lambda] < 1)$ where r is the distance from the crack-tip. The stresses normal to the crack ahead of a crack-tip can be expressed as $\sigma = K_I \cdot r^{-\lambda}$. The stress singularity of a micro-crack in laminated composites is governed by anisotropic properties at the vicinity of a crack-tip.

The stress singularity describes the behavior of crack propagation. The Material 1 and the Material 2 are composite layers with specific fiber orientations. When a transverse crack reaches a ply-interface of composite layers with identical fiber orientation, stress singularity is equal to ½, which is conventional singularity for homogeneous materials. When a transverse crack propagates from the Material 1, which is stiffer than the Material 2, the transverse crack penetrates the ply-interface and continues to propagate through the Material 2 until the crack reaches a stiffer layer (ref. 5). In this case, the stress singularity becomes larger than ½. When the Material 1 is softer then the Material 2, the transverse crack deflects to the ply-interface and becomes delamination. The stress singularity becomes lower than ½. In this study, conditions under which a transverse crack becomes a delamination are studied, and the fracture toughness of the transverse crack is quantified and measured.

Williams (ref. 6) estimated the singularity for isotropic bi-material systems by solving a set of eigenfunctions developed by the continuity equations of normal and tangential stresses and displacements at the ply-interface. Ting and Chou (ref. 7) have developed methods to predict singularity at the free edge of a ply-interface of laminated composites. In this study, stress singularity of a transverse crack in a laminated composite is calculated using Ting's methods (refs. 7 and 8), and finite element analysis is used to compute the crack tip stress fields in various laminated composite models.

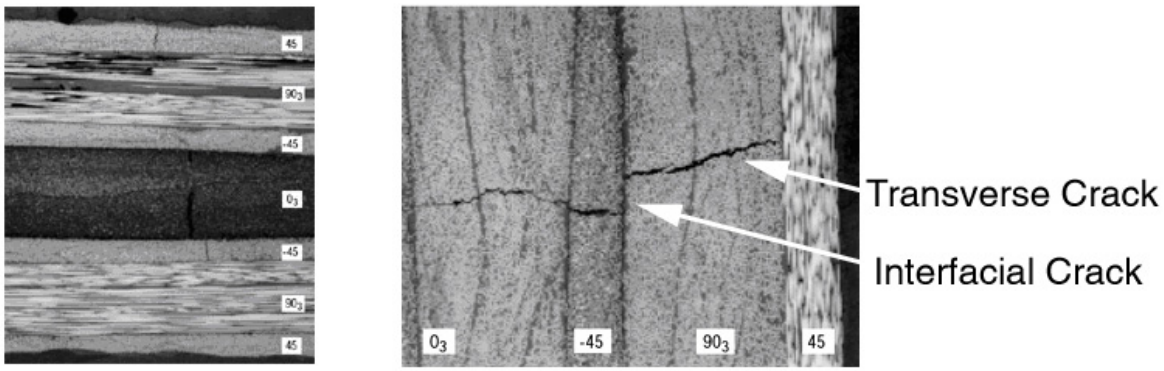

Figure 2.—SEM images of micro-crack propagation in composite laminates after thermo mechanical cycles.

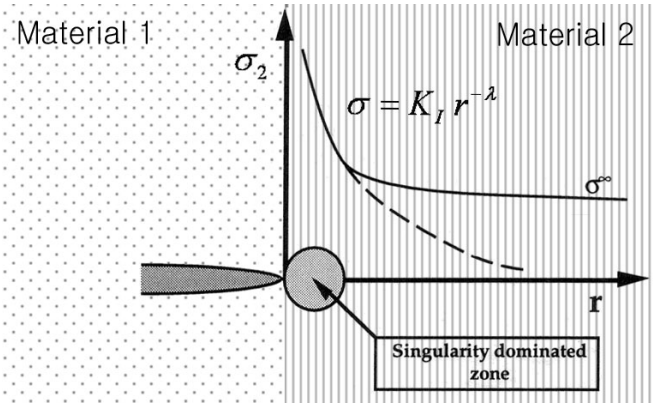

Figure 3.—Variation of stresses acting normal to a crack tip, when the crack reaches a bi-material interface.

The purpose of the study was to develop the finite element model, which provides a confidence in capturing the stress singularity, and evaluate fracture toughness of a transverse crack in laminated composites at room and cryogenic temperatures. This study was useful to investigate the cryogenic effects on fracture toughness for composite laminates. The results of the fracture study can be found in reference 2.

Permeability of Graphite Fiber Composite Materials at Cryogenic Conditions

A fundamental issue in using composite materials for cryogenic tanks is hydrogen permeability; particularly since the failure of the liquid hydrogen composite tank could be caused by hydrogen leakage. Micro-cracking can also occur due to thermal and structural loads and fatigue. The liquid hydrogen storage composite tank is required to sustain large thermal and structural loads, and additionally must be able to endure several cycles of thermal loading without hydrogen permeation. The purpose of the study is to present the experimental work to measure the gas permeability of various types of composite systems.

The permeability testing on IM7/BMI laminated composites under bi-axial strains was performed by Stokes (ref. 9) following the ASTM Standard D-1434 (ref. 10). The permeability was calculated by measuring the pressure difference across the specimen as a function of time. The permeability was measured as the strain was increased at room temperature. The permeability increase was steady until the specimen failed. Stokes found that the permeability is a time dependent parameter under constant strain condition. The crack densities for each layer were measured using microscopic optical inspection. The advantage of this test approach is that it minimizes the error due to the ambient pressure differences during the test. However, a precision pressure transducer is required to measure the accurate pressure difference across the specimen accurately.

The gas leakage through laminated composite was investigated by Kumazawa, et al. (ref. 11) using experimental and finite element analysis. A finite element model with initial crack path was subjected to mechanical and thermal loads. The leakage rate decreased as temperatures decreased under constant crack density assumptions. The FE results were compared with experimental results. Helium detector was used to measure the permeability of a laminated composite under biaxial loading.

The permeability test of hybrid composites and related films was performed by Grimsley et al. (ref. 12) following the ASTM Standard D-1434. The volume-flow rate was estimated by measuring the rate of moving distance of a liquid indicator in a glass capillary tube. The gas transmission rate is converted to volume-flow rate using the ideal gas law. The permeance is calculated by the gas transmission rate per upstream pressure. The permeability results for various types of hybrid composites

and films were provided. Also, Herring (ref. 13) investigated the permeability of thin film polymers after pre-conditioning samples. The permeability is calculated according to ASTM D-1434.

The volumetric method to calculate the permeability is verified by Nettles (ref. 14). The purpose of this study was to investigate the permeability of laminated composites after experiencing impact loads. Moreover, the study investigated the possible cases of testing condition, which influence the permeability results. When the glass capillary tube is mounted vertically or horizontally, the variation in permeability results is insignificant. The permeability tests were performed using various types of liquid indicators in a capillary tube. The variation of permeability results was found to be insignificant. Also, the length of liquid indicator does not affect the permeability results. However, the glass capillary tube with inner diameter 0.4 mm underestimated permeability than the capillary tubes with 1.2 and 3 mm diameters.

The permeability test on laminated composites and bonding materials were performed by Nettles (ref. 15). The permeability results before and after cryogenic cycles were compared. Glass et al. (ref. 16) investigated the permeability for core materials of a composite sandwich when it is subjected to shear loads. The Hexcel (Hexcel Corp.) HRP honeycomb and the Dupont Korex (The Korex Companies) honeycomb were chosen for core materials. The composite sandwich specimens were fabricated and air inlet holes were drilled through one of the face sheets. The permeability is calculated by measuring the flow rate of upstream air.

In this study, the permeability was estimated for various composite material systems after the composite laminates underwent cryogenic cycling. An optical microscope was used to understand the nature of microcrack propagation after cryogenic cycling. The permeability increased rapidly and became constant as the number of cryogenic cycles increased. The permeability is proportional to the crack density since increasing number of cracks produces a larger flow path though the thickness of the material. The optical inspection on composite specimens was performed to investigate the behavior of microcrack propagation after cryogenic cycling. The optical results were compared before and after cryogenic cycling on various composite specimens.

Permeability Testing of Composite Materials for a Liquid Hydrogen Storage System

The permeability is defined by the amount of gas that passes through a given material of unit area and unit thickness under a unit pressure gradient in unit time. The SI unit of the permeability is mol/sec/m/Pa. Experiments were performed to investigate the effect of cryogenic cycling on permeability of laminated composites and to provide useful comparison of permeabilities of various composite material systems.

Standard Test Method for Determining Gas Permeability

The standard test method for determining gas permeability is documented in ASTM D1434-82 (Re-approved in 1997) “Standard Test Method for Determining Gas Permeability Characteristic of Plastic Film and Sheeting” (ref. 10). The permeability can be measured by two methods, manometric determination method and volumetric determination method. The permeability experiment using the monometric determination method is shown in figure 4. The lower pressure chamber is initially vacuumed and the transmission of the gas through the test specimen is indicated by an increase in pressure.

The permeability is measured using volumetric determination as shown in figure 5. The lower pressure chamber is exposed to atmospheric pressure and the transmission of the gas through the test specimen is indicated by a change in volume. The gas volume-flow rate is measured by recording the rise of liquid indicator in a capillary tube per unit time. The gas transmission rate (GTR) is calculated using the ideal gas law. The permeance is determined as the gas transmission rate per pressure differential across a specimen. The permeability is determined by multiplying permeance by the specimen thickness.

The monometric determination method was not considered for this study since it is dangerous to handle the mercury compound, which is considered as a health hazardous material. Therefore, the permeability facility was constructed based on the volumetric determination method as shown in figure 5.

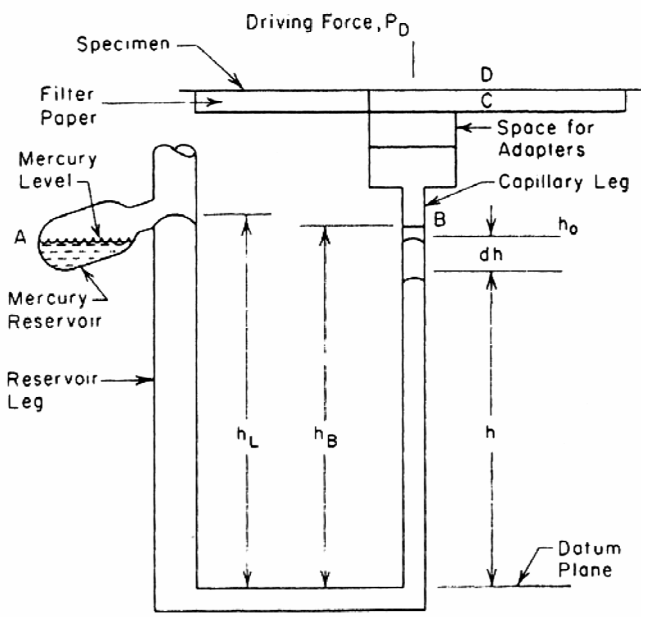

Figure 4.—Permeability experimental setup for manometric determination method.

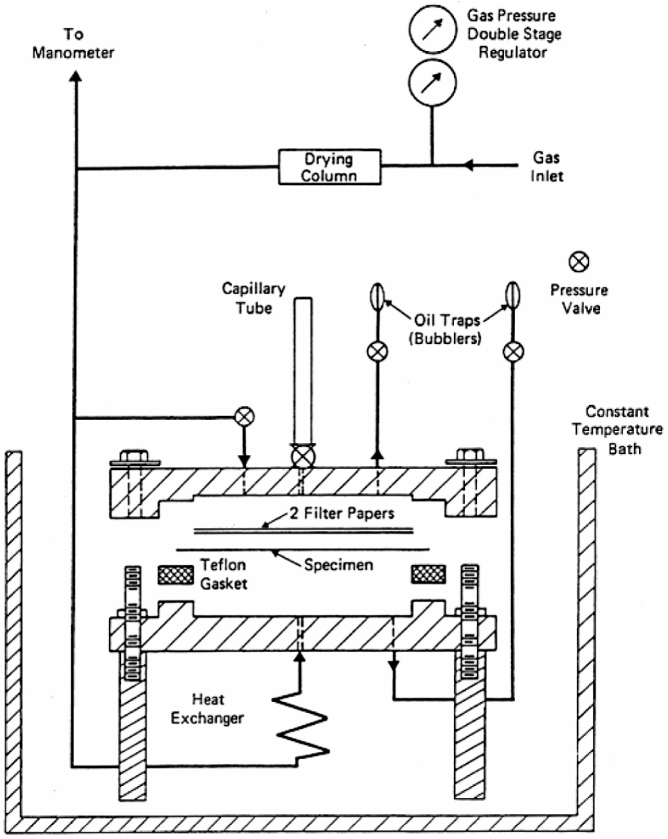

Figure 5.—Permeability experimental setup for volumetric determination method

Permeability Apparatus

This apparatus basically consists of a specimen placed between two chambers as shown in figure 6. The test gas is pressurized in the upstream chamber. The gas permeates through one side of the specimen and escapes out of the other side. The escaped gas is collected in the downstream chamber and flows into a glass capillary tube. The amount of gas escaping per unit time is measured. The permeance is determined by gas transmitted rate and the partial pressure differential across the specimen. The permeability $\overline{P}$ is defined by the product of permeance P and the specimen thickness t.

The gauge pressure of the gas in the upper upstream chamber is measured using a pressure transducer (P-303A from the Omega Engineering Inc). The ambient pressure is measured by a barometric sensor (2113A from the Pasco Scientific). A precision pressure regulator provides constant gas pressure to the upstream chamber. The ambient temperature was measured using a glass capillary thermometer.

The specimens are mounted horizontally between the upstream and downstream chambers and clamped firmly by applying a compressive load as shown in figure 7. The specimen is sealed with a rubber gasket and an O-Ring (38 mm i.d.). A force gauge mounted at the top measures the compressive load to ensure that the same amount of compressive load is applied on the specimens for every test. The compressive load should be enough to prevent gas leakage, but should not damage the specimens. The upstream chamber has an inlet vent and an outlet vent. The inlet vent allows the gas flow into the upstream chamber and the outlet vents is used to purge the test gas to atmosphere (fig. 7). The downstream chamber has two outlet vents. One is used to purge the test gas to atmosphere and the other allows the gas flow to the glass capillary tube for measurements. The sensitivity of permeability measurement can be improved by increasing the gas transmitting area of a specimen.

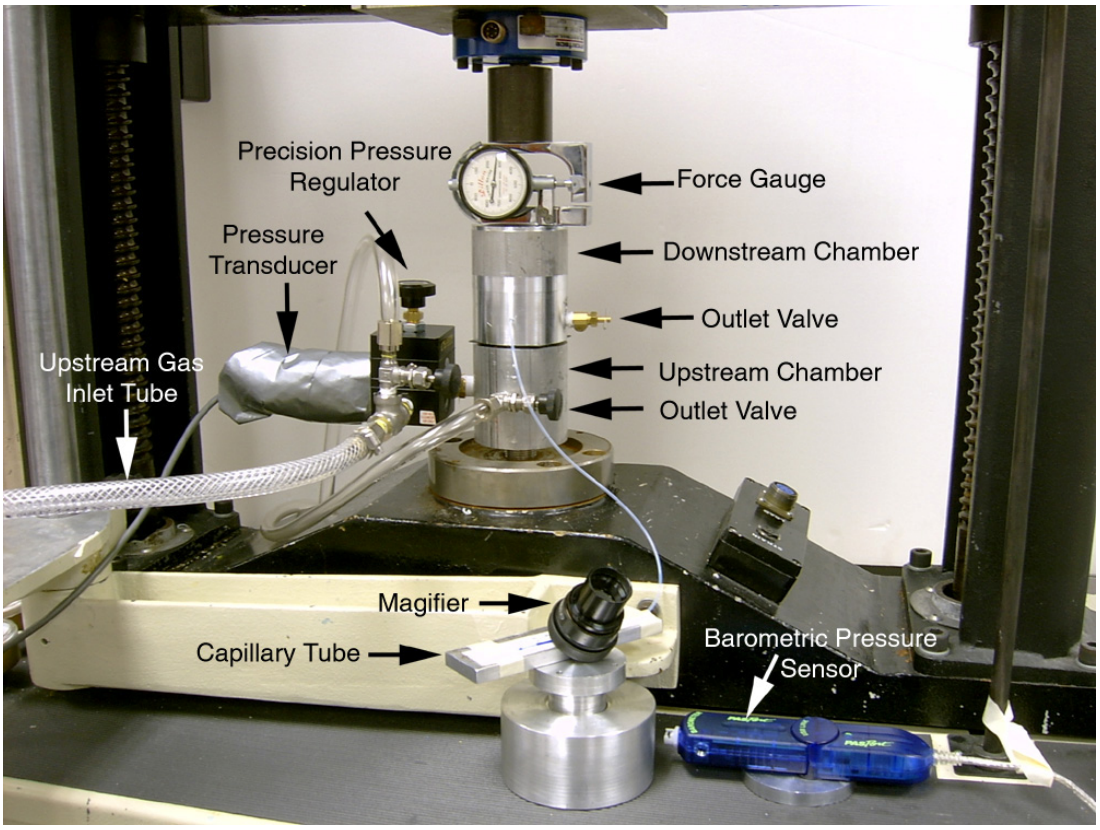

Figure 6.—Permeability testing apparatus

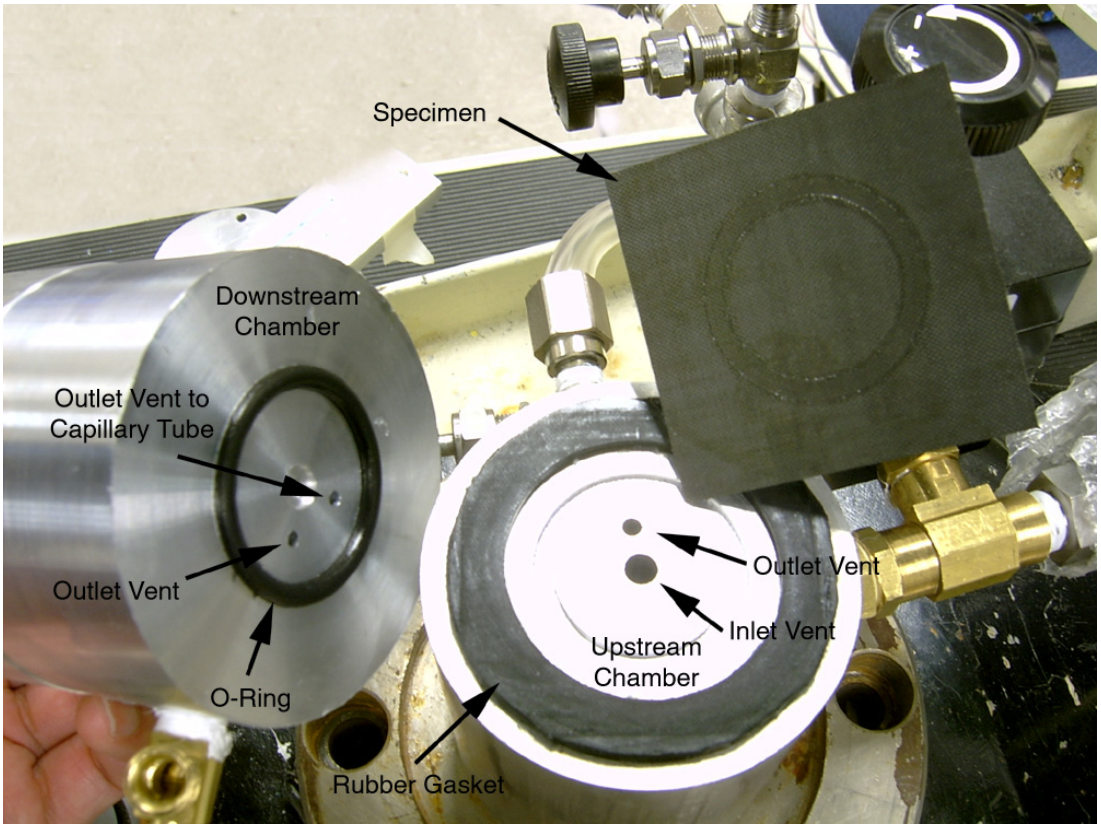

Figure 7.—Specimen installation between upstream and downstream chambers.

The glass capillary tube is mounted on a rigid aluminum base horizontally to minimize the gravity effect on the capillary indicator and for easy reading of the scale marks on the capillary tube. Nettles (ref. 14) found that there was no significant difference in the volumetric flow rate when capillary tube is placed vertically or slanted. The inner diameter of the glass capillary tube is 1.05 mm and the length is 100 mm. A magnifying glass is used to read the scale marks at the top of the meniscus of the liquid indicator.

The liquid indicator in the glass capillary tube is used to measure the rate of rise of the liquid indicator. The rate is used to calculate the volume flow rate of the escaped gas across the specimen. Nettles (ref. 14) investigated the effects on the volume flow rates by using various types of liquid. The volume flow rates obtained using water, alcohol and alcohol with PhotoFlo® were not significantly different. In the present study, methyl alcohol is chosen as the liquid indicator since alcohol has low viscosity and weight. The methyl alcohol is colored with a blue dye to obtain precise readings on the scale marks.

The primary investigation is the hydrogen permeability of a liquid hydrogen composite storage system. Since hydrogen gas is highly flammable and explosive when it mixed with air, it needed to be handled carefully during the test. Hence, other permeate gases were considered as a substitute for the hydrogen gas. The molecular diameter of various gases is listed in table 1 (ref. 17). To choose a permeate gas, the molecular diameter determined from viscosity measurement is mainly considered since the permeability is related with the volumetric flow rate directly. Since helium has the smallest molecular diameter, the helium predicts higher values compared to other gases (ref. 17). Therefore, in the study, helium was chosen as the permeate gas instead of hydrogen.

TABLE 1.—MOLECULAR DIAMETER OF VARIOUS GASES
(CRC HANDBOOK OF CHEMISTRY AND PHYSICS, 54TH EDITION)

Type of gas	Molecular diameter (cm)		
	From viscosity	From van der Waal's equation	From heat conductivity
Helium	1.9×10^{-8}	2.6×10^{-8}	2.3×10^{-8}
Hydrogen	2.4×10^{-8}	2.3×10^{-8}	2.3×10^{-8}
Nitrogen	3.1×10^{-8}	3.1×10^{-8}	3.5×10^{-8}

Specimen Description

The permeability tests were performed with various composite material systems. The details of specimens are described in table 2. The specimens C1, C2 and C3 are various graphite/epoxy laminated composites. The specimen T1 is a textile composite. The specimen N1 is a laminated composite embedded with 36 μm aluminum oxide (Al_2O_3-alumina) nano-particles. The aluminum oxide was dissolved in alcohol and the compound was applied on a surface on a laminated prepreg using a paint blush. The nano-particles are capable of relieving the thermal stresses due to contraction of fiber and matrix phases. Also, it can prevent the crack propagation in matrix phase by relieving the stress concentration at the crack-tip.

The graphite/epoxy prepregs were fabricated with designed stacking orientations. The graphite/epoxy prepregs were cured in an autoclave and machined by a diamond saw to 3×3-in. specimens at low speed to avoid fiber shattering. The surface is cleaned with acetone and prepared carefully to avoid contamination or damages on the surface of the specimen during machining and subsequent handling.

TABLE 2.—DESCRIPTION OF COMPOSITE SPECIMENS

Specimen	Prepreg type	Stacking sequence	Thickness (mm)
C1	Graphite/epoxy laminates	$[0/90/0/90/0/90]_S$	1.52
C2	Graphite/epoxy laminates	$[0_2/90_2/0_2]_T$	0.787
C3	Graphite/epoxy laminates	$[0/90/0_2/90/0]_T$	0.914
C5	Graphite/epoxy laminates	$[0/90_2/0]_T$	0.533
T1	Plain weave textile(SP Systems SE-84)	4 layers	0.686
N1	Graphite/epoxy laminates with nano-particles	$[0/90/NP/90/0]_T$	0.483

The specimens were subjected to cryogenic cycling at specified number of times, representing multiple refueling process of a space vehicle. A single cryogenic cycle consisted of cooling down from room temperature to cryogenic temperature and then warming up to room temperature. Initially, specimens were placed at room temperature (T = 300 K). And, then the specimens completely submerged in an insulated container filled with liquid nitrogen. The specimens stayed in the container for approximately 2 min. When the specimen reached the boiling temperature of liquid nitrogen (T = 77 K), the liquid nitrogen boiling disappears. The specimens were taken out of the container and placed at room temperature. The specimen was held at room temperature for approximately 5 min. The cryogenic cycling procedure is repeated for desired number of times.

Testing Procedure

Before starting the permeability test, a thin coat of silicon grease was applied on the gasket and an O-ring was placed to improve sealing of contact surfaces on a specimen. The excessive silicon grease was wiped out to avoid obstructions of permeated gas on the transmitting surface of the specimen. All outlet valves were opened initially to avoid sudden pressurization of test gas. The specimen was placed horizontally on the gasket of the upstream chamber. And then, the downstream chamber was placed on the top surface of a specimen. The specimen was mounted between the chambers. Both chambers were aligned and mated as close as possible. The specimen was mounted between the chambers and clamped

firmly with a compressive force. Then, even distributed forces were applied to the sealing materials of the chambers.

The test gas was admitted to the upstream chamber by opening the gas release valve of the gas tank. While all outlet valves remained opened, the test gas was filled in the upstream chamber and ventilated though the outlet vent to atmosphere. Any residual air in the upstream chamber was purged for 1 minute. The outlet valve on the upstream chamber was closed and the test gas was allowed to permeate across the specimen for a sufficient time to purge any residual air at downstream chamber. At this time, only test gas filled the chambers. When the outlet valve of the upstream chamber was closed, the upstream pressure increased slowly. The upstream pressure can be adjusted by controlling the pressure regulator. Sufficient time was allowed for attaining steady state of moving rate of the liquid indicator before beginning to take readings. The distance of rise of the liquid indicator was measured while the ambient pressures were recorded.

Calculations

The volumetric methodology is used to calculate the permeability by measuring gas volume transmitted through a specimen. The rate of rise of the liquid indicator is measured using the capillary tube. The volume flow rate is calculated as follows.

$$V_r = slope \times a_c \tag{1}$$

where a_c is the cross-sectional area of a capillary tube. The slope is the rate of rise of the liquid indicator in the capillary tube. The gas transmission rate (GTR) is calculated using the ideal gas law as follows.

$$GTR = \frac{p_o \cdot V_r}{ART} \tag{2}$$

where p_o is ambient pressure, A is transmitting area of a specimen, R is the universal gas constant (8.3143×10^3 L·Pa/{mol·K}) and T is ambient temperature. The permeance P is defined by the ratio between the gas transmission rate and pressure differential across the thickness of a specimen. Therefore, the permeance P is calculated as follows.

$$P = \frac{GTR}{p - p_o} \tag{3}$$

where p is the upstream pressure. The S.I. unit of permeance is [mol/(m^2·s·Pa)]

According to the standard test method, the permeability $\overline{P}$ is defined by the product of permeance P and the specimen thickness t and "the permeability is meaningful only for homogeneous materials. In this study, although the laminated composites are considered as orthotropic materials, its permeability $\overline{P}$ is calculated by following the corresponding definition for isotropic materials.

Calibration

The position of capillary indicator is very sensitive to even small variations of testing conditions such as ambient pressure and temperatures caused by closing doors or air-conditioning system in the laboratory. For example, during one test, the variation of the ambient pressure was approximately 0.3 percent for a 13-hr period (fig. 8). For the permeability calculation, the ambient pressure is assumed to be constant. However, the variation is large enough to cause error in measuring the rate of rise of the capillary indicator. The moving distance needs to be calibrated to compensate for error due to the variation of ambient pressure.

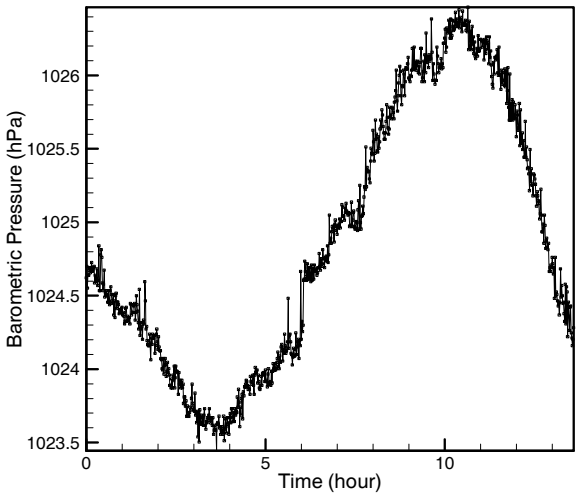

Figure 8.—Variation of ambient pressure for 13 hr at test condition.

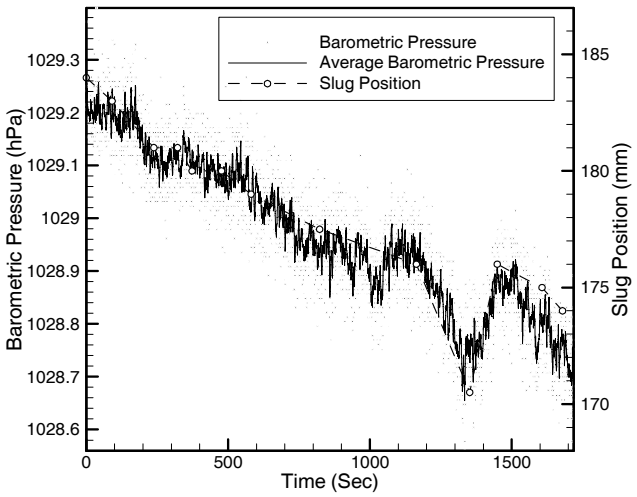

Figure 9.—Variation of barometric pressure and indicator position as a function of time.

The error correction factor due to the variation of ambient pressure was calculated by performing the permeability test without applying the upstream pressure. An aluminum plate is used for the test to ensure that there is no gas permeation to the downstream chamber. Since there was not much variation in the ambient temperature, only ambient pressure causes changes in the position of the capillary indicator. After the outlet valve of the downstream chamber was closed, the displaced position of the capillary indicator and ambient pressure were measured simultaneously as shown in figure 9.

The correction factor k is calculated by $k = \Delta h / \Delta p$ where h is the moving distance of the capillary indicator and p is the ambient pressure. The average correction factor is found to be 0.21 mm/Pa. Therefore, the corrected moving distance of the capillary indicator is calculated as follows:

$$h_{corrected} = h_{actual} + k \cdot \Delta p$$

where Δp is differential of ambient pressure between the beginning and end of the test.

Permeability Test Results

The permeability tests were performed with various composite material systems at room temperature. The permeability was measured at six different levels of upstream pressure. The average permeance P and average permeability $\overline{P}$ are tabulated in table 3 for laminated composites, the results for textile composites are in table 4 and the results for laminated composites with embedded with nano-particles in table 5.

TABLE 3.—PERMEABILITY OF LAMINATED COMPOSITES FOR VARIOUS NUMBER OF CRYOGENIC CYCLES

Specimen	Cryogenic cycles	Permeance, P (mol/sec/m^2/Pa)	Permeability, $\overline{P}$ (mol/sec/m/Pa)	Logarithm of $\overline{P}$
C1	0	5.60×10^{-18}	8.54×10^{-21}	−20.1
	1	1.52×10^{-17}	2.32×10^{-20}	−19.6
	5	2.39×10^{-17}	3.65×10^{-20}	−19.4
	10	2.39×10^{-17}	3.65×10^{-20}	−19.4
	20	2.11×10^{-17}	3.22×10^{-20}	−19.5
C2	0	7.02×10^{-18}	1.07×10^{-20}	−20.0
	1	1.06×10^{-17}	1.62×10^{-20}	−19.8
	5	1.47×10^{-15}	2.23×10^{-18}	−17.7
	10	1.42×10^{-15}	2.16×10^{-18}	−17.7
	20	1.49×10^{-15}	2.27×10^{-18}	−17.6
C3	0	6.22×10^{-18}	9.48×10^{-21}	−20.0
	1	7.56×10^{-18}	1.15×10^{-20}	−19.9
	5	7.60×10^{-18}	1.16×10^{-20}	−19.9
	10	8.37×10^{-18}	1.28×10^{-20}	−19.9
C5	0	5.85×10^{-18}	8.92×10^{-21}	−20.0
	1	9.52×10^{-16}	1.45×10^{-18}	−17.8
	5	8.67×10^{-16}	1.32×10^{-18}	−17.9
	20	8.81×10^{-16}	1.34×10^{-18}	−17.9

TABLE 4.—PERMEABILITY OF TEXTILE COMPOSITES FOR VARIOUS NUMBER OF CRYOGENIC CYCLES

Specimen	Cryogenic cycles	Permeance, P (mol/sec/m^2/Pa)	Permeability, $\overline{P}$ (mol/sec/m/Pa)	Logarithm of $\overline{P}$
T1	0	4.79×10^{-18}	7.30×10^{-21}	−20.1
	1	6.77×10^{-18}	1.03×10^{-20}	−20.0
	5	8.41×10^{-18}	1.28×10^{-20}	−19.9
	20	8.75×10^{-18}	1.33×10^{-20}	−19.9

TABLE 5.—PERMEABILITY OF LAMINATED COMPOSITES EMBEDDED WITH NANO-PARTICLES FOR VARIOUS NUMBER OF CRYOGENIC CYCLES

Specimen	Cryogenic cycles	Permeance, P (mol/sec/m^2/Pa)	Permeability, $\overline{P}$ (mol/sec/m/Pa)	Logarithm of $\overline{P}$
N1	0	6.82×10^{-18}	1.04×10^{-20}	−20.0
	1	2.72×10^{-15}	4.15×10^{-18}	−17.4
	5	1.30×10^{-14}	1.98×10^{-17}	−16.7
	20	9.83×10^{-15}	1.50×10^{-17}	−16.8

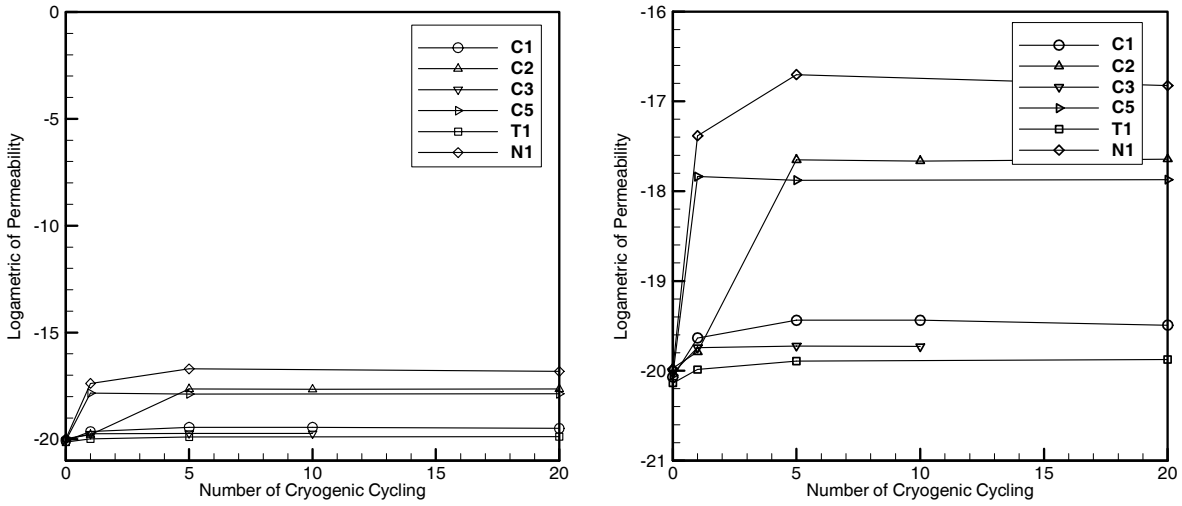

Figure 7.—Logarithm of the permeability for composite specimens with increase of cryogenic cycles.

The test results show the permeability increases as the number of cryogenic cycles increases (see fig. 7). The permeability increased rapidly and becomes constant with further increase of cryogenic cycles. For specimens C2 and C3, which have approximately same thickness, the permeability of the specimen C3 was lower since the specimen C3 has the plies dispersed and not grouped together compared to the specimen C2. The textile specimen T1 maintained constant permeability with the increase of cryogenic cycles. The textile composites resulted lower permeability than the laminated composites.

The specimen N1 has same layer stacking orientations with the specimen C5 and nano-particles were dispersed between two 90° layers. Before cryogenic cycling, the permeabilities of the specimens N1 and C5 were approximately the same. However, as the number of cryogenic cycles increased, the permeability of the specimen N1 became higher. The use of nano-particles did not improve the permeability of laminated composites.

Optical Microscopic Analysis

The optical microscopic inspection was performed to evaluate the microcrack propagation and void content of various composite systems after cryogenic cycling. In the previous section, the experimental results showed that the permeability increases as the composite specimen underwent more cryogenic cycles. As the crack density increases, gas flow becomes easier though the specimen. Therefore, the microcrack propagation is correlated with cryogenic cycling.

The specimens were cut through the center using a diamond saw. A LECO grinder/polisher was used for the sample preparation process. The rough edge through the center was ground with 600-grit sand paper with water for 30 sec. The fine grinding was performed with the 1000- and 1500-grit papers for 30 sec. The surface of the edge was polished with the 58 μm aluminum oxide powder (Al_2O_3-alumina) dissolved in distilled water. The purpose of the lubricant is to both dissipate the heat from polishing and to act as a carrier for the abrasive materials. The ultrasonic cleaner was used to remove any abrasive particles and contaminants on the polished surface of a specimen. The optical analysis was conducted with a Nikon EPIPOT (Nikon, Inc.) microscope.

The laminated composite specimen C2 and the textile composite specimen T1 were chosen for optical inspection. The specimen details are described in table 2. The microscopic images for the specimens were compared before and after cryogenic cycling.

For the graphite/epoxy specimen C2 before cryogenic cycling, no microcrack propagation observed (see fig. 8). Some voids formed in the middle of the 90° layers and between the 0° layer and the 90° layers. The voids probably formed during composite fabrication in autoclave. When the graphite/epoxy prepreg was cured at high temperature, some air bubbles could have been trapped between layers. It is possible that external pressure applied on the vacuum bag was insufficient to remove the bubbles.

After cryogenic cycling on the specimen C2, microcracks were observed in the 90° layer as shown in figure 9. The fiber breaks were not observed in the in 0° layer were not observed since the thermal stresses were not large enough. The delaminations propagated along the middle of the 90° layer where some voids were found. The transverse cracks branched with the delaminations. Since the gas can be transmitted through the transverse cracks across the specimen, the permeability increased after cryogenic cycling. For the textile composite specimen T1 before cryogenic cycling, no microcracks were observed as shown in figure 10. Voids were observed at the location where two yarns are merging.

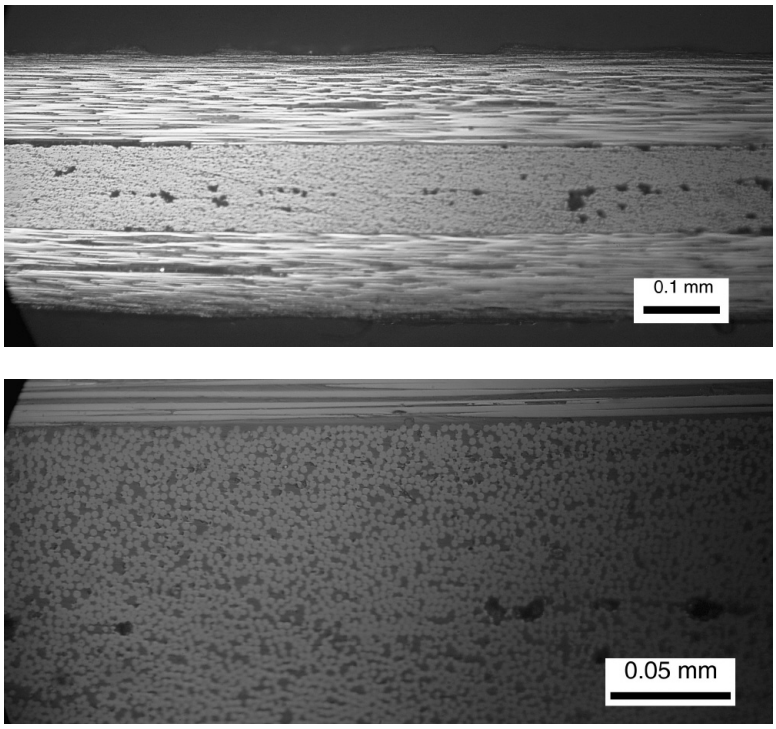

Figure 8.—Cross sectional view of the graphite/epoxy composite specimen C2 before cryogenic cycling: (a) 10X magnification; (b) 40X magnification

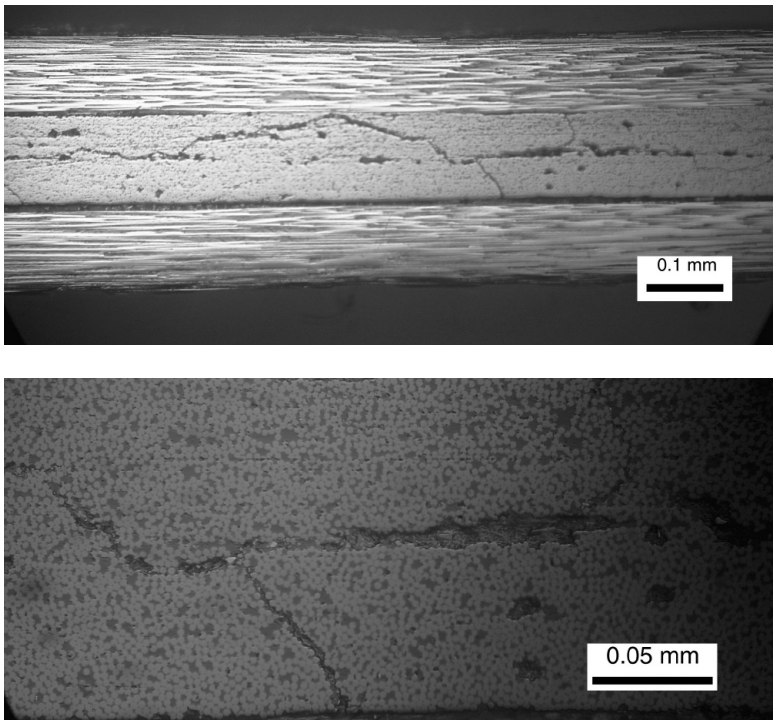

Figure 9.—Microcrack propagation on the graphite/epoxy composite specimen C2 after cryogenic cycling: (a) 10X magnification; (b) 40X magnification.

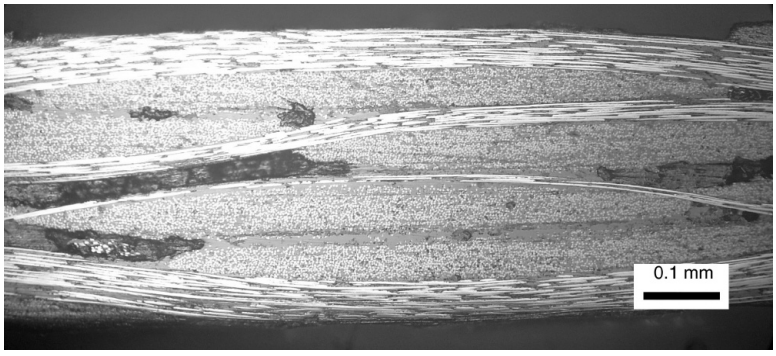

Figure 10.—Cross sectional view of the textile specimen T1 before cryogenic cycling, 10X magnification.

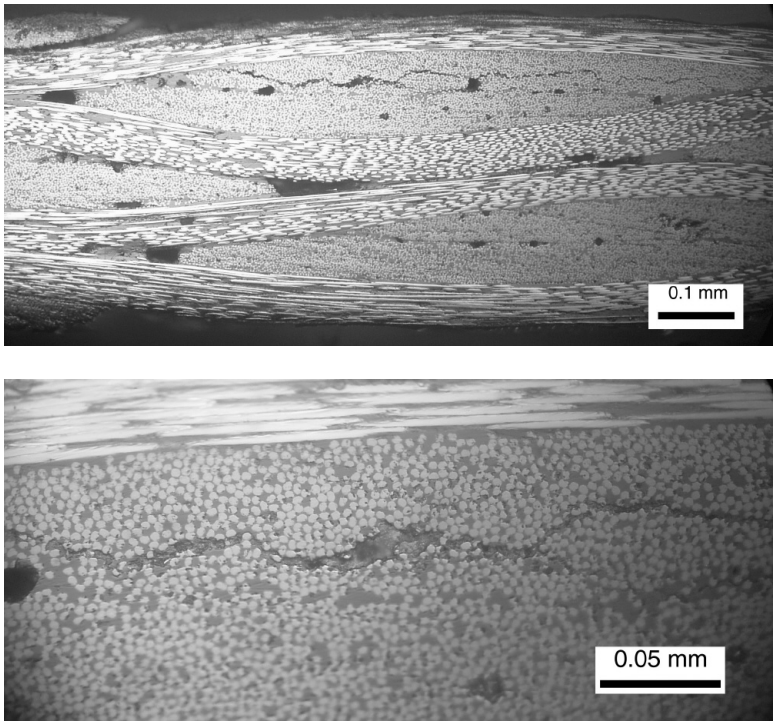

Figure 11.—Microcrack propagation in the textile specimen T1 after cryogenic cycling: (a) 10X magnification; (b) 40X magnification.

After the textile specimen T1 underwent cryogenic cycles, microcrack were observed in 90° yarn as shown in figure 11. The microcracks propagated in the in-plane direction of the specimen. Since transverse cracks were not propagated, the permeability of textile composites was almost the same before and after cryogenic cycling. For the laminated composite specimen, the microscopic results showed that transverse crack propagation and delaminations of composite laminates provide an easier path for gas permation. For the textile composite specimen, the transverse cracks propagation was not observed, which resulted in low permeability of textile composites even after cryogenic cycling.

Results and Discussion

A test program was conducted to measure the gas permeability of various composite material systems for the liquid hydrogen composite tank and the effect of cryogenic cycling of composite laminates on the permeability was investigated. The permeability test facility was constructed following the standard test method documented in ASTM D1434-82 (Re-approved 1997). The permeability test was conducted at room temperature. The sensitivity of permeability measurement can be improved by increasing the gas transmission area of a specimen. Since hydrogen is flammable and explosive when it mixed with air, the helium gas was substituted for hydrogen. The calibration is performed to compensate the ambient pressure differences during the test. The correction factor is found as 0.21 mm/Pa. The actual moving distance of the liquid indicator is calibrated by the correction factor.

The permeability of laminated composite was found to degrade after undergoing cryogenic cycling process. For the thin laminate specimens C2 and C5, the permeability increases significantly after cryogenic cycling. For the thick laminated specimens C1 and C3, the increase of permeability is less. The textile composite specimen T1 has lower permeability than laminated specimens and the variation of permeability is very small with the increase of cryogenic cycles. The laminated composites were embedded with nano-particles which are capable of reducing thermal stresses in the matrix phase.

However, under the conditions of the experiments carried out, the nano-particles did not show the expected improvement on permeability. Further studies are needed to investigate the effects of nano-particles. Optical micrographic analysis was performed to investigate microcrack propagation and delamination in test specimens. For the laminated composite specimen, the microscopic examination showed the existence of transverse crack propagation and delaminations. Transverse cracks propagation was not observed in textile composite specimens, which resulted in low permeability of textile composites even after cryogenic cycling.

References

1. Final report of the X-33 Liquid Hydrogen Tank Test Investigation Team, Marshall Space Flight Center, Huntsville, AL, May 2000.
2. Choi, Sukjoo, "Micromechanics, Fracture Mechanics And Gas Permeability Of Composite Laminates For Cryogenic Storage Systems," Doctoral Dissertation, University of Florida, Gainesville, Florida, 2005.
3. Marrey, R.V. and Sankar, B.V., "Micromechanical Models for Textile Structural Composites," *NASA Contractor Report*, 198229, October 1995.
4. Zak, A.K., and Williams, M.L., "Crack Point Singularites at a Bi-material Interface," *ASME Journal of Applied Mechanics*, 30, 142–143, 1963.
5. Gupta, V., Argon, A.S. and Suo, Z., "Crack Deflection at an Interface between Two Orthotropic Media," *Journal of Applied Mechanics*, 59, 79–87, June 1992.
6. Willams, M.L., "On the Stress Distribution at the Base of a Stationary Crack," *Journal of Applied Mechanics*, 24, 109–114, 1957.
7. Ting, T.C.T and Chou, S.C., "Stress Singularities in Laminated Composites," *Fracture of Composite Materials*, eds. Proceedings of the 2nd USA-USSR Symposium, Lehigh Univ., Bethlehem, PA, March 9–12, 1981, 265–277, 1982.
8. Ting, T.C.T. and Hwang, P.H., "Singularities at the Tip of a Crack Normal to the Interface of an Anisotropic Layered Composite," *International Journal of Solids and Structures*, 20(5), 439–454, 1984.
9. Stokes, E., "Hydrogen Permeability of Polymer Based Composite Tank Material Under Tetra-Axial Strain," Proceedings of the fifth conference on aerospace materials, processes and environment technology (AMPET), Huntsville, Alabama, September 16–18, 2002, http://www2.southernresearch.org/pdf/tetraaxial_strain.pdf, last accessed, May 20, 2005.
10. ASTM D1434–82 (Reapproved 1992), "Standard Test Method for Determining Gas permeability Characteristics of Plastic Film and Sheeting," ASTM, 203–213, 1992.
11. Kumazawa, H., Aoki, T. and Susuki, I., "Analysis and Experiment of Gas Leakage Through Composite Laminates for Propellant Tanks." AIAA Journal, 41(10), 2037–2044, October 2003.
12. Grimsley, B., Cano, R., Johston, N., Loos, A. and McMahon, W., "Hybrid Composites for LH2 Fuel Tank structure," Proceedings of the 33rd International SAMPE Technical Conference, NASA Langley Research Center, November 4–8, 2001.
13. Herring, H., "Characterization of Thin Film Polymers through Dynamic Mechanical Analysis and Permeation," NASA/CR—2003-212422, 2003.
14. Nettles, A.T., "Permeability Testing of Impacted Composite Laminates for Use on Reusable Launch Vehicles," NASA/TM—2001-210799, 2001.
15. Nettles, A.T., "Permeability Testing of Composite Materials and Adhesive Bonds for the DC-XA Composite Feedline Program," NASA Technical Memorandum 108483, March 1995.
16. Glass, E., Venkat, V. and Sankaran, S., "Honeycomb Core Permeability Under Mechanical Loads," NASA/CR–97–206263, 1997.
17. Horiuchi, T. and Ooi, T., "Cryogenic Properties of Composite Materials," *Cryogenics*, 35: 677–679, 1995.

Project Title: Zero Boil-Off (ZBO) Pressure Control

Task PI: Jacob N. Chung, Department of Mechanical and Aerospace Engineering

Project Goals

A unique facet of storing liquid cryogens is that a sizable amount of heat will continually flow from the surrounding ambient to the low temperature fluid. Despite the fact that excellent multilayer insulations have been developed for storing cryogens, there will always be a finite amount of heat flow into the storage vessels, especially in the vicinity of supporting structures. As the heat accumulates, it will eventually vaporize a finite amount of liquid. Due to the large volumetric expansion from vaporization, the pressure in the vessel will significantly increase unless the vapor is exhausted from the vessel. Thus, there exists continual purging of excess vapor from the cryogenic storage tank. This is not efficient, and depending on the duration of storage, a significant amount of cryogens can be wasted. In order to preserve the cryogens in storage for a long duration space flight, an active heat removal system is required to balance the heat that permeates into the storage vessel. Such a system would eliminate the need for purging the cryogen vapor from the storage tank. We expect to develop a zero-boil-off (ZBO) system model that would determine whether active mixing of the cryogen is required for ZBO and whether the benefits outweigh the complications. Next the model would provide a comparison study between a sensible heat transport system and a latent heat transport system. We also will design an optimal latent heat transport system and determine the appropriate degree of sub cooling.

Accomplishments

Abstract

This report documents the research work performed under the NASA hydrogen funding for the past two years. This project was focused on the evaluation of the feasibility of a cryogenic storage system based on phase-change heat transfer processes in microgravity. The basic mechanisms were designed following the fundamental concept of ZBO pressure control. To maintain ZBO, the heat transfer from the tank depends on bubble removal from the tank wall, entrainment of the bubbles by the swirling jet flow and eventual total condensation of the entrained bubbles by the cryocooler. The conceptual design was evaluated by scaled-down laboratory models, mathematical models and numerical simulations.

I. Introduction

A unique facet of storing liquid cryogens is that a sizable amount of heat will continually flow from the surrounding ambient to the low temperature fluid. Despite the fact that excellent multilayer insulations have been developed for storing cryogens, there is always a finite amount of heat flow into the storage vessels, especially in the vicinity of supporting structures. As the heat accumulates, it will eventually vaporize a finite amount of liquid. Due to the large volumetric expansion from vaporization, the pressure in the vessel will significantly increase unless the vapor is exhausted from the vessel. Thus there exists continual purging of excess vapor from the cryogenic storage tank. This is not efficient, and depending on the duration of storage, a significant amount of cryogens can be wasted. In order to preserve the cryogens in storage for a long duration space flight, an active heat removal system is required to balance the heat that permeates into the storage vessel. Such a system would eliminate the need for purging the cryogen vapor from the storage tank. We expect to develop a ZBO system model with phase-change heat transfer that would determine whether active mixing of the cryogen is required for ZBO and whether the benefits outweigh the complications. Next the model would provide a comparison study between a sensible heat transport system and a latent heat transport system. We also will design an optimal latent heat transport system and determine the appropriate degree of subcooling.

Since the main mechanism for controlling the boil off relies on the total condensation of the vapor generated as a result of the heat leakage through the tank insulation, it is very important to make sure that the mixing jet is properly designed such that it can efficiently entrain the vapor and mix it with the subcooled liquid for a complete condensation. In a terrestrial condition, the vapor bubbles would detach from the tank wall after they grow to a certain size and rise up to the top of the tank due to gravity where all the bubbles would gather and coalesce to form an overhead vapor void. So mixing jets are designed to break up the large vapor chunks and then mix the vapor fragments with the subcooled liquid for condensation. In microgravity, however, the vapor bubbles would tend to grow and stick around the tank surface where they are nucleated because of the surface tension dominance in the absence of buoyancy in space. Therefore, in microgravity the mixing jets must be properly designed such that they can first shear off the vapor bubbles from the wall, entrain them, and then mix them with the subcooled liquid for condensation. Please see figure 1 for a schematic that explains this proposed process in microgravity. Based on the microgravity scenario, two tasks of the ZBO project are given as follows:

Task 1: To investigate the removal (shear-off) characteristics of a vapor blob from the heater surface by a parallel flow which simulates a wall jet during the jet mixer operation. The expected outcome is a relationship between the threshold jet flow rate and the wall heat flux for bubble removal from the tank wall.

Task 2: To study the bubble entrainment capability of a swirling jet flow, vapor bubble transport in the jet flow, and condensation rate of vapor bubble.

For the microgravity experiment, we will use the currently available 1.8-sec drop tower at the University of Florida. The 1.8-sec drop tower is believed to be able to provide sufficient preliminary data for the vapor blob shear-off experiment because that the formation of bubble blobs of a size around 1 to 2 cm only takes about less than 0.7 sec under certain conditions and it only needs less than 1 second for the planned slowest flow to travel through the test section. According to a report submitted to NASA by Merte, Lee and Keller (1995), their microgravity experiment of pool boiling with R-113 on board Space Shuttle STS 60 showed that bubbles grew to a size of 5 mm in just 0.05 sec under the heat flux of 2 W/cm^2. Our own experiment also revealed a similar phenomenon. An experimental apparatus for performing Task 1 has been competed and calibration and testing of the loop has started. Figure 2a is a schematic of the experimental apparatus and figure 3a is a photograph of the apparatus. The apparatus is

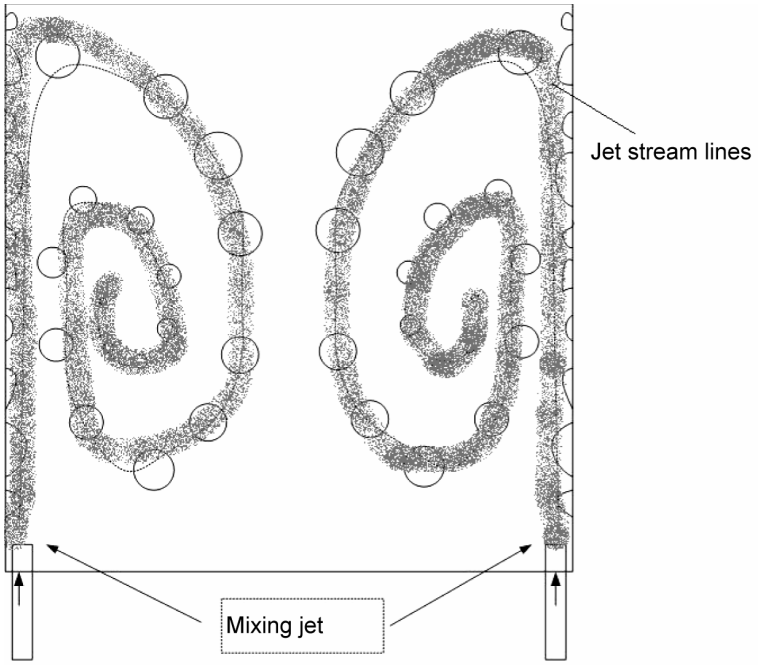

Figure 1.—Jet mixer interaction with the vapor blobs.

composed of a flow loop with the velocity maintained by a variable-speed pump. The square test section is made with transparent plexiglass for visualization and image acquisition by CCD and high-speed camera. A downward-facing gold-film heater is located on the top surface of the test section. The downward-facing heater is designed to simulate zero-gravity in a terrestrial condition. Justification is given in the "Additional Information" section. For Task 2, the experimental apparatus is under design and construction. A schematic of that is shown in figure 2b. Figure 3b shows the design of Task 2 apparatus. The Task 2 apparatus is intended to study the entrainment and condensation of bubbles by the jet flow.

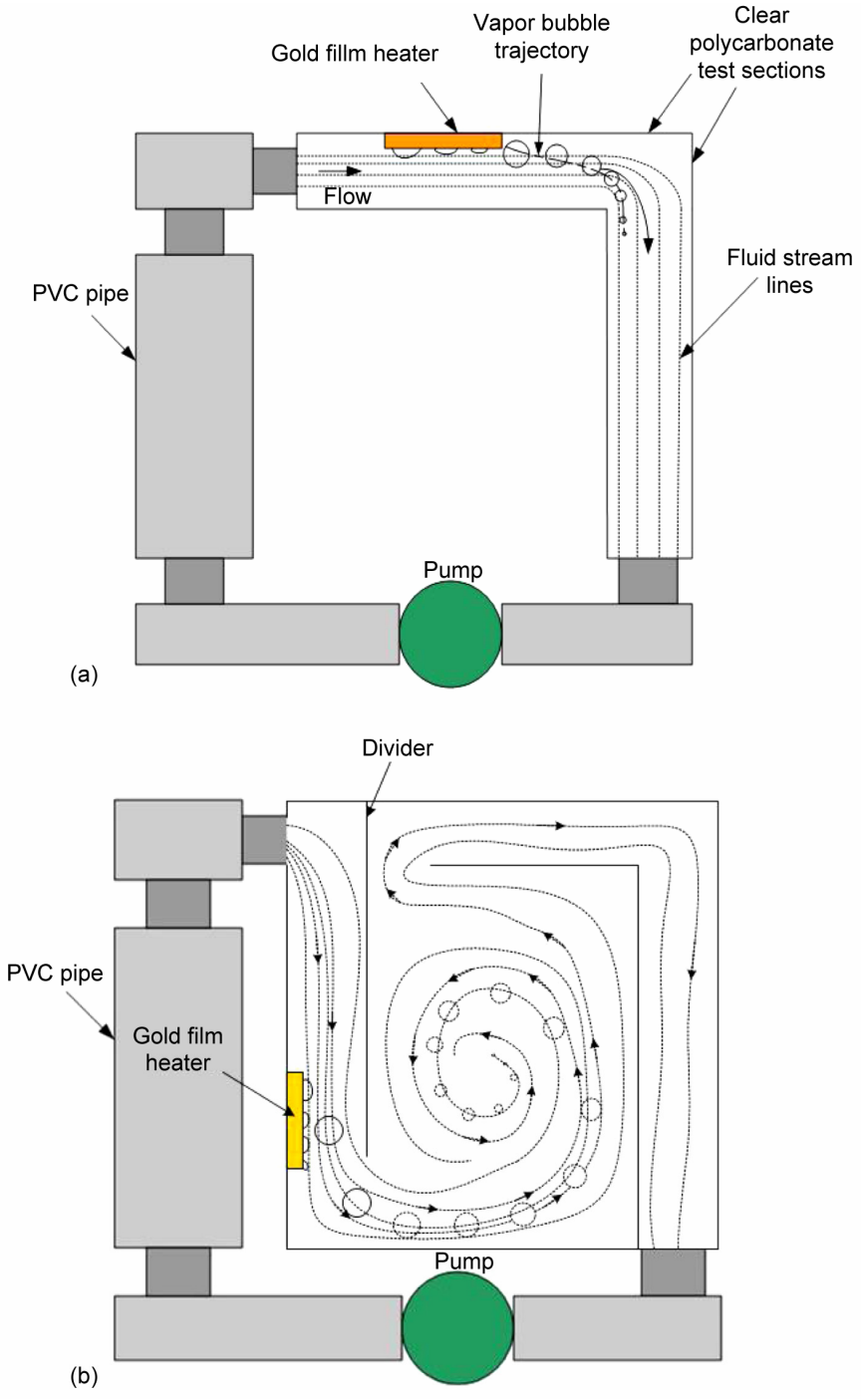

Figure 2.—(a) Schematic of Task 1 experimental apparatus, and (b) Schematic of Task 2 experimental apparatus.

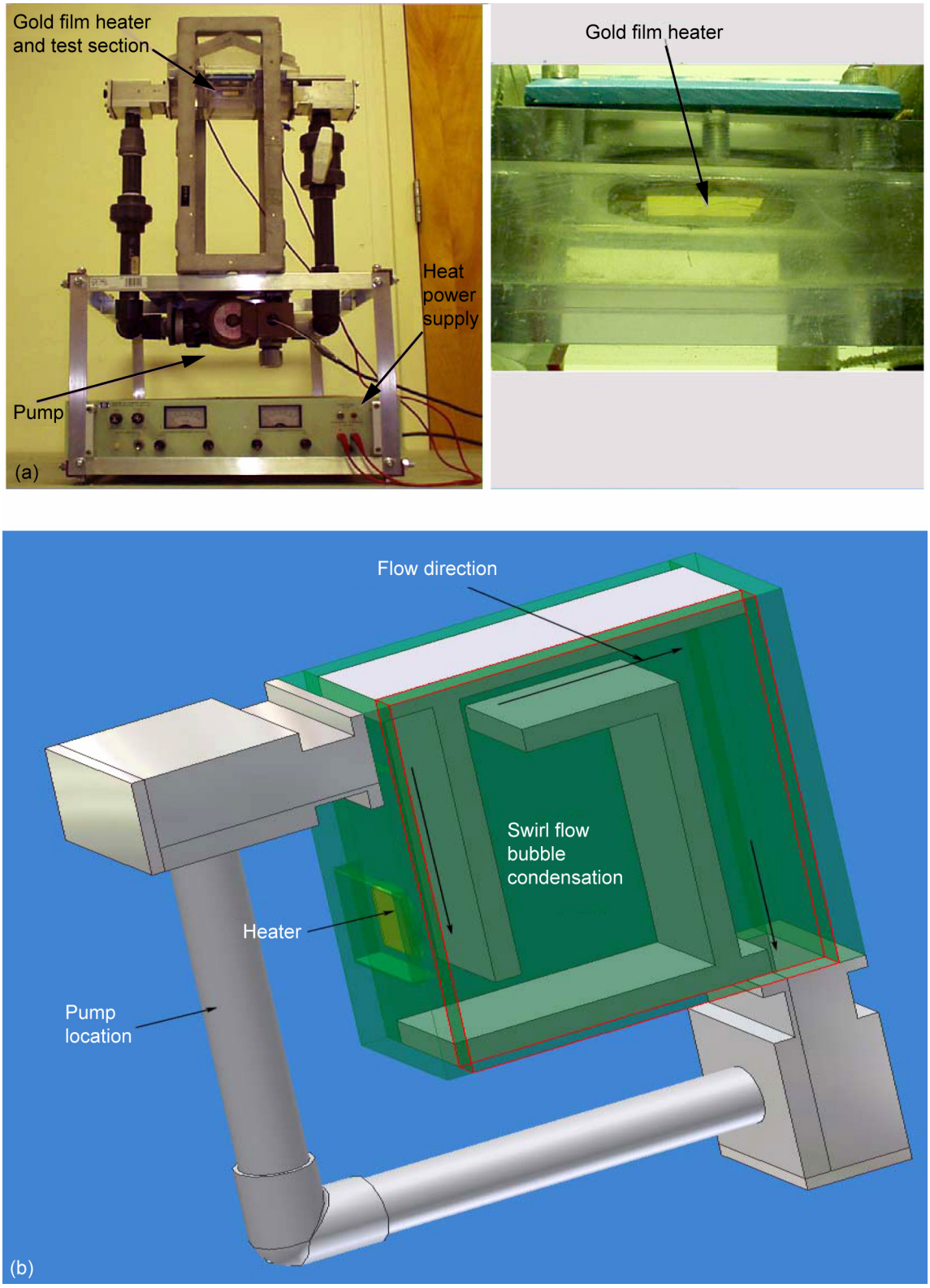

Figure 3.—(a)Photograph of the Task 1 experiment, and (b) Design of Task 2 experimental apparatus.

Experimental Apparatus

A flow controlled loop was built for Task 1 as shown in figure 3a. The experimental fluid is refrigerant-113. As shown in the “Additional Information” section, scaling analysis based on three dimensionless parameters (Ri, Bo, We) proves that the flow loop built can be used to model cryogenic convective heat transfer in microgravity conditions for some special cases. A gold-film heater has been used to model heat leaks in cryogenic propellant tank in space. Based on the scaling analyses, the heater was placed in an inverted horizontal position. Upon bubble formation on the heater surface, the pump, used to drive the fluid, would be turned on to the desired flow rate.

The test section, where the heater was placed, was made of clear polycarbonate. A high speed CCD camera was used to view the formation and departure of the bubbles. The flow loop is approximately 16x17x20 in. and designed to expand into NASA's standard drop tower cubicles' dimensions.

Flow Loop Components

Test section.—The flow loop's test section, shown in figure 4 was made of clear 0.5 in. thick polycarbonate. The test section is 8x3x2 in. A 2x0.25 in. deep square hole was cut on the test section to place the base of the heater. Below the square hole, a 1.75 in. diameter whole by 0.25 in. deep was cut to place the heater, which is attached to the square base, and an O-ring, to prevent leaks. The test section was attached at the seams with leak proof adhesive that could withstand the fluid's boiling temperature of 48 °C and high impacts, for experiments in the drop tower.

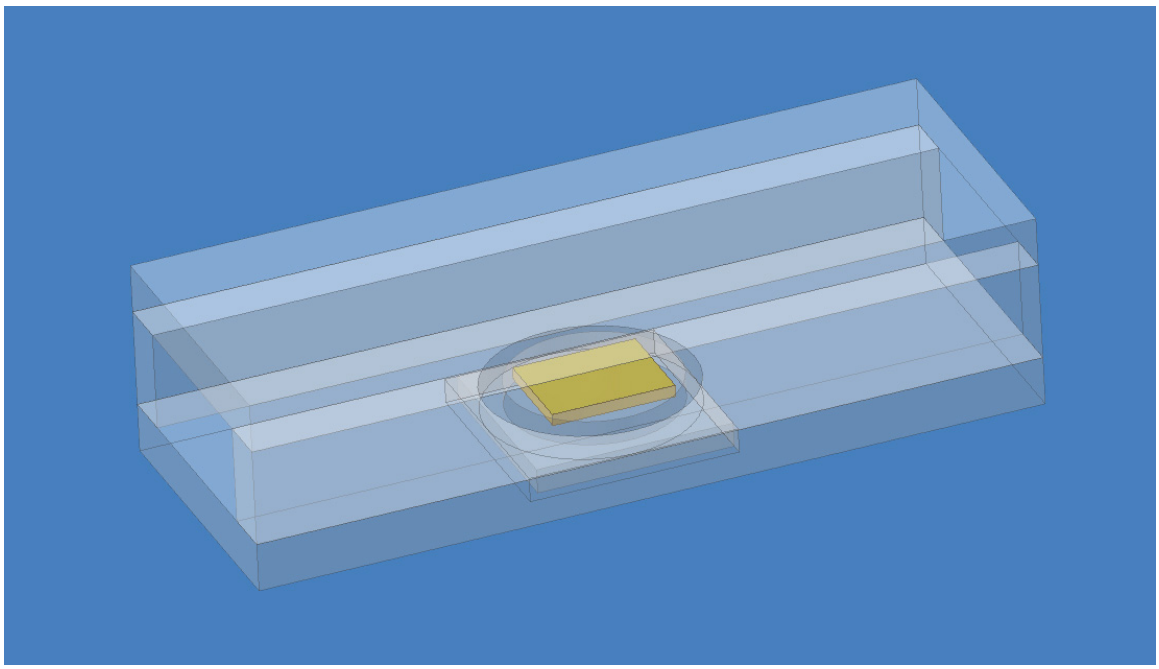

Figure 4.—Loop’s test section drawing.

Figure 5.—Pump.

Pump.—The pump used is the following: In-Line Circulator Pump - Centrifugal Type: Wet Rotor, Model Number: Astro 30B, Flange Size: 0.75,1,1.25,1.5 in., Horsepower: 1/25, Voltage: 115, Phase: 1, Housing Material: Bronze, Flow rate 0 to 20 gpm. Figure 5 shows the pump's picture.

Heater.—The heater used in the loop is a 1x1x0.125 in. piece of polycarbonate with a thin gold film layer on top. The heater was attached to a 1.75 in. diameter by 0.25 in. deep piece of polycarbonate that served as the base for the heater. The round base of the heater was connected to a 2 in. square (0.25 in. thick) piece of polycarbonate in order to connect and secure the base of the heater to the test section. Four 0.125 in. diameter holes were drilled through the square piece for power and voltage leads.

The gold film was used to transfer heat from a power supply to the fluid via the lead brass screws. The gold film was sputtered on the polycarbonate piece to a thickness of 400 Å (40 nm) in the center and 5000 Å (500 nm) on the leads of the screws. The Hummer VII (Anatech, Ltd.) sputtering system with etch/plate control was used to sputter the gold film to the polycarbonate section. Cathode sputtering was the method used with the Hummer VII. This method uses high voltage (>10,000 V) across two electrodes. An ion bombardment vaporizes the cathode metal and deposits it as a crystalline, fine-grained coating on material placed near the anode. To connect the gold film surface to the lead screws, silver filled epoxy was applied from the top of the lead screws to the surface of the heater. The heater was then baked under 170 °F for 2 hr to allow for the epoxy to set.

Pipes.—Standard 1 in. NPT-PVC pipes were used to connect the loop together. Teflon tape was used at the connections to prevent leakage under moderate pressure.

Fluid.—The fluid used is refrigerant-113 (1,1,2-trichloro-1,2,2-trifluoroethane 99.9 percent) used to simulate cryogenic fluids, specifically liquid hydrogen, at near saturation conditions. The fluid was purchased from ChemNet in Sarasota, Florida. The trade name for R-113 is Trichlorotrifluoroethane. Below are some specifications for R-113:

Molecular weight	187.38
Boiling point	118 °F (48 °C)
Vapor pressure	6.46 Psia at 77 °F (25 °C)
Liquid density	1,511 kg/m^3
Vapor density	3.48 kg/m^3
Surface tension	15.9E–03 N/m
Viscosity	497E–06 N-s/m^2

Heater calibration.—Based on the research of Oker and Merte (1981), it was found that there is a linear relationship between the heater resistance and surface temperature. It was also found that small shifts in calibration would happen with time, but the slope of the line would remain the same. To verify Oker and Merte's results, a calibration was done on our heaters. The gold film heater was calibrated over

a temperature range of 18 to 80 °C. The calibration was performed with a double-heating system. The inner container size is 6x6x6 in. and is made of 0.25 in. thick aluminum plate with 6.125 in. thick and 1 in. fins protruding inward for maximum heat transfer. There were two 0.5 in. fins that protrude out of the bottom to prevent direct contact with the outer container. A Corning PC-35 heater was used to heat up the outer container and the water between the two containers. The inner container was filled with Dow Corning 200 fluid. The heater calibration assembly contains a base for the heater and the thermocouple was immersed in the fluid. The heat output from the PC-35 heater transfers through the outer container and water uniformly into the inner container.

Data was taken when the heater was turned off and the temperature and resistance were steady, the process was repeated until all the required data was taken. The temperature data was taken with a type T thermocouple and a digital thermometer. The resistance data was taken using a Keithley 197 Autoranging Microvolt DMM with a double-ohm method to get rid of the connecting resistance of the leads. The current leads of the gold-film heater were connected to the input side of the DMM, and the voltage leads were connected to the Ω sense sides of the DMM, as shown in figure 6.

The calibration curve is shown in figure 7 with a linear relation:

$$T = 317.3295*R-894.1226$$

Because of the small shifts in calibration, a single point calibration for finding the y-intercept is necessary before each experiment.

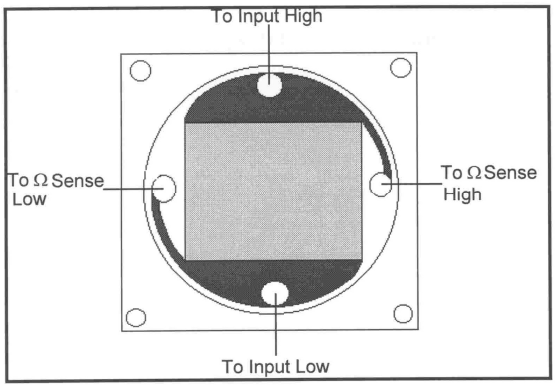

Figure 6.—Heater calibration schematic.

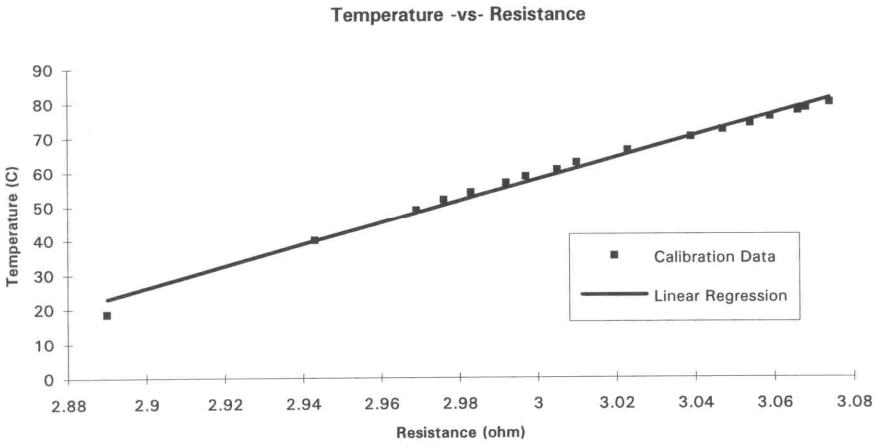

Figure 7.—Heater calibration curve.

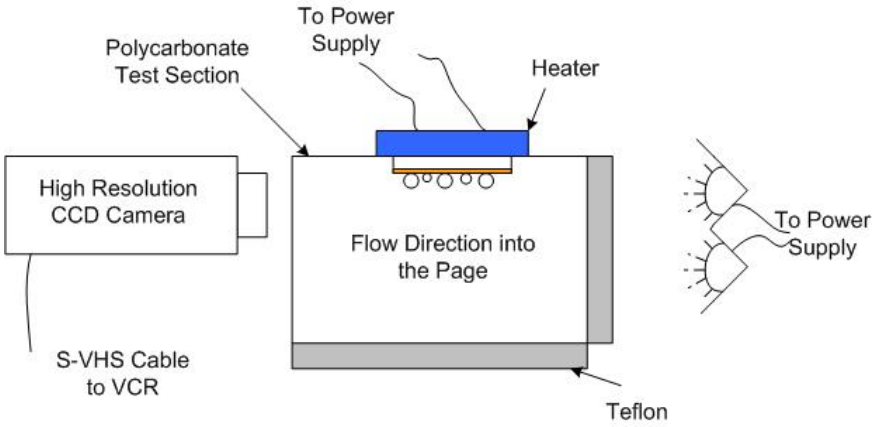

Figure 8.—Video system setup.

Video system.—To observe the bubbles coming from the heater surface, a video system was setup. The video system consisted of a high speed CCD camera (CV-255E) with a ½ in. HAD Interline Transfer CCD sensor. The camera's electronic shutter speed was from 1/1,000 to 1/10,000 sec. A Ceptre PD-1212ARD5 (12 VDC 1.2 A) power supply was used to provide power to the camera. A piece of Teflon was used as insulation to prevent the heat of the lights to affect the fluid. The Teflon also provided a better contrast background to see the bubbles. Figure 8 shows the schematic.

Power supplies.—A Hewlett Packard power supply (model no. 6263B) provided electrical power to the heater with variable voltage input between 0 to 20 V. The power supply to the camera and pump was a standard 110 VAC outlets.

III. Experimental Process

Several procedures needed to be performed before beginning each experiment. First, the single point heater calibration must be completed. Second, the desired heat flux must be set via the power heater's power supply. Finally, the desired flow rate is chosen.

Single Point Calibration

A single point calibration was performed before each experiment. A digital thermometer was connected to the lower thermocouple in the test section to take the temperature data. A double-ohm method was used to eliminate the connection resistance.

Temperature and resistance reading were taken once the temperature and resistance were stabilized. The y-intercept was calculated based on the linear relation,

$$T_r = \frac{dT}{dR} R_r + b$$

where T_r is the temperature reading, R_r is the resistance reading. The slope, dt/dR, is known from the calibration of the heater. This calibration procedure has to be done before each experiment because the y-intercept varies between experiments.

Heat Flux

The heat flux was obtained by varying the voltage on the power supply to the heater. The heat fluxes chosen for the experiment varied between 1 to 3 W/cm^2. The heat flux from the heater was calculated from the measured values of voltage and current by eq. (2),

$$q'' = \frac{V \cdot I}{A}$$

where V is voltage, I is current, and A is the heater's surface area (1 by 1 in.). The current reading was calculated from the measured values of voltage and current by eq. (3),

$$I = \frac{V_s}{R_s}$$

where V_s is the voltage across the shunt resistance and R_s is the resistance of the shunt resister.

Flow System

According to the numerical analyses' results, the flow rates for the experiments conducted were between 0 to 2 gpm. These flow rates yielded maximum heat transfer to condensate the bubbles, minimum kinetic energy from the fluid to the bubbles, and allowed for microgravity simulation in earth's gravity. The pump was turned on and allowed to reach steady state; approximately in 2 min. Several flow rates were used for each heat flux chosen.

Experimental Procedure

The experimental procedure is summarized as follows:

1. Setup required software (LabView) and hardware (power supply, heater, pump, and CCD camera).
2. Select the desired heat flux.
3. Perform the single point calibration
4. Select the desired flow rate.
5. Allow for steady state to be reached.
6. Activate LabView to record data.
7. Turn off all equipment once data has been collected.

Data Reduction

The raw data recorded by LabView was copied into spreadsheet. The heater temperature was converted from resistance to temperature by the calibration curve. The bulk liquid temperature was measure with type-T thermocouples and a cold junction compensator. The voltage reading was converted to temperature with the aid of a reference table provided by Omega. After all data was converted to readable data, curves were plotted and results were analyzed.

IV. Experimental Results

Flow Visualization

Flow visualization results have been obtained by our research group for three heating levels and one flow rate. The flow rate corresponds to a bulk velocity of 7.7 cm/s. Both the 1-g and microgravity results are shown together. The no-flow and with flow photographs are displayed side by side with each other for a direct comparison. Figures 9, 10 and 11 show the results for a heat flux level of 2.9 W/cm^2. For a higher heating rate, figures 12 and 13 provides visualization photographs for a heat flux level of 4.6 W/cm^2. Figure 14 and 15 represent the highest heating rate of 7.6 W/cm^2. As seen from these photographic results, the velocity of 7.7 cm/s is able to sweep off about 30 percent of the bubbles for the 2.9 W/cm^2 case. No bubble was removed for both 4.6 and 7.6 W/cm^2 cases. It is also noted that the sizes of the bubbles increase with the heating rate. It is confirmed that in microgravity, the generated bubble size can be as large as 1 cm after only 0.067 sec for the lowest heating level of 2.9 W/cm^2.

C.1 Heat flux = 2.9 w/cm^2

Velcocity = 0 cm/s

Velcocity = 7.7 cm/s

Earth gravity (1 g)

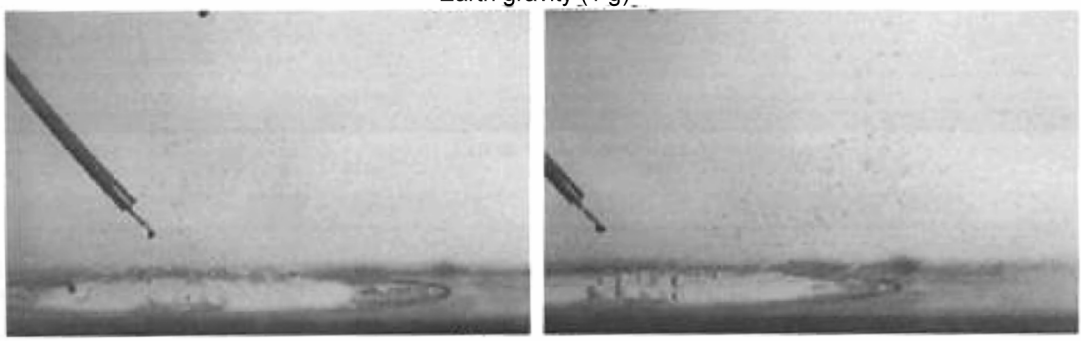

Time = 0 sec

Microgravity (approx 10^{-3} g)

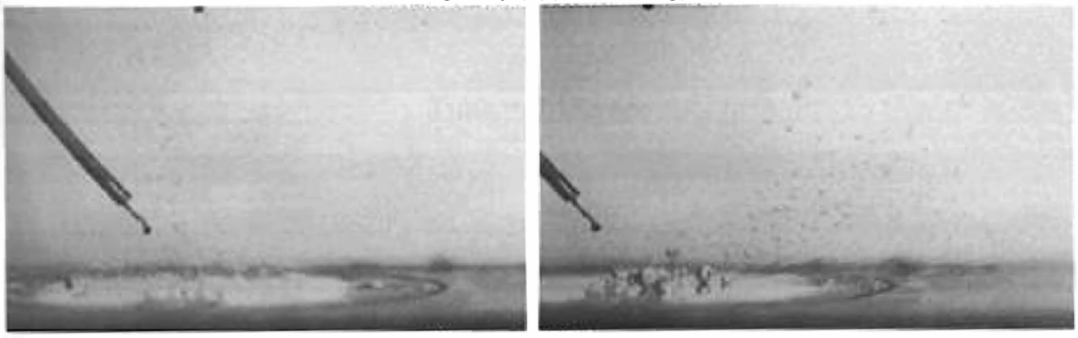

Time = 0.033 sec

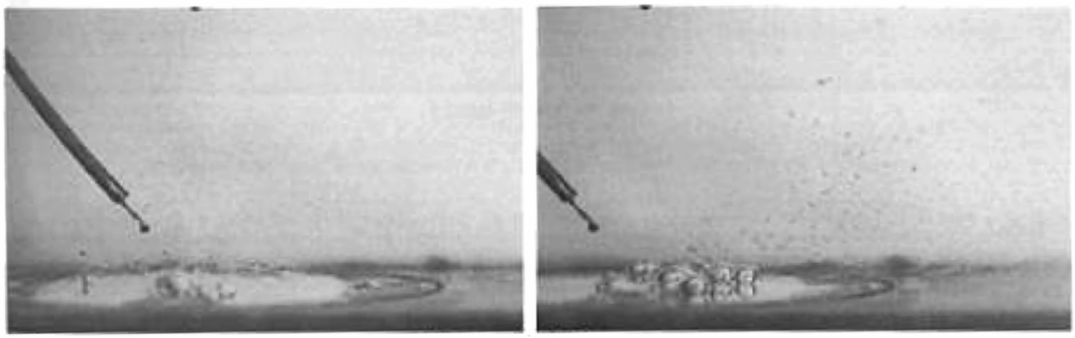

Time = 0.067 sec

Figure 9.—Heat flux level of 2.9 W/cm^2.

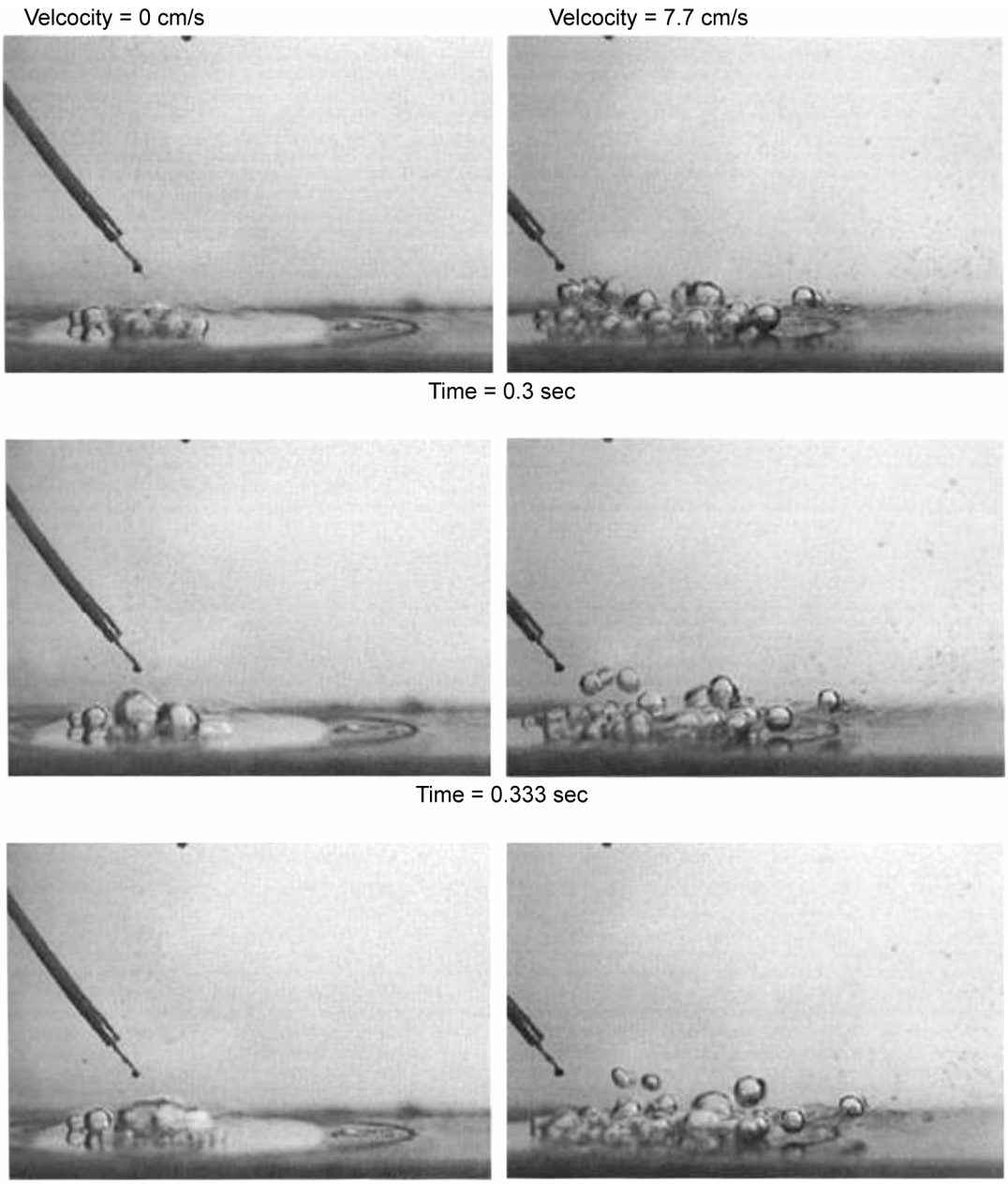

Figure 10.—Heat flux level of 2.9 W/cm^2.

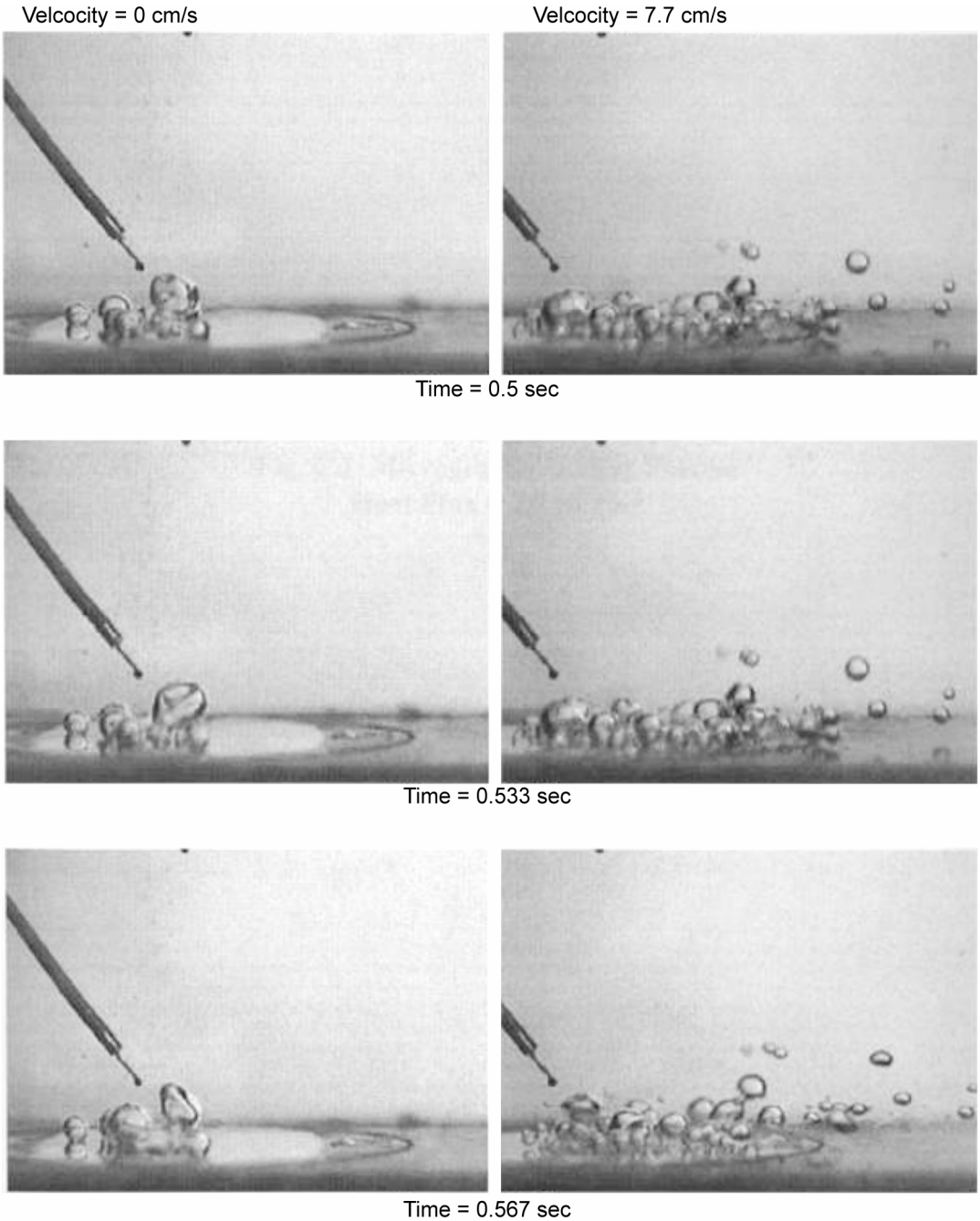

Figure 11.—Heat flux level of 2.9 W/cm^2.

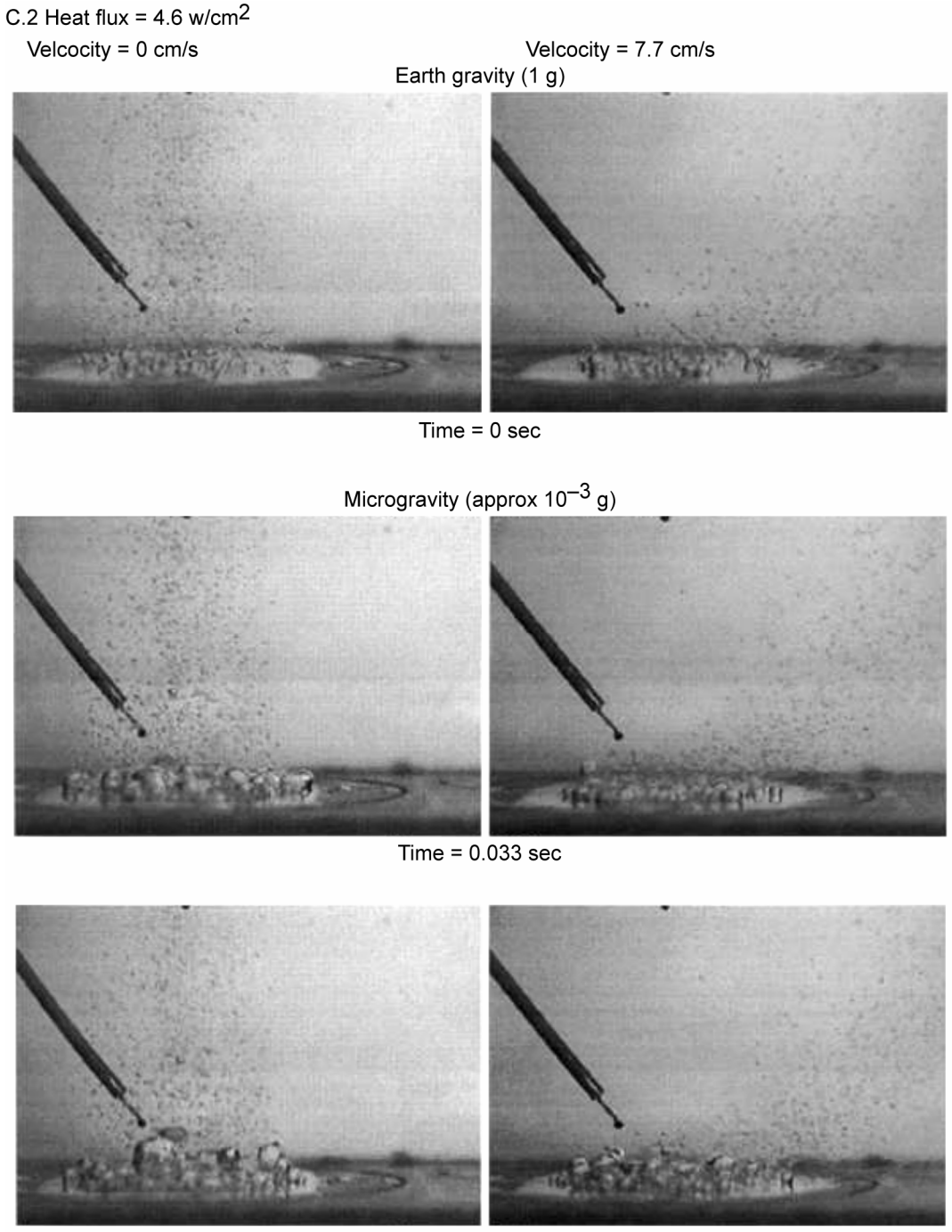

Figure 12.—Heat flux level of 4.6 W/cm^2.

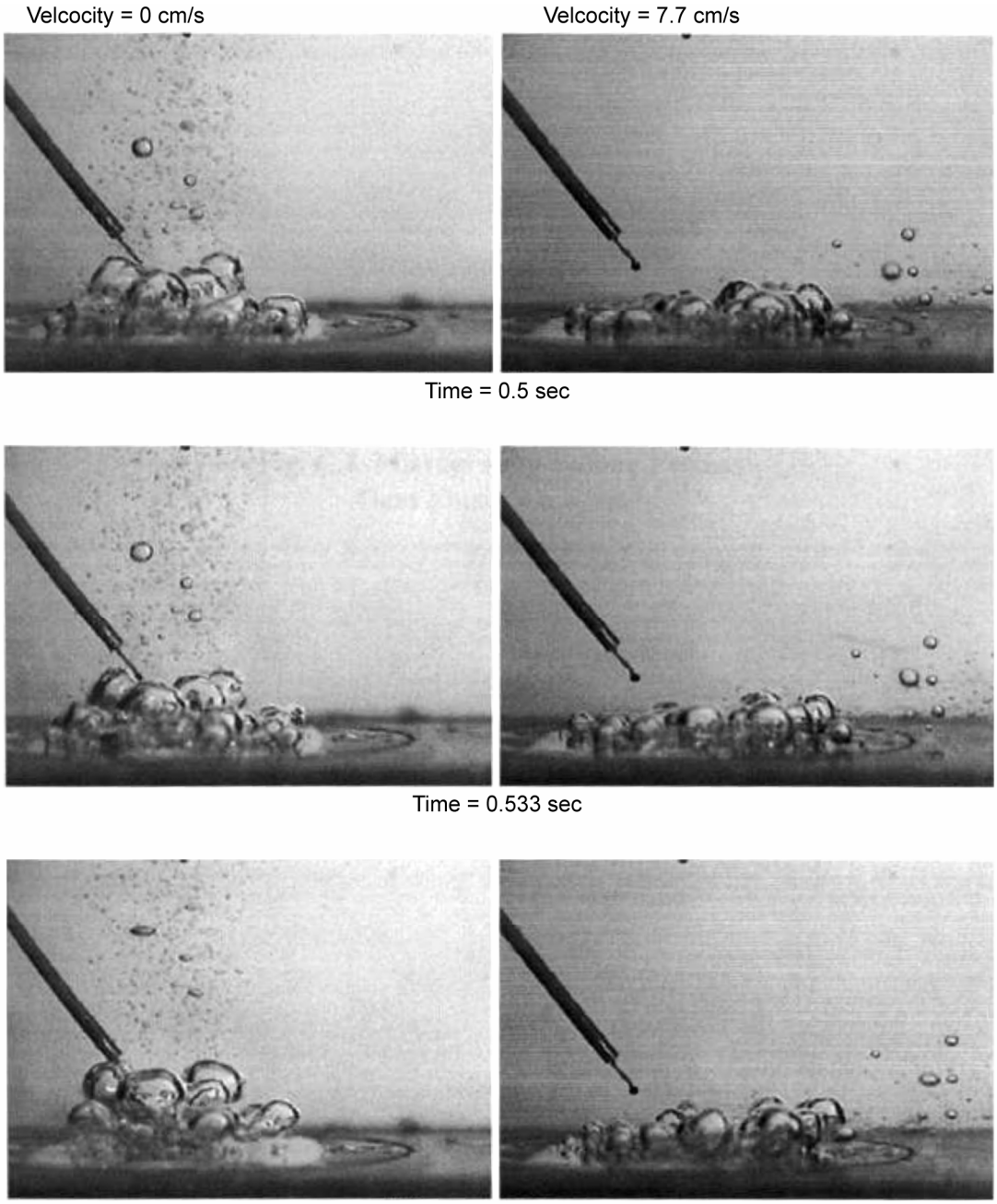

Figure 13.—Heat flux level of 4.6 W/cm^2.

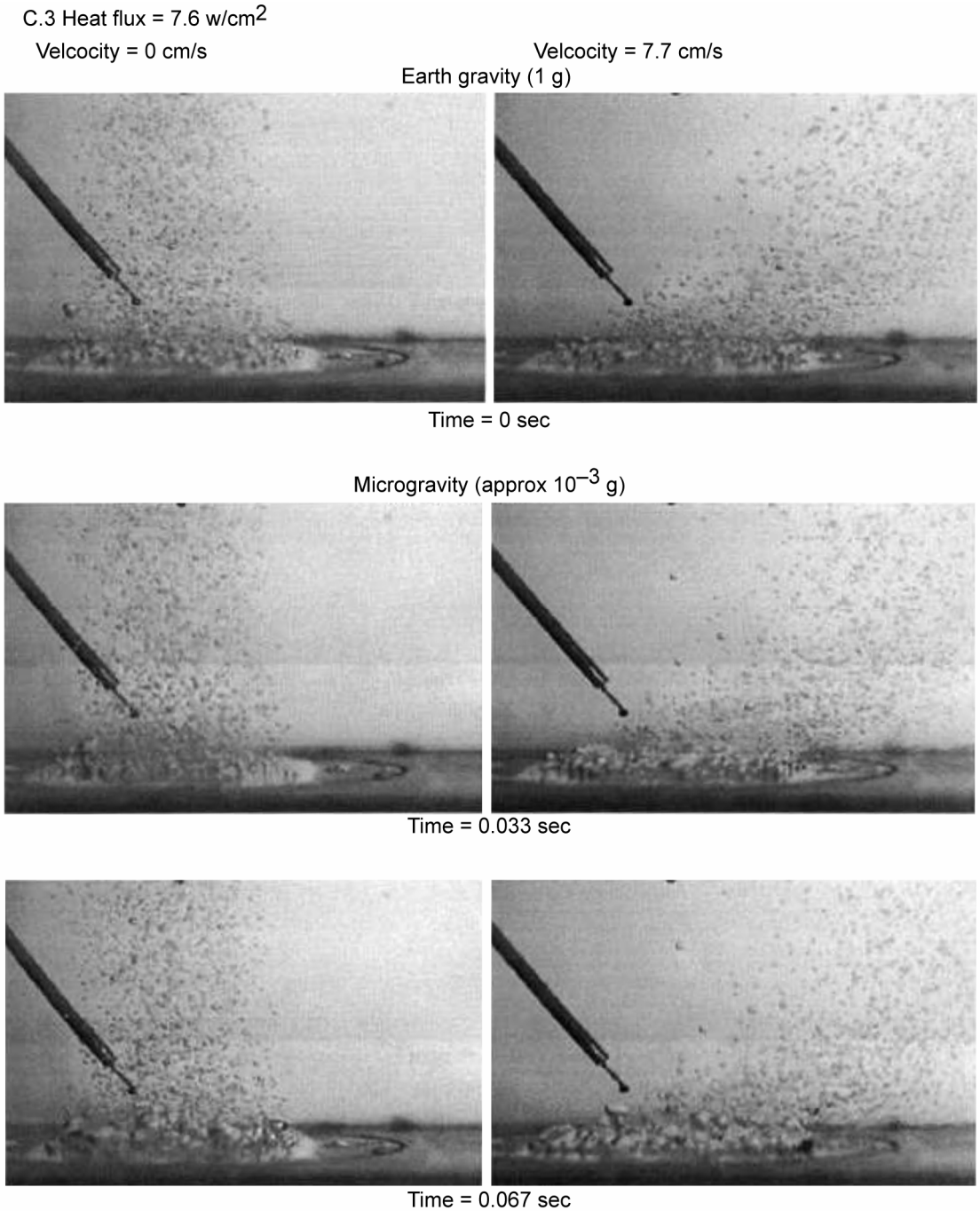

Figure 14.—Heat flux level of 7.6 W/cm^2.

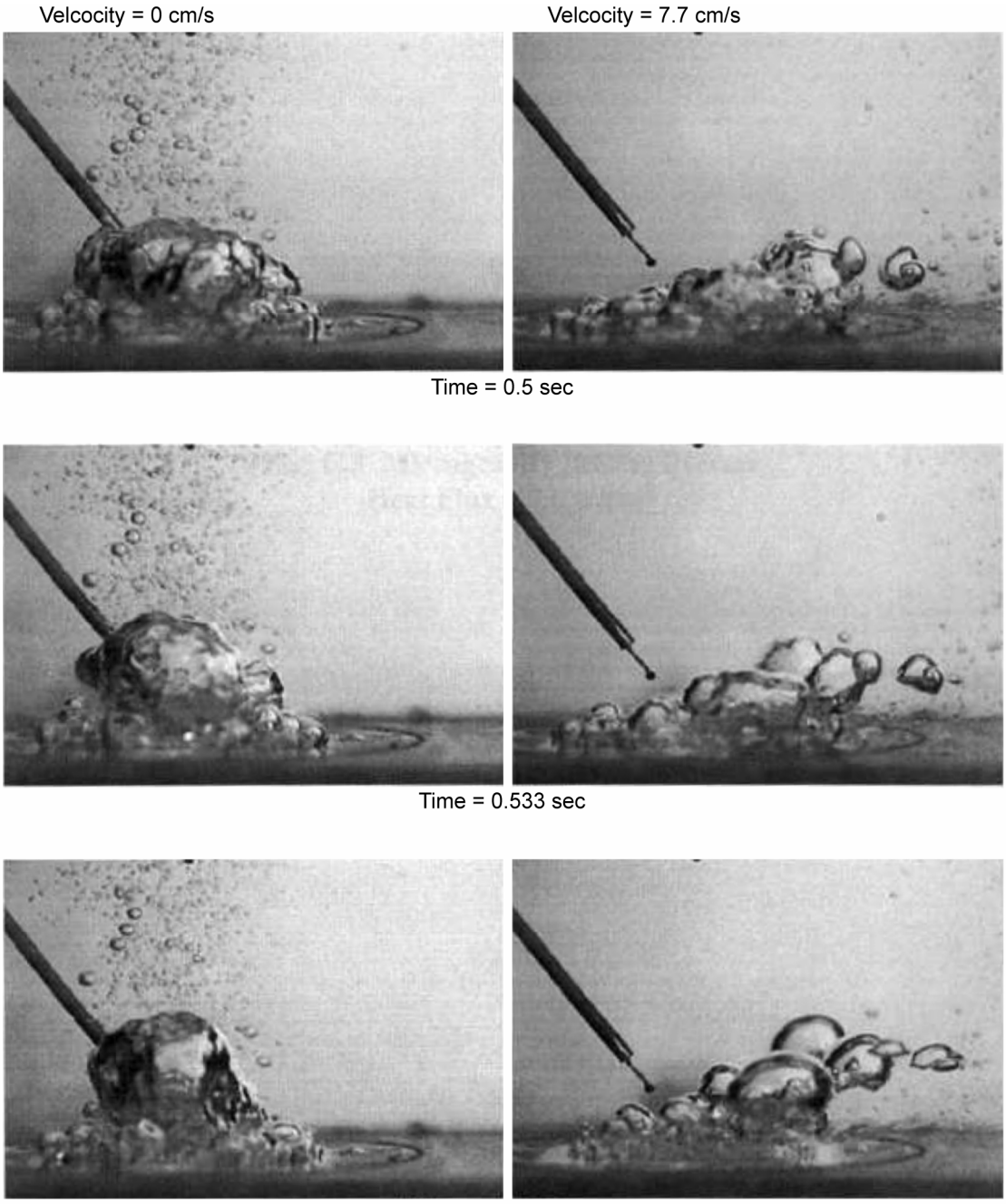

Figure 15.—Heat flux level of 7.6 W/cm^2.

The Heater Surface Roughness Effect

The effects of the heater surface roughness on the bubble removal are presented next. Two heaters with different roughness levels are shown in figure 16(a) and (b). Heater no. 2 is rougher than heater no. 1. Figure 17 gives the threshold values for flow rates and heat fluxes for the two heaters. It is noted that the rougher the heater surface, the more power is available for the surface to hold on to the bubble. Therefore, the threshold flow rate is higher for the rougher surface at the same heat flux. For the threshold heat flux, a higher flow rate is needed for the rougher surface. While for the threshold heat flux, at the same flow rate, the heat flux is higher for the less rough surface.

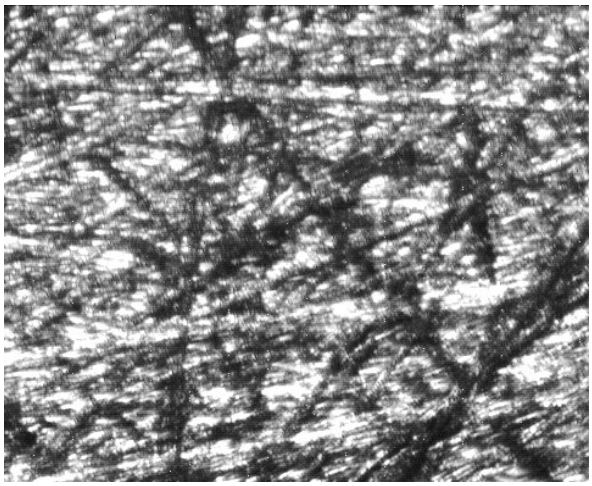

Figure 16(a).—Rough heater no. 1.

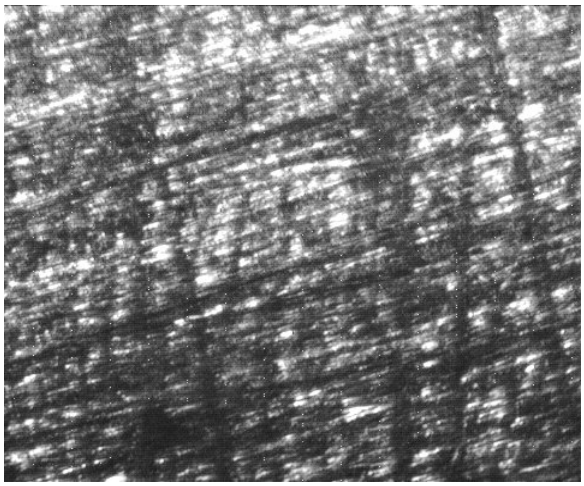

Figure 16(b).—Rough heater no. 2.

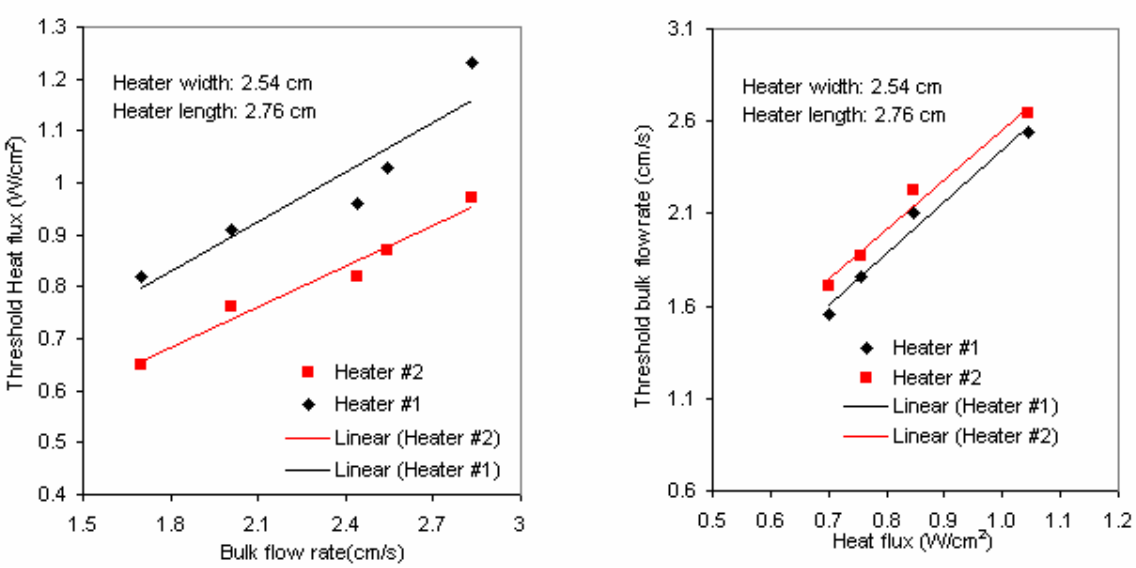

Figure 17.—Threshold flow rates and heat fluxes.

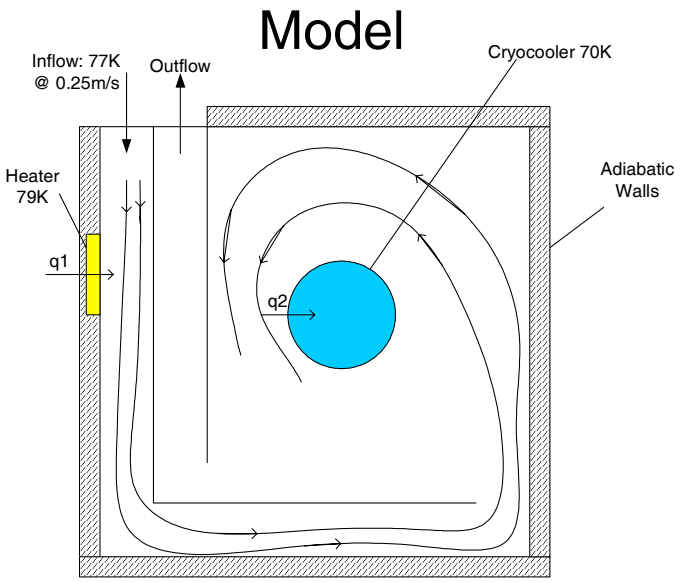

Figure 18.—Schematic of the model.

V. Thermodynamic and Mathematical Modeling

System Model

In order to evaluate the performance and optimize the compact storage module, a model that correctly describes the actual physical process is needed. Figure 18 shows the schematic of the model that corresponds directly to the compact storage system shown in figure 2(b). For the model, it is seen that the heat input to the system is represented by a heater (on the side wall) and the heat sink by a cryocooler (condenser - circular shape, in the center).

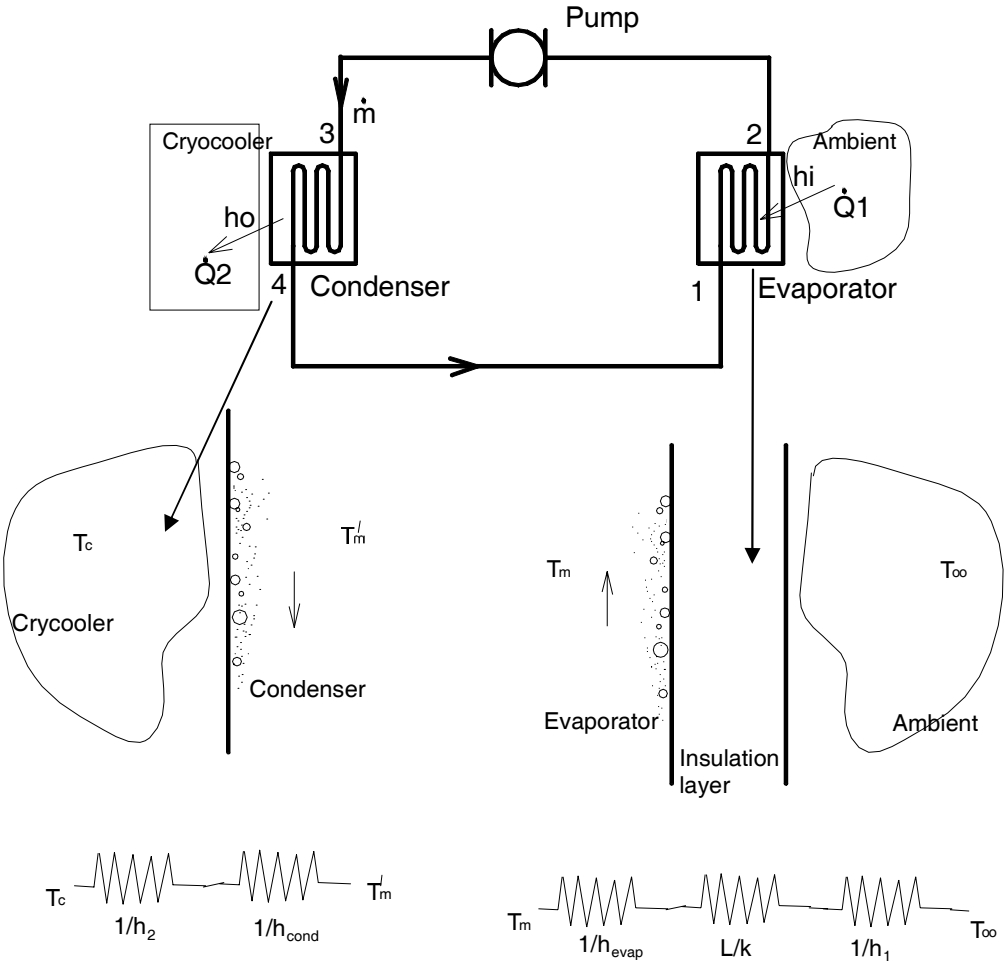

Figure 19.—Thermodynamic and mathematical model.

The thermodynamic and heat transfer diagram for the model is given in figure 19 where the system is composed of an evaporator, a condenser and a jet pump. Further more; the heat transfer processes in the evaporator and the condenser are given in figure 19 using electrical equivalent circuits, respectively.

The evaporator represents the boiling process on the wall that uses the heat entering the storage tank from outside through the insulation. There are three heat transfer resistances involved. They are convection resistance on the outer surface, conduction resistance of the wall insulation and boiling resistance on the inner surface. For the condenser, there are two resistances, one with the condensation heat transfer and the other with the cryocooler.

The governing equations are given below :

$$\frac{\dot{Q}_1}{A_{evap}} = \frac{\left(T_\infty - T_m\right)}{\frac{1}{h_s} + \frac{L}{K} + \frac{1}{h_{evap}}}$$, $\dot{Q}_1$ is evaporation rate, A_{evap} is evaporator surface area.

$$\frac{\dot{Q}_2}{A_{cond}} = \frac{\left(T'_m - T_c\right)}{\frac{1}{h_2} + \frac{1}{h_{cond}}}$$ $\dot{Q}_2$ is condensation rate, A_{cond} is condenser surface area.

$$\dot{Q}_1 = \dot{Q}_2$$

Comparison Study

For the sample calculation, nitrogen is used as the storage liquid. The insulation layer is 10 cm thick Kapton (DuPont) with thermal conductivity of 0.2 W/mK. The ambient temperature is set at 300 K. The jet flow rate is assumed to be 0.1 kg/s. The cryocooler heat transfer coefficient is estimated to be at 10 W/m2K.

The overall heat transfer coefficients for the evaporator and the condenser are presented in figure 20 with single-phase and two-phase flow regimes indicated in the figures. Whereas the effectiveness values for the evaporator and the condenser are plotted in figure 21.

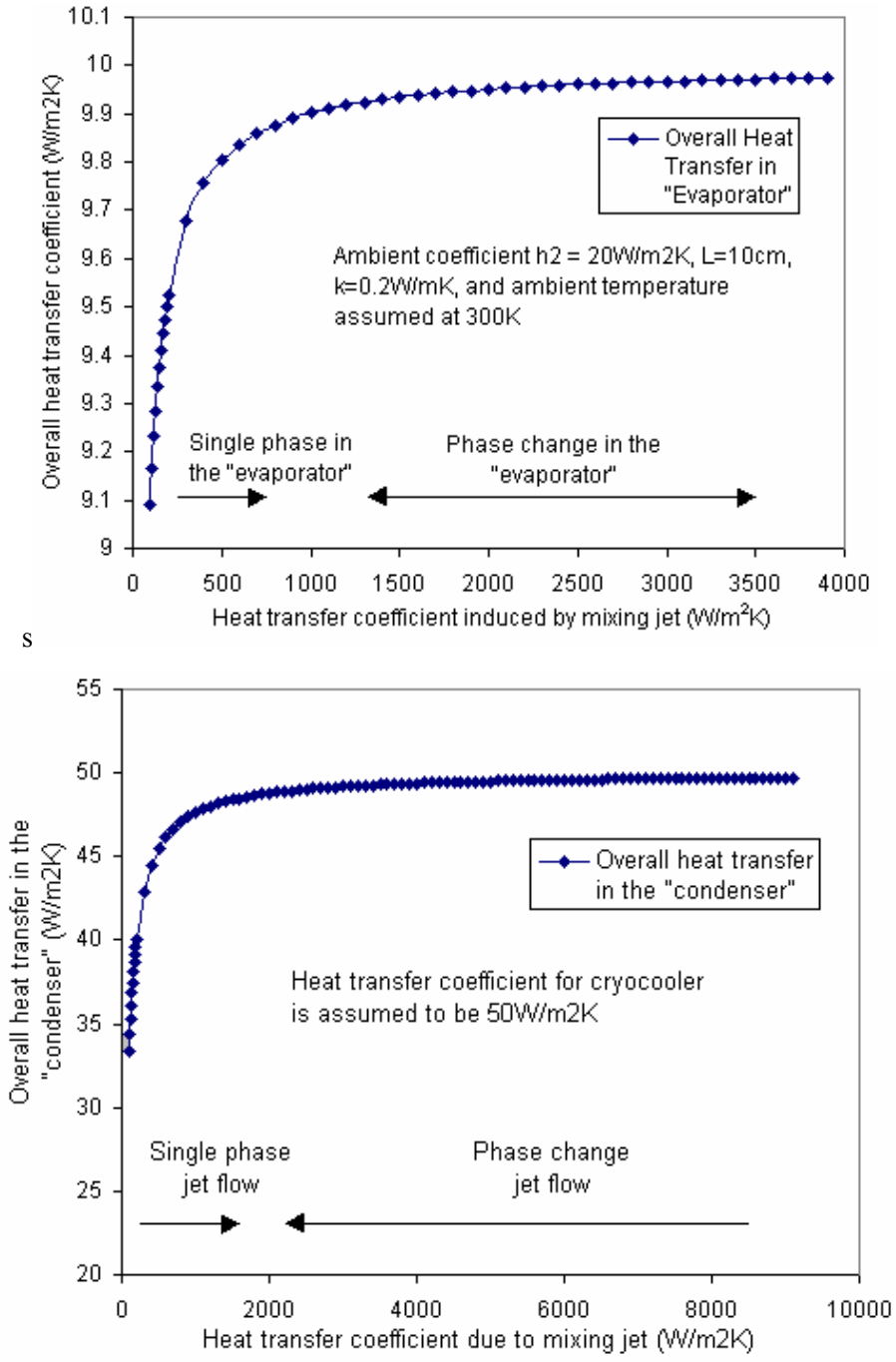

Figure 20.—Overall heat transfer coefficients for the evaporator and the condenser.

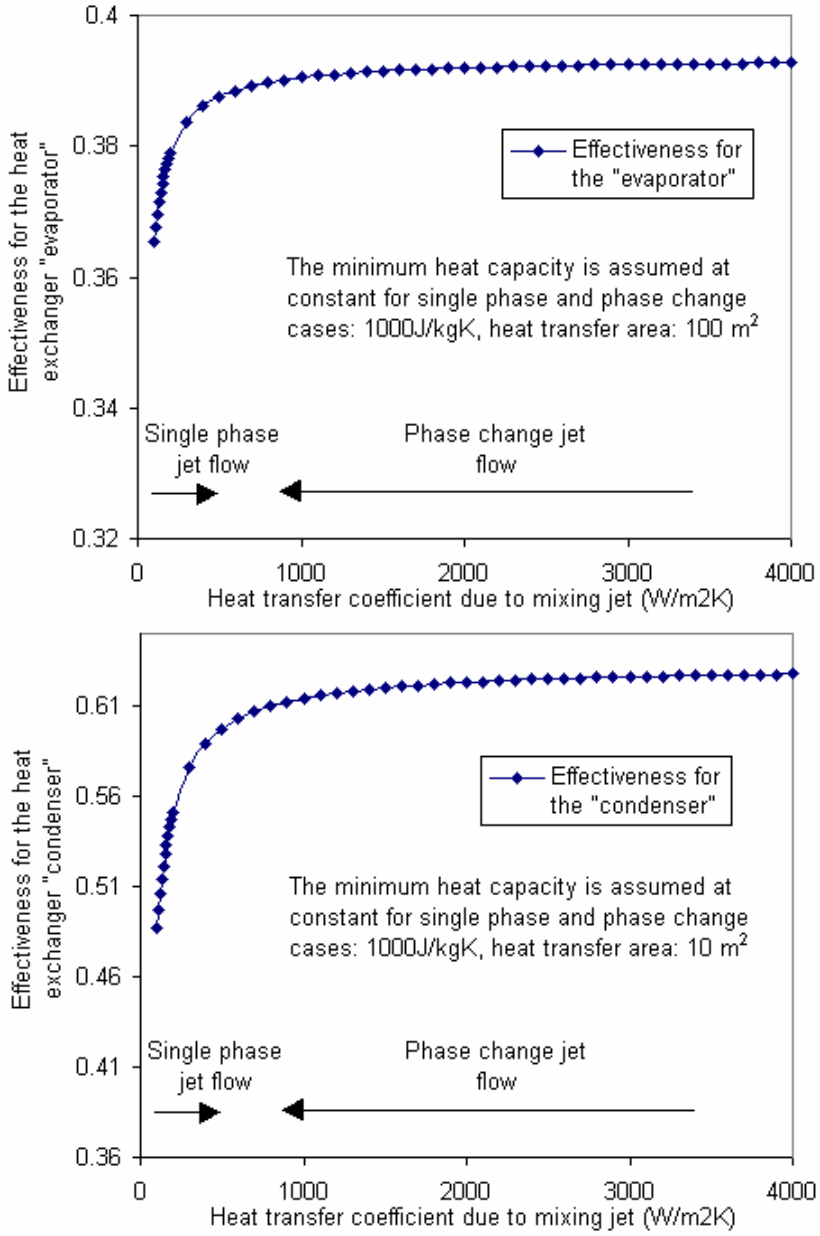

Figure 21.—Heat exchanger effectivenesses for the evaporator and the condenser.

The performance evaluation for the entire system is illustrated in figures 22 and 23 where the overall system effectiveness as a heat exchanger and the cryocooler size are provided. We see that the average effectiveness is 0.2 for the single-phase system while it is around 0.24 for the two-phase system. The improvement is approximately 20 percent. On the cryocooler size study, the average is 1.4 m for the single-phase system and is 1.15 m for the two-phase system, respectively. The reduction in the cryocooler size is also 20 percent for the two-phase system.

Numerical Simulation

Based figure 18, numerical simulations using the commercial code FLUENT (Fluent, Inc.) were also performed. The results are plotted in figure 23 for the flow streamlines and in figure 24 for the bubble trajectories, respectively. The streamline pattern basically verified the design objective that the flow

would form a strong recirculation around the cryocooler for bubble entrainment and condensation. In figure 24, in addition to the bubble trajectories, the plot also shows the bubble temperatures. In these preliminary calculations, we can see that the bubbles are cooled down as they are entrained in the recirculation.

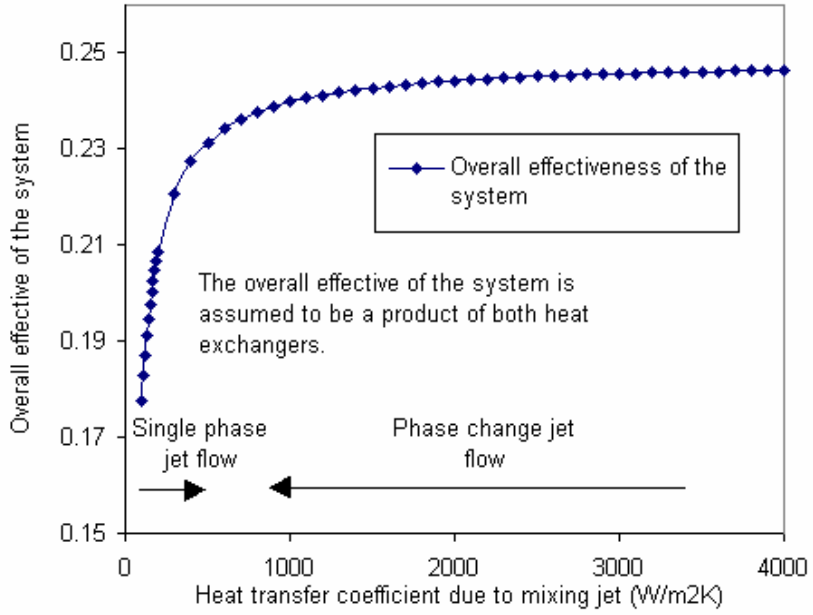

Figure 22(a).—Overall effectiveness of the system.

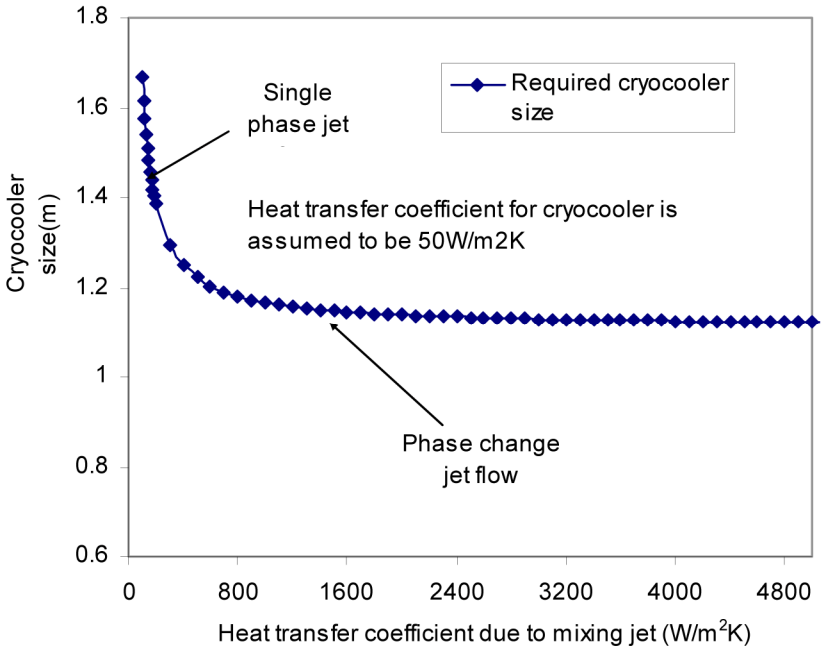

Figure 22(b).—Cryocooler size.

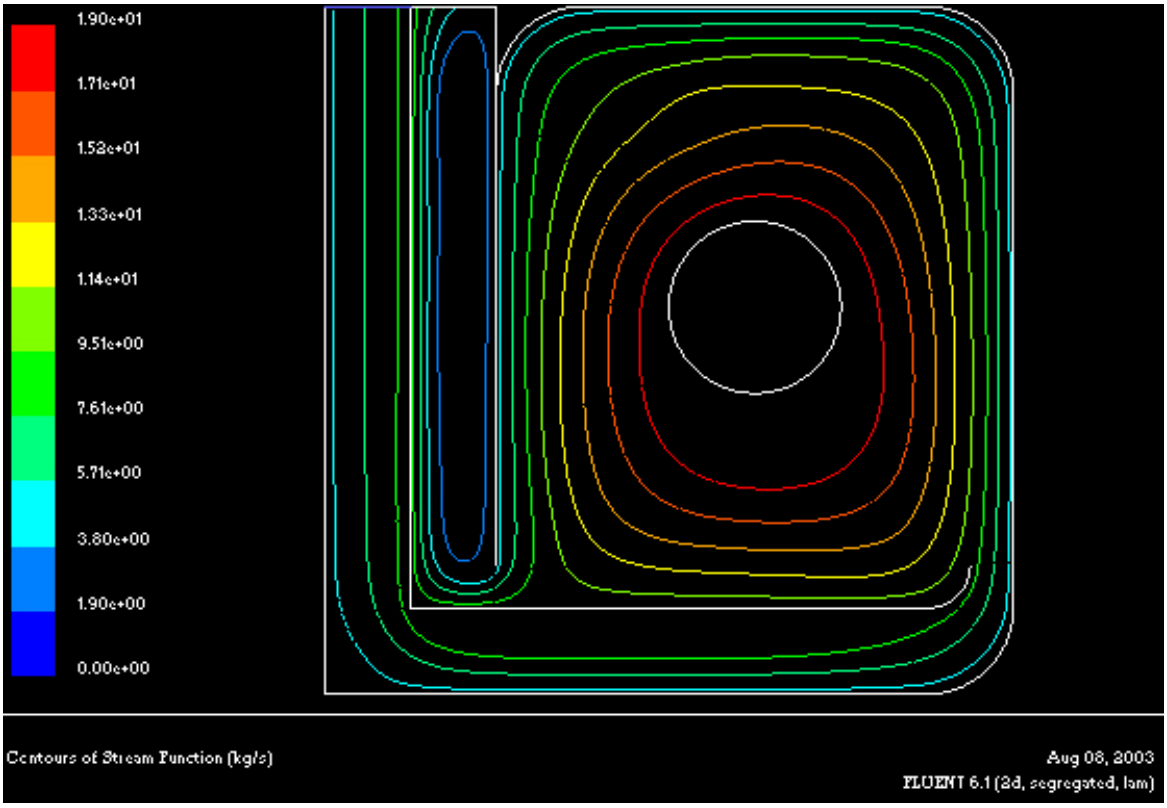

Figure 23.—Flow streamlines.

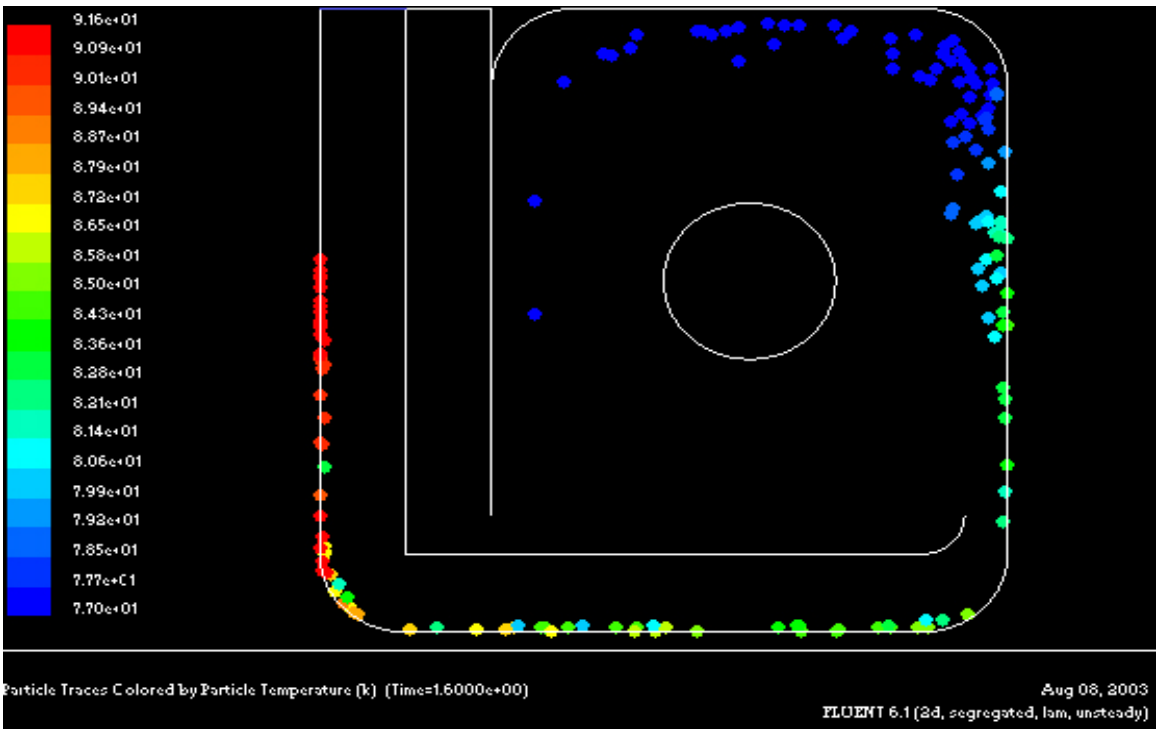

Figure 24.—Bubble trajectories and their temperatures.

References

H. Merte, H.S. Lee and R.B. Keller, "Report on Pool Boiling Experiment Flown on STS–47,STS–57 and STS–60," Report no. UM–MEAM–95–01, Department of Mechanical engineering and Applied Mechanics, University of Michigan, Feb. 1995.

E. Oker and H. Merte, "Semi-Transparent Gold Films as Simultaneous Surfaces Heater and Resistance Thermometer for Nucleate Boiling Study," J. Heat Transfer, vol. 113, pp. 65–68, 1981.

Additional Information

Scaling Analysis

In addition to the drop tower work, we also plan to run terrestrial experiments that can simulate the microgravity condition. The following is a study that provides criteria on how to perform terrestrial experiments that would simulate microgravity conditions.

Basis for Simulating Microgravity with Terrestrial Experiment

Scaling analysis for convective boiling heat transfer.—Flow boiling is a complicated subject because that it is involved with both convection and boiling. First we would investigate the forces that are present in the flow boiling process. The flow boiling behavior is governed by the inertia force of the convection flow and the dynamics behavior of the vapor generated through nucleation and vaporization, which itself is a consequence of the forces acting at the interface between the liquid and vapor phases. These would be more precisely expressed in terms of local force balance.

Flow boiling over a flat plate (applicable to vapor shear-off experiment for ZBO).—For the current evaluation, we would only consider the global nature of the forces as suggested by Merte et al. (Criteria for approximating certain microgravity flow boiling characteristics in earth gravity, Proceedings of the Microgravity Transport Processes in Fluid, Thermal, Biological and Materials Sciences, Banff, Alberta, Canada, 2001)

The potential forces are listed below:

I. Buoyancy – arising from gravity due to density difference between the vapor and liquid.

II. Momentum associated with the liquid flow that is imposed on the vapor bubbles in the form of drags.

III. Interfacial (surface tension) – considered here as liquid/vapor and liquid/solid/vapor. The former Primarily controls the liquid/vapor surface geometry, while the latter controls the adhesion or departure of the vapor bubble from the solid heater surface.

VI. Viscous shear - arising principally from the liquid viscosity.

V. Lift - arising from the externally imposed liquid flow around the vapor bubble and it acts normal to the flow.

VI. Internal vapor pressure - generated by the mean liquid/vapor interface temperature, provides the driving force for vapor bubble growth /collapse dynamics.

For the purpose of assessing the degree to which flow boiling over a flat surface in earth gravity may approximate that in microgravity, advantage will be taken of ratios of certain of the above forces, in particular those associated with the removal of the vapor bubble from its nucleation site on the heater in the inverted horizontal or nearly horizontal position relative to earth gravity. Since the bulk liquid flow is parallel to the heater surface, only those components of the forces that are parallel to the heater surface will be considered, including buoyancy. Because of the absence of terrestrial gravity in space, the normal component of buoyancy as a vapor bubble removal mechanism is eliminated by the inversion of the heater such that the removal of bubble would be effected by other forces. However, the influence of lift, which is also normal to the heater surface, must be given consideration, and could be of special

significance in microgravity. For spherical particles moving in an inviscid fluid parallel to a plane wall, it has been demonstrated that the lift moves the sphere toward the wall. With a viscous fluid, on the other hand, the resulting velocity gradient in duct flow causes the sphere to migrate away from the stationary wall. This away lift force is important for bubble removal in microgravity. In earth gravity, buoyancy acting to push the vapor bubble towards the wall for the case considered here, order of magnitude analysis shows that such away lift can be neglected relative to the buoyancy for the conditions involved in the current experiment. In addition, the internal vapor pressure giving rise to the bubble dynamics will be neglected for present purposes because of its minor effects as compared to other forces. This leaves the forces related to buoyancy, momentum (or inertial drag), surface tension, and viscous shear.

Several dimensionless numbers, defined in terms of ratios of these forces acting on the vapor bubbles, will now be examined to estimate the conditions under which certain aspects of the flow boiling process in microgravity might be approximated in earth gravity. These are:

Richardson number, Ri, = buoyancy/inertia force
Weber number, We, = inertia forced/surface tension
Bond number, Bo, = buoyancy/surface tension
Capillary number, Ca, = viscous force/surface tension
Reynolds number, Re, = inertia force/viscous force
Ca = We/Re

The Capillary number can be expressed as the ratio of the Weber number to the Reynolds number: If the Viscous Drag in the Capillary number were to be replaced by the Inertial Drag, which would correspond to a Reynolds number of unity, the Capillary number would become equivalent to the Weber number. Since lift is being neglected, the Capillary number will be given no further consideration here. Because of the involvement of both vapor and liquid phases, a two-phase Richardson number, $\mathrm{Ri}_{2\phi}$, has been defined in which the buoyant and drag forces acting on a vapor bubble are defined in terms of the bubble radius, the relative velocity between the bubble and the bulk liquid, U_{rel}, and coefficients, C_b and C_d, given as:

$$F_B = c_b (4/3)\pi R^3 g_e \Delta\rho \tag{A1}$$

$$F_D = c_d \pi R^2 \rho_\ell (U_{rel}^2 / 2) \tag{A2}$$

The buoyancy coefficient, C_b, accounts for the difference between a spherical bubble of radius, R, and that of a non spherical bubble of equal mean radius, and C_d is the drag coefficient, determined empirically. The drag force can be considered to be a manifestation of the net bulk flow momentum effects acting on the vapor bubble. The characteristic bubble radius, R, in eqs. (A1) and (A2) is taken to be the departure bubble radius R_d. In the above, g_e is the effective gravity depending on the inclination angle between the heater and the gravity. $\Delta\rho$ is the difference between the liquid and vapor densities. ρ_ℓ is the liquid density and U_{rel} is the relative velocity between the liquid and vapor bubble. If the bubble is stationary with the heater, then U_{rel} is equal to the liquid velocity, U_ℓ. Once the vapor bubble has departed its local nucleation site, it can be considered to no longer directly influence the local heat transfer processes. An expression for the departure radius was obtained from a force balance on a vapor bubble growing from its nucleation site, utilizing eqs. (A1) and (A2), along with a surface tension force, F_s, at the solid/liquid/vapor contact line, as:

$$F_s = C_s \sigma R \tag{A3}$$

The surface tension coefficient, C_s, was obtained empirically by Kirk and Merte (A study of the relative effects of buoyancy and liquid momentum in forced convective nucleate boiling, Final Report, NASA Grant NAG3–1310, 1992) from the balance of buoyancy and surface tension forces for the case of pool boiling by equating eq. (A3) to (A1) with $C_b = 1$. Using the measured departure radius of 0.50 mm for R113, the surface tension coefficient was found to be approximately unity.

An estimate of the drag coefficient, C_d, was determined aslo by Kirk and Merte (1992) empirically from a balance of the buoyant and drag forces, eqs. (A1) and (A2), parallel to a heating surface at which an immediately adjacent spherical bubble was moving. Measurements of the bubble rise velocities, sizes and liquid velocities were made for various orientations of the flat heating surface relative to the horizontal face-up position, such that g_e, in eq. (A1) is replaced by:

$$g_e = g \sin\theta \tag{A4}$$

Where g is earth gravity and θ is the inclination angle (0° heater facing upward and 180° heater facing downward). Over a range of bubble Reynolds numbers from 24 to 920, Kirk and Merte (1992) found that the drag coefficient, C_d, is roughly constant and equal to 0.56. This compares well with the turbulent drag coefficient of 0.50 for a solid sphere.

Taking the ratio of eqs. (A1) and (A2) as the two-phase Richardson number, together with the coefficients given above:

$$\mathrm{Ri}_{2\phi} = F_B / F_D \tag{A5}$$

$$\mathrm{Ri}_{2\phi} = \frac{8 g C_b (\Delta\rho / \rho_\ell) R}{3 C_d U_{rel}^2} \tag{A6}$$

Assuming that both buoyancy and drag act to detach the bubble and the surface tension tends to hold the bubble, then at the bubble departure, we can write :

$$F_b + F_d - F_s = 0 \tag{A7}$$

Next we solve eq. (A7) to obtain the departure radius, R_d, as follows :

$$R_d = \left(\frac{3 C_d \rho_\ell U_{rel}^2}{16 C_d \Delta\rho g_e} \right) \left(\sqrt{1 + \frac{64 C_s C_b \sigma \Delta\rho g_e}{3\pi C_d^2 \rho_\ell^2 U_{rel}^4}} - 1 \right) \tag{A8}$$

Substituting R_d for R in eq. (A6), we obtain the following :

$$\mathrm{Ri}_{2\phi} = (1/2) \left(\sqrt{1 + \frac{64 C_s C_b \sigma \Delta\rho g_e}{3\pi C_d^2 \rho_\ell^2 U_{rel}^4}} - 1 \right) \tag{A9}$$

The best estimates for C_b, C_s and C_d are 1.0, 1.0 and 0.56, respectively based on most boiling conditions as discussed above. With these constants inserted, eq. (A9) becomes :

$$\mathrm{Ri}_{2\phi} = (1/2) \left(\sqrt{1 + \frac{21.7 \sigma \Delta\rho g_e}{\rho_\ell^2 U_{rel}^4}} - 1 \right) \tag{A10}$$

By the same approach, we can show that the two-phase Weber number (inertia drag/surface tension), $\mathrm{We}_{2\phi}$ and the Bond number (buoyancy/surface tension), Bo as follows :

$$\mathrm{We}_{2\phi} = (0.1/M)\left(\sqrt{1+21.7M}-1\right) \tag{A11}$$

$$\mathrm{Bo} = 0.42\left(21.7 - 4\frac{\mathrm{Ri}_{2\phi}}{M}\right) \tag{A12}$$

Where $M = \dfrac{g_e \Delta\rho\sigma}{\rho_\ell^2 U_{rel}^4}$.

The liquid velocity U_ℓ is taken for U_{rel} and g_e is given by eq. (A4).

Equations (A10), (A11) and (A12) are plotted in figures A1, A2 and A3 for R-113, nitrogen and hydrogen at atmospheric pressure, for three orientation angles of 90°, 135° and 175° and the range of velocities used here are 0 to 25 cm/s.

Outcome of the scaling analysis.—For the inclination angle of θ = 180°, the heater is upside down and facing downward, we have the following:

$$\mathrm{Ri}_{2\phi} \to 0$$
$$\mathrm{We}_{2\phi} \to 1$$
$$\mathrm{Bo} \to 0$$

Therefore, when both the $\mathrm{Ri}_{2\phi}$ and the Bo are zero the gravity effects are excluded. For convective flow boiling, if we intend to simulate a microgravity condition in earth gravity we only have to focus on the $\mathrm{Ri}_{2\phi}$ and the Bo because that the buoyancy force is only associated with these two numbers. As for the $\mathrm{We}_{2\phi}$ it only gives an indication on the extent of bubble shape deviation from a sphere. It is generally agreed that a bubble can be approximated as a sphere if the $\mathrm{We}_{2\phi}$ is less than four.

For the inclination angle of 180°, theoretically the buoyancy is totally irrelevant. But in actual experiments, the gravity would still play some role due to the following reasons:

1. The low-level vibrations and shaking of the laboratory floor that are inherent in most buildings would produce buoyancy force purterbations to the boiling experiments.
2. The upward buoyancy force that pushes the bubble against the heater surface could cause the bubble to flatten and have larger base area on the heater surface. As a result, more inertia force might be required to detach the bubble.

Based on these two possible buoyancy effects, we would use the inclination angle of 175° to select the conditions that would allow us to simulate microgravity in earth gravity. In other words, the 5° deviation from the upside down (180°) would hopefully represent the two buoyancy purterbations mentioned above.

For our experiments with R-113, we may conclude that if the liquid velocity is greater than 15 cm/s that would result in both the $Ri_{2\phi}$ and the Bo less than one which allows us to do earth gravity experiment to simulate microgravity conditions.

The other important information we learn from the scaling analysis is that, for all three numbers, R-113 and Nitrogen give almost identical values for the velocity ranges selected. It basically verify that we

will be able to use the R-113 results to predict the nitrogen phenomena for cases that are dominated by the $Ri_{2\phi}$, the Bo and the $We_{2\phi}$. Based on the values of the Richardson number, the buoyancy is negligible for the liquid velocity higher than 20 cm/s.

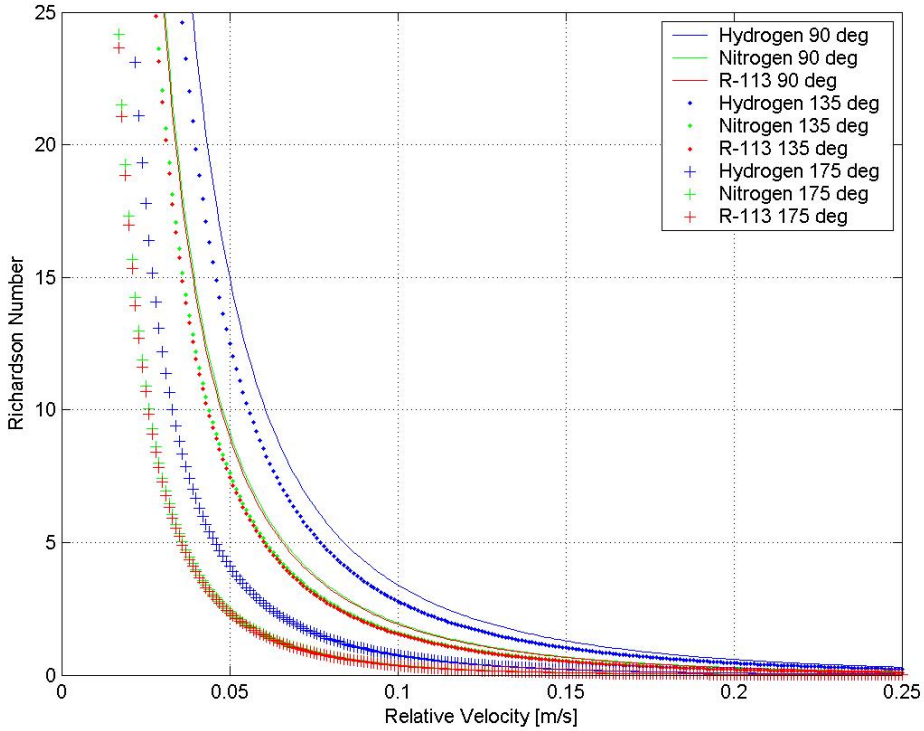

Figure A1.—Richardson number vs. flow velocity.

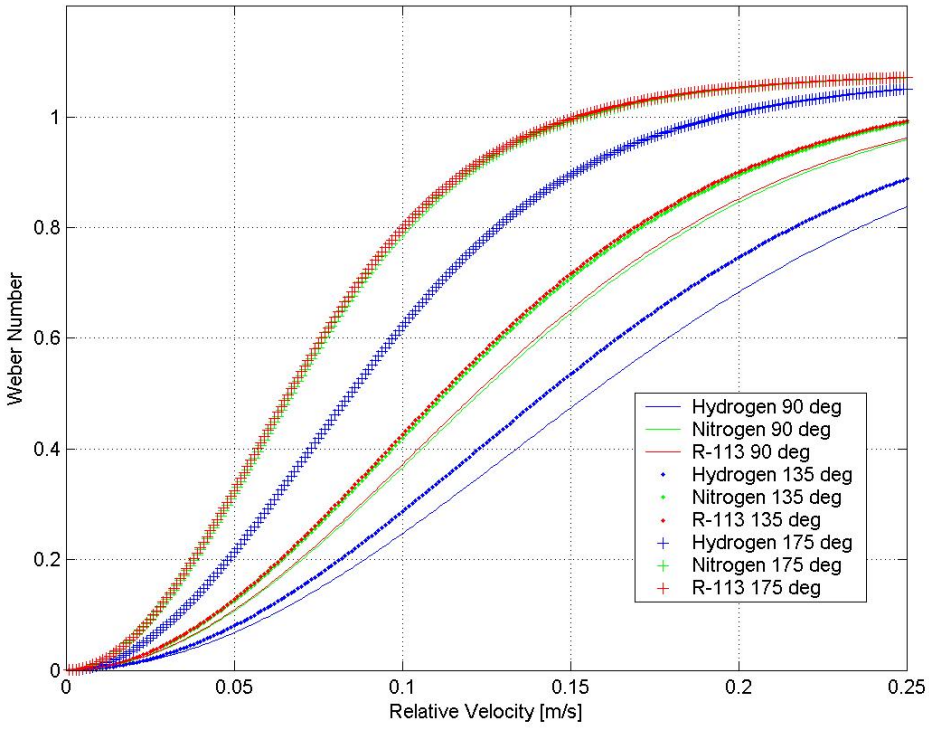

Figure A2.—Weber number vs. flow velocity.

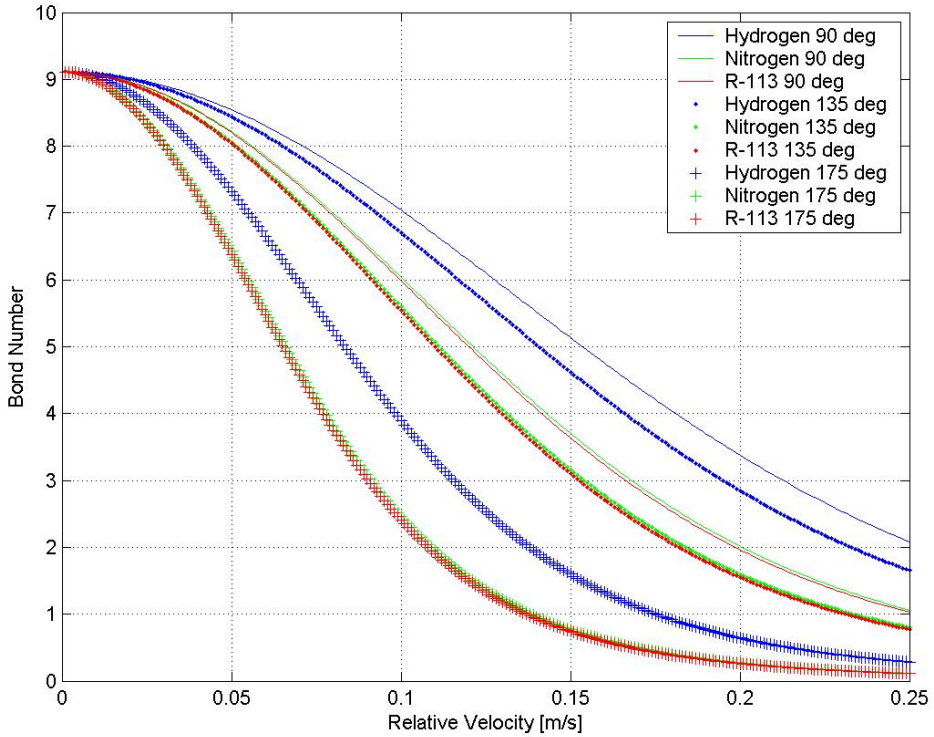

Figure A3.—Bond number vs. flow velocity

Project Title: Fluid Distribution for In-Space Cryogenic Propulsion

Task PI: William Lear, Department of Mechanical and Aerospace Engineering

Project Goals

The ultimate goal of this task is to enable the use of a single supply of cryogenic propellants for three distinct spacecraft propulsion missions: main propulsion, orbital maneuvering, and attitude control. A fluid distribution system is sought which allows large propellant flows during the first two missions while still allowing control of small propellant flows during attitude control. Existing research has identified the probable benefits of a combined thermal management/power/fluid distribution system based on the Solar Integrated Thermal Management and Power (SITMAP) cycle. Both a numerical model and an experimental model are constructed in order to predict the performance of such an integrated thermal management/propulsion system. This research task provides a numerical model and an experimental apparatus which will simulate an integrated thermal/power/fluid management system based on the SITMAP cycle, and assess its feasibility for various space missions. Various modifications are done to the cycle, such as the addition of a regeneration process that allows heat to be transferred into the working fluid prior to the solar collector, thereby reducing the collector size and weight. Fabri choking analysis was also accounted for. Finally the cycle is to be optimized for various space missions based on a mass based figure of merit, namely the System Mass Ratio (SMR).

The theoretical and experimental results from these models are be used to develop a design code (JETSIT code) which is able to provide design parameters for such a system, over a range of cooling loads, power generation, and attitude control thrust levels. The performance gains and mass savings will be compared to those of existing spacecraft systems.

Accomplishments

Overview

After an extensive review of fluid distribution technology, it was decided that the most promising avenue of research for this project would involve a combined thermal management/power generation/ propellant distribution system that is based on the SITMAP cycle. The SITMAP cycle integrates a vapor compression (refrigeration) thermal management subsystem, which uses a jet pump rather than a compressor, and a power subsystem that is essentially a Rankine cycle in which the jet pump replaces a turbine. In the current implementation, the working fluid would be one or more cryogenic propellants. The SITMAP cycle's physical setup within a spacecraft could provide a constant flow of propellant to the spacecraft's extremities, and this flow could easily be tapped into at an ideal location in order to bleed off propellant for attitude control purposes.

This leads to another benefit of the SITMAP cycle for fluid distribution purposes. Because of the SITMAP cycle operational characteristics; there is a region in the cycle where pressurized superheated vapor exists – after the waste heat recovery unit and/or solar collector and before the turbine inlet. This part of the cycle could easily be tapped and the superheated vapor used directly as a thrust source for attitude control.

Using the fluid in its highest energy state within the SITMAP cycle would optimize its effectiveness as a propellant and could eliminate the need for any type of burner, resulting in a simple and more reliable means of spacecraft attitude control. Figure 1 illustrates such a system.

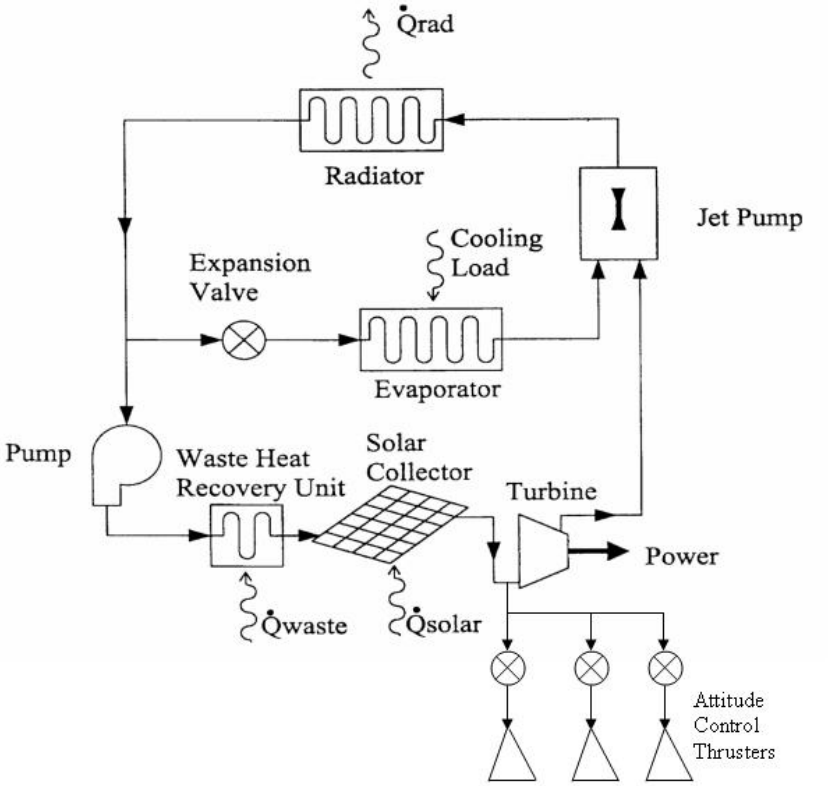

Figure 1.— Solar Integrated Thermal Management and Power (SITMAP) based integrated thermal management/power generation/propellant delivery system.

A parallel University of Florida research project has focused on the numerical and experimental analysis of a SITMAP cycle that does not include a mass flow bleed. The results of this parallel research have been and will continue to be utilized in the development of the modified SITMAP cycle (with a mass flow bleed, or bleeds). Both computer codes and experimental apparatus have been constructed which will be progressively modified for use in the analysis of a modified SITMAP cycle.

Research work done on the SITMAP cycle is comprised of two parts, an analytical part, and an experimental part. Following are summaries of both parts of the program.

Analytical Program

The analytical part went through different stages starting with the development of a computer code (JetSit, which is short for Jet-pump and SITMAP) for the thermodynamic simulation of the cycle. An expression was then needed to measure the mass based performance of the cycle. For that purpose a System Mass Ratio (SMR) expression was derived and incorporated in the simulation code JetSit. Further development of the code involved incorporating thermodynamic properties software to calculate thermodynamic properties instead of the use of a data file. The software used is called REFPROP and is made by NIST. Recuperation was then included in the SITMAP cycle as an effort to decrease the weight of the system (see fig. 2). Fabri choking is an important phenomenon that might take place in the mixing chamber of the Jet-pump. Fabri choking refers to conditions when the primary flow expands in the mixing chamber constricting the available flow area for the secondary stream, causing it to accelerate. It is possible for the secondary stream to reach sonic velocity, therefore causing the secondary mass flow rate to become independent of downstream conditions. The Fabri choking analysis was included in the JetSit cycle simulation code to make sure that the input entrainment ratios are physically possible.

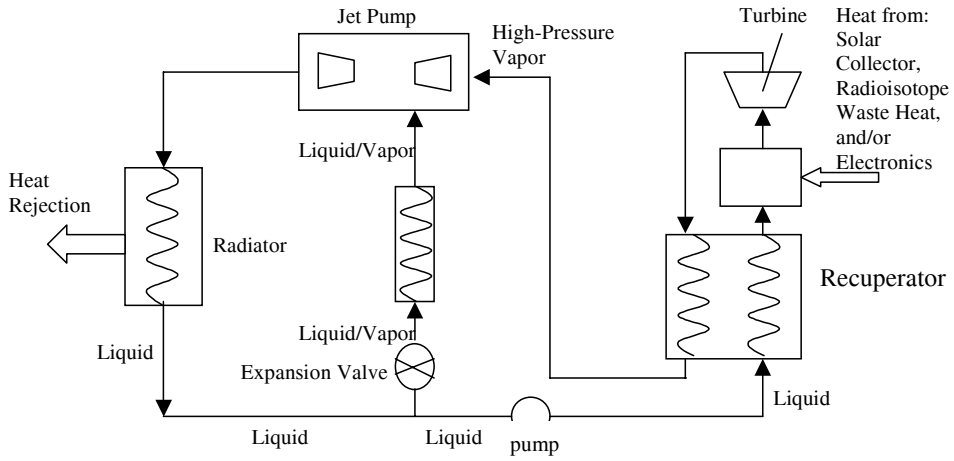

Figure 2.—Schematic of the SITMAP cycle with regeneration.

The current and most recent stage of the analytical part in the SITMAP program is the optimization of the cycle to minimize the mass for different space missions. To achieve this, an optimization program was incorporated in the cycle simulation code. The optimization routine is written by Leon Lasdon of the University of Texas in Austin and it utilizes a Generalized Reduced Gradient algorithm, and is hence called GRG2.

The most results of the analytical part of the program are presented below. The "Additional Information" section includes the more recent work that hasn't been published yet, including the Fabri choking, and optimization analyses.

Results of the preceding analysis are presented in tables 1 through 5. Each of the five sets has the same primary inlet pressure, while varying the secondary pressure. The ratio $\left(P_{pi}/P_{si}\right)_{bo}$ is the break-off pressure ratio. This is the ratio below which the flow operates either in the mixed regime or in the saturated supersonic regime (inlet choking regime), and above which the flow operates either in the mixed regime or the supersonic regime (Fabri choking regime).

There are some general trends that can bee seen in all data sets. First, once the pressure ratio P_{pi}/P_{si} is larger than its break-off value, ϕFabri becomes the upper limit (supersonic flow regime). When P_{pi}/P_{si} is less than its break-off value the limiting value for the entrainment ratio is ϕinlet choke (saturated supersonic regime). For any line of data in all data sets, if the entrainment ratio drops below the limiting value, the jet-pump will be operating in the "mixed regime," where ϕ is dependent on the downstream conditions (or the back pressure). It should also be noted that as long as the ratio P_{pi}/P_{si} is above the break-off ratio, the pressure ratio P_{se}/P_{ne} drops below unity, which is important for the primary flow to expand into the secondary causing Fabri choking to take place.

The second general trend is the increase of the limiting value of the entrainment ratio with higher secondary pressure. This should be expected because since the primary inlet pressure is fixed, a higher secondary stagnation pressure corresponds to a lower backpressure. The lower backpressure allows for more secondary flow entrainment before choking occurs.

Data sets 1 to 3 show the effect of the ratio of primary and secondary stagnation temperatures on the maximum entrainment ratio. Figure 3 is a graphical representation of tables 1 to 3. It can be seen that higher entrainment ratios can be achieved for higher stagnation temperature ratios. The effect of T_{pi}/T_{si} on maximum ϕ is less significant at higher P_{pi}/P_{si} ratios, but the same trend still holds.

Tables 3 and 4 show the effect of varying the primary nozzle geometry. Figure 4 shows the same effect in graphical form. It can be seen that lower A_{nt}/A_{ne} ratios (i.e., higher M_{ne}) allow more secondary flow entrainment. This makes sense, since the entrainment mechanism is by viscous interaction between

the secondary and primary streams. Therefore, faster primary flow should be able to entrain more secondary flow.

Tables 4 and 5 show the effect of the area ratio A_{ne}/A_{se}. Figure 5 shows that lower primary-to-secondary area ratios allow for more entrainment. This trend is expected since a lower area ratio means more area for the secondary flow and thus more secondary mass flow rate. Figure 6 shows the variation of the compression ratio with P_{pi}/P_{si}, for different jet-pump geometries. The compression ratio was calculated for maximum allowable entrainment ratio. It can be seen that as the ratio P_{pi}/P_{si} increases the compression ratio increases as well, which is expected.

TABLE 1.—DATA SET NO. 1. $T_{pi} = 200$, $T_{si} = 100$, $A_{nt}/A_{ne} = 0.25$, $A_{ne}/A_{se} = 0.1$

Ppi	Psi	Ppi / Psi	PHlinlet	PHlfabri	Pse	Pse/Pne	(Ppi / Psi)bo	Pne
3200000	1600000	2	144.996		752031.170	7.30495	16.51	102948
3200000	1066666.667	3	85.465		766654.157	7.447		Mne
3200000	640000	5	11.1029		366170.684	3.55685		3.07605
3200000	320000	10	5.58389		169866.433	1.65002		
3200000	213333.3333	15	3.67901		113017.917	1.09781		
3200000	160000	20		2.683032	100556.41	0.97677		
3200000	128000	25		2.083661	86249.331	0.83779		
3200000	106666.6667	30		1.676613	76063.5258	0.73885		
3200000	91428.57143	35		1.383796	68217.1583	0.66264		
3200000	80000	40		1.164268	61920.2561	0.60147		
3200000	71111.11111	45		0.9936368	56761.0127	0.55136		
3200000	64000	50		0.8574538	52445.6223	0.50944		

TABLE 2.—DATA SET NO. 2. $T_{pi} = 100$, $T_{si} = 100$, $A_{nt}/A_{ne} = 0.25$, $A_{ne}/A_{se} = 0.1$

Ppi	Psi	Ppi / Psi	PHlinlet	PHlfabri	Pse	Pse/Pne	(Ppi / Psi)bo	Pne
3200000	1600000	2	23.2413		752031.17	1.8963	4.62411	396579
3200000	1066666.667	3	13.6961		766654.081	1.93317		Mne
3200000	533333.3333	6		1.416579	376543.452	0.94948		2.57789
3200000	320000	10		0.6935064	264842.461	0.66782		
3200000	213333.3333	15		0.3329346	195893.323	0.49396		

TABLE 3.—DATA SET NO. 3. $T_{pi} = 400$, $T_{si} = 100$, $A_{nt}/A_{ne} = 0.25$, $A_{ne}/A_{se} = 0.1$

P_{pi}	P_{si}	P_{pi}/P_{si}	$\phi_{inletchoke}$	ϕ_{Fabri}	ϕ	P_{se}/P_{ne}	P_{de}/P_{si}	$(P_{de}/P_{si})_{bo}$	P_{ne}
3200000	1600000.000	2	213.904		213.904	7.968	0	18.009699	94375.5814
3200000	640000.000	5	16.3609		16.36093	3.880	1.0485		M_{ne}
3200000	320000.000	10	8.22779		8.227792	1.800	1.19303		2.957
3200000	213333.333	15	5.42427		5.424266	1.198	1.34552		
3200000	160000.000	20		3.9997	3.999688	0.878	1.49797		
3200000	128000.000	25		3.1214	3.121448	0.773	1.65079		
3200000	106666.667	30		2.5321	2.532101	0.691	1.80439		
3200000	91428.571	35		2.1111	2.111098	0.627	1.95876		
3200000	80000.000	40		1.7958	1.795751	0.574	2.11383		
3200000	71111.111	45		1.5509	1.55091	0.543	2.26951		
3200000	64000.000	50		1.359	1.359	0.529	2.427		

TABLE 4.—DATA SET NO. 4. $T_{pi} = 400$, $T_{si} = 100$, $A_{nt}/A_{ne} = 0.6$, $A_{ne}/A_{se} = 0.1$

P_{pi}	P_{si}	P_{pi}/P_{si}	$\phi_{inletchoke}$	ϕ_{Fabri}	ϕ	P_{se}/P_{ne}	P_{de}/P_{si}	$(P_{de}/P_{si})_{bo}$	P_{ne}
3200000	1600000.000	2	89.060			1.816	0.637	4.433	414056.656
3200000	640000.000	5		6.738	6.704	0.995	1.187		M_{ne}
3200000	320000.000	10		3.052	3.052	0.575	1.508		1.996
3200000	213333.333	15		1.810	1.810	0.420	1.842		
3200000	160000.000	20		1.194	1.194	0.334	2.183		
3200000	128000.000	25		0.832	0.832	0.278	2.527		
3200000	106666.667	30		0.594	0.594	0.239	2.876		
3200000	91428.571	35		0.428	0.428	0.210	3.228		
3200000	80000.000	40		0.305	0.305	0.187	3.583		
3200000	71111.111	45		0.2109	0.210895	0.165	3.941		
3200000	64000.000	50		0.137	0.137	0.153	4.301		

TABLE 5.—DATA SET NO. 5. $T_{pi} = 400$, $T_{si} = 100$, $A_{nt}/A_{ne} = 0.25$, $A_{ne}/A_{se} = 0.3$

P_{pi}	P_{si}	P_{pi}/P_{si}	$\phi_{inletchoke}$	ϕ_{Fabri}	ϕ	P_{se}/P_{ne}	P_{de}/P_{si}	$(P_{de}/P_{si})_{bo}$	P_{ne}
3200000	1600000.000	2	71.301		71.301	7.968	0.715	18.009699	94375.581
3200000	640000.000	5	5.459		5.459	3.876	1.131		M_{ne}
3200000	320000.000	10	2.745		2.745	1.800	1.658		2.957
3200000	213333.333	15	1.810		1.810	1.198	2.185		
3200000	160000.000	20		1.008	1.008	1.112	2.712		
3200000	128000.000	25		0.789	0.789	0.942	3.108		
3200000	106666.667	30		0.631	0.631	0.850	3.507		
3200000	91428.571	35		0.513	0.513	0.772	3.908		
3200000	80000.000	40		0.421	0.421	0.706	4.311		
3200000	71111.111	45		0.401	0.401	0.650	4.561		
3200000	64000.000	50		0.348	0.348	0.602	4.716		

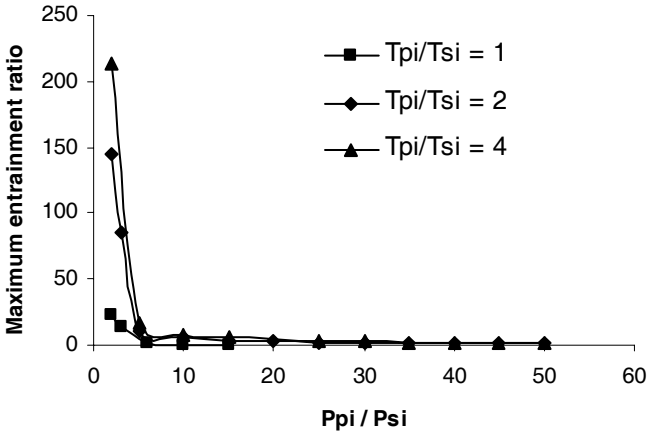

Figure 3.—Maximum entrainment ratio variation versus the stagnation pressure ratio for different stagnation temperatures ratio. Based in ϕinletchoke and ϕFabri only

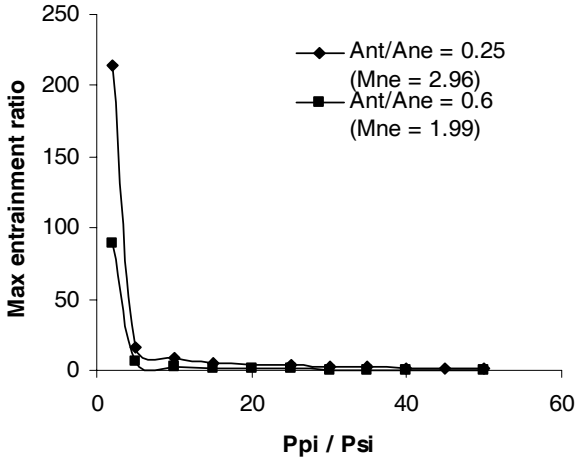

Figure 4.—Maximum entrainment ratio variation versus the stagnation pressure ratio for different primary nozzle geometry. Based in ϕinletchoke, and ϕFabri only.

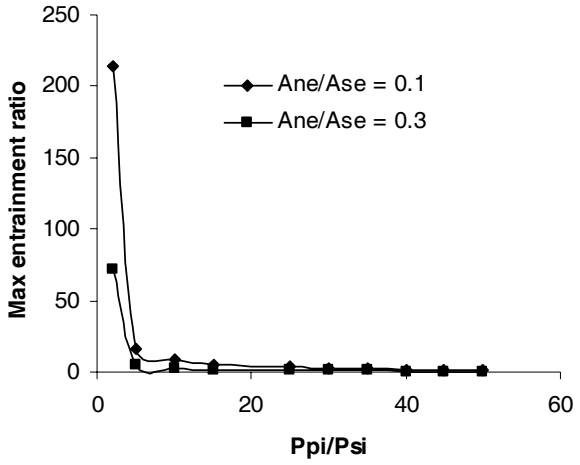

Figure 5.—Maximum entrainment ratio variation versus the stagnation pressure ratio for different primary to secondary nozzles area ratios. Based in ϕinletchoke, and ϕFabri only.

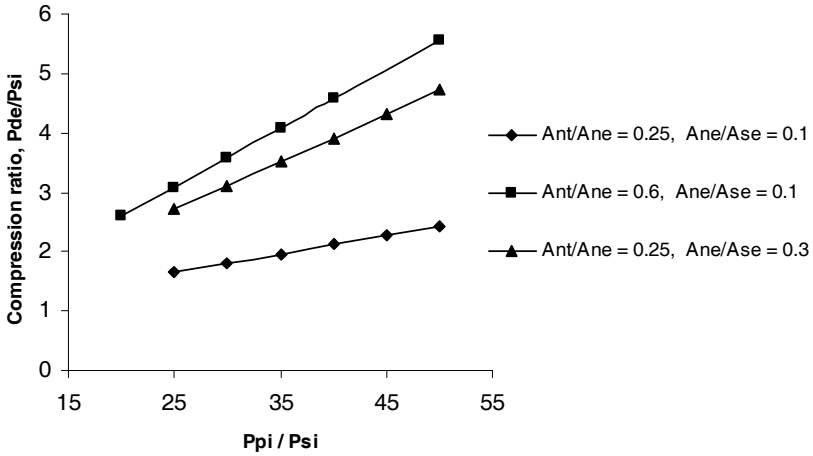

Figure 6.—Compression ratio variation versus the stagnation pressure ratio.

Experimental Program

The initial consideration in the experimental design process was to conceptually develop the best method of designing an ejector test rig that will be used to study the phenomena of two-phase flow mixing and compression. The primary design criterion established stated that the ejector primary and secondary nozzle inlet states were to be varied over a wide range of pressures, temperatures, and qualities in order to obtain a general database. The wide range of conditions is vital in thoroughly investigating the effects to two-phase flow. A second design requirement dealt with the ability to change the area ratios of the primary and secondary inlet and outlet nozzles. The simulation program JetSit aided in the design of the ejector nozzles.

The first and most important design feature to accommodate was how to vary nozzle inlet states. Conceptually, some kind of loop must be designed to heat and cool the primary and secondary fluid flow. This heating and cooling process would necessarily incorporate the use of one or more heat exchangers. In order to gain control of the pressure, a valve (e.g., adjustable throttling valve) would be needed. The working fluid must also be circulated through the loop; consequently, a pump would be needed. All of the

components listed above are basic parts of a system operating on the SITMAP cycle. From this reasoning it was resolved that in order to gain relatively good control of the experimental apparatus, all components of that system would need to be incorporated. Since it was deemed advantageous to also obtain system-level data for the SITMAP cycle, the choice of ejector rig design was driven towards implementing that cycle directly.

Another important design consideration was the selection of a working fluid for the two-phase flow ejector test rig. The main criterion used in the fluid selection involved the temperature and pressure ranges where the fluid would be in the two-phase region. For safety reasons it was decided that the loop would be operated near ambient temperature and pressure. Information about individual fluids was found by examining their Material Safety Data Sheets (MSDS). Those sheets provide information that cover hazardous ingredients, health effects, handling details, fire and explosion hazard data, first-aid procedures, and critical fluid properties. An important critical fluid property found in the MSDS is the boiling point of a fluid. Since the fluid will be operated in the two-phase region, only fluids with a boiling point temperature slightly above ambient temperature were considered. Based on this information, R-141b was selected. Once the working fluid was selected, the components were sized. Shown below in Figure 7 is a schematic of the final layout of the experimental setup.

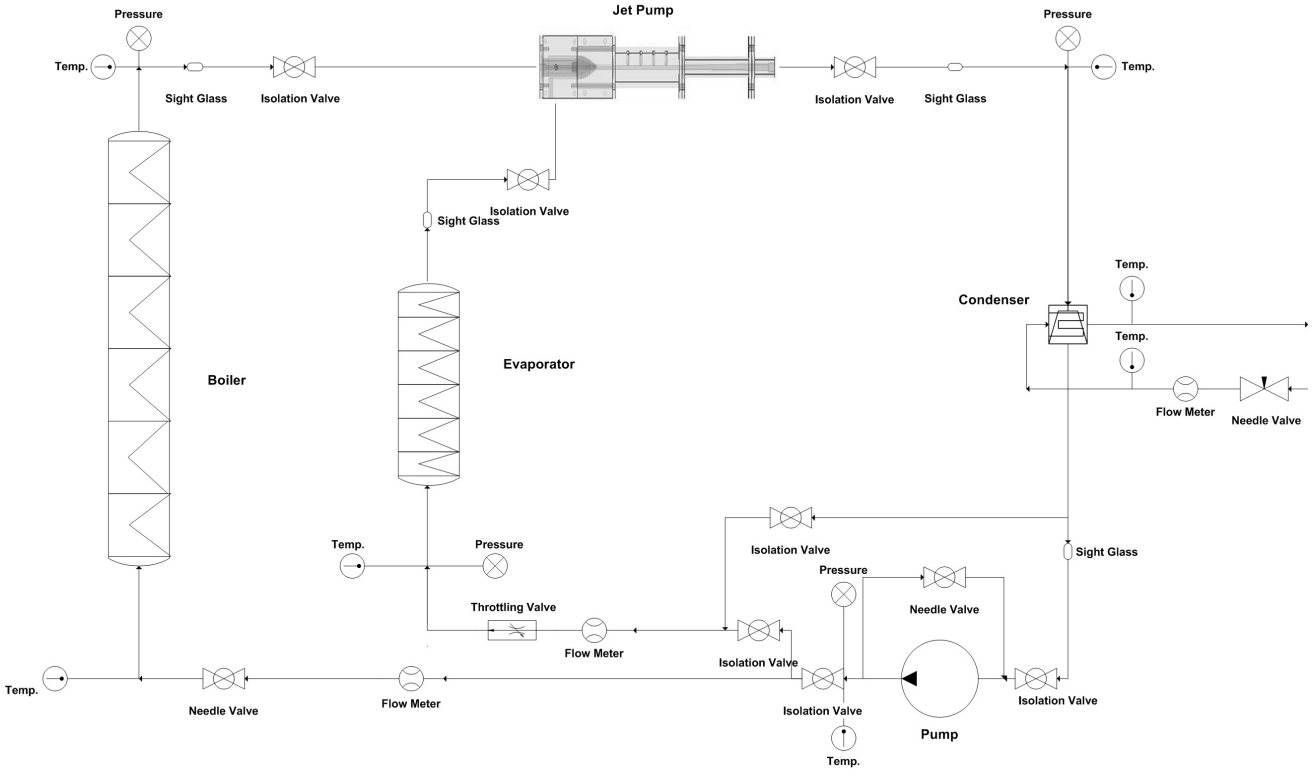

Figure 7.—Schematic of the experimental testing apparatus

Nomenclature

A	cross-sectional area, m^2
a	speed of sound, m/s
COP	coefficient of performance, dimensionless
h	specific enthalpy, kJ/kg
M	Mach number, dimensionless
m	mass, kg
$\dot{m}$	mass flow rate, kg/s
P	pressure, MPa
P_r	compression ratio
Q`	heat transfer rate, kW
r	heat exchanger pressure ratio
T	temperature, °C
V	velocity, m/s
w`	work rate, kW
ϕ	Entrainment ratio, $\dot{m}_s / \dot{m}_p$
ρ	Density, kg/m^3

Subscripts

de	diffuser exit
ei	evaporator inlet
evap	evaporator
me	mixing chamber exit
*n*2	primary flow passage where fabri choking occurs
ne	primary nozzle exit
nt	primary nozzle throat
p	primary flow
pi	primary nozzle inlet
pe	pump exit
pump	mechanical pump
rad	radiator
re	radiator exit
s	secondary flow
*s*2	secondary flow passage where fabri choking occurs
sc	solar collector
se	secondary flow exit
si	secondary flow inlet
ss	state immediately downstream of shock wave
i	turbine
ti	turbine inlet
ts	isentropic turbine exit state

Additional Information

Fabri Choking Analysis

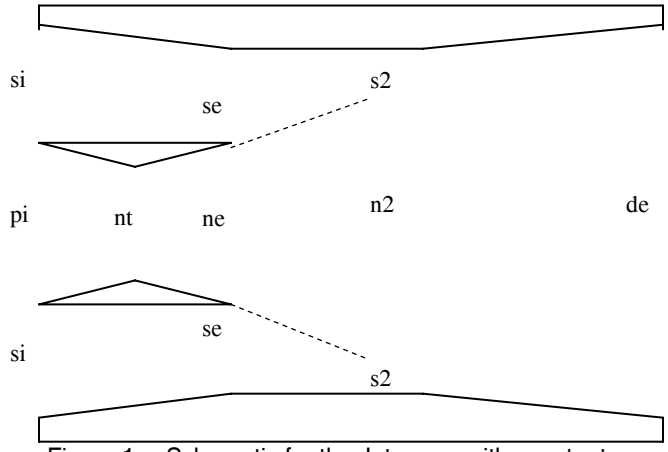

Figure 1.—Schematic for the Jet-pump with constant area mixing, showing the Fabri choked state s2.

The momentum equation for the control volume over the mixing chamber can be written as

$$P_{se}A_{se} + P_{ne}A_{ne} - P_{s2}A_{s2} - P_{n2}A_{n2} = \dot{m}_p V_{n2} + \dot{m}_s V_{s2} - \dot{m}_p V_{ne} - \dot{m}_s V_{se} \tag{1a}$$

dividing by $\dot{m}_p$ yields

$$\frac{1}{\dot{m}_p}\left(P_{se}A_{se} + P_{ne}A_{ne} - P_{s2}A_{s2} - P_{n2}A_{n2}\right) = \left(V_{n2} - V_{ne}\right) + \phi_{Fabri}\left(V_{s2} - V_{se}\right) \tag{1b}$$

$$\therefore \phi_{Fabri} = \frac{\left(P_{se}A_{se} + P_{ne}A_{ne} - P_{s2}A_{s2} - P_{n2}A_{n2}\right)}{\dot{m}_p\left(V_{s2} - V_{se}\right)} - \frac{\left(V_{n2} - V_{ne}\right)}{\left(V_{s2} - V_{se}\right)} \tag{1c}$$

$$\therefore \phi_{Fabri} = \frac{\left(P_{se} + P_{ne}\dfrac{A_{ne}}{A_{se}} - P_{s2}\dfrac{A_{s2}}{A_{se}} - P_{n2}\dfrac{A_{n2}}{A_{ne}}\dfrac{A_{ne}}{A_{se}}\right)}{\rho_{ne}V_{ne}\dfrac{A_{ne}}{A_{se}}\left(V_{s2} - V_{se}\right)} - \frac{\left(V_{n2} - V_{ne}\right)}{\left(V_{s2} - V_{se}\right)} \tag{1d}$$

The iteration scheme starts by guessing a value for P_{se}, knowing that $s_{se} = s_{si}$, that defines the state (*se*). From the energy equation

$$V_{se} = \left[2\left(h_{si} - h_{se}\right)\right]^{1/2} \tag{2}$$

then ϕ_{Fabri} can be calculated as

$$\phi_{Fabri} = \frac{\rho_{se} V_{se} A_{se}}{\rho_{ne} V_{ne} A_{ne}} \tag{3}$$

It should be noted that the area ratio A_{ne}/A_{se} is an input to the SITMAP code.

Then a guess is made for P_{s2}, and $s_{s2} = s_{se}$, that defines the state ($s2$). The velocity V_{s2} can be obtained from the energy equation between *se* and *s*2

$$V_{s2} = \left[2\left(h_{se} - h_{s2} + \frac{V_{se}^2}{2} \right) \right]^{1/2} \tag{4}$$

calculate $M_{s2} = \frac{V_{s2}}{a_{s2}}$, and check if it is equal to 1. If not another value for P_{s2} is guessed till $M_{s2} = 1$.

The area ratio A_{s2}/A_{se} can be calculated from the continuity equation between *se* and *s*2,

$$\frac{A_{s2}}{A_{se}} = \frac{\rho_{se} V_{se}}{\rho_{s2} V_{s2}} \tag{5}$$

knowing that for constant-area mixing $A_{ne} + A_{se} = A_{s2} + A_{n2}$, then

$$\frac{A_{n2}}{A_{ne}} = 1 + \frac{A_{se}}{A_{ne}} - \left(\frac{A_{s2}}{A_{se}} \frac{A_{se}}{A_{ne}} \right) \tag{6}$$

From eq.(1d) another value for ϕ_{Fabri} can be obtained. Iterate on P_{se} till the values for ϕ_{Fabri} from eqs. (1d) and (3) match.

ϕ_{Fabri} is the maximum possible entrainment ratio for a given geometry and inlet states. Therefore the simulation code JetSit sets $\phi = \phi_{Fabri}$, if the input value is greater than ϕ_{Fabri}.

Optimization Analysis

As mentioned before the optimization analysis is performed by incorporating a Generalized Reduced Gradient algorithm into the simulation code. The optimization algorithm is written by Leon Lasdon of the University of Texas in Austin, and is called GRG2.

All the input variables to the simulation program JetSit are the variables in the optimization process. A list of these variables is

- Jet-pump primary inlet pressure, P_{pi}
- Jet-pump primary inlet entropy, S_{pi}.
- Jet-pump secondary inlet pressure, P_{si}
- Jet-pump secondary entropy, S_{si}
- Jet-pump entrainment ratio, ϕ
- Area ratio A_{nt}/A_{ne} in the jet-pump primary nozzle
- Area ratio A_{ne}/A_{se} in the jet-pump
- Turbine inlet pressure, P_{ti}

The constraints on the optimization process are

- $P_{ti} - P_{te}$ > 0
- $P_{pe} - P_{re}$ > 0
- $P_{pi} - P_{si}$ > 0
- $P_{jpe} - P_{se}$ > 0
- Q_{evap} > 0
- Q_{boiler} > 0
- Q_{cond} > 0
- SMR > 0 (objective function, to be minimized)

The objective function is the SMR, which is to be minimized for space applications. All the optimization variables are changed within a specified range to obtain the minimum value for the objective function, SMR, provided all the aforementioned constraints are satisfied.

The most recently published paper on the experimental work is shown in reference 1.

References

1. J.A. Bray, W.E. Lear, and S.A. Sherif, "Experimental Study of a Constant-Area Ejector with Two-Phase Fluid," Proceedings of the FEDSM'03 4TH ASME/JSME Joint Fluids Engineering Conference, Honolulu, Hawaii, USA, July 6–11, 2003, FEDSM2003–45703.

Project Title: New Propellants and Cryofuels

Task PI: Neil S. Sullivan, Department of Physics
Co-I: Jaha Hamida
NASA Contact: Bryan Palasezski, NASA Glenn Research Center
External collaborator: V. Kokshenev, Univ. Federale de Minas Gerais, Brazil

Project Goals

The proposed research will investigate the stability and cryogenic properties of solid propellants that are critical to NASA's goal of realizing practical propellant designs for future spacecraft. We will determine the stability and thermal properties of a solid hydrogen-liquid helium stabilizer in a laboratory environment in order to design a practical propellant. In particular, we will explore methods of embedding atomic species and metallic nano-particulates in hydrogen matrices suspended in liquid helium. We will also measure the characteristic lifetimes and diffusion of atomic species in these candidate cryofuels.

The most promising large-scale advance in rocket propulsion is the use of atomic propellants; most notably atomic hydrogen stabilized in cryogenic environments, and metallized-gelled liquid hydrogen (MGH) or densified gelled hydrogen (DGH). The new propellants offer very significant improvements over classic liquid oxygen/hydrogen fuels because of two factors: (1) the high energy-release, and (ii) the density increase per unit energy release. These two changes can lead to significant reduced mission costs and increased payload to orbit weight ratios. An achievable 5 to 10 percent improvement in specific impulse for the atomic propellants or MGH fuels can result in a doubling or tripling of system payloads.

The high-energy atomic propellants must be stored in a stabilizing medium such as solid hydrogen to inhibit or delay their recombination into molecules. The goal of the proposed research is to determine the stability and thermal properties of the solid hydrogen-liquid helium stabilizer. Magnetic resonance techniques will be used to measure the thermal lifetimes and the diffusive motions of atomic species stored in solid hydrogen grains. The properties of metallic nano-particulates embedded in hydrogen matrices will also be studied and analyzed. Dynamic polarization techniques will be developed to enhance signal/noise ratios in order to be able to detect low concentrations of the introduced species. The required lifetimes for atomic hydrogen and other species can only be realized at low temperatures to avoid recombination of atoms before use as a fuel.

Goals for 2005

I. Manufacture and characterization of particulates.—The goal is to test different techniques for producing the solid hydrogen matrices; slow adiabatic cooling of gas mixtures versus rapid injection of hydrogen gas into a pressurized cold helium gas cell. We propose to determine the particle size, diffusion constants and lifetimes of species introduced into matrices prepared by each method to determine optimum conditions for producing a stable cryogenic environment.

II. Introduction of metallic species into the hydrogen particles.—We will test methods of introducing metals into the hydrogen matrices by using two different techniques: (i) radio-frequency (RF) discharge dissociation of molecular hydrogen in the cryogenic injection path, and (ii) evaporation of metallic atoms from hot filaments in the hydrogen/helium gas stream in the condensation stream. Magnetic resonance (MR) techniques are the most effective for studying the atomic species *in-situ* because the MR frequency of each species is unique and can be studied independently. By this means we can determine the stability and obtain information about the surroundings of different atomic species.

Accomplishments

Samples of finely divided hydrogen and methane suspended in liquid helium have been made. Two different methods were tested: condensation from gas mixtures onto cold surface, and injection of H_2/He gas mixtures into cold helium gas.

The thermal characteristics, notably the relaxation times and thermal diffusion were determined form NMR measurements of the relaxation times T_2 and T_1 that are directly related to the critical path of thermal stability and the internal diffusion of the host matrix.

Methane samples were explored and found to be significantly more favorable than hydrogen slush. The two cryogenic matrices were compared by measuring T_1 and T_2 on CH_4/He slush and comparing with H_2/He slush.

Important Conclusions

Based on our experimental findings we conclude that solid H_2 is not suitable as a host matrix due to the strong surface interactions of ortho-hydrogen molecules with helium at the surface of the hydrogen granules. Since solid H_2 has a strong surface scattering due to its large electric quadrupole moment and its rotational motion that persists to low temperatures, we explored solid methane which has no quadrupole moment as a new matrix.

The results determined from the analysis for the microscopic correlation times τ leads to the following conclusions:

- For hydrogen slush the NMR relaxation rate is consistent with scattering at grain boundaries and/or surface (due to large quadrupole moment Q of hydrogen).
- For methane slush the NMR relaxation rate is consistent with the limiting factor in thermalization being internal diffusion as opposed to surface scattering.
- In terms of a host matrix for atomic propellants methane is therefore a better host than hydrogen because the grains of methane are better isolated from the helium bath.

New Results on CH_4/He Slush

From spin-spin relaxation times for freshly prepared methane-helium slush at 4.2 K we found two different exponents which show the existence of two time scales in the system. As methane has a very complex ground state at low temperature we carried out our measurement on CH_4/He slush as the sample was aging with time. The new results show more than one time scales as the sample was aged.

Publications and Presentations

1. Marcin Matusiak, Jaha Hamida, Gary G. Ihas, Neil Sullivan, *NMR measurements in hydrogen/helium slush at 4.2 K*, Bull. Am Phys. Soc. **48**, 928 (2003).
2. M. Matusiak, J.A. Hamida, G.G. Ihas, N.S. Sullivan, *Measurements of the nuclear spin relaxation times for small grains of solid hydrogen suspended in liquid helium,* Presented at Quantum fluids and Solids International Symposium, 2003.
3. M. Matusiak, J.A. Hamida, G.G. Ihas and N.S. Sullivan, Journal of Low Temperature Physics (to be published).
4. J.A. Hamida and N.S. Sullivan, *Transport properties of bulk hydrogen and hydrogen-helium slush at 4 MHz using NMR measurements,* Bull. Am. Phys. Soc. **49**, 550 (2004).
5. J.A. Hamida and N.S. Sullivan, Nuclear spin relaxation times in hydrogen-helium and methane-helium slush at 4 MHz using pulse NMR, was presented at APS March Meeting 2005.
6. J.A. Hamida and N.S. Sullivan, *Nuclear Spin Relaxation Times for Methane-Helium "Slush" at 4 MHz using Pulsed NMR* submitted to the JLTP, Proceedings of the Internat. Low Temp Conference, Orlando, 2005.

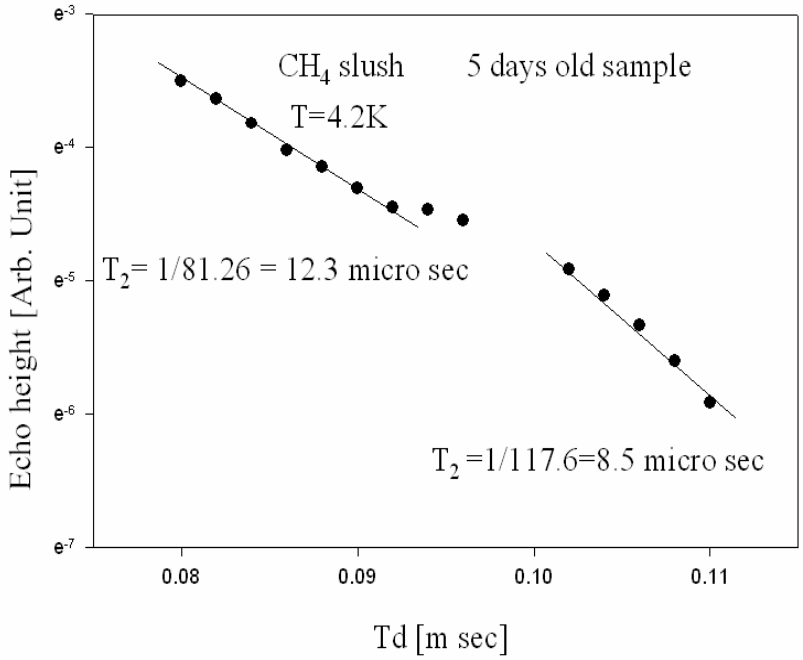

Figure 1.—Spin-spin relaxation times for methane-helium slush at 4.2 K for 5 days old sample. Two different exponents show existence of two time scales in the system.

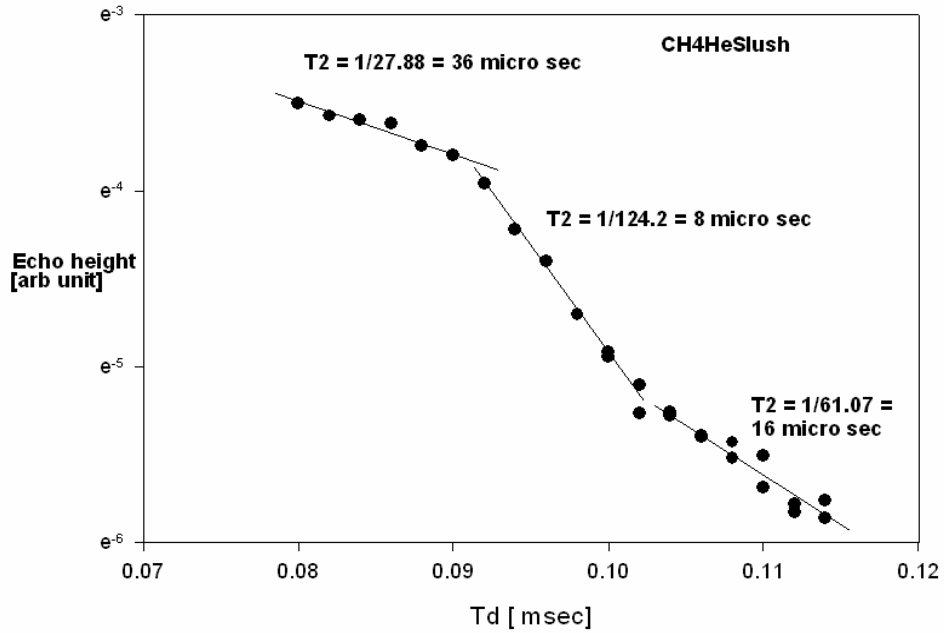

Figure 2.—Spin-spin relaxation times for methane-helium slush at 4.2 K for 21 days old sample. Three exponents show three different time scales in the system.

Project Title: Ortho-Para Hydrogen Ratiometry

Task PI: Neil S. Sullivan, Department of Physics
Collaborator: Dawei Zhou

Project Goals

The research is devoted to developing efficient techniques to measure the ratio of the ortho and para hydrogen concentrations in gaseous samples. Special cells have been designed to measure the thermal conductivity of the gas mixtures at temperatures in the vicinity of 100 K. The thermal conductivity is very different for the two molecular species and this enables one to determine the ratio of ortho to para hydrogen very reliably. The effort has been focused on the need for a fast, high accuracy measurement using a simple compact cell. Tests of the design have been successful, and the last trimester of research was dedicated to optimizing an electronic readout package and demonstrating the sensitivity, stability, and speed of response of the ratiometer. We have also developed the basic design for a cryogen free ratiometer**.** We have also explored the development of high efficiency ortho-para converters.

Methods of measuring the ortho-para hydrogen ratio is very important for the manufacture, transport and storage of liquid hydrogen, and therefore critical for the space missions of NASA where liquid hydrogen fuels are employed. Because of the large heat of ortho-para conversion (670 J/g), incomplete conversion during liquefaction results in severe losses due to boil-off during storage and transport. Most manufacturers use a two-stage catalytic converter, at 77 K, and at 20.3 K in the liquefying process. At 300 K, the equilibrium concentration is 75 percent ortho, while at the boiling point (20.3 K), the equilibrium ortho concentration is 0.21 percent. The conversion at 77 K can produce 50 percent para-H_2, and the remaining conversion at 20.3 K consumes a significant fraction (~ 50 percent) of liquid hydrogen. From these considerations, one of the most important considerations in the production and storage of liquid hydrogen is the need for efficient cost-effective means of conversion from ortho to para hydrogen (ref. 1). We are investigating a new conversion process using a highly efficient ortho-para hydrogen converter in the form of Cr_2O_3 powder as the active element. The oxide is contained in a continuous heat exchanger that allows the heat of conversion to be removed by the hydrogen gas flow.

Accomplishments

1. We have modified the electronic readout circuit for the ortho-para ratiometer to optimize the speed of response of the thin-film circuit used to measure the thermal conductivity of the gas in the ortho-para hydrogen cell. The circuit diagram is given in figure 1. The results of tests for the circuit to control current to maintain the resistance (temperature indicator) at a constant value is given in table 1. The cell is shown in figure 2.
2. We have changed one of the critical parameters of the ortho-para hydrogen ratiometer, namely the gap between the thin film sensor and the cold plate from 0.75 to 1.575 mm. The results for the new configuration are shown in figure 3(c). The data is consistent with the change in geometry. The thermal conductivity of nitrogen gas has also been measured to provide a calibration test. The results show a similar pressure independent behavior for a wide range of pressure as seen in studies of hydrogen for similar current settings. The thermal conductivity data has shown a wide range of pressure independence up to 1.4 bar. This region of independence is consistent with theory and indicates the design is successful in eliminating the effects of convection. The new results for the test are shown in figure 3(a) and an expanded view is shown in figure 3(b). We will also carry out measurements for different gases and different mixtures of ortho and para hydrogen.
3. Research has been initiated to test the efficiency of Cr_2O_3 as a catalytic agent for rapid ortho-para conversion. An ultra-fine chromic oxide powder (~1 micrometer diameter) is being considered for temperatures ranging from 4 to 25 K (fig. 4).

TABLE 1.—BRIDGE CONTROLLER PERFORMANCE
(MAINTAIN RESISTANCE AS A CONSTANT)

Operating Point:	6.9
Current Gain:	4.0
Cell Current:	70.01 mA
Cell Resistance:	10.05 Ω
Cell Power:	49.26 mW
Cell Current:	69.89 mA
Cell Resistance:	10.09 Ω
Cell Power:	49.29 mW
Cell Current:	70.13 mA
Cell Resistance:	10.01 Ω
Cell Power:	49.23 mW

Operating Point:	6.9
Current Gain:	8.0
Cell Current:	69.71 mA
Cell Resistance:	10.05 Ω
Cell Power:	48.84 mW
Cell Current:	69.39 mA
Cell Resistance:	10.09 Ω
Cell Power:	48.58 mW
Cell Current:	70.03 mA
Cell Resistance:	10.01 Ω
Cell Power:	49.09 mW

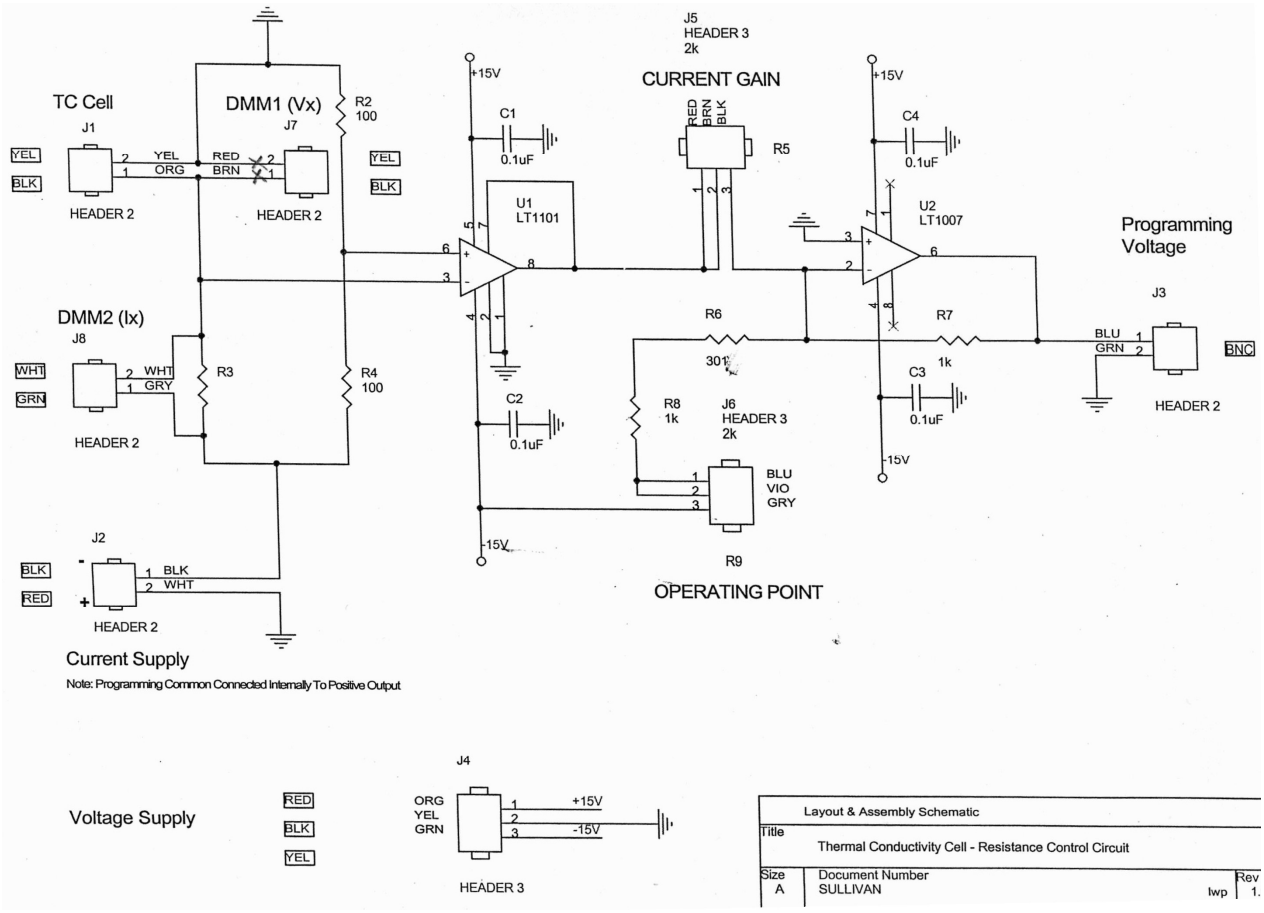

Figure 1.—Schematic circuit diagram of bridge control for a constant resistance.

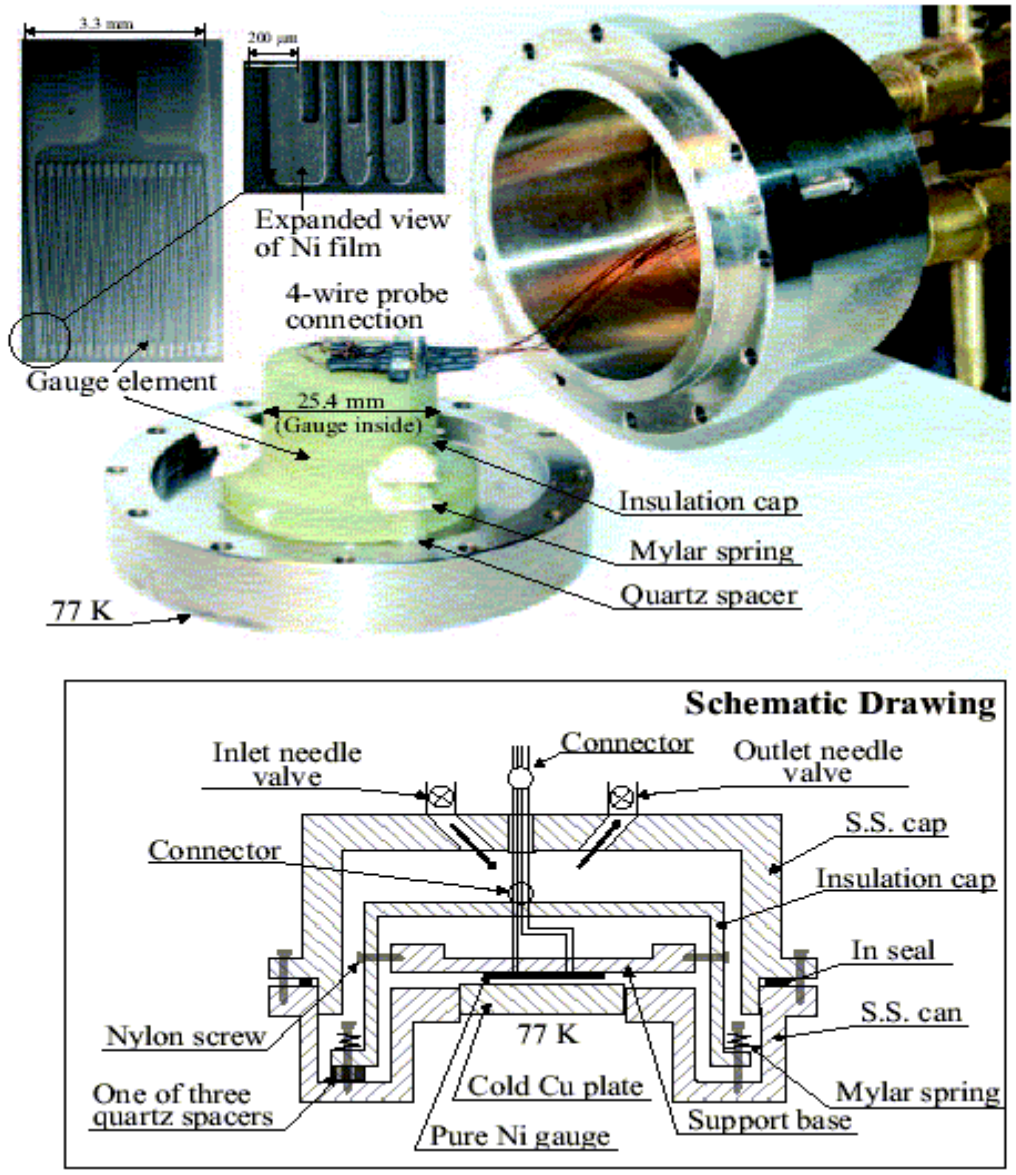

Figure 2.—Ratiometer design and construction.

Measurement by the Constructed Ratiometer

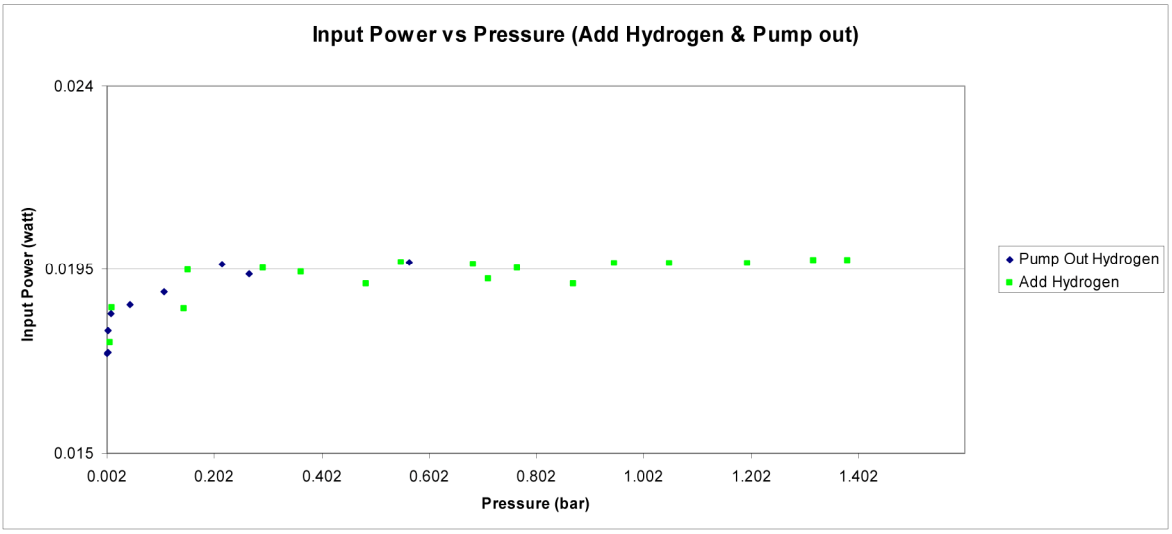

Figure 3(a)

Expanded View

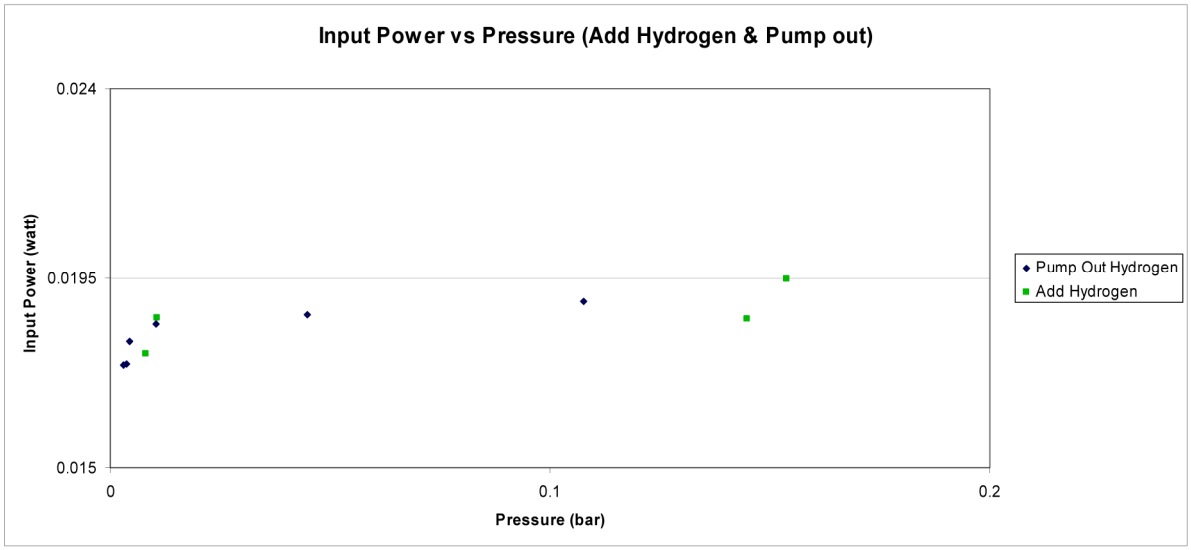

Figure 3(b)

Hydrogen &Nitrogen Gas Measurement

(Gap between film and cold plate changed to 1.575 mm)

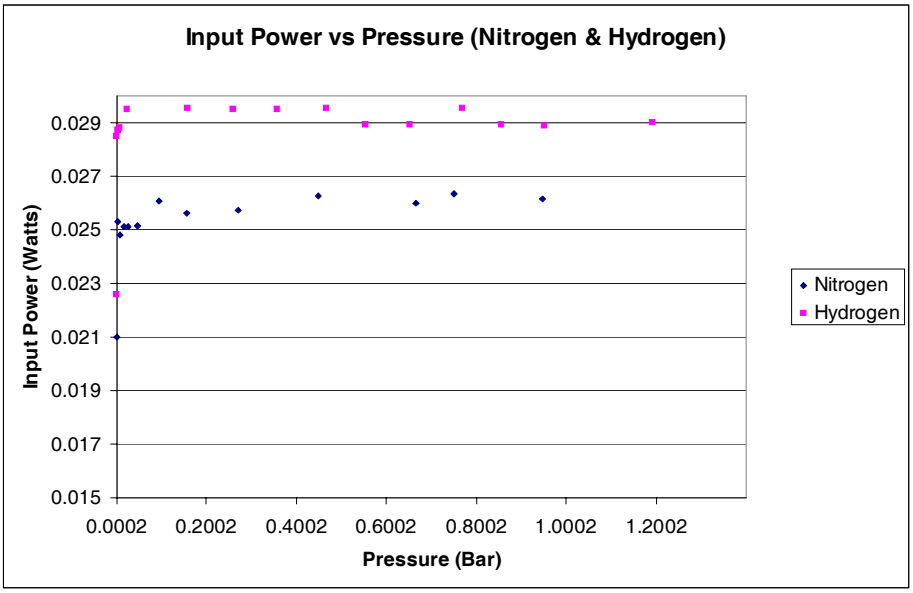

Figure 3(c)

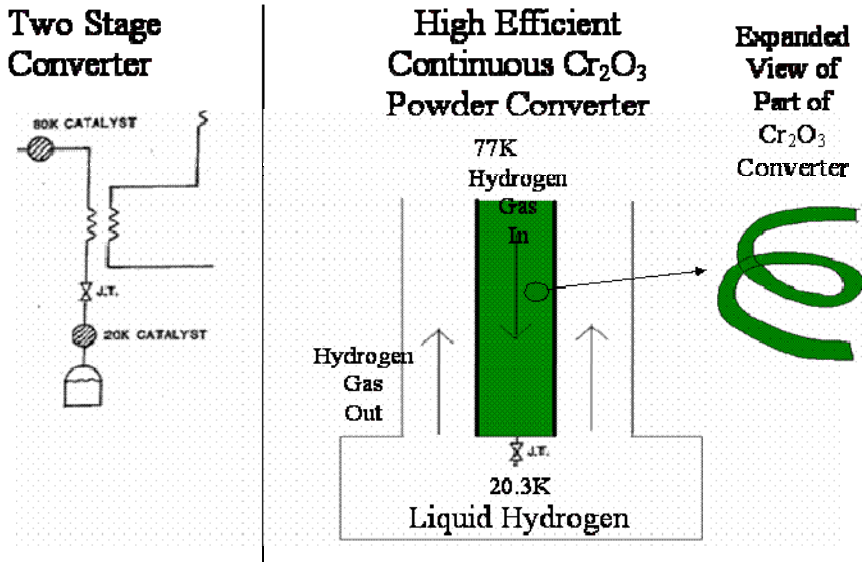

Figure 4.—Cr_2O_3 as a catalytic agent for rapid ortho-para conversion.

References

1. A. Farkas, *Orthohydrogen, parahydrogen and heavy hydroge*n, Cambridge University Press, Cambridge, UK, 1935.
2. I.F. Silvera, *Rev. Mod. Phys.* **52**, 393 (1980).
3. G. K. White, *Experimental Techniques in Low Temperature Physics*, Clarendon Press, Oxford, 1968, p. 47, 119.
4. T.M. Flynn, *Cryogenic Engineering, Marcel Dekker*, Inc., New York, 1977, p. 130.
5. N.S. Sullivan, D. Zhou and C.M. Edwards, *Cryogenics,* **30**, 734 (1990).
6. K.D. Williamson, Jr., F.J. Ederskuty, *Liquid Cryogens V1*, CRC Press Inc., 1983, p. 96–100.
7. E.R. Grilly, *Rev. Sci. Instr.* **24**, 72 (1953).
8. M. Devoret, N.S. Sullivan, D. Esteve and P. Deschamps, *Rev. Sci. Instr.* **51**, 1220 (1980).
9. N.V. Tsederberg, *Thermal Conductivity of Gases and Liquids*, Technology Press, Cambridge, Mass., 1965.
10. J.E. Jensen, R.B. Stewart and W.A. Tuttle, *Natl. Bur. Standards. Rept.* 8812 (1955).
11. J.O. Hirshfelder, C. F. Curtiss, and R.B. Bird, *Molecular Theory of Gases and Liquids*, Wiley, New York, 1954.
12. W.A. Wakeham, *J. Phys. E* **4**, 443 (1971).
13. A.B. Littlewood, *Gas Chromatography, Academic Press*, New York, 1962, Chap. 10.
14. D. Zhou, G.G. Ihas, and N.S. Sullivan, *Bull. Am Phys. Soc.,* **48**, 1277 (2003).
15. Vishay Measurements Group Inc., Rayleigh, NC.

Publications

1. D. Zhou, G.G. Ihas and N.S. Sullivan, Determination of Ortho-Para Ratio in Gaseous Hydrogen Mixtures, Journal of Low Temperature Physics, **134**, 401 (2004).
2. D. Zhou and N.S. Sullivan, Presentation at NASA Hydrogen Review Meeting, March 4, 2004.
3. D. Zhou and N. Sullivan, Ortho-*para hydrogen ratiometer design*, presented at Proceedings of the Internat. Low Temp. Physics Conference, Orlando, 2005.

Project Title: High Energy Densified Materials

Task PI: Gary G. Ihas, Department of Physics
Post Doctoral Associate: John T. Graham, Department of Physics

Project Goals

The major impetus in the recent surge in the study of solid hydrogen and in particular the study of chemical species isolated in solid hydrogen has been the possible use of the material as rocket fuel. The incentive to this was the suggestion that metal atoms could be used as performance improving additives to the current state of the art liquid oxygen/liquid hydrogen propellant system. The major point of interest is the specific impulse I_{sp} of the propellant system, which is a measure of the momentum transferred to the vehicle per mass of the working fluid expelled from the rocket engine, and is proportional to the mean velocity of the exhaust. The specific impulse is proportional to the specific enthalpy of the chemical reaction occurring in the engine, and so can be changed by introducing dopants. Table 1 shows the theoretical specific impulses and their percentage change for 5 percent mole concentration of atoms in solid hydrogen propellants compared with the current liquid hydrogen system, reprinted from Fajardo et al. (ref. 1).

TABLE 1.—THEORETICAL SPECIFIC IMPULSES OF ATOM DOPED SOLID HYDROGEN PROPELLANTS

Additive	I_{sp}	Percent improvement
None	389	-
H	407	5
Li	401	3
Be	451	16
B	470	21
C	469	21
N	414	6
O	411	6
F	398	2
Na	373	–4
Mg	398	2
Al	425	9
Si	432	11
Ti	404	4

Clearly the systems of interest in this study are beryllium, boron, carbon, silicon and possibly aluminum. The major point of note is that this is a theoretical study and assumes that there is no interaction between the atomic species and the solid hydrogen. Several questions are raised by this study. First, can the atomic species of interest be actually produced and entrapped in solid hydrogen at 2 or 4 K? Second, to what degree does the atom interact with the solid hydrogen, and are molecular species produced?

These questions may be answered by reviewing the open academic literature considering either studies of species in solid hydrogen or matrix isolation studies in noble gas matrices where the matrix is doped with a small amount of hydrogen.

In our earlier reports we reviewed the open academic literature considering the entrapment of either boron or carbon in hydrogen matrices or in noble gas matrices where the matrix is doped with a small amount of hydrogen. In review, although it appears that both boron and carbon vaporizing species interact with hydrogen, boron vaporizes as an atomic or dimeric species whereas carbon vaporizes in a plethora of carbon chain species the nature of which is being studied extensively by many research groups using matrix isolation. See, for example, studies by Larson (ref. 2) and Meirs (ref. 3), including detailed studies using hydrogen as the isolating matrix.

Accomplishments

Boron in Solid Hydrogen

Boron and carbon are considered of interest due to the high percentage improvements in the I_{sp}. Our first candidate for study was be boron. It is well known that boron vaporizes as boron atoms and the dimeric species B_2 (ref. 4), and it is believed that boron atoms may be easily trapped in solid hydrogen. A theoretical study (ref. 5) indicated that the reaction path

$$B + H_2 \rightarrow BH_2$$

was unlikely to occur. To date, two major studies have vaporized boron into solid hydrogen. Fajardo et al. (ref. 6) used ultraviolet \ visible spectroscopy to study the process and noted that although the resulting spectra were similar to those observed in rare gas matrices, there were significant frequency shifts. In the field of matrix isolation spectroscopy, major frequency shifts between matrices can sometimes be an indicator of the isolated species interacting with the surrounding matrix. The second study vaporizing boron into solid hydrogen was done by Weltner et al. (ref. 7) using electron spin resonance (esr) as the identifying technique. The sole species identified was boron tetrahyride (BH_4); no boron atoms were observed. The esr spectrum of boron atoms is complex but very distinctive and has been the subject of much study (refs. 8 and 9).

There is clearly a conflict in the open literature, with one study indicating the possibility of boron atoms, and the other study concluding that all of the boron reacts with hydrogen to form BH_4. Supplementary clues are obtained by the studies of Andrews et al. (refs. 10 and 11). In a detailed study Andrews and Tague (ref. 10) vaporized boron in argon matrices doped with amounts of hydrogen and found that a plethora of boron hydride species were formed. Increasing the hydrogen content and trapping in neon resulted in the production of the species BH_4 and BH_4^- (ref. 11); all of these species were characterized using infrared spectroscopy. The literature evidence suggests that boron readily reacts with hydrogen to possibly form a variety of species but predominately hydrogen boron tetrahydride. In addition, boron readily reacts with trace impurities in the matrix gas (see for example discussion in ref. 10). This is known and has been studied extensively, but may increase the difficulty in interpreting results if ignored.

Carbon in Solid Hydrogen

Studies of the vaporization of graphite and the subsequent entrapment of the vapor in hydrogen have followed the pattern of the noble gas matrices. Van Zee et al. (ref. 12) vaporized graphite and using esr spectroscopy identified the species C_4 in solid hydrogen, whereas by using deuterium obtained spectra for C_4, C_6, C_8 and C_{10}. Using infrared spectroscopy Shida et al. (ref. 13) identified the species C_3 C_5 C_9 and other clusters. It is interesting to note that no hydrocarbon species were observed. Tam et al. (ref. 14) vaporizing graphite into hydrogen matrices also observed the carbon species C_3 ,C_6 ,and C_9, as well as the hydrocarbon species CH_4 and CH_3. It was noted that the CH_4: C_3 ratio increased dramatically as the laser ablation energy increased. This is consistent with the mass spectrometric study by Kato et al. (ref. 15) of the vaporization of graphite in the presence of hydrogen and deuterium gasses. The conclusion of this study was that hydrocarbon species originate mainly from the reaction of carbon species and the thermally decomposed hydrogen atoms produced by the intense vaporization pulses.

The major conclusion from the literature on carbon species entrapped in solid hydrogen is that there is a general consensus on which carbon species are isolated and that the infrared spectra are of a very high quality. This was the main reason that we chose to make our initial studies on the boron / hydrogen system.

Apparatus

In our previous reports we described the construction and initial testing of our cryostat. In summary, cool down of the polished aluminum support from room temperature to circa 4 K was achieved routinely in less than 10 min. Figure 1 shows a cross sectional view of the lower section of the cryostat showing the positioning of the boron sample relative to the polished aluminum sample support and the access window for the laser. Figure 2 shows a typical experiment in progress. The cryostat (a) is mounted on a custom made optical bench, which enables consistent positioning of the cryostat relative to the external sampling port of the Bruker infrared spectrometer (b). The movable pumping station (c), consisting of a diffusion pump and a backing rotary pump, is connected to the cryostat via a flexible vacuum line. The computer console (d) runs the spectrometer and analyzing spectra. The panel (e) is the hydrogen handling and purification system. Liquid helium is transferred from the liquid helium dewar (f) via the flexible transfer line (g) to the cryostat; exhaust gas is collected by the flexible recovery line (h), which is connected to the permanent laboratory recovery system (i). The Nd:YAG laser (j) with steering optics have been temporarily moved aside. The movable pumping station with flexible vacuum line (c) and the flexible recovery line (h) are features that enable the rotation of the top section of the cryostat and the inner cold finger under cryogenic and high vacuum conditions

The spectrometer used is a Bruker IFS-113 with p.c. control, the laser used is a Nd:YAG pulsed q switched and frequency doubled, and is used under conditions known to vaporize the vast majority of materials.

Deposition of Solid Hydrogen at 4 K

To produce a sample for study, a solid hydrogen film was formed on the polished aluminum support by cooling the cryostat down to 4 K and then slowly bleeding hydrogen into the hydrogen inlet line using a needle valve. Figure 3 shows a typical infrared spectrum obtained after about 20 min deposition, without utilizing the purification system. The infrared spectrum exhibits the fundamental vibrations for carbon dioxide and monomeric water (ref. 16), in addition to weak features labeled (*) due to hydrocarbons. All three species are known to be trace impurities in many gasses including hydrogen, and carbon dioxide and water have been characterized in solid hydrogen (refs. 17 and 18). The bands assigned to carbon dioxide and water are particularly striking as those molecules are very strong infrared absorbers and are often used as internal calibrants. Utilizing the cold trap in the purification apparatus removes all of these features apart from a very weak absorbance at about 2345 cm^{-1}, which is the strong fundamental for carbon dioxide.

Vaporization and Trapping of Boron in Solid Hydrogen at 4 K

As shown in figure 1 the sample of solid boron is mounted in the vacuum chamber in such a way that the plume of laser ablated material is mixed with the large excess of hydrogen before being deposited on the cold polished support. Typically a thin bed of solid hydrogen is laid down on the polished surface prior to commencement of laser ablation. Infrared spectra are acquired every 10 min of laser ablation in order to observe band growth and to assist spectral assignment. Occasionally laser ablation lasts up to 1 hr but is usually 20 to 30 min in duration. A typical experiment lasts several hours with no noticeable deterioration in spectral quality or relative band intensity changes.

Figure 4 shows a typical early infrared spectrum produced after the deposition of boron vapor and hydrogen without purifying the hydrogen, as usual residual impurities water, carbon dioxide and hydrocarbons are observed. However, two new bands are observed in the region 2250 to 2000 cm^{-1} that are within the B-H stretching region. The feature at about 2017 cm^{-1} is identified as a hydrolysis species such as HOBO. Later experiments exhibit spectra typical of figure 5 in which the feature at 2017 cm^{-1} is absent but a feature at about 474 cm^{-1} consistent with the species HBO is observed. In all of the experiments involving boron, a sharp band at 2138 cm^{-1} is observed. When this band is strong a feature at

1305 cm^{-1} appears to be growing with it. Purifying the hydrogen prior to deposition eliminates the infrared absorptions due to water and virtually eliminates the feature at 2345 cm^{-1} assignable to the strong fundamental of carbon dioxide. However, the features at 2138 and 1305 cm^{-1} are still produced.

We tentatively assign the infrared absorption at 2138 cm^{-1} to the chemical species BH_4 in addition to the feature at 1305 cm^{-1}. Andrews and Wang (ref. 11) assign four infrared absorptions to BH_4 in neon. However, it is believed they have a distorted tetrahedral system consisting of two short and two long B-H bonds with the bond angle between the two long B-H bonds a mere 46.7°. This structure is consistent with the structure proposed by Weltner et al. (ref. 7) who characterized BH_4 in hydrogen at 2 K. We are proposing that BH_4 in hydrogen at 4 K is more like the classic tetrahedral with all four B-H bonds essentially equivalent. It is known that solid hydrogen at 4 K is a lot softer than the same solid at 2 K, which would enable the species to relax to the tetrahedral we are postulating. The difference in softness between 2 and 4 K is one of the reasons that the majority of researchers operate at 2 K. Clearly further work is required to clarify the situation.

Vaporization and Trapping of Carbon in Solid Hydrogen at 4 K

A small chunk of high purity graphite was mounted in our sample chamber in a similar manner to that of boron, was ablated using the Nd:YAG laser, and the resulting vapor isolated in a hydrogen matrix. Figure 6 shows a typical infrared spectrum after about 30 min of vaporization/deposition. By comparison with the earlier literature studies, we can readily identify the carbon species C_3 ,C_6 ,C_5 ,and C_9, as well as a very weak absorbtion assignable to the species CH_3 . It is important to note that we did not observe the species CH_4 which has been extensively studied in hydrogen matrices (ref. 19) and was observed by Tam et al. (ref. 14). Of interest are the two weak features marked * and may be the species $C(H_2)$. This species has been the subject of extensive interest and questions have been recently raised (ref. 20) concerning how atomic carbon interacts with molecular hydrogen, whether it forms an adduct species $C(H_2)$, or if it goes all the way and inserts into the hydrogen molecule to form the molecular species CH_2. The positions and relative intensities of the two infrared bands will help to tackle this question as a dipole induced by the carbon atom in the hydrogen molecule may induce infrared activity.

Continuous Flow Liquid Helium Cryostat

We have constructed a ‘bare bones’ continuous flow liquid helium cryostat designed for infrared studies of solid hydrogen and isolated molecular species at either 2 or 4 K. A detailed description of the cell construction and testing has been published (ref. 21). The use of a heater we installed will enable studies up-to about 6 K, which opens up the possibility of diffusion and stability studies. To date, all of our studies have been at 4K which is a testament to the skill and expertise of the Physics Department Machine Shop and Cryogenic Services in the construction and design of the cell.

We have been able to routinely trap high temperature chemical species in solid hydrogen at 4 K using this apparatus and produce stable matrices for study at leisure. The majority of researchers usually operate at 2 K when trapping species in hydrogen due to the fickle nature of solid hydrogen. A temperature of 2 K is obtained by pumping on the liquid helium coolant with a roughing vacuum pump resulting in evaporative cooling, but at the expense of higher liquid helium consumption.

In this project we have demonstrated the vaporization of both boron and carbon and trapped the resulting vapors in solid hydrogen as initially proposed by us. In addition, preliminary analysis of the infrared spectra, indicate that molecular species such as boron hydrides and carbon chains or clusters are formed rather than solely atomic species.

This work was briefly mentioned in an article in *Cold Facts*, the magazine of the Cryogenic Society of America, Inc., authored by Van Sciver (ref. 22). In the article our aims, goals, and techniques were gratefully mentioned. However, the article claimed that our work was the first to embed carbon and boron in solid hydrogen. This is not the case. Many groups have preceded our work (Weltner, Fajardo, Andrews, Momose, and Shida to list a few), and we have benefited greatly from them.

Further Studies

The theoretical specific impulses calculated by Carrick (ref. 23) and quoted by Fajardo et al. (ref. 1) assumed the ability to produce solely atomic species at a concentration of 5 percent in solid hydrogen. This would result in a significant improvement in the specific impulse of the rocket. We have demonstrated that the vaporization of either boron or carbon results in the generation of a plethora of molecular species, which is entirely consistent with previous studies of the systems in noble gas matrices and mass spectrometric studies.

In order to accurately access the validity of high energy densified fuels based on impurity doped solid hydrogen as the new generation of rocket fuels, calculations need to be made on solid hydrogen doped with molecular species such as C_3 or BH_4, rather than the imagined atomic species.

The next step in this work would be to improve the quality of the infrared spectra and to confirm the spectral assignments. The use of isotopes such as ^{12}C, ^{13}C, ^{10}B, ^{11}B, ^{1}H, and ^{2}H (D) is one of the most powerful tools available to the matrix isolationist for spectral identification. Further analysis of the data will be needed to order to attempt to quantify the relative concentrations of the chemical species, in particular the carbon system. The possible presence of $C(H_2)$ in the carbon system offers the exciting possibility of being able to monitor the interaction of an atomic species with hydrogen, whether it is with the bulk hydrogen or a single hydrogen molecule.

The use of infrared spectroscopy to monitor the generation of species produced by the reaction of boron atoms and dimmers with trace impurities such as water and carbon dioxide (not just hydrogen) is of immense value as impurities will always be present and they should not be ignored.

We are at present unable to pursue any of this exciting research, as our funding was not renewed. We are aware that this research offers few if any immediate applications or financial savings to NASA, but it is much more difficult to dismiss the long term applications of such exciting research results.

References

1. M.E. Fajardo, S. Tam, T.L. Thompson, M.E. Cordonnier, Chem. Phys. **1994** 189 351 and references therein.
2. C. Larson, W. Harper, J. Presilla-Marquez, Matrix Isolation of Boron and Carbon Vapor. (2000), 15(Pt. 1, High Temperature Materials Chemistry, Part 1), 349–352. AN 2001:340042
3. J. P Maier, J. Phys. Chem. A **1998**, 102(20), 3462.
4. L.B. Knight, B.W. Gregory, S.T. Cobranchi, D. Feller, E.R. Davidson. J. Am. Chem. Soc. **1987** 109 3521.
5. M.H. Alexander. J. Chem. Phys. **1993** 99 6014.
6. S. Tam, M. Macler, M.E. DeRose, M.E. Fajardo. J. Chem. Phys. **2000** 113 9067.
7. M.E. Fajardo, S. Tam J. Chem. Phys. **1998** 108 4237.
8. R.J. Van Zee, A.P. Williams, W. Weltner Jr. J. Chem. Phys. **1997**, 107 4756.
9. A detailed description of the esr of boron atoms is given in :-W. Weltner Jr. Magnetic Atoms and Molecules Publ Dover pub New York 1989.
10. T. Kiljunen, J. Eloranta, J. Ahokas, H. Kunttu, J. Chem. Phys. **2001**, 114(16), 7144.
11. J. Tague Jr., L. Andrews J. Am. Chem. Soc. **1994**, 116, 4970.
12. L. Andrews, X. Wang. J. Am. Chem. Soc. **2002** 124 7280.
13. R.J. Van Zee, S. Li, W. Weltner Jr. J. Phys. Chem. **1993** 97 9087.
14. M. Miki, T. Wakabayashi, T. Momose, T. Shida. J. Phys. Chem. **1996** 100 12135.
15. S. Tam, M. Macler, M.E. Fajardo. J. Chem. Phys **1997** 106 8955.
16. Y. Kato T. Wakabayashi, T. Momose, Chem. Phys. Lett. **2004** 386 279.
17. K. Nakamoto Infrared and raman of inorganic and coordination compounds Publ. J. Wiley New York 1997.
18. S. Tam M.E. Fajardo. Low Temp. Phys. **2000** 26 653.
19. M.E. Fajardo, S. Tam, M.E. DeRose J. Mol. Struct. **2004** 695 111.

20. The sharpness and quality of the infrared spectra of methane isolated in hydrogen matrices is remarkable and the observation of rotational fine structure offers the ability for detailed analysis see for example a) T. Momose, T. Shida Bull. Chem. Soc. Jpn. **1998** 71 1 b) L. Li, J.T. Graham, W. Weltner Jr. J. Phys. Chem. **2001** 105 11018 c) T. Momose. H. Hoshina, M. Fushitani, H. Katsuki, Vibrational Spectroscopy **2004** 34 95 d) S. Tam, M.E. Fajardo, H. Katsuki, H. Hoshina, T Wakabayashi, T. Momose, J. Chem. Phys. Phys. **1999** 111 4191 e) T. Momose, M. Miki, T. Wakabayashi. T. Shida, M. Chan, S.S. Lee, T. Oka J. Chem. Phys. **1997** 107 7707 f) Y. J. Wu, X. Yang, Y.P. Lee, J. Chem. Phys. **2004** 120 1168
21. M. Vala, J. Szczepanski personal communication.
22. J.T. Graham, G.G. Ihas J. Low Temp. Phys. **2005** 138(3/4) 923.
23. S. Van Sciver Cold Facts Summer **2004** 20(3) p6.
24. P.G. Carrick Specific Impulse Calculations of High Energy Density Solid Cryogenic Rocket Propellants 1: Atoms in Solid Hydrogen NTIS Report **1993** (PL–TR–93–3014 Order no. AD–A263208

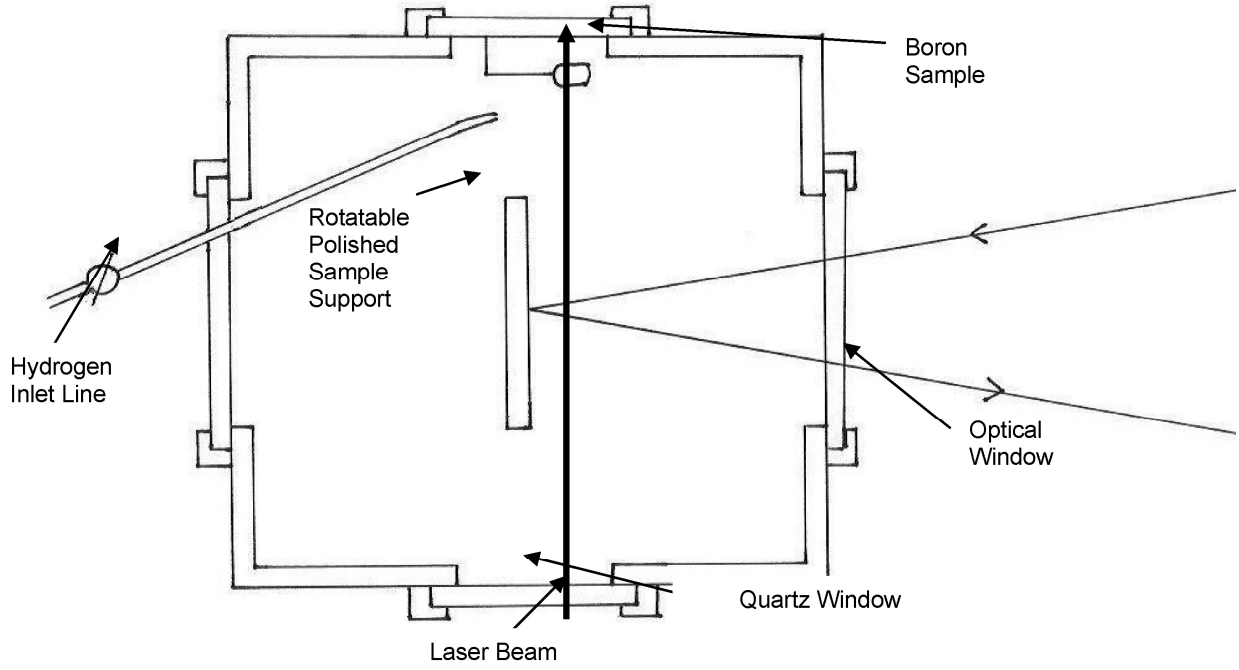

Figure 1.—Cross sectional view of the Cryostat.

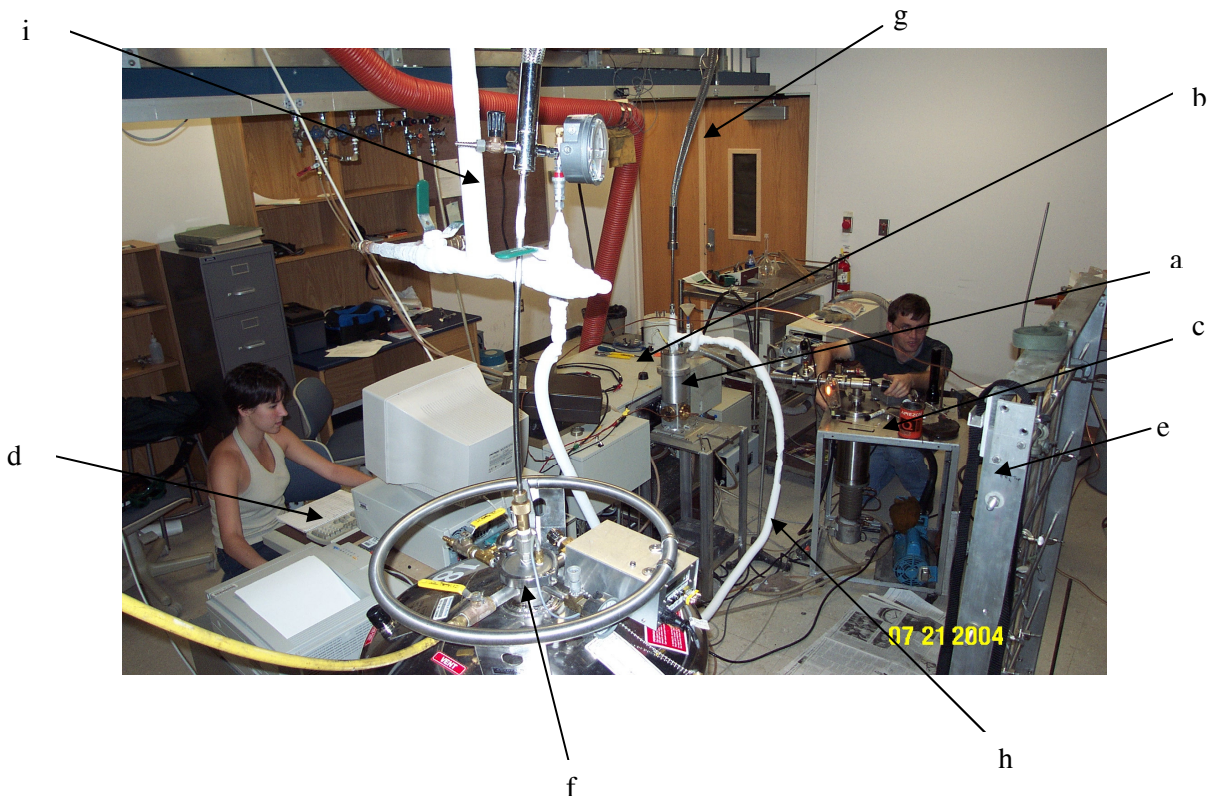

Figure 2.—Typical experimental setup in progress. The cryostat (a) is mounted on a custom made optical bench, which enables consistent positioning of the cryostat relative to the external sampling port of the Bruker infrared spectrometer (b). The movable pumping station (c), consisting of a diffusion pump and a backing rotary pump, is connected to the cryostat via a flexible vacuum line. (d) is the computer console for running the spectrometer and analyzing spectra. (e) is the hydrogen handling and purification system. Liquid helium is transferred from the liquid helium dewar (f) via the flexible transfer line (g) to the cryostat, exhaust gas is collected by the flexible recovery line (h), which is connected to the permanent laboratory recovery system (i). The Nd:YAG laser (j) with steering optics have been temporarily moved aside. The movable pumping station with flexible vacuum line (c) and the flexible recovery line (h) are features, which enable the rotation of the top section of the cryostat and the inner cold finger under cryogenic and high vacuum conditions

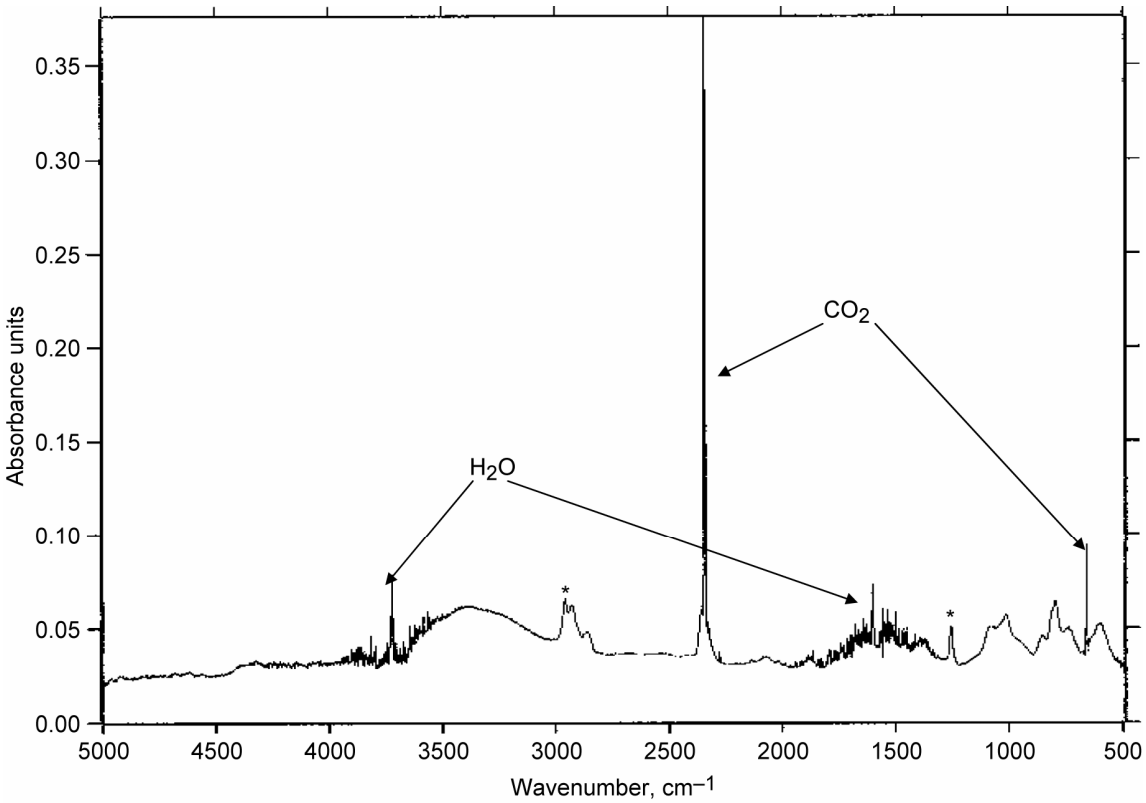

Figure 3.—Infrared spectrum of solid hydrogen film at 4 K.

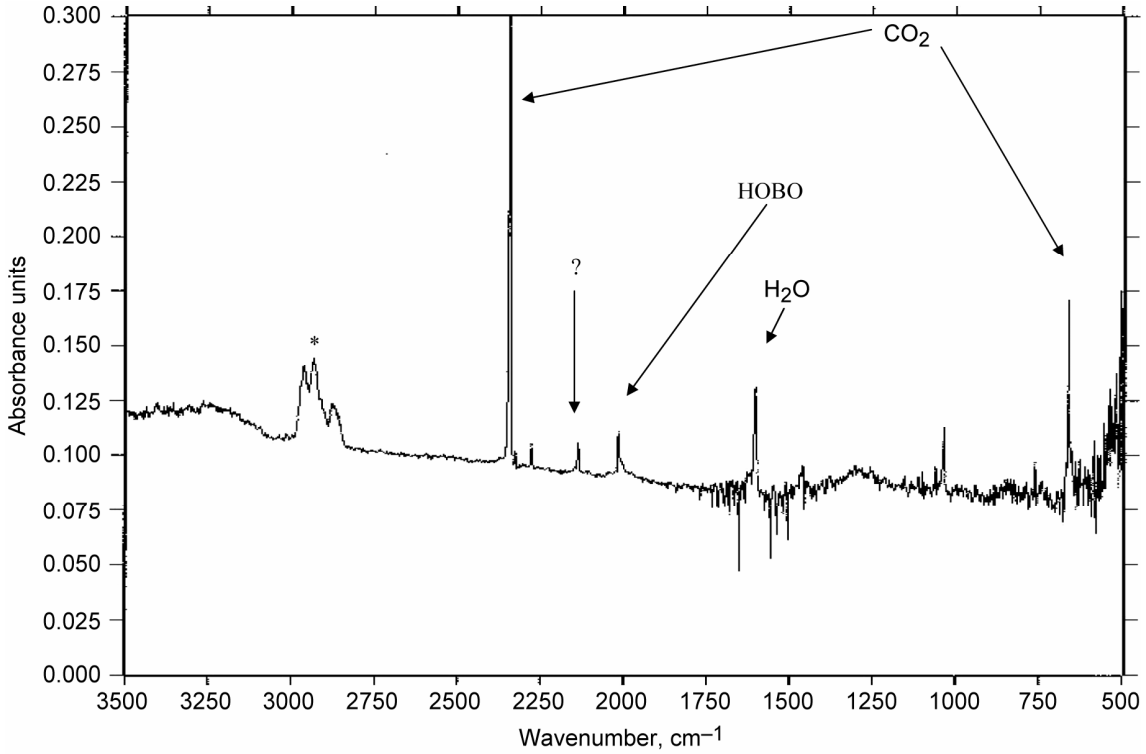

Figure 4.—Infrared spectrum produced by laser ablating boron and trapping in solid hydrogen at 4 K

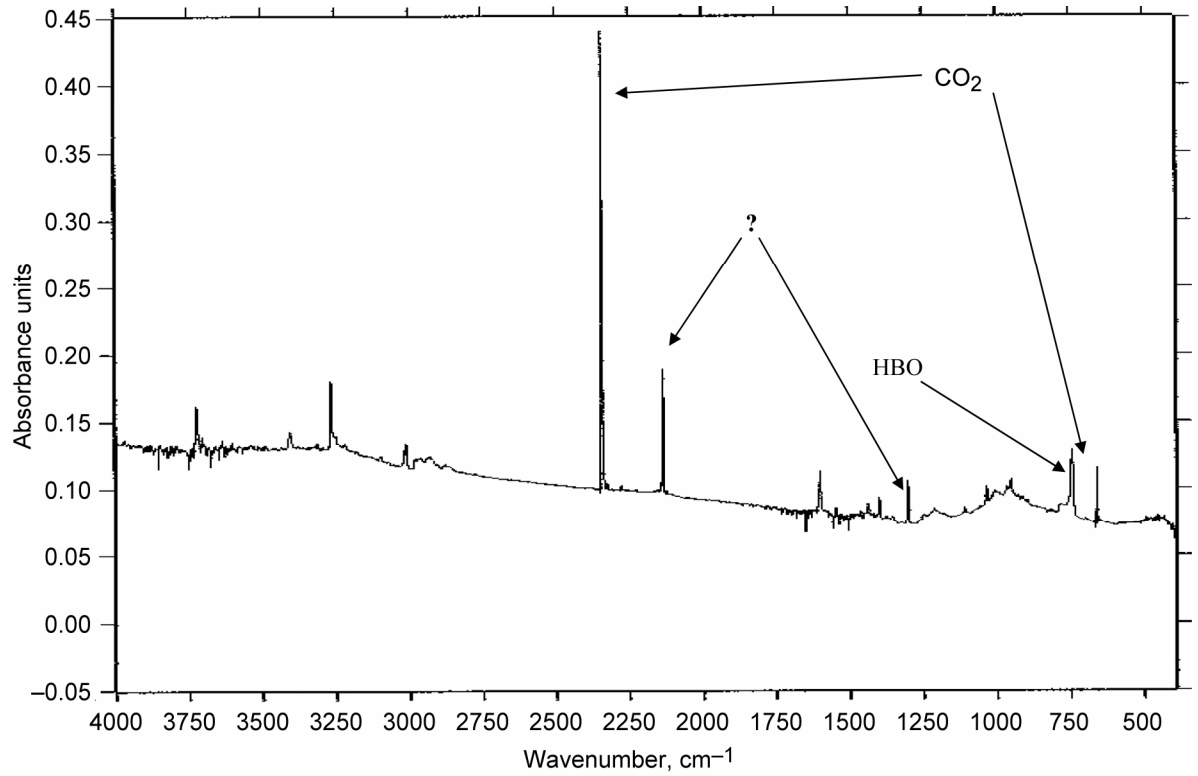

Figure 5.—Infrared spectrum produced by laser ablating boron and trapping in solid hydrogen at 4 K.

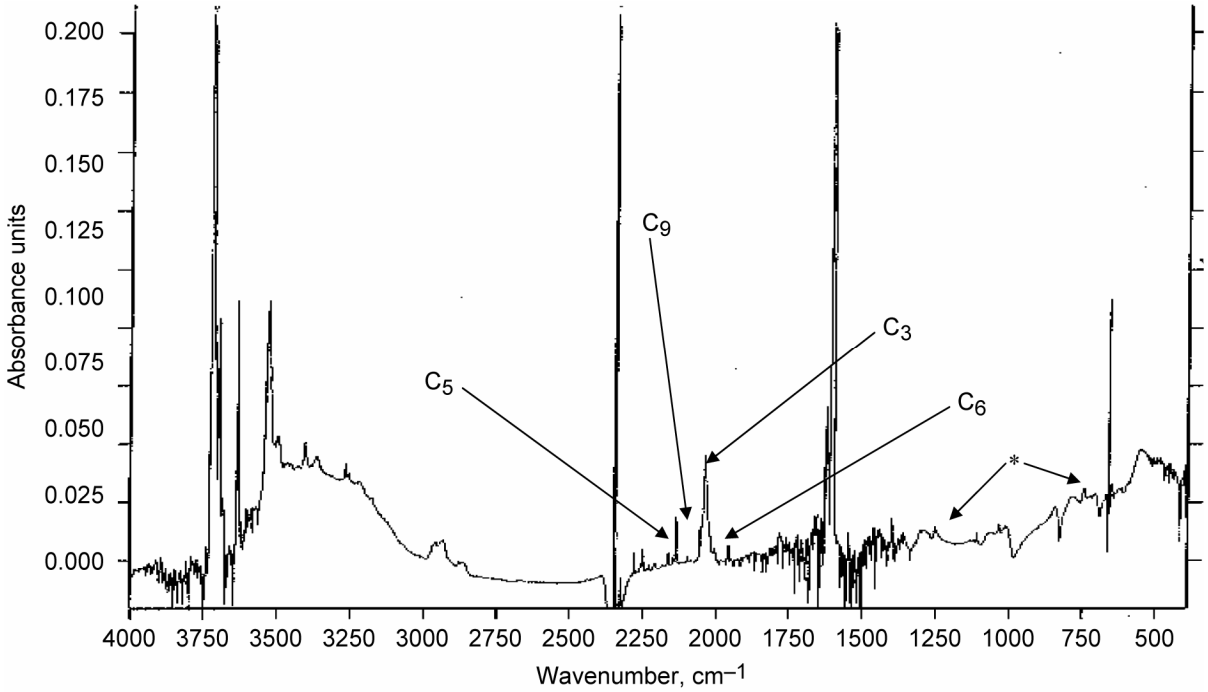

Figure 6.—Infrared spectrum produced by laser ablating carbon and trapping in solid hydrogen at 4 K.

REPORT DOCUMENTATION PAGE

Form Approved
OMB No. 0704-0188

1. AGENCY USE ONLY (*Leave blank*)	2. REPORT DATE	3. REPORT TYPE AND DATES COVERED
	July 2006	Final Contractor Report—August 1, 2003 to August 1, 2005

4. TITLE AND SUBTITLE

NASA Hydrogen Research for Spaceport and Space Based Applications

5. FUNDING NUMBERS

WBS 561581.02.01.03.12

6. AUTHOR(S)

Tim Anderson

7. PERFORMING ORGANIZATION NAME(S) AND ADDRESS(ES)

University of Florida
300 Weil Hall
Gainesville, Florida 32611

8. PERFORMING ORGANIZATION REPORT NUMBER

E–15428

9. SPONSORING/MONITORING AGENCY NAME(S) AND ADDRESS(ES)

National Aeronautics and Space Administration
Washington, DC 20546–0001

10. SPONSORING/MONITORING AGENCY REPORT NUMBER

NASA CR—2006-214091

11. SUPPLEMENTARY NOTES

Project manager, Timothy D. Smith, Aeronautics Division, NASA Glenn Research Center, organization code PRV, 216–977–7546.

12a. DISTRIBUTION/AVAILABILITY STATEMENT

Unclassified - Unlimited
Subject Categories: 28, 33, and 34

Available electronically at http://gltrs.grc.nasa.gov

This publication is available from the NASA Center for AeroSpace Information, 301–621–0390.

12b. DISTRIBUTION CODE

13. ABSTRACT ***(Maximum 200 words)***

The activities presented are a broad based approach to advancing key hydrogen related technologies in areas such as hydrogen production, distributed sensors for hydrogen-leak detection, laser instrumentation for hydrogen-leak detection, and cryogenic transport and storage. Presented are the results form 15 research projects, education, and outreach activities, system and trade studies, and project management. The work will aid in advancing the state-of-the-art for several critical technologies related to the implementation of a hydrogen infrastructure. Activities conducted are relevant to a number of propulsion and power systems for terrestrial, aeronautics, and aerospace applications.

14. SUBJECT TERMS

Hydrogen; Cryogenic fluids; Cryogenic storage; Thermodynamics; Sensors; Hydrogen production

15. NUMBER OF PAGES

185

16. PRICE CODE

17. SECURITY CLASSIFICATION OF REPORT	18. SECURITY CLASSIFICATION OF THIS PAGE	19. SECURITY CLASSIFICATION OF ABSTRACT	20. LIMITATION OF ABSTRACT
Unclassified	Unclassified	Unclassified	